Final Report

RELATIVE EFFECTS OF FLOW AND ORIENTATION ON THE CRITICAL HEAT FLUX IN SUBCOOLED FORCED CONVECTION BOILING

By

Matthew J. Brusstar
Herman Merte, Jr.
Robert B. Keller

NASA Grant NGT-50928
Report No. UM-MEAM-95-15

Conducted under:

Graduate Student Researchers Program
National Aeronautics and Space Administration Headquarters
Washington, D.C.
and
Lewis Research Center
Cleveland, Ohio

Grant NGT-50928
and
Grant NAG3-1310

July 1995

ABSTRACT

RELATIVE EFFECTS OF FLOW AND ORIENTATION ON THE
CRITICAL HEAT FLUX IN SUBCOOLED FORCED CONVECTION BOILING

by

Matthew Joseph Brusstar
Herman Merte, Jr.
Robert B. Keller

This study is intended to clarify the relative significance of buoyancy and bulk flow inertia forces to the critical heat flux (CHF) in forced convection boiling, which will also serve to enhance the understanding of the CHF in microgravity, where buoyancy effects are absent. Measurements of the CHF in subcooled forced convection boiling of R113 were made on a flat copper heater surface at varying orientations relative to gravity for low flow velocities, where buoyancy is substantial compared to flow forces. An analytical model describing the effects of the flow velocity, heater orientation and subcooling was developed, relying partly on empirical relationships derived from hot wire anemometer measurements of the void fraction and bubble frequency.

The forced convection boiling experiments were conducted for subcoolings ranging from 2.8°C to 22.2°C, bulk flow velocities from 4 cm/s to 55 cm/s and heater orientations spanning 360 degrees. Included with the CHF Measurements are bubble frequency and void fraction measurements for downward facing orientations at various locations tangent and normal to the heater surface. A semi-transparent gold film heater on a quartz substrate was also used to permit high speed photography of the boiling process from beneath the heater surface, unencumbered by the vapor formed on the surface.

The experiments show that the CHF is a strong function of the heater surface orientation at very low flow velocities, and that orientation has a considerable effect on the CHF for flow velocities below 55 cm/s. In orientations where the buoyancy and flow forces oppose each other, the CHF is generally much lower than in orientations where they act in the same direction, owing to the increase in time during which the bubbles are resident at the heater surface. The analytical model of the CHF considers the motion of larger bubbles on the heater surface, relating the inverse of the bubble residence time to the CHF. The model also includes the effects of subcooling, which act to reduce the net vapor generation rate, thereby deferring the onset of the CHF to higher levels of heat flux.

This report is a major part of the dissertation submitted by the first author in partial fulfillment of the requirements for the degree of Ph.D. in Mechanical Engineering in the University of Michigan. Support was furnished in part under the NASA Graduate Student Researchers Program.

TABLE OF CONTENTS

LIST OF FIGURES

Figure

LIST OF TABLES

Table

LIST OF APPENDICES

Appendix

NOMENCLATURE

A_f	frontal area	[m^2]
$A_{\mu g}$	unit area in microgravity, Eqn. (3.64)	[m^2]
A_s	unit surface area	[m^2]
c	specific heat	[J/kg K]
c_{pl}	specific heat of the liquid	[J/kg K]
Ca	modified Capillary number, Eqn. (3.53)	[-]
C_d	drag coefficient	[-]
C_L	lift coefficient	[-]
D_b	bubble diameter	[m]
D_H	hydraulic diameter of the test section	[m]
ΔE	potential drop	[V]
E''	product of q_c and τ_{res}	[J/ m^2]
$\bar{f}$, f	mean bubble frequency	[Hz]
f^i_{drag}	drag force summation variable	[N]
f^i_{lift}	lift force summation variable	[N]
F_B	buoyancy force	[N]
$F_{buoy, x}$	buoyancy force component, x-direction	[N]
$F_{buoy, y}$	buoyancy force component, y-direction	[N]
F_{drag}	drag force	[N]
F_B	buoyancy force	[N]
F_{lift}, F_L	lift force	[N]
$F_{m.a., x}$	mass acceleration, x-direction	[N]
$F_{m.a., y}$	mass acceleration, x-direction	[N]
g	gravitational acceleration	[N/kg]
Gz	Graetz number (= (L/D)/RePr)	[-]
h_{fg}	latent heat of evaporation	[J/kg]
$\bar{I}$	mean current	[amp]
Ja	Jakob number (= $\rho_l c_p \Delta T_{sub}/\rho_v h_{fg}$)	[-]
K	gain	[various]
k	wavenumber, thermal conductivity	[1/m], [W/m K]
k_c	critical wavenumber, Eqn. (3.63)	[1/m]
L, L_{heat}	length of the heater surface	[m]
L_c	characteristic length given by Eqn. (3.52)	[m]
$m_{l, eff}$	virtual mass of a bubble	[kg]
$\dot{m}_v$	mass flow rate of vapor	[kg/s]
m_v	mass of the vapor	[kg]
P	pressure	[kPa]

$\dot{P}_{gen}$	total power input	[W]
Pr	Prandtl number (= ν/α)	[-]
q_c	CHF	[W/cm^2]
q_{co}	CHF in pool boiling w/subcooling, Eqn. (5.1)	[W/cm^2]
q_s, q_{surf}	surface heat flux	[W/cm^2]
q_z	CHF in saturated pool boiling, Eqn. (5.2)	[W/cm^2]
$\dot{Q}_{lh}$	rate of latent heat transfer	[W]
$\dot{Q}_{sp}$	rate of single phase heat transfer	[W]
$\dot{Q}_{loss}$	peripheral heat loss	[W]
R	characteristic radius	[-]
$\overline{R}$	mean bubble radius	[m]
R(t)	temporally-varying hot wire resistance	[Ω]
Re, Re_D	Reynolds number based on hydraulic diameter	[-]
Re_b	Reynolds number based on bubble diameter	[-]
$Ri_{2\phi}$	two-phase Richardson number, Eqn. (5.5)	[-]
s_i	total displacement of the bubble CM	[m]
t	time	[s]
ΔT_{sub}	bulk liquid subcooling	[°C]
ΔT_{sup}	wall superheat	[°C]
T_{sat}	saturation temperature	[°C]
u_*	friction velocity	[m/s]
u^+	dimensionless velocity	[-]
u, $\overline{u}$	local mean flow velocity	[m/s]
u_{vap}	velocity of the vapor	[m/s]
U_b, U_{bulk}	bulk flow velocity	[m/s]
U_{rel}	relative velocity	[m/s]
U_∞	buoyant terminal velocity of the vapor	[m/s]
ν'	volumetric rate of vapor generation	[m^3/s]
V	bubble volume	[m^3]
ΔV	potential drop	[V]
w_{heater}	heater width	[m]
We	Weber number based on heater length	[-]
We_D	Weber number (= $\rho U^2 D/\sigma$)	[-]
x_i	x-component of the bubble displacement	[m]
x_v	displacement of bubble, x-direction	[m]
y_i	y-component of the bubble displacement	[m]
y^+	dimensionless distance normal to the wall	[-]
y_v	displacement of bubble, y-direction	[m]

Greek

α	void fraction, thermal diffusivity	[vol/vol], [m^2/s]
β	wetting angle	[radians]
χ	fraction of total energy going into evaporation	[-]
χ_0	χ evaluated at saturation temperature	[-]
δ_E	equivalent evaporation layer thickness	[m]
δ_T	thickness of the thermal boundary layer	[m]
δ_{BL}	thickness of the bubble boundary layer	[m]
ε	surface roughness	[μm]
ε_i	uncertainty of i	[-]
Φ	correlation variable, Eqn. (3.51)	[-]
γ	ratio of vapor stem area to total area	[-]
$\lambda_{K\text{-}H}$	Kelvin-Helmholtz wavelength	[m]
λ_T, λ_D	most unstable Rayleigh-Taylor wavelength	[m]
μ, μ_l	dynamic viscosity of liquid	[Ns/m]
μ_v	dynamic viscosity of vapor	[Ns/m]
θ	heater orientation	[degrees]
ρ_l	liquid density	[kg/m^3]
ρ_v	vapor density	[kg/m^3]
σ	surface tension	[N/m]
τ	elapsed time during bubble growth	[s]
τ_{res}	bubble residence time	[s]
τ_w	wall shear stress	[Pa]
ξ	ratio of buoyancy to flow inertia, Eqn. (5.3)	[-]
ψ	intermediate form of Φ, Eqn. (3.49)	[-]

CHAPTER 1

INTRODUCTION

The study of the critical heat flux (CHF) in nucleate boiling originates with the work of Nukiyama (1934), in which the high rate of heat transfer in nucleate boiling was observed to reach an upper limit, beyond which a sudden deterioration in the heat transfer occurred. This limit, subsequently termed the "burnout heat flux" because of the potentially hazardous consequences of exceeding it, has since become the focus of many studies of nucleate boiling, as it represents the maximum or optimum heat flux attainable under a given set of conditions. More pessimistically, however, the CHF also represents the boundary of the transition to the film boiling regime, where the heat transfer coefficient may be degraded by several orders of magnitude.

Traditionally, research in nucleate boiling has been directed primarily toward terrestrial and marine power generation systems, where energy from a fuel source is transferred to water to generate high pressure steam. Nucleate boiling finds many important modern applications as well, since it offers rates of heat transfer far superior to those for single-phase convection, and therefore presents a path toward optimization in processes whose effectiveness is limited by the rate of heat transfer. Nucleate boiling is used in microelectronics cooling, for example, where the high rates of heat transfer made

available through the change of phase enables the design of smaller circuits with higher power densities. Boiling is also viewed as a particularly attractive means of transporting heat in applications to the space program, where payload considerations are paramount, as it permits minimization of the surface area in heat exchangers used for future power generation and thermal management systems. In both of these applications, optimization necessitates developing a means to predict the CHF for a specific set of operating conditions, so that the process may be designed to operate as close to the CHF as possible with minimal safety margins. The present work is intended to be a step towards that end, combining an experimental study of the CHF in flow boiling with an analytical model.

Predicting the CHF in the general case using a deterministic approach poses a formidable challenge, since many important aspects of boiling required for model closure are not yet well understood. On a local basis, boiling is a highly chaotic phenomenon in that the temporally-observed behavior of the vapor and liquid phases varies so vastly as to be considered nearly random. Despite this, the gross aspects of boiling, such as the heat transfer and CHF, behave consistently and repeatably for a given set of test conditions, owing to the invariant mean probability of the two phases behaving in a specific manner. Therein lies the problem to be resolved: reconciling the measured gross behavior of boiling with the locally observed behavior through an analytical expression. This often requires considerable empiricism and experimental evaluation, at the cost of generality. Precisely for this reason, well over a hundred different theoretical models of the CHF have been proposed on various grounds for a broad range of operating conditions.

The focus of the present study is the relative effect of buoyancy and flow forces on the CHF in forced convection, with particular emphasis on the development of a means for predicting the CHF with forced convection in microgravity. Past efforts to characterize the relative effects of buoyancy and flow forces have contrasted the CHF in downflow and upflow in vertical tubes at various flow rates, where the direction of the flow is changed relative to the buoyancy, since varying the magnitude of the buoyancy force in the laboratory presents many practical difficulties. The experiments of the present work examine the relative influence of buoyancy and flow inertia forces by changing the orientation of the entire flow system with respect to gravity, thereby varying both the direction *and* magnitude of the buoyancy force component in the direction of flow. It is anticipated that the results would aid in defining future flow boiling research in microgravity.

Four basic flow regimes have been identified in forced convection boiling for modeling purposes: bubbly flow, slug flow, annular flow and mist flow. In this context, the term CHF is conventionally used to denote the transition between the annular flow and mist flow regimes, which occurs upon dryout of the annular liquid film wetting the heated flow duct, often circular in cross-section. The present work is concerned primarily with the bubbly flow boiling regime, whose behavior is analogous to pool boiling in that the vapor is dispersed in discrete masses in the bulk liquid instead of in continuous slugs or strata characteristic of the slug and annular flow regimes. Consequently, the mechanisms for the CHF in the bubbly flow regime are expected to be similar to those observed for pool boiling, and the term "CHF" is used in a general fashion in the present

work to describe the heat flux level which effects the transition to film boiling on the heater surface.

One of the fundamental mechanisms related to the occurrence of the CHF in subcooled forced convection, the dryout of the heater surface, is examined experimentally in this work by relating the local statistically-averaged behavior of the liquid and vapor above the heater surface to the surface heat flux and surface temperature. In these experiments, the independent parameters of heat flux, bulk flow velocity, bulk liquid subcooling and heater surface orientation with respect to gravity are varied systematically. In addition, comparisons of the CHF for two heater lengths and two heater substrate materials are made. The principal objectives of this study are summarized as follows:

1. To identify the mechanisms which govern the onset of the CHF in subcooled forced convection boiling through experiments in which the major parameters identified above are varied, with an emphasis placed on clarifying the relative roles of buoyancy and flow forces.

2. To incorporate the results of these experiments into an analytical model which explicitly accounts for the effects of gravity, flow velocity, subcooling and heater length, and which may be used as an initial prediction for the CHF in microgravity.

CHAPTER 2

PREVIOUS RELATED WORKS

The CHF is a complex phenomenon influenced by many elements. Identifying and isolating the various forces and heat transfer mechanisms which affect the CHF provide in some cases insuperable challenges in the laboratory, and hence make the CHF difficult to model. A particularly relevant example to the present work is in forced convection boiling at low flow velocities under Earth gravity, where the buoyancy force acting on the vapor bubbles is quite large and tends to obscure the effects of other forces which would otherwise play a significant role in the absence of gravity. An examination of the influences of various parameters on the CHF as demonstrated in previous works is given below, and establishes the context of the experimental results to be presented in Chapter 5. In addition, the successes and shortcomings of previous models in characterizing the CHF in pool and forced convection boiling will be assessed in view of the experimentally observed behavior, perhaps lending insight into a means of modeling the CHF at low flow velocities under both Earth gravity and microgravity.

2.1. Parametric effects on the CHF

Principal dimensionless groups describing the CHF in both forced convection and pool boiling were identified by Katto (1978). Assuming that the CHF is brought about by a hydrodynamic instability between the vapor and liquid phases, the superficial vapor velocity, $q_{co}/\rho_v h_{fg}$, was correlated with the thermodynamic state and the viscous, inertial, gravitational and surface tension forces on dimensional grounds:

$$\frac{q_{co}/\rho_v h_{fg}}{U_{bulk}} = f\left(\frac{\rho_l}{\rho_v}, \frac{\mu_l}{\mu_v}, \frac{\sigma}{\rho_l U_{bulk}^2 L}, \frac{\mu_l}{\rho_l U_{bulk} L}, \frac{g(\rho_l - \rho_v)L}{\rho_l U_{bulk}^2}, \frac{D_H}{L}\right) \tag{2.1}$$

A similar result was obtained earlier by Ahmad (1973), using the Buckingham-Pi theorem applied to forced convection boiling in tubes. In pool boiling, the flow velocity and flow channel effects can be eliminated by rearrangement of Eqn. (2.1) to yield the following dimensionless groups:

$$\frac{q_{co}/\rho_v h_{fg}}{\sqrt[4]{\sigma g(\rho_l - \rho_v)/\rho_v^2}} = f\left(\frac{\rho_l}{\rho_v}, \frac{\mu_l}{\mu_v}, \frac{L}{\sqrt{\sigma/g(\rho_l - \rho_v)}}\right) \tag{2.2}$$

In addition to the parameters in Eqns. (2.1) and (2.2), the bulk liquid subcooling, the heater surface orientation with respect to gravity and the heater material have also been

found to have a significant effect on the CHF. Experimental observations in previous works, which generally do not support the hydrodynamic instability mechanism for the CHF as assumed by Katto (1978), demonstrate the individual influence of each of these parameters, and are discussed below.

2.1.1. Effects of the bulk flow velocity

The bulk flow velocity generally aids in the removal of vapor from the heater surface, and therefore should increase the CHF. This is confirmed by the measurements of the CHF by Yilmaz and Westwater (1980) in a study of forced convection boiling of R113 in vertical tubes with the imposed flow in the direction of the buoyancy, in which the CHF was found to correlate with the velocity to the 0.48-power. In similar studies by Mudawar and Maddox (1989) and by Katto and Ishii (1978) with flow over a flat, vertically-oriented heater surface, however, the CHF was shown to depend approximately on the flow velocity to the 1/3-power. At very low flow velocities, McGillis et al. (1991) observed that the CHF departed from the 1/3-power correlation developed by Mudawar and Maddox (1989) and became virtually independent of the imposed flow velocity, since the buoyancy acting on the vapor dominated over the influence of the bulk flow.

2.1.2. Effects of gravity and heater surface orientation

The effect of reduced gravity on forced convection boiling is yet to be studied, although some results have been reported for pool boiling. In a correlation of the CHF

based on dimensional considerations for horizontal cylinders in pool boiling under Earth gravity, Kutateladze (1948) predicted the CHF to depend on the gravitational acceleration, g, to the 1/4-power. Siegel (1967) attempted to apply this correlation to pool boiling data taken in fractional gravity with little success, possibly since the experiments were so brief as to not allow steady boiling conditions to be established. In microgravity tests of extended duration, the pool boiling CHF measurements by Merte, et al. (1994) and by Zell et al. (1984) show clearly that the CHF is substantially higher than that predicted by the 1/4-power scaling law, although it is much lower than in 1g. Visual observations in microgravity suggest that the nature of the boiling in the vicinity of the CHF is significantly different from that observed under 1g; bubbles much larger in diameter than those seen at 1g blanket the heater surface, and the buoyancy-driven circulation of liquid to the surface is supplanted by surface tension-driven flow in the thin liquid regions lying between the vapor blanket and the heater surface. As a consequence, unlike under 1g, the transition to film boiling occurs gradually with increasing heat flux.

In forced convection boiling, the orientation of the heater surface with respect to gravity is expected to affect the CHF up to some limiting flow velocity, until the buoyancy force becomes insignificant in relation to the inertia forces associated with the bulk flow. In varying the angle of inclination of the heater surface, the direction and relative magnitude of the buoyancy force components tangent and parallel to the heater surface are varied, which alters the departure velocity of the vapor and hence its residence time on the surface. In an experimental study of pool boiling with water by Katto and Yokoya (1968), it was found that the CHF could be significantly lowered by artificially

constraining the bubbles on the surface to increase their residence time. Logically, then, the CHF is expected to depend strongly on the heater orientation, as demonstrated in an earlier study of forced convection boiling at low flow velocities (Brusstar and Merte, 1994). At very low flow velocities, the CHF was found to be strongly influenced by orientation, particularly in the downward-facing heater orientations. As the flow velocity was increased, however, the dependence on orientation was diminished, although a significant effect was still observed for the case where the buoyancy force opposed the direction of the bulk flow. A similar result is reported by Papell (1967) in a comparison study of the CHF with upflow and downflow in a vertical passage, where the CHF with downflow was reduced by as much as 85 % of that for upflow, with this reduction decreasing as the bulk flow velocity was increased. In a visual study by Simoneau and Simon (1966), the lowering of the CHF in downflow was attributed to the accumulation of vapor above the heater surface resulting from a near balance of buoyancy and flow forces. This is an especially significant observation, as it provides an indication as to the physical mechanism which produces the orientation effects described in the other works.

2.1.3. Effects of the bulk liquid subcooling

The subcooling of the bulk liquid represents the energy which must be added to the liquid to bring it to the saturated state, and is generally expressed in terms of the difference between the liquid temperature and its saturation temperature. The subcooling has a dual effect: first, it decreases the rate of vapor production by increasing the amount

of energy required to bring the liquid on the surface to the saturation temperature; second, it decreases the volume of the vapor bubbles through condensation, and thereby decreases the magnitude of the body forces acting on the vapor relative to the surface forces (i.e., drag and lift) which may be of significance in forced convection boiling. Assuming the former effect of subcooling, Ivey and Morris (1962) drew upon a considerable number of data points for pool boiling over a relatively wide range of subcoolings and pressures, mostly for water, to develop a linear correlation between the CHF and subcooling:

$$q_{co} = q_{c,sat}\left[1 + 0.102\left(\frac{\rho_v}{\rho_l}\right)^{1/4} Ja\right] \tag{2.3}$$

Here, $q_{c,sat}$ is the CHF at saturated conditions, and Ja is the Jakob number. A comprehensive qualitative study of the effects of subcooling on the CHF in pool boiling over relatively large isothermal cylinders was conducted by Elkassabgi and Lienhard (1988), in which three basic regimes were identified:

1. At low levels of subcooling, the CHF increases linearly with subcooling, in a manner similar to the correlation developed by Ivey and Morris (1962).

2. At intermediate levels of subcooling, the CHF varies with the subcooling to the 3/8-power, as the heat transported from the tops of the bubbles to the subcooled bulk region becomes limited by natural convection in the surrounding liquid.

3. At high levels of subcooling, the CHF becomes independent of subcooling, insofar as the properties of the bulk liquid remain constant with the changes in

temperature and pressure. The CHF in this case is thought to be limited by the net rate of vapor transport allowable by the kinetic theory.

While this classification system characterizes the differences between high- and low-subcooling CHF mechanisms, it provides no means of identifying the subcooled boiling data *a priori* as belonging to a specific regime.

The secondary effect of subcooling has been observed in forced convection boiling, in which the volume of the vapor bubbles near the heater surface decreases through condensation, and thereby increases the influence of the drag and lift forces associated with the bulk flow relative to the buoyancy force. This effect was quantitatively demonstrated in the study of upflow and downflow at low flow velocities by Papell (1967). The flow velocity at which the buoyancy effects became negligible could be lowered significantly through increases in the bulk liquid subcooling, indicating a substantial enhancement in the flow forces relative to buoyancy through increases in the bulk subcooling. A similar effect was also reported by Gersey and Mudawar (1993) for flow over small heater surfaces at various heater orientations, where the effects of the orientation on the CHF were diminished considerably by increases in subcooling at a given flow velocity.

2.1.4. Effects of the heater surface material

Two separate effects of the heater surface material on the CHF have been reported; the first relating to the transient thermal conduction properties, the other to the

surface character. The former arises from unsteady conduction in the solid material when a portion of the heater surface becomes temporarily covered with vapor, as often occurs at high levels of heat flux. Assuming a uniform heat flux, the magnitude of the local temperature rise on the portion of the surface insulated by the vapor is approximated from the thermal conductivity and heat capacity of the heater material using order-of-magnitude arguments, as follows:

$$q_{surf} \propto k_{solid} \frac{\Delta T_{local}}{\sqrt{\alpha_{solid} t}} = \sqrt{(k\rho c)_{solid}} \frac{\Delta T_{local}}{\sqrt{t}} \tag{2.4}$$

Based on a similar analysis, Bar-Cohen and McNeil (1992) proposed an empirical correlation for the effects of the unsteady conduction properties of the heater on the CHF in pool boiling of dielectric fluids, including the effects of the heater thickness, as follows:

$$\frac{q_c}{q_{c,\max}} = \frac{S}{S + 0.8} \tag{2.5}$$

Here, $q_{c,max}$ is the CHF predicted for pool boiling over an infinite flat plate in the absence of heater material effects, and S is the heater "conpacitance", defined as follows:

$$S = \delta_{wall} \sqrt{(k\rho c)_{solid}} \tag{2.6}$$

An extensive survey of CHF measurements for heater surfaces of various materials and thicknesses by Carvalho and Bergles (1992) found somewhat poor correlation with the conpacitance, although no alternative relation was proposed.

Secondary but nonetheless substantial effects of the heater material on the CHF are the heater surface roughness and wettability. An early study of the effects of heater surface character on the CHF in pool boiling by Costello and Frea (1965) found that the CHF could be increased by approximately fifty percent by increasing the degree of oxidation of an initially polished heater surface, thereby changing its wetting characteristics. More recently, Ramilison, et al. (1992) examined several different combinations of heater materials and test fluids to obtain a variety of surface roughnesses and wetting angles, and proposed an empirical correlation for the CHF as follows:

$$\frac{q_c}{q_{c,\max}} = 0.0336\varepsilon^{1/8}(\pi - \beta)^3 \tag{2.7}$$

Whereas the influence of the surface roughness is relatively small, that of the wetting angle is significant, this difference likely stemming from their respective roles in the dynamics of the thin liquid films observed on the heater surface at high levels of heat flux. The strong dependence on wetting angle predicted by Eqn. (2.7) was obtained for wetting angles ranging only from zero to 40 degrees, and may be somewhat exaggerated in light of the mere forty percent variation in the CHF reported by Liaw and Dhir (1989) for wetting angles ranging between 14 and 90 degrees.

2.1.5. Effects of surface tension and viscosity

Capillary and viscous effects on the CHF can be significant, particularly in the absence of buoyancy. In the dynamics of thin films, specifically those existing at the heating surface during nucleate boiling at high levels of heat flux, surface tension and viscous forces dominate the motion of the liquid to the evaporating region at the solid-liquid-vapor interface (Bankoff, 1990). In the presence of forced convection, however, other mechanisms for the feed of liquid to the surface can supplant capillary and viscous forces as the dominant effect. Consequently, the effects of surface tension and viscosity on the CHF in forced convection may be difficult to observe experimentally, unless the effects of the liquid motion are minimal. Nevertheless, previous studies show these parameters to have an apparent effect on the CHF under certain circumstances.

Surface tension appears in Eqn. (2.1) among the fundamental dimensionless groups for both pool boiling and forced convection boiling at low flow velocities, where the dependence of the CHF on surface tension is often assumed to relate to an interfacial instability between the vapor and liquid (e.g., Katto, 1978). The effects of surface tension on the CHF can also be observed in boiling at high heat flux levels on heater surfaces with small radii of curvature, where the influence of the surface tension is large in relation to that of buoyancy. This effect is expressed using an empirical correlation of the CHF for relatively small heated wires and spheres by Lienhard and Dhir (1973), with the characteristic dimensionless length scale appearing above in Eqn. (2.2). As the radius of

curvature of the heater surface becomes increasingly small, the surface tension has increasing influence over the bubble departure size, and acts to raise the CHF.

The influence of viscosity on the CHF is customarily neglected, since the viscosity of the liquid phase is generally much greater than that of the vapor phase, and the interaction between phases is therefore usually assumed inviscid. Analytical models of the effects of viscosity on the CHF by Dhir and Lienhard (1974), and by Borishanskii (1956) show that the viscosity acts to increase the CHF, although the enhancement is negligibly small for all but the most viscous fluids. This contradicts the experimental findings by Noyes (1963), who compared the CHF for sodium with data taken from the literature for water and other fluids. Using these few data points available, Noyes found that the CHF correlated as $q_c \propto \mathrm{Pr}^{-1/4}$, suggesting that a more viscous fluid would have a correspondingly lower CHF. However, this effect is of minor consequence over the relatively narrow range of liquid Prandtl numbers of most fluids of interest.

2.2. Analytical models of the CHF

More than one hundred analytical models and empirical or semi-empirical correlations of the CHF in pool and forced convection boiling which attempt to describe the parametric influences discussed above have been identified in the literature. Table 2.1 lists six major categories of models applicable to pool boiling and to low-quality forced convection boiling, classified according to the primary mechanism assumed for the onset

of CHF. Also listed are the most prominent works from which each model originates, discussed below.

2.2.1. Instability model

The instability models apply primarily to pool boiling, and assume that the CHF is brought about by a buoyancy-driven Kelvin-Helmholtz instability at the interface between the liquid and vapor. Zuber (1958) was the first to establish a firm mathematical basis for the hydrodynamic instability mechanism for the CHF over an infinite flat plate in an inviscid saturated liquid. In the model, the vapor is assumed to leave the heater surface in continuous columns whose spacing is determined by the most unstable Taylor wavelength, λ_D, as illustrated in Figure 2.1. The columns become unstable when the relative velocity between the vapor leaving the surface and the liquid flowing counter to it exceeds a critical value determined by the Kelvin-Helmholtz stability criterion. Lienhard and Dhir (1973) later extended the hydrodynamic instability model to cylindrical and spherical geometries, introducing a semi-empirical correction factor to account for the curvature of the heater surface.

Equivalent to the hydrodynamic model is the mechanical energy stability model, first introduced by Lienhard and Eichhorn (1976) for the CHF in saturated pool boiling over horizontal cylinders and later generalized to other configurations by Lienhard and Hasan (1979). The model assumes that the CHF occurs when the kinetic energy of the

vapor leaving the heater surface in vapor columns exceeds the surface energy at the interface between the two phases.

The advantage of the instability models is their simplicity: the CHF in saturated pool boiling can be predicted by a single expression as a function of the fluid properties:

$$q_z = C_o \rho_v h_{fg} \left[\sigma g(\rho_l - \rho_v)/\rho_v^2\right]^{1/4} \tag{2.8}$$

Here, C_o is predicted as 0.13 by Zuber (1958), and was later modified to 0.15 by Lienhard and Dhir (1973). Taking C_o as 0.13, q_z is given in Table 2.2 for a variety of fluids commonly used in two-phase heat transfer applications. For highly wetting fluids, Eqn. (2.8) predicts the CHF reasonably accurately over a wide range of fluid properties. This success may be somewhat fortuitous, however, since essential elements of the theory, such as vapor columns, have never been conclusively proven to exist in the laboratory. Visual observations by Bergles (1988) and Mattson, et al. (1973) rather convincingly dispute the existence of a capillary instability between the liquid and vapor. Moreover, the large departures from the instability models with changes in the surface wettability (Dhir, 1992) and level of gravity (Zell, et al., 1984) suggest that the controlling mechanisms of the CHF are not related to a hydrodynamic instability, and that the success of such models may be a dimensional coincidence.

2.2.2. Macrolayer dryout model

The macrolayer dryout model assumes a two-step transient mechanism for the CHF, consisting of the formation of a vapor blanket above a thin liquid "macrolayer", which evaporates during the time in which the vapor blanket is resident in the vicinity of the surface, giving rise to the CHF. The model was originally developed by Haramura and Katto (1983) for saturated pool boiling and forced convection boiling at relatively low flow velocities, based on the observations of transient bubble growth at high levels of heat flux by Katto and Yokoya (1968). While different mechanisms for the formation of the macrolayer have been proposed in various works, the macrolayer models generally assume the existence of a uniform liquid layer on the heater surface which evaporates into the overlying vapor mass, as depicted in Figure 2.2. In the model proposed by Haramura and Katto (1983) illustrated in Figure 2.2(a), it is assumed that the vapor departs the heater surface through a series of tiny "stems"; these stems become Kelvin-Helmholtz unstable to form a vapor blanket, and give rise to the macrolayer as a result of the suppression of the capillary waves at the heater surface. In the model proposed by Bhat, et al. (1983a) shown in Figure 2.2(b), however, the formation of the macrolayer is attained through coalescence of bubbles growing on the surface, and the thickness is correlated empirically as a function of the heat flux from "measurements" of the macrolayer.

The CHF predicted for pool boiling by Haramura and Katto (1983) and by Bhat, et al. (1983) agree exactly, since both models use the prediction by Zuber (1958) as a

reference value for determining empirical coefficients. In forced convection boiling, a survey of various forced convection models by Celata, et al. (1994) indicates the accuracy of the model by Haramura and Katto (1983) for the low-quality bubbly flow regime to be reasonably good, within about ± 25 % RMS. This accuracy, however, belies the dubious validity of the principal assumptions in the model. First, the macrolayer is a very crude representation of the actual evaporation and dryout processes on the surface. Second, the vapor stems are artificial representations of the actual vapor structures, as they have never been observed in photographs of the boiling surface at high levels of heat flux. Finally, the solid-liquid-vapor interface is neglected in the model, implying that neither the effects of the surface character nor the heater substrate material can be explicitly included. The success of the two-step modeling approach nonetheless suggests some physical validity in the bubbly flow and pool boiling regimes.

2.2.3. Enthalpy obstruction model

The enthalpy obstruction model applies strictly to the bubbly flow regime, and assumes that the vapor forms a blanket above the surface and blocks the exchange of enthalpy between the heater surface and the bulk region, as illustrated in Figure 2.3. Kutateladze and Leont'ev (1966) developed an expression for the CHF in flow boiling with saturated inlet conditions, assuming that a vapor blanket resulted from intense evaporation in the stagnation regions in the hydrodynamic boundary layer, which effectively insulated the heater surface and caused the surface temperature to rise beyond

the Leidenfrost point. Tong (1968) improved upon this idea, combining the result of Kutateladze and Leont'ev (1966) with a second-order model describing the effects of the inlet quality. The resulting expression was unsuccessful at correlating CHF data for water and orthoterphenyl within satisfactory limits. Weisman and Pei (1983) developed a model for the CHF based on turbulent exchange between the bulk region and the bubbly layer near the wall. The CHF was assumed to occur when flow quality, predicted using homogeneous flow theory, reached a critical pre-determined limit. The advantage of this approach is that it is consistent with visual observations of boiling at high levels of heat flux and may be solved using conventional two-phase computational methods, such as the two-fluid models and the drift-flux models. On the other hand, Weisman and Pei (1983) assumed a uniform axial heat flux, and also neglected the void fraction distribution across the flow cross section, both which are likely significant to the CHF in highly subcooled flow boiling. These assumptions can be incorporated using more sophisticated modeling approaches, but this would inevitably involve a higher degree of empiricism.

2.2.4. Interfacial liftoff model

The interfacial liftoff model was initially conceived by Galloway and Mudawar (1993b) to describe the CHF in forced convection boiling, and is based on the formation of wetting fronts at the troughs of capillary waves forming on the upper surface of a vapor blanket on the heater surface, as illustrated in Figure 2.4. At high levels of heat flux, the momentum of the vapor formed through evaporation at these wetting fronts is sufficient

to overcome the inertia of the liquid at the liquid-vapor interface. Among the forced convection models for bubbly flow, the interfacial liftoff model alone considers the effects of heater surface orientation with respect to gravity. Gersey and Mudawar (1995) used this approach to model the CHF for FC-72 over a relatively narrow range of heater orientations, ranging from horizontal facing upward to the vertical with upflow orientation, for various heater lengths and flow velocities, yielding the results shown in Figure 2.5. The agreement with the model falls within about a ± 30 % tolerance band, which is especially poor in light of the range for the measured CHF of only about ± 25 % of the mean. Also, the particularly high amount of scatter for low values of the CHF, presumably corresponding to the lower flow velocities, possibly indicates that the wetting fronts are not a function of the Kelvin-Helmholtz instability at low flow velocities.

2.2.5. Geometric model

One of the simplest approaches to modeling the CHF was taken by Rohsenow and Griffith (1956). In this model, bubbles from neighboring nucleation sites are assumed to become so tightly packed together at high heat flux that they eventually coalesce to form large vapor masses which cover the surface and thereby lower the local heat transfer rate. While the dimensionless correlation derived by Rohsenow and Griffith (1956) yields generally poor results, a similar assumption was employed by Bhat, et al. (1983a) to describe the mechanism of macrolayer formation. Moreover, photographs of boiling at relatively high levels of heater flux and void fraction measurements near the heater

surface suggest that coalescence plays an important role in triggering the onset of the CHF, indicating some validity to the fundamental assumptions of Rohsenow and Griffith (1956).

2.2.6. Kinetic theory model

Kinetic theory was employed by Gambill and Lienhard (1989) to predict the maximum attainable CHF. The highest heat flux that may conceivably be obtained through phase change occurs when the exchange of molecules at the liquid-vapor interface occurs such that none of the vapor molecules return to the liquid state. Assuming the vapor to be an ideal gas as a first approximation, the upper bound to the CHF was estimated:

$$q_{c,\max} = \rho_v h_{fg} \sqrt{\frac{RT_{sat}}{2\pi}} \tag{2.9}$$

A comparison with measurements of the CHF in highly subcooled forced convection boiling at relatively low reduced pressures revealed that the highest measured CHF values approached only about 0.1 of the upper bound predicted by Eqn. (2.9). The reason given for this relatively poor performance was that in order for the transition from liquid to vapor to be unidirectional from a given source (in this case, from the liquid-vapor interface on the heater surface), there must also exist a corresponding sink capable of absorbing energy at the same rate. The rate of molecular effusion of the vapor molecules

from the heater surface was said to be limited by the thermal diffusion into the subcooled liquid, which imposes an upper limit to the net rate of phase change.

2.3. Concluding remarks

The works discussed above illustrate that the CHF is a complicated process of evaporation and dryout which is influenced by a number of specific system parameters, and consequently is difficult to model in the general case. Whereas the present work focuses on forced convection boiling at relatively low flow velocities, where the effects of the buoyancy and flow forces predominate, only the interfacial liftoff model among those discussed above presents an explicit method for describing the effects of both heater surface orientation and flow velocity on the CHF. The other forced convection models nonetheless provide useful insight into a means of describing various aspects of bubbly flow, some of which are incorporated into the analytical model of the CHF in forced convection boiling to be described in Chapter 3.

Model classification	CHF trigger mechanism	References
1. Instability Models		
1a. Hydrodynamic instability	Kelvin-Helmholtz instability at the liquid-vapor interface	Zuber (1958); Lienhard and Dhir (1973)
1b. Mechanical energy instability	Kinetic energy of the vapor exceeds the interfacial surface energy	Lienhard and Eichhorn (1976); Lienhard and Hasan (1979)
2. Macrolayer dryout	Dryout of a thin liquid layer beneath a continuous vapor blanket	Haramura and Katto (1983); Bhat, et al. (1983a)
3. Enthalpy obstruction		
3a. Boundary layer separation	Formation of a vapor blanket due to separation of the hydrodynamic boundary layer from the heater surface	Kutateladze and Leont'ev (1966); Tong (1968)
3b. Bubble crowding	Crowding of bubbles at the heater surface blocks enthalpy exchange with the bulk region	Weisman and Pei (1983)
4. Interfacial liftoff	Evaporation of the wetting fronts established beneath a wavy vapor layer	Galloway and Mudawar (1993); Gersey and Mudawar (1995)
5. Geometric limit	Bubble site population exceeds a critical value	Rohsenow and Griffith (1956)
6. Kinetic theory	Kinetic transport limits the maximum rate of liquid-vapor exchange	Gambill and Lienhard (1989)

Table 2.1. Categorization of the main CHF models for bubbly flow and pool boiling

Fluid	Sat. Temp. (°C)	q_z (W/cm^2)
Water	100	111
R113	47.6	21
FC-72	56.6	15
LN2	-196.1	16
LH2	-252.8	7

Table 2.2. CHF in saturated pool boiling at atmospheric pressure for various fluids predicted using Eqn. (2.8)

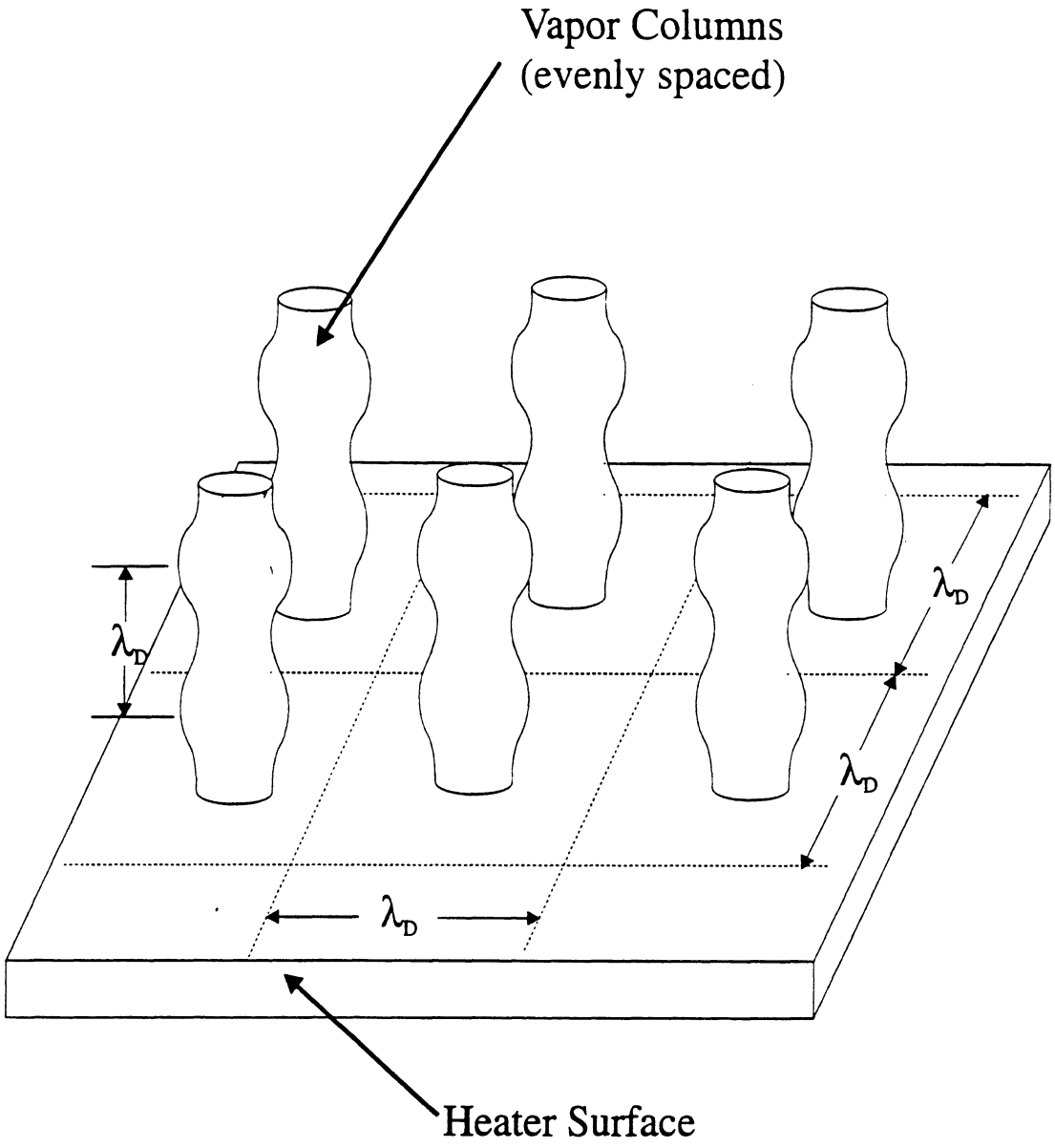

Figure 2.1. Illustration of the hydrodynamic instability model

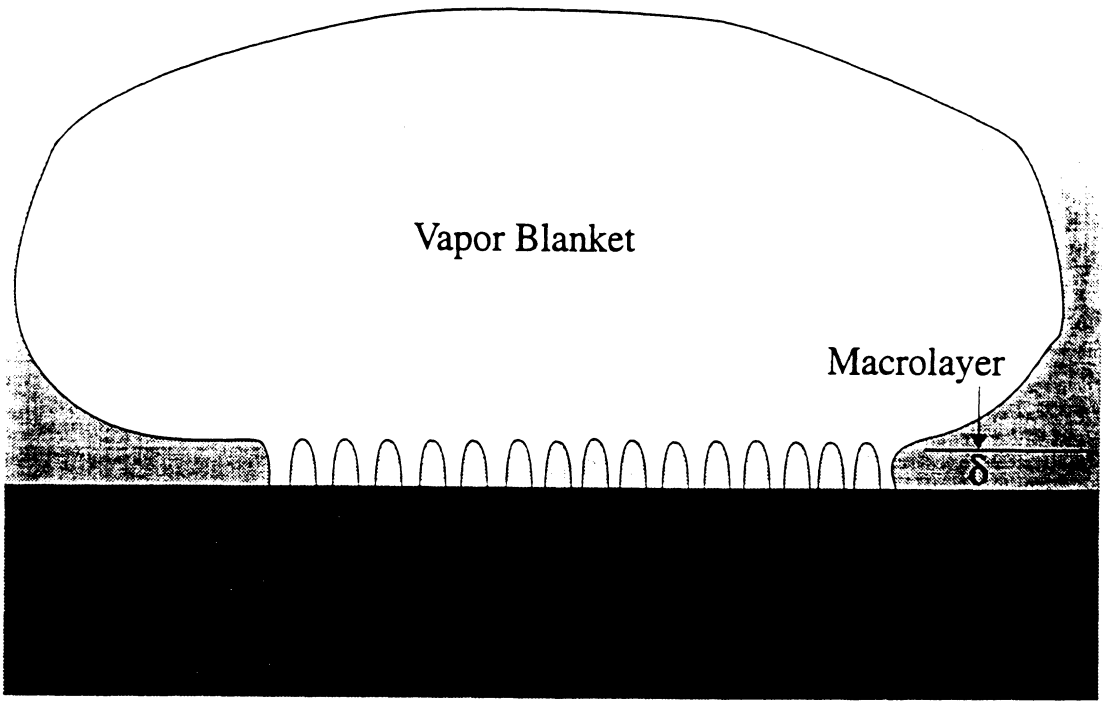

Assumed configuration: vapor blanket above a thin liquid layer

Mechanisms for macrolayer formation:

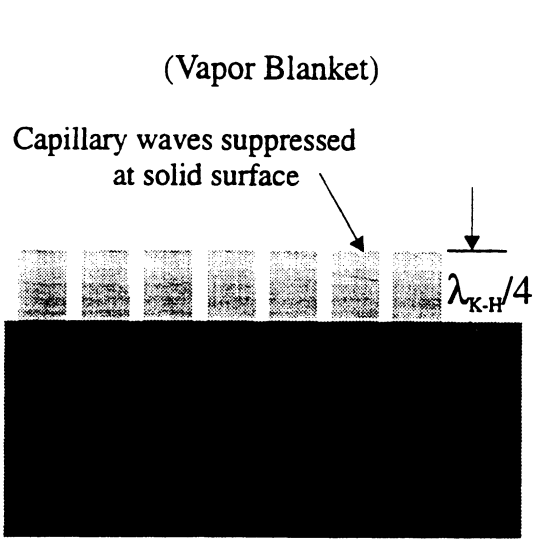

Figure 2.2(a). Mechanism for macrolayer formation; Haramura and Katto (1983)

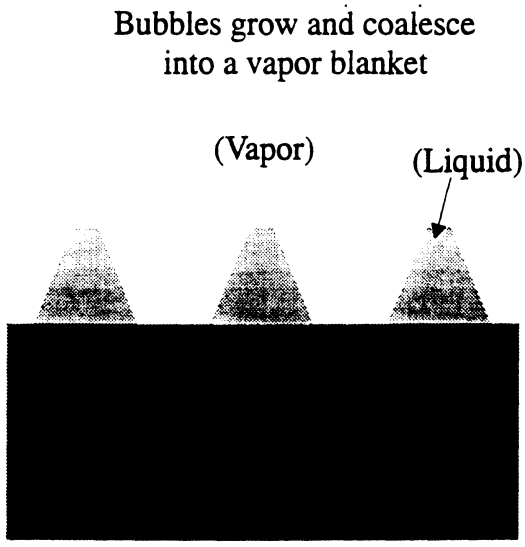

Figure 2.2(b). Mechanism for macrolayer formation; Bhat, et al. (1983a)

Figure 2.2. Illustration of the macrolayer model

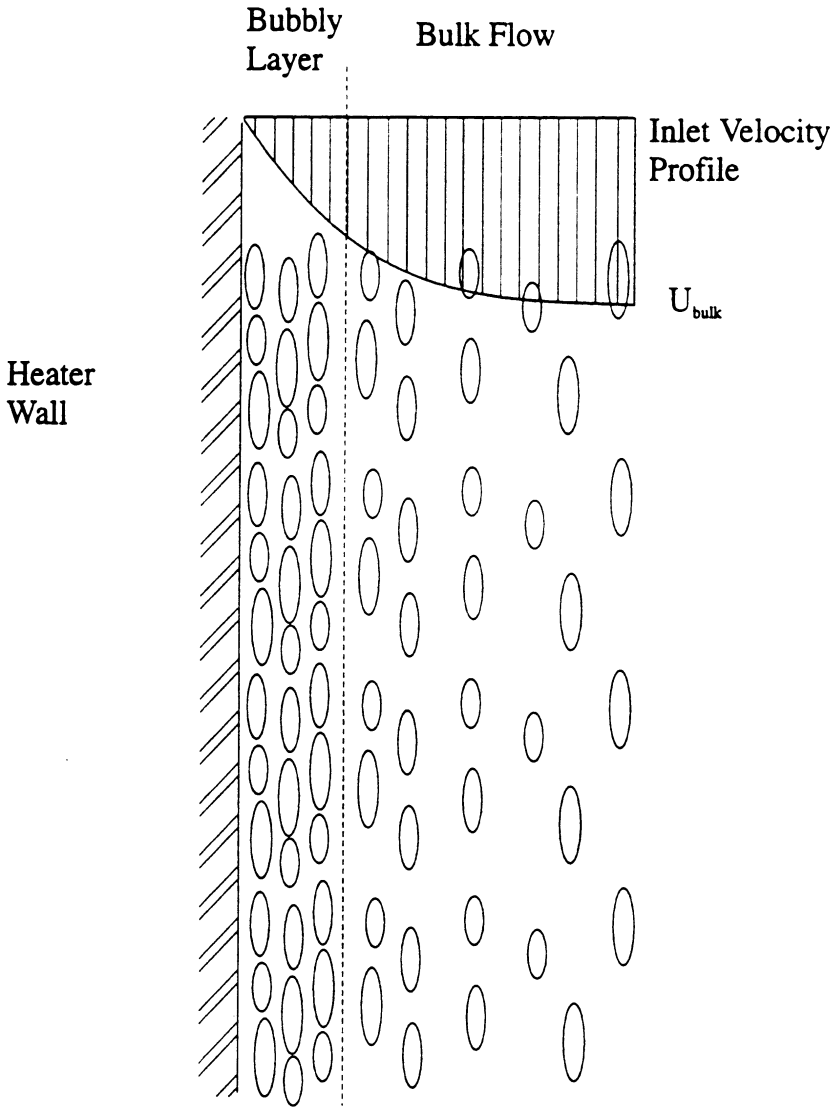

Figure 2.3. Illustration of the enthalpy obstruction model

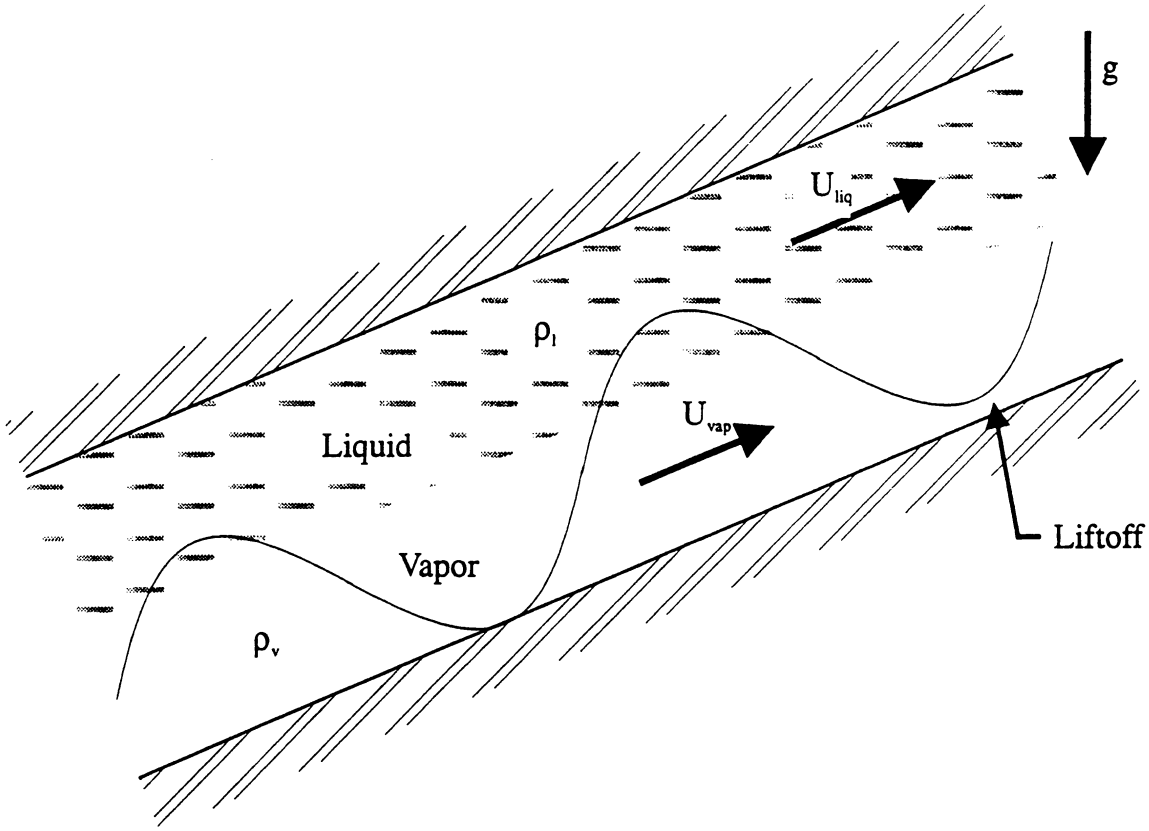

Figure 2.4. Illustration of the interfacial liftoff model (Galloway and Mudawar, 1993)

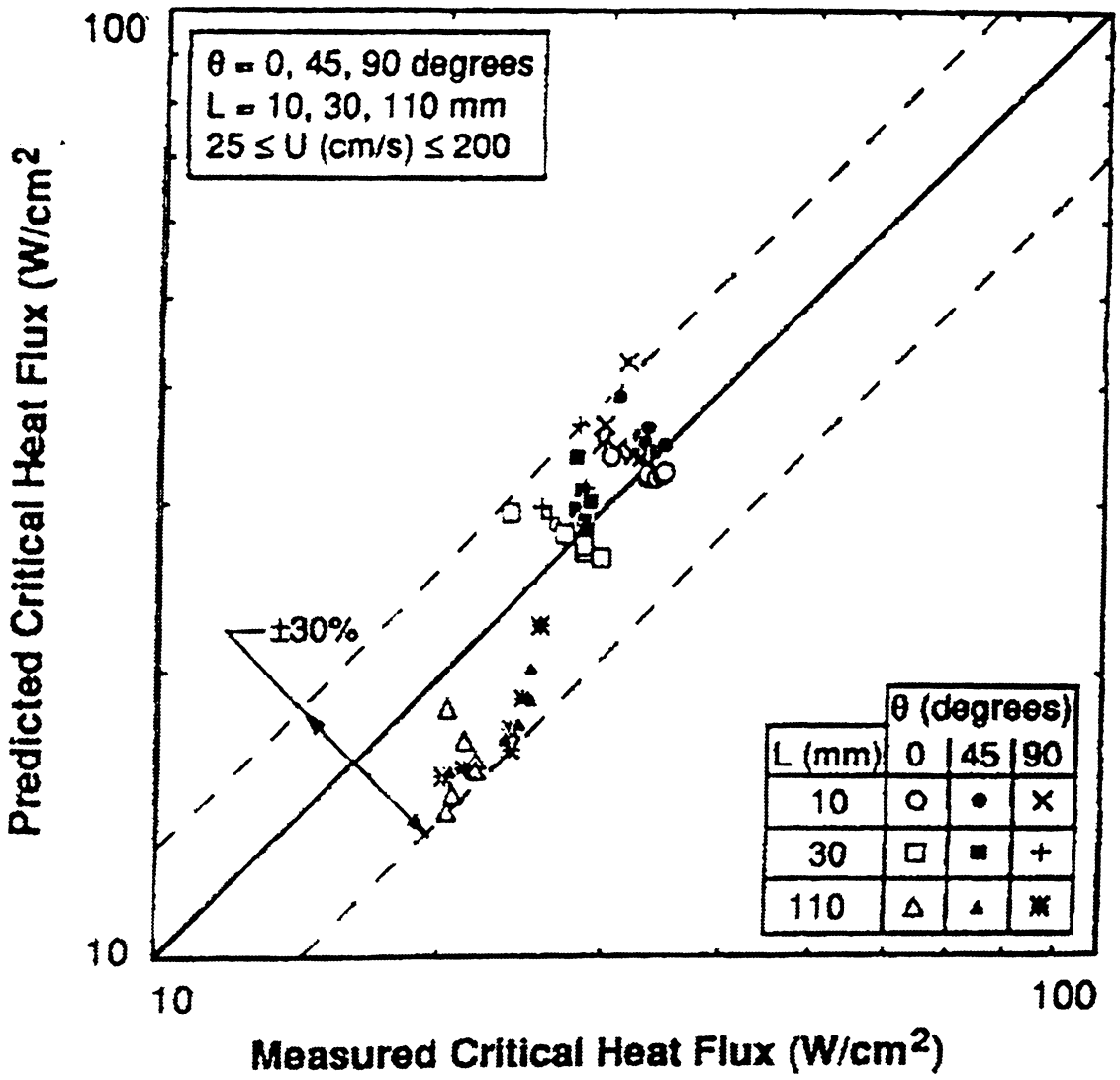

Figure 2.5. Comparisons of the measured CHF with the model predictions by Gersey and Mudawar (1995) for various flow velocities, heater orientations and heater lengths; FC-72, $\Delta T_{sub} = 4^{\circ}C$.

CHAPTER 3

FORCED CONVECTION CRITICAL HEAT FLUX MODEL DESCRIPTION

3.0. Model Introduction

A model of the critical heat flux, consisting of two main components, is developed below, which incorporates the effects of several parameters, including the heater surface orientation and the imposed flow velocity. The first component is an analytical, two-dimensional description of the motion of a single bubble growing rapidly above a heated surface in forced convection, solved numerically. The second component is a correlation derived from physical arguments which provides closure to the model solution by linking the motion of the vapor to the evaporation of the underlying liquid on the heated surface. Collectively, the model equations will be referred to as the "FCCHF model" in subsequent chapters.

While the present model considers the growth and motion of only a single vapor bubble, the model is, in fact, a simplified solution to the two-fluid models (Lahey, 1992) applied to a single computational volume element above the heater surface. A flowchart diagram of the model is given in Figure 3.1, showing the relationship between the motion of the liquid and vapor phases and the CHF, indicating areas where some degree of empiricism is introduced. In the first part of the model, the momentum equations for the two phases are solved independently, but are coupled through the hydrodynamic drag and lift forces at the interface between the liquid and vapor. For convenience, the net exchange of mass and energy between the vapor and liquid phases is lumped into a semi-empirical net vapor generation term, avoiding a more sophisticated description of the

evaporation and condensation and coalescence and breakup near the heater surface. The momentum equation for the liquid phase is solved by assuming the law of the wall approximation for the mean turbulent velocity profile. The momentum equation for the vapor phase, meanwhile, is solved by considering the virtual mass, buoyancy and flow forces acting on the relatively large bubbles that are often observed at high levels of heat flux (Kumada and Sakashita, 1992). These bubbles are assumed to be of prime importance in the mechanisms of dryout by virtue of the large surface area they occupy. This assumption is supported by two earlier photographic studies: one by Gaertner (1965) of pool boiling with water, which showed the prevalence of large coalesced vapor masses at heat flux levels close to the CHF, portending the onset of dryout; the other by Kirby and Westwater (1965) taken from beneath the heater surface, which showed dry patches on the surface beneath overlying coalesced vapor masses. Given these observations, and for simplicity, the first component of the model exclusively considers the growth and motion of large vapor bubbles.

The second component of the model is a dimensional analysis, which predicts the relationship between the motion of the vapor and the CHF for a given set of bulk flow conditions. The analysis assumes that a critical amount of energy goes into the evaporation of liquid during the time the growing bubble is resident on the heater surface, which triggers the onset of the CHF. The intermittent formation of dry spots on the heater surface at heat flux levels below the CHF has been documented by considerable experimental evidence, and the model therefore does not assume the existence of a uniform liquid layer, or macrolayer, on the heater surface. Instead, studies of transition boiling of water by Ishigai and Kuno (1966), Dhuga and Winterton (1985) and Torikai, et al. (1991) show that a substantial portion of the heater surface remains covered with liquid through the CHF into the transition boiling regime, suggesting the existence of a critical dry area fraction, above which nucleate boiling can no longer be sustained. The dimensional analysis accordingly considers the effects of the flow velocity, subcooling

and heated length on the evaporation and partial depletion of the liquid on the heater surface at the CHF.

The momentum equation for the vapor phase is solved for the residence time of the bubble over the heater surface, from bubble inception to departure, which is found to relate directly to the CHF. Evidence of this relation is given in the experimental study of pool boiling in water by Katto and Yokoya (1968), where the CHF was lowered significantly when the bubbles were artificially constrained to increase their residence times on the heater surface. This dependence on the residence time, they concluded, was a result of the obstruction in the supply of liquid to the surface by the bubble, compounded with the increase in the time over which the liquid on the surface could be consumed prior to being replenished. These effects of the bubble residence time were later incorporated into a model of the CHF in pool boiling by Haramura and Katto (1983), in which a liquid layer of uniform thickness δ_E is assumed to evaporate completely on the heater surface during the bubble residence time, τ_{res}, according to:

$$q_c \tau_{res} = \rho_l h_{fg} \delta_E (1-\gamma) \tag{3.1}$$

In this expression, γ is the fraction of the surface area occupied by vapor, assumed to be constant. Subsequent measurements of the bubble residence time on a heated wire at the CHF by Haramura (1990) demonstrated that the product of the CHF and the bubble residence time was constant. Further experimental evidence of this will be given in Chapter 5.

3.1. Part One: Model of the growth and departure of a single vapor bubble

The buoyancy, drag and lift forces are balanced against the virtual mass acceleration of a bubble in two dimensions. These forces, in turn, are dependent on the

instantaneous bubble size and on the volumetric rate of vapor generation, and require a thermodynamic analysis of the evaporation process at the heater surface. Some fundamental simplifications are made for convenience: first, a single volume element is considered in the model, defined by the unit bubble spacing and the test section height. The unit bubble spacing at relatively low flow velocities is assumed to behave as in pool boiling over a horizontal surface, and therefore is determined by the most unstable Rayleigh-Taylor wavelength. Second, it is assumed that the net rate of vapor generation is constant, and that the spatial and temporal average rate is sufficiently accurate to describe the bubble growth. The success of the model, to be demonstrated in Chapter 5, is taken to corroborate the validity of these assumptions.

A formulation similar to the one given below was derived by Davidson and Schueler (1960a) to predict the rapid growth of bubbles in an inviscid liquid, and was later used by Haramura and Katto (1983) to describe bubble growth at high heat flux levels in pool boiling. The present model adds a description of the imposed turbulent flow field, and includes the drag and lift forces between the liquid and vapor phases. Figure 3.2 illustrates the forces considered in the momentum equation for the vapor bubble, assuming the buoyancy, drag and lift forces to dominate over the surface tension and viscous shear. The components of the bubble displacement normal to the heater surface and parallel, in the direction of flow, are calculated based on an Eulerian reference frame fixed at a point on the surface where the bubble originates, with the directions normal and parallel designated as the x- and y-directions, respectively.

3.1.1. Force balance on the parallel to the heater surface (x-direction)

Balancing the buoyancy and drag forces against the mass acceleration of the vapor and displaced liquid in the x-direction gives:

$$F_{buoy,x} + F_{drag} = F_{m.a.,x} \tag{3.2}$$

The surface tension force of adhesion is neglected, since it is small compared to the forces considered, except perhaps in the early stages of bubble growth, and is especially so for the case of typical highly-wetting fluids, including R113. Viscous shear between the two phases is also neglected, except at very low bubble Reynolds numbers. This force balance may be expressed explicitly as:

$$g\sin\theta(\rho_l - \rho_v)V - \tfrac{1}{2}C_d\rho_l U_{rel}|U_{rel}|A_f = \frac{d}{dt}\left[\left(m_{l,eff} + m_v\right)u_{vap}\right] \tag{3.3}$$

The relative velocity in this case is defined as the velocity of the vapor relative to the mean flow velocity over the bubble. The right hand side of the equation represents the inertia of the vapor contained in the bubble and the virtual mass of the displaced liquid. Although the mass of the vapor is generally small in comparison to the virtual mass of the bubble, it is retained for generality.

The instantaneous volume of the growing bubble is expressed as:

$$V = v'\tau = \tfrac{4}{3}\pi\bar{R}^3 \tag{3.4}$$

where v' is defined as the temporal mean value of the volumetric rate of vapor generation averaged over the heater surface area, given as:

$$v' \equiv \frac{1}{\tau}\int_0^{\tau}\left(\frac{1}{A_s}\int_{A_s} v'(A_s,t)dA_s\right)dt \tag{3.5}$$

Using Eqn. (3.5), coalescence with neighboring bubbles is not necessarily neglected, provided the coalescence period is relatively small compared to the total bubble growth time. Therefore, while the growth of a bubble may actually consist of a series of discrete events, it can still be modeled as a smooth, continuous one. Also, while the majority of the evaporation likely occurs in the thin liquid regions at the base of bubbles forming on the surface, Eqn. (3.5) represents the spatial average value for the volumetric vapor generation rate. The precedent for such an expression for v' arises from a model of the CHF in pool boiling by Haramura and Katto (1983), which based this approximation on measurements of bubble growth rates taken from high speed photographs of saturated pool boiling in water at high heat flux by Katto and Yokoya (1968). Experimental evidence contrary to this result is given by Haramura (1990), however, in which a sequence of steps were observed in the transient growth of vapor bubbles on a heated wire maintained at a nearly constant temperature. From measurements of the periodic fluctuations in the wire temperature at high heat fluxes, he deduced a three-step cyclic process consisting of evaporation, dryout and rewetting on the wire which was, nonetheless, dominated by the evaporation step. Therefore, were the average vapor generation rate computed for this process using Eqn. (3.5), a reasonable estimate of the bubble growth rate over time would be obtained.

Noting that the frontal area of the bubble, A_f, can be expressed in terms of the mean bubble radius as

$$A_f = \pi \overline{R}^2 = \pi \left(\frac{3}{4\pi} V \right)^{\frac{2}{3}} \tag{3.6}$$

and substituting Eqn. (3.4) for the bubble volume, Eqn. (3.3) can be written as:

$$g\sin\theta(\rho_l-\rho_v)\nu'\tau-\frac{\pi}{2}C_d\rho_l U_{rel}|U_{rel}|\left(\frac{3\nu'\tau}{4\pi}\right)^{\frac{2}{3}}=\frac{d}{dt}\left[(c_1\rho_l+\rho_v)\nu'\tau\frac{dx_v}{dt}\right] \qquad (3.7)$$

Note that u_{vap} has been replaced by dx/dt. While the acceleration term must account for the changes in the velocity of the surrounding liquid as well as the vapor, it is assumed that the mean velocity profile of the liquid about the moving bubble is quasi-steady. Rearranging and integrating once, assuming constant transport properties, an expression for the velocity component of the vapor parallel to the heating surface can be obtained as:

$$\frac{g\sin\theta(\rho_l-\rho_v)}{(c_1\rho_l+\rho_v)}\frac{\tau}{2}-\frac{\pi}{2}\frac{\rho_l}{(c_1\rho_l+\rho_v)}\left(\frac{9}{16\pi^2\nu'}\right)^{\frac{1}{3}}\frac{1}{\tau}\int_0^\tau C_d U_{rel}|U_{rel}|t^{\frac{2}{3}}dt=\frac{dx_v}{dt} \qquad (3.8)$$

From potential flow theory (Milne-Thomson, 1956), the virtual mass of a sphere moving parallel to a wall is 19/32 times the mass of the displaced liquid. Despite the fact that relatively large bubbles accelerating from the surface have a tendency to distort into ellipsoidal or hemispherical shapes, particularly in the presence of gravity and a subcooled bulk liquid, the shape is taken here as a sphere for simplification, and c_1 is accordingly assigned the value of 19/32. Assuming the density of the liquid phase to be far greater than that the density of the vapor phase, as is generally true far from the critical state, Eqn. (3.8) then may be reduced to the following form:

$$g\sin\theta\frac{16\tau}{19}-\frac{16}{19}\left(\frac{9\pi}{16\nu'}\right)^{\frac{1}{3}}\frac{1}{\tau}\int_0^\tau C_d U_{rel}|U_{rel}|t^{\frac{2}{3}}dt=\frac{dx_v}{dt} \qquad (3.9)$$

Finally, the displacement of the center of mass of the bubble in the x-direction is obtained by integrating Eqn. (3.9) as:

$$x_v = \int_0^{\tau} \frac{dx_v}{dt} dt \tag{3.10}$$

3.1.2. Force balance normal to the heater surface (y-direction)

Following a development similar to that in section 3.1.1, the equation of motion for a bubble in the direction normal to the heater surface is expressed as:

$$F_{buoyancy} + F_{lift} = F_{m.a.,y} \tag{3.11}$$

In the case of downward-facing heater orientations, the heater surface also exerts a force on the bubble such that the bubble remains static until the lift is sufficient to produce a net force away from the surface. As such, this force balance is valid under the condition that the lift force is greater than the buoyancy force component, and the bubble displacement is otherwise zero. The surface tension force of adhesion is neglected, as is the viscous shear between the two phases. Thermocapillary forces, while perhaps significant under microgravity, are also neglected for two reasons: first, while the temperature difference between the heated wall and the bulk liquid may be large, the surface area of the bubbles is also large, and the surface tension gradient is thereby diminished; second, natural convection and turbulent mixing in the vicinity of the bubbles likely reduce the significance of the thermocapillary convection. The drag force in the direction normal to the surface is also neglected, since the motion of the bubble in the absence of an imposed flow in the normal (y-) direction can be assumed to be essentially irrotational, as demonstrated by Davidson and Schueler (1960a).

Similar to the development of Eqn. (3.8), the force balance normal to the surface may be written explicitly as:

$$g\cos\theta(\rho_l-\rho_v)\nu'\tau+\frac{\pi}{2}C_L\rho_l U_{rel}^2\left(\frac{3\nu'\tau}{4\pi}\right)^{\frac{2}{3}}=\frac{d}{dt}\left[(c_2\rho_l+\rho_v)\nu'\tau\frac{dy_v}{dt}\right] \tag{3.12}$$

Rearranging and integrating, the velocity component of the vapor normal to the heating surface is:

$$\frac{g\cos\theta(\rho_l-\rho_v)}{(c_2\rho_l+\rho_v)}\frac{\tau}{2}+\frac{\pi}{2}\frac{\rho_l}{(c_2\rho_l+\rho_v)}\left(\frac{9}{16\pi^2\nu'}\right)^{\frac{1}{3}}\frac{1}{\tau}\int_0^\tau C_L U_{rel}^2 t^{\frac{2}{3}}dt=\frac{dy_v}{dt} \tag{3.13}$$

From potential flow theory (Milne-Thomson, 1956), the virtual mass of a sphere moving normal to a wall is 11/16 times the mass of the displaced liquid, and c_2 is accordingly assigned the value of 11/16 as a first approximation. Assuming the density of the liquid phase to be much greater than the density of the vapor phase, Eqn. (3.13) becomes:

$$g\cos\theta\frac{8\tau}{11}+\frac{8}{11}\left(\frac{9\pi}{16\nu'}\right)^{\frac{1}{3}}\frac{1}{\tau}\int_0^\tau C_L U_{rel}^2 t^{\frac{2}{3}}dt=\frac{dy_v}{dt} \tag{3.14}$$

The displacement of the center of mass of the bubble in the y-direction results from integration of Eqn. (3.14) as:

$$y_v=\int_0^\tau\frac{dy_v}{dt}dt \tag{3.15}$$

3.1.3. Description of the turbulent velocity profile in the liquid phase

Consistent with the experiments performed in the forced convection flow loop, here, the bubbles are assumed to grow in the presence of an imposed turbulent flow field. The mean flow velocity over the bubble and, correspondingly, the drag and lift coefficients are estimated assuming a turbulent velocity profile, described below.

From Schlichting (1979), the mean velocity distribution for internal flow at relatively high Reynolds numbers in smooth ducts can be expressed in terms of dimensionless velocity and displacement variables, as defined below. First, the friction velocity, which is characteristic of the turbulent, fluctuating motion of the flow, is defined in terms of the mean turbulent shear stress as

$$u_* = \sqrt{\frac{\tau_w}{\rho_l}} \tag{3.16}$$

where τ_w is assumed constant for a given set of conditions, according to Prandtl's hypothesis. An appropriate correlation for the wall shear stress in a rectangular duct is given by the Blasius formula for smooth pipes as:

$$\tau_w = \frac{1}{8}\rho U_b^2 \left(0.3164\,\mathrm{Re}^{-\frac{1}{4}} \right) \tag{3.17}$$

Here, U_b refers to the bulk flow velocity. Substituting Eqn. (3.17) into Eqn. (3.16) then yields:

$$u_* = 0.1988\,\mathrm{Re}^{-\frac{1}{8}} U_b \tag{3.18}$$

The dimensionless velocity and distance from the wall are then defined in terms of the friction velocity as:

$$u^+ = \frac{\bar{u}(y)}{u_*} \tag{3.19}$$

and:

$$y^+ = \frac{u_* y}{\nu} \tag{3.20}$$

In the viscous sublayer region nearest the wall, the velocity profile is given by:

$$u^+ = y^+ \qquad \text{for } y^+ < 5. \tag{3.21}$$

In the inertial sublayer, often referred to as the logarithmic layer, the universal velocity distribution law for large Reynolds numbers in smooth ducts has the form

$$u^+ = 2.5 \ln y^+ + 5.5 \qquad \text{for } 5 < y^+ < 70. \tag{3.22}$$

In the core region, it can be shown using Blasius' correlation (Eqn. (3.17)) that the velocity distribution should approximately follow a 1/7th-power law, as follows:

$$u^+ = 8.74\left(y^+\right)^{\frac{1}{7}} \qquad \text{for } y^+ > 70. \tag{3.23}$$

In the model here, the mean velocity over the surface of the growing bubble is estimated by calculating the velocity at one half of the bubble height from the wall, which in this case is equal to the bubble radius. Additionally, the model accounts for the case

where the diameter of the bubble exceeds one half of the channel height by assuming the mean flow velocity to be symmetric about the channel midplane.

3.1.4. Drag coefficient

Several studies of the drag coefficient over individual bubbles exist (Harmathy, 1960; Peebles and Garber, 1953; Al-Hayes and Winterton, 1981), with some differing results. Firstly, Al-Hayes and Winterton take into account the presence of the wall, while the others do not. Secondly, each of these considers the case of isolated bubbles, and does not explicitly consider the effects of increasing bubble population densities. For the present model, the drag coefficient over the bubbles is estimated from the correlations given by Ishii and Zuber (1979) for a system of many deformable particles, in this case bubbles, moving together through a continuous medium. In the earlier stages of growth, where the Reynolds number based on the bubble diameter is accordingly small and the bubbles are nearly spherical, viscous effects dominate and the drag coefficient is given by:

$$C_d = \frac{24}{\mathrm{Re}_b}\left(1 + 0.1\,\mathrm{Re}_b^{\frac{3}{4}}\right) \tag{3.24}$$

It may be noted that the first term on the right hand side is the viscous drag over a rigid sphere in Stokes flow, to which is added a correction term to extend the correlation to higher Reynolds numbers. An expression similar to this one is given by Mei and Klausner (1992) for $\mathrm{Re}_b < 1000$.

For large bubbles, the drag coefficient is assumed independent of the Reynolds number (Ishii and Zuber, 1979; Harmathy, 1960), but depends on the void fraction according to:

$$C_d = 0.45\left[\frac{1+17.67 f_\alpha^{\frac{6}{7}}}{18.67 f_\alpha}\right]^2 \tag{3.25}$$

For the case of vapor bubbles moving through a continuous liquid medium,

$$f_\alpha = \sqrt{1-\alpha} \quad , \tag{3.26}$$

assuming the viscosity of the continuous liquid phase to be much greater than that for the dispersed vapor phase. A plot of Eqn. (3.25) is given in Figure 3.3, showing the drag coefficient as a function of the void fraction. As a simplification, α is assumed to be constant at 0.6 based on many of the experimental measurements presented later in Chapter 5, with the corresponding value of C_d being 0.54. This establishes the lower limit for C_d in Eqn. (3.24) in the limit of relatively high bubble Reynolds numbers.

3.1.5. Lift coefficient

Relatively few studies of the lift coefficient in a two-phase flow exist, particularly ones which directly apply to bubbles growing on a wall in a shear flow. In the case of creeping flow around a solid sphere touching a wall, the net lift force is toward the wall. For the case of bubbles, where the viscosity of the liquid phase is generally much greater than that for the vapor phase, the lift is better predicted by inviscid flow theory, which results in a net lift force away from the wall. Klausner, et al.(1993) developed an interpolation between the high and low Reynolds number limits to predict the lift coefficient over a bubble applicable to a wide range of Reynolds numbers based on bubble diameter as follows:

$$C_L = 3.877 G_s^{\frac{1}{2}} \left[\mathrm{Re}_b^{-2} + (0.344 G_s)^2 \right]^{\frac{1}{4}} \tag{3.27}$$

where G_s is the dimensionless rate of shear of the incoming flow field, given by:

$$G_s = \left| \frac{d\bar{u}(y)}{dy} \right| \frac{R_b}{U_{rel}} \tag{3.28}$$

Li, et al. (1993) computed the lift coefficient numerically for a sphere growing at a wall in an irrotational flow field, arriving at a value of 0.577771. Auton (1987) evaluated the lift coefficient around a sphere in a weakly rotational flow field in an inviscid fluid, giving a result of 0.500. Auton's result was used in the present model as the lower limit on the lift coefficient for high values of the bubble Reynolds number.

3.1.6. Volumetric rate of vapor generation

The volumetric rate of vapor generation, v', is determined by applying the first law of thermodynamics to the heater surface. The rate of energy input to the fluid is separated into two components: the net fraction going into sensible energy, and that going into latent heat:

$$q_s A_s = \dot{Q}_{sp} + \dot{Q}_{lh} \tag{3.29}$$

The coefficient χ is defined as the net fraction of the surface heat energy that goes into latent heat, with which the second term on the right hand side of Eqn. (3.29) can be expressed as:

$$\dot{Q}_{lh} = \chi q_s A_s = \dot{m}_v h_{fg} \tag{3.30}$$

The variation in χ with subcooling was determined through experimental measurements of the vapor flux at the heater surface over time, given in Appendix F, such that v' at the CHF is invariant with subcooling. The correlation used to describe χ as a function of subcooling is therefore given by the inverse of the Ivey and Morris (1962) subcooling correlation:

$$\chi = \frac{\chi_0}{1 + 0.102\left(\frac{\rho_v}{\rho_l}\right)^{\frac{1}{4}} Ja} \tag{3.31}$$

where χ_0 is χ evaluated at the saturated state, and is estimated from experimental data as 0.3. The analytical arguments and experimental measurements upon which Eqn. (3.31) is based are presented in Appendix F.

The volumetric rate of vapor generation is then given from Eqn. (3.30) above as:

$$v' = \frac{\chi q_s A_s}{\rho_v h_{fg}} \tag{3.32}$$

Here, A_s is a characteristic unit surface area for large bubbles leaving a heated surface, assumed in this model to be equivalent to the most unstable Taylor wavelength squared, given by the expression (Chandrasekhar, 1961):

$$A_s = \lambda_T^2 = \left[2\pi\sqrt{\frac{3\sigma}{g(\rho_l - \rho_v)}}\right]^2 \tag{3.33}$$

Although using the unstable Taylor wavelength as a representative length scale for a variety of orientations and flow conditions seems erroneous, experimental evidence suggests common characteristic bubble sizes among these different conditions which are described by the Taylor instability. Katto and Otokuni (1994), for example, photographically studied the effects of orientation on the hydrodynamic behavior of air slugs discharged into water through a porous plug, and determined that the size and shape of the vapor masses escaping from the surface was similar for both vertical and horizontal surfaces. Further, at low flow velocities, Brusstar and Merte (1994) and Katto (1985) demonstrated many similarities with pool boiling, where the most unstable Taylor wavelength is generally agreed to be the representative length scale.

3.2. Solution technique for the motion of the vapor bubble

3.2.1 Numerical iteration procedure

The Fortran-77 code FCMODEL.FOR, given in Appendix G, solves the momentum equation for the vapor in the x- and y-directions to determine the residence time of the bubble on the surface from inception to departure. It then evaluates the product of the surface heat flux and the residence time to determine if it lies within some tolerance about a prescribed value, which is used as the criterion for designating the CHF.

The solution procedure consists of iterating the surface heat flux, and determining the corresponding bubble residence times through numerical integration of the momentum equation for the vapor phase. First, the volumetric rate of vapor generation is calculated from the heat flux using Eqn. (3.32). Next, the instantaneous mean bubble radius is calculated from Eqn. (3.4) as:

$$\overline{R}(t) = \left(\frac{3}{4\pi} v'\tau\right)^{\frac{1}{3}} \tag{3.34}$$

where the time is given as:

$$\tau_i = \sum_i dt \tag{3.35}$$

and i denotes the summation step. When the total displacement of the center of mass, given by the resultant of the x- and y-displacement components as:

$$s_i = \left(x_i^2 + y_i^2\right)^{\frac{1}{2}} \tag{3.36}$$

exceeds the instantaneous bubble radius calculated in Eqn. (3.34), then the bubble is considered to have departed. This criterion was described by Davidson and Schueler (1960b) as the point at which the outward velocity of the bubble surface relative to its center is equal to the upward velocity of the center of mass of the bubble. Figure 3.4 illustrates the convergence of the displacement of the center of mass and the geometric center of the bubble during various stages of growth up to departure.

The components of the displacement of the center of mass are calculated by integrating the momentum equations for the vapor (Eqns. (3.8) and (3.13)) as follows:

$$\frac{dx_i}{dt} = \frac{1}{\left(\frac{19}{32}\rho_l + \rho_v\right)\tau_i}\left[g\sin\theta\left(\rho_l - \rho_v\right)\frac{\tau_i^2}{2} + f_{drag}^i\right] \tag{3.37}$$

and:

$$\frac{dy_i}{dt} = \frac{1}{\left(\frac{11}{16}\rho_l + \rho_v\right)\tau_i}\left[g\cos\theta(\rho_l - \rho_v)\frac{\tau_i^2}{2} + f_{lift}^i\right] \tag{3.38}$$

The numerical integration of the drag and lift forces is given by:

$$f_{drag}^i = \sum_i \left(-sign(U_{rel}^{i-1})\frac{\pi}{2}\rho_l\left(\frac{9}{16\pi^2\nu'}\right)^{\frac{1}{3}} C_d^i\left(U_{rel}^{i-1}\right)^2 \tau_i^{\frac{2}{3}} dt \right) \tag{3.39}$$

and

$$f_{lift}^i = \sum_i \left(\frac{\pi}{2}\rho_l\left(\frac{9}{16\pi^2\nu'}\right)^{\frac{1}{3}} C_L^i\left(U_{rel}^{i-1}\right)^2 \tau_i^{\frac{2}{3}} dt \right) \tag{3.40}$$

The drag and lift forces are calculated using the relative velocity carried forward from the previous time step, which is also used to calculate the updated drag and lift coefficients. The y-velocity component is always greater than or set equal to zero, since the bubble can not have a negative y-displacement through the wall, and since the force balance normal to the wall is valid only when the lift force exceeds the buoyancy force, as mentioned previously.

The x- and y-components of the displacement of the center of mass are finally obtained through integration using the trapezoidal rule, expressed as follows:

$$x_i = \sum_i \frac{1}{2}\left(\frac{dx_i}{dt} + \frac{dx_{i-1}}{dt}\right) \cdot dt \tag{3.41}$$

and

$$y_i = \sum_i \frac{1}{2}\left(\frac{dy_i}{dt} + \frac{dy_{i-1}}{dt}\right) \cdot dt \tag{3.42}$$

The time step size, dt, is chosen appropriately small such that the error in the integration converges within an established tolerance and such that the growth of the bubble between successive steps does not exceed an acceptable accuracy tolerance on the final bubble radius.

3.3. Part Two: dimensional analysis of the evaporating liquid on the heated surface

In the model calculations described above in section 3.2, each incremental level of heat flux yields a unique value for the bubble residence time, given the flow conditions and heater surface orientation. Therefore, a constraint on the heat flux level must be imposed to distinguish the CHF, which is achieved by setting a constant upper bound on the product of the surface heat flux and the bubble residence time for a given set of flow conditions, as follows:

$$E'' \equiv q_c \tau_{res} = const. \tag{3.43}$$

E'' represents a quantity of energy per unit area leaving the heater surface during the bubble residence time. In the dimensional analysis below, it is assumed that this energy evaporates a sufficient amount of liquid on the surface to produce dry areas of significant

proportion to the total surface area to trigger the CHF. It is further assumed that E'' is independent of the motion of the vapor, and is instead described by the momentum and energy equations applied to the liquid very near the heater surface, where the evaporation occurs. The bubble residence period calculated from the force balance on the vapor merely establishes the time during which the liquid on the surface is depleted through evaporation, which is found to vary in inverse proportion to the CHF such that Eqn. (3.43) holds true for all heater surface orientations.

Below, the factors affecting the transient depletion of the thin liquid regions underlying the growing vapor bubbles are characterized to establish a link between the bubble residence time and the CHF. In experimental measurements of the local heater surface temperature, Yu and Mesler (1977) characterized the transient evaporation and depletion of the liquid beneath the growing bubbles, demonstrating the periodic drying out and rewetting of portions of the surface during bubble growth and departure. In photographs of pool boiling with water, Katto and Yokoya (1968) identified a very thin, perhaps non-uniform layer of liquid at the heater surface, which was vaporized almost completely during the residence time of the bubble growing above the surface. In light of these observations, the present model accounts for the factors affecting the thickness of the thin liquid layer on the surface, in addition to the enthalpy flow in it, assuming that the evaporation of the layer during the bubble residence time is the primary mechanism of the CHF.

Two salient dimensionless groups arise from the dimensional analysis below, from which the CHF can be predicted for any combination of flow conditions, heater

sizes and test fluids. The latent heat of evaporation and the advection of enthalpy in the liquid layer are characterized by one dimensionless group, while the effects of viscosity and surface tension on the liquid layer thickness are characterized by the other. A correlation between the two is then derived empirically to predict the value of E'', which can be used with part one of the model to calculate the CHF.

3.3.1. Correlation of the Thermal Effects

E'' is non-dimensionalized with respect to the latent heat energy contained in the liquid which is evaporated during the bubble residence time to form dry spots on the heater surface as:

$$\psi \equiv \frac{\text{Energy supplied by the heater surface}}{\text{Energy of evaporation of the liquid on the surface}} = \frac{q_c \tau_{res}}{\rho_l h_{fg} \delta_E} = \frac{E''}{\rho_l h_{fg} \delta_E} \qquad (3.44)$$

ψ differs from the latent heat fraction, χ, in Eqn. (3.30), in that ψ characterizes only the evaporation in the thin liquid regions beneath the growing bubbles that results directly in the formation of dry spots, and therefore does not describe the net evaporation rate. In Eqn. (3.44), δ_E represents the equivalent thickness of the liquid evaporated on surface beneath the bubbles, which is assumed to be proportional to the thickness of the superheated portion of the thermal boundary layer. In addition, the heater surfaces are assumed to be relatively short, and the thermal boundary layer is therefore assumed to be relatively thin compared to the fully-developed hydrodynamic boundary layer. The

thermal boundary layer thickness is approximated to a first order by simple conduction into a uniform, laminar flow, giving the order of magnitude thickness as:

$$\delta_T \sim \sqrt{\alpha \frac{L}{u}} \tag{3.45}$$

Where L is the heated length, and the characteristic velocity, u, is determined from the turbulent velocity profile in the laminar sublayer, where $u^+ = y^+$ for y^+~1-10, as:

$$u \sim u_* \sim \mathrm{Re}_D^{-\frac{1}{8}} U_b \tag{3.46}$$

Substituting Eqn. (3.46) into Eqn. (3.45) gives:

$$\delta_T \sim D_H \left(\frac{L/D_H}{\mathrm{Re}_D \, \mathrm{Pr}} \right)^{\frac{1}{2}} \mathrm{Re}_D^{\frac{1}{16}} \tag{3.47}$$

The superheated boundary layer thickness over a surface with an imposed uniform surface temperature is then assumed to be proportional to the thermal boundary layer thickness, i.e.,

$$\delta_E \sim \delta_T \tag{3.48}$$

While this expression becomes an equality in the case of saturated boiling, the superheated layer thickness decreases relative to the thermal boundary layer thickness with increasing subcooling. Using Eqn. (3.48), Eqn. (3.47) is then substituted into Eqn. (3.44) to yield:

$$\psi \equiv \frac{E''}{\rho_l h_{fg} D_H \, \mathrm{Re}_D^{\frac{1}{16}}} Gz^{\frac{1}{2}} \tag{3.49}$$

Including the correction term for the effects of subcooling, based on the correlation of Ivey and Morris (1962), Eqn. (3.49) becomes:

$$\psi' = \frac{\psi}{\left(1 + 0.102\left(\frac{\rho_v}{\rho_l}\right)^{\frac{1}{4}} Ja\right)} \tag{3.50}$$

E'' depends on the subcooling in the same manner as the CHF due to the expression used for χ, given in Eqn. (3.31), which assumes the vapor generation rate at the CHF to be the same for all levels of subcooling. Following that assumption, the bubble residence time at the CHF for a given heater orientation and flow velocity is also therefore independent of subcooling, and E'' should then correlate with subcooling as in Eqn. (3.50).

Based on experimental data to be presented in Chapter 5, the dependence of E'' on the length of the heater surface was determined empirically as:

$$\Phi \equiv \frac{\psi'}{\left(L/\lambda_T\right)^{-0.9}} = \frac{E''}{\rho_l h_{fg} D_H \, \mathrm{Re}_D^{\frac{1}{16}}} \frac{Gz^{\frac{1}{2}}\left(L/\lambda_T\right)^{0.9}}{\left(1+0.102\left(\frac{\rho_v}{\rho_l}\right)^{\frac{1}{4}} Ja\right)} = \frac{E''}{\rho_l h_{fg} L_c} \frac{\mathrm{Re}^{\frac{7}{16}}}{\left(1+0.102\left(\frac{\rho_v}{\rho_l}\right)^{\frac{1}{4}} Ja\right)} \tag{3.51}$$

where the characteristic length, L_c, is defined as:

$$L_c \equiv \frac{D_H^{\frac{1}{2}} \lambda_T^{0.9}}{L^{0.4}} \tag{3.52}$$

E'' decreases with increasing heated length due to an increase in the local quality with increasing distance from the leading edge of the heater, as well as to the increase in the thickness of the bubble boundary layer along the heated length, which blocks the enthalpy exchange with the bulk region more effectively.

3.3.2. Correlation of the flow velocity effects

The effects of shear in the thinning of the liquid layer on the heater surface counter the capillary forces, which tend to thicken the layer. The relative effects of these forces is described by a modified capillary number, defined for this case as:

$$Ca \equiv \frac{\mu\left|\frac{du}{dy}\right|}{\sigma/R} = \frac{\text{thinning due to shear force}}{\text{thickening due to capillary force}} \tag{3.53}$$

Since E'' is assumed independent of the relative velocity between the two phases, since this is a function of the heater surface orientation, the bubble-induced shear stress in the liquid near the wall must therefore be negligible. Accordingly, the shear rate in the numerator is determined according to the Blasius formula given by Eqn. (3.17). Also, the bubble radius is assumed to scale with the most unstable Taylor wavelength, such that the modified capillary number, Eqn. (3.53), is given by:

$$Ca \sim \frac{\rho U_b^2 \, \mathrm{Re}_D^{-\frac{1}{4}}}{\sigma/\lambda_T} = \frac{We_D}{\mathrm{Re}^{\frac{1}{4}}} \frac{\lambda_T}{D_H} \tag{3.54}$$

3.3.3. Correlation of Φ as a function of Ca

Using values for E'' obtained from the best fit with the experimental measurements of the CHF in Chapter 5, Φ is evaluated and correlated with the corresponding value of Ca. The resulting relationship, given in Chapter 6, allows for the prediction of E'' for a given flow velocity, subcooling and heated length, thus providing a general means of completing the solution to the forced convection CHF model.

3.4. The limiting case of pool boiling (no imposed flow)

As a first step to understanding the effects of heater surface orientation on the CHF, the case of pool boiling is first considered, which, unlike the case of forced convection boiling, yields equations in a form which may be solved explicitly. The solution for this case reveals the individual effects of various parameters on the CHF in pool boiling, such as gravity, subcooling and the bubble shape. This lends insight into the analogous effects in the forced convection case which might not otherwise be obvious, given the absence of an analytical solution for the CHF. Concentrating specifically on the downward-facing heater surface orientations, where the motion of the vapor, if any, is entirely parallel to the surface, the force balance for a single bubble in the direction of motion is given by:

$$F_{buoy,x} = F_{m.a.,x} \tag{3.55}$$

Written explicitly, as in the development of the forced convection model in section 3.1.1, Eqn. (3.55) may be expressed as:

$$g\sin\theta(\rho_l - \rho_v)t = \frac{d}{dt}\left[(c_1\rho_l + \rho_v)t\frac{dx_v}{dt}\right] \tag{3.56}$$

Integrating this expression twice and evaluating it at the condition of bubble departure gives:

$$R_d = \frac{g\sin\theta(\rho_l - \rho_v)}{\left(\frac{19}{32}\rho_l + \rho_v\right)}\frac{\tau_d{}^2}{4} \tag{3.57}$$

Evaluating Eqn. (3.34) at τ_d, a second, independent expression for the mean bubble radius at departure is obtained, which is substituted into Eqn. (3.57) and solved for τ_d as:

$$\tau_d = \left(\frac{3v'}{4\pi}\right)^{\frac{1}{5}} \left[\frac{4}{g\sin\theta}\frac{\frac{19}{32}\rho_l + \rho_v}{\rho_l - \rho_v}\right]^{\frac{3}{5}} \tag{3.58}$$

Further substitution of the expressions for v' and the unit surface area given by Eqns. (3.32) and (3.33) yields:

$$\tau_d = \left(9\pi \frac{\chi q_c}{\rho_v h_{fg}} \frac{\sigma}{g(\rho_l - \rho_v)}\right)^{\frac{1}{5}} \left[\frac{4}{g\sin\theta}\frac{\frac{19}{32}\rho_l + \rho_v}{\rho_l - \rho_v}\right]^{\frac{3}{5}} \tag{3.59}$$

Through the buoyancy term and the dependence of the bubble size on g, Eqn. (3.59) shows a strong dependence of the residence time, τ_d, on gravity. It is also a relatively strong function of the virtual mass of the bubble, indicating the importance of the shape assumed for the bubble. If fluid property variations with pressure are neglected, however, the residence time at the onset of dryout becomes independent of subcooling, in light of the correlation used for χ and the variation in q_c with subcooling.

To gain an expression for E'', each side of Eqn. (3.59) is multiplied by the CHF, q_c, giving:

$$E'' = q_c \cdot \tau_d = \left(\frac{q_c^2}{\sin\theta}\right)^{\frac{3}{5}} \left(9\pi \frac{\chi}{\rho_v h_{fg}} \frac{\sigma}{g(\rho_l - \rho_v)}\right)^{\frac{1}{5}} \left[\frac{4}{g}\frac{\frac{19}{32}\rho_l + \rho_v}{\rho_l - \rho_v}\right]^{\frac{3}{5}} \tag{3.60}$$

Rearranging Eqn. (3.60) to isolate the CHF and heater orientation angle gives the following:

$$\left(\frac{E''}{\left(9\pi \frac{\chi}{\rho_v h_{fg}} \frac{\sigma}{g(\rho_l - \rho_v)} \right)^{\frac{1}{5}} \left[\frac{4}{g} \frac{\frac{19}{32}\rho_l + \rho_v}{\rho_l - \rho_v} \right]^{\frac{3}{5}}} \right)^{\frac{5}{3}} = \left(\frac{q_c''}{\sin\theta} \right) \tag{3.61}$$

Therefore, assuming E'' and χ to be independent of heater surface orientation, q_c will correlate with $(\sin\theta)^{1/2}$ in the downward-facing domain. Moreover, assuming E'' and χ to depend on subcooling according to Eqns. (3.31) and (3.49), then q_c will vary with subcooling as predicted by the Ivey and Morris (1962) correlation. Both results are identical to the semi-empirical CHF model developed by Brusstar and Merte (1994) for pool boiling, which was based on the pumping action of bubbles departing the heated surface at their terminal velocity.

Using Eqn. (3.59), a unique value of the bubble residence time can be calculated from a given heat flux level, which is also true in the forced convection model. Figure 3.5 is a plot of the bubble residence time as a function of the heat flux level according to Eqn. (3.59), in which the imposed value of the constant E'' determines the locus of CHF values along the family of curves associated with the various heater surface orientations. In this same way, the value of E'' determines the calculated value of the CHF for the various orientations in the forced convection model.

3.5. The limiting case of microgravity

While a model of the CHF in forced convection boiling under microgravity can not yet be validated, given the total lack of experimental data, the experimental observations at various heater orientations exhibit general characteristics which may be extended to the case of reduced gravity or microgravity. Boiling in microgravity differs

in three main ways from boiling under Earth gravity. First, nucleate boiling as such does not exist at relatively high levels of heat flux; rather, as the quasi-steady pool boiling measurements of Zell, et al. (1984) in microgravity demonstrate, the vapor forms large coalesced slugs beneath which film boiling prevails. Second, the Taylor instability does not exist in microgravity, and the photographs by Merte, et al. (1994) show that the bubble sizes become exceedingly large in the absence of an imposed geometric constraint, such as a relatively small heater surface. Third, capillary and thermocapillary driven flows are generally of greater significance at low flow velocities in microgravity, given the substantial solid-liquid-vapor contact area on the heater surface as well as the sometimes exceedingly large temperature differences between the surface and the bulk liquid region.

In the present model of the CHF under microgravity, surface tension driven flows are neglected, although it is conceded that they may be somewhat significant at very low flow velocities. The equations of motion for the vapor forming on the heater surface are given by Eqns. (3.8) and (3.13), in the limit of zero gravity. The dynamics of the thin liquid regions on the surface are assumed independent of buoyancy, and the characteristic bubble size used in Eqns. (3.52) and (3.54) in the derivation of Φ and Ca are changed to reflect the expected bubble sizes under microgravity. The unit bubble spacing under microgravity is predicted using the Kelvin-Helmholtz instability at the interface between the liquid and vapor in place of the most unstable Taylor wavelength used under 1 g. Photographs of experiments by Galloway and Mudawar (1993a) in high-velocity forced convection boiling at high levels of heat flux demonstrate the role of the Kelvin-Helmholtz instability in determining the bubble size when buoyancy effects are relatively small. The Kelvin-Helmholtz instability is derived considering the relative motion of two superimposed layers of fluid of different density. A wavefront perpendicular to the direction of the relative motion is formed, which is unstable when the condition

$$U_{rel}^2 > \frac{\rho_l^2 - \rho_v^2}{\rho_l \rho_v}\left(\frac{g}{k} + \frac{k\sigma}{\rho_l - \rho_v}\right) \tag{3.62}$$

is met. In the absence of gravity, this expression implies the existence of an unstable range of wave numbers for any relative flow velocity, which are less than or equal to the critical wave number, given according to:

$$k_c = \frac{\rho_l \rho_v}{\sigma(\rho_l + \rho_v)} U_{rel}^2 \tag{3.63}$$

In microgravity, this instability would divide a large vapor mass forming on the surface into a series of cylinders spanning perpendicular to the direction of flow, whose spacing is determined by the minimum unstable Kelvin-Helmholtz wavelength, as shown in Figure 3.6. In the presence of surface tension, however, the bubbles will abhor the cylindrical shape and tend toward a more spherical one, dividing the cylindrical bubbles into rows consisting of spherical or hemispherical bubbles. The unit bubble area in microgravity is therefore defined according to the minimum Kelvin-Helmholtz wavelength squared, as:

$$A_{\mu g} = \lambda_{K-H}^2 = \frac{1}{k_c^2} = \left(\frac{\sigma(\rho_l + \rho_v)}{\rho_l \rho_v U_{rel}^2}\right)^2 \tag{3.64}$$

This expression replaces Eqn. (3.33) for the unit bubble area in the case of forced convection in microgravity. The model predictions based on this assumption are given in the context of the results obtained in the laboratory in Chapter 6, section 6.7.

Figure 3.1. Flowchart representation of the FCCHF model

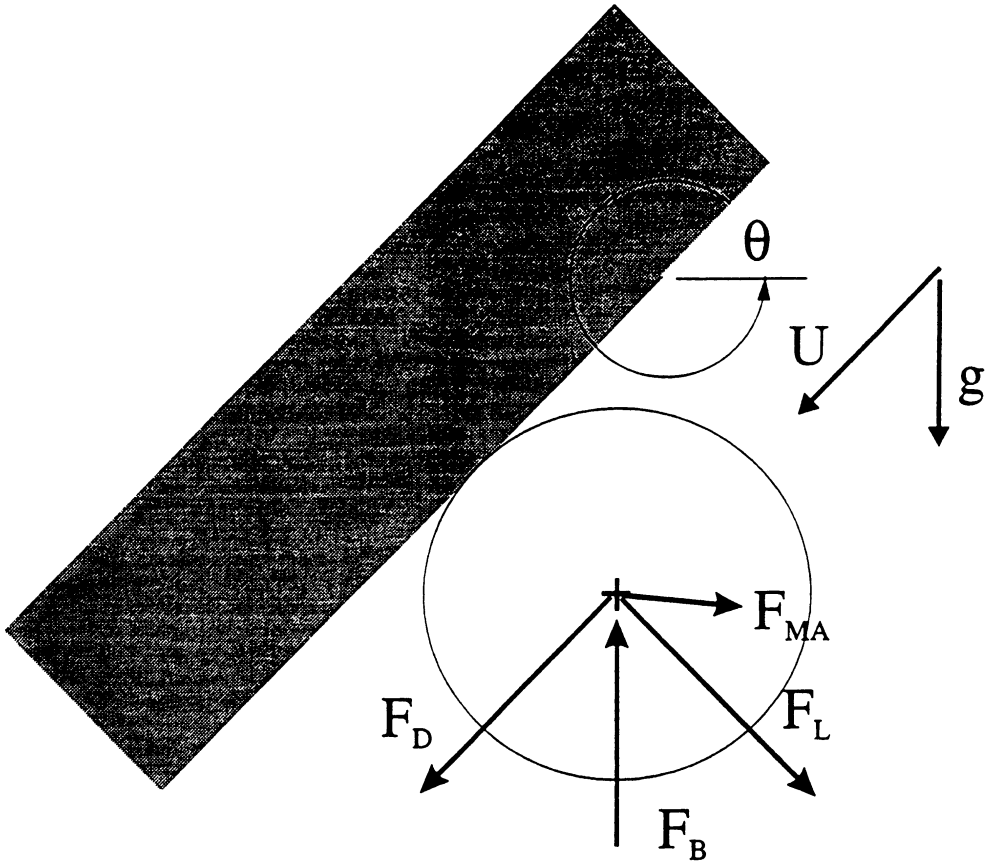

Figure 3.2. Free body diagram of a bubble growing in the presence of forced convection

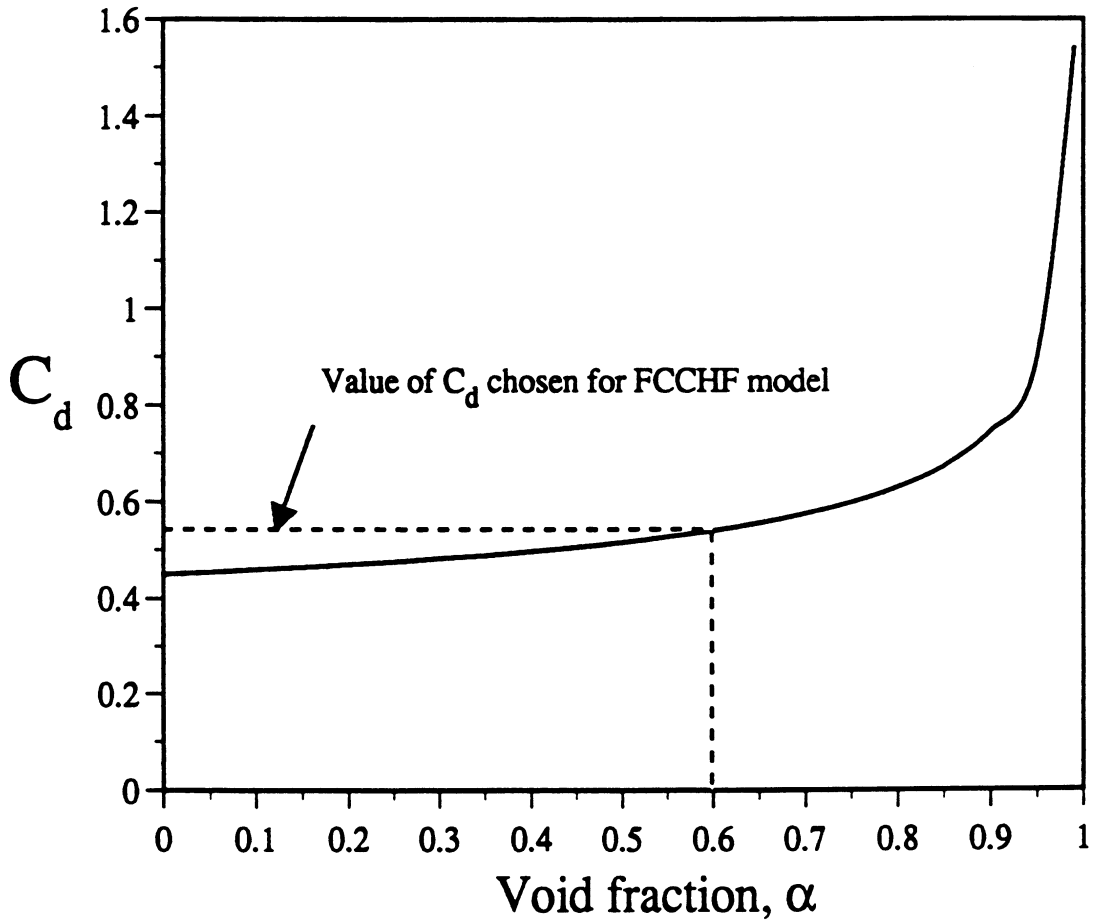

Figure 3.3. Graph of the drag coefficient of a bubble as a function of the void fraction (Eqn. 3.25)

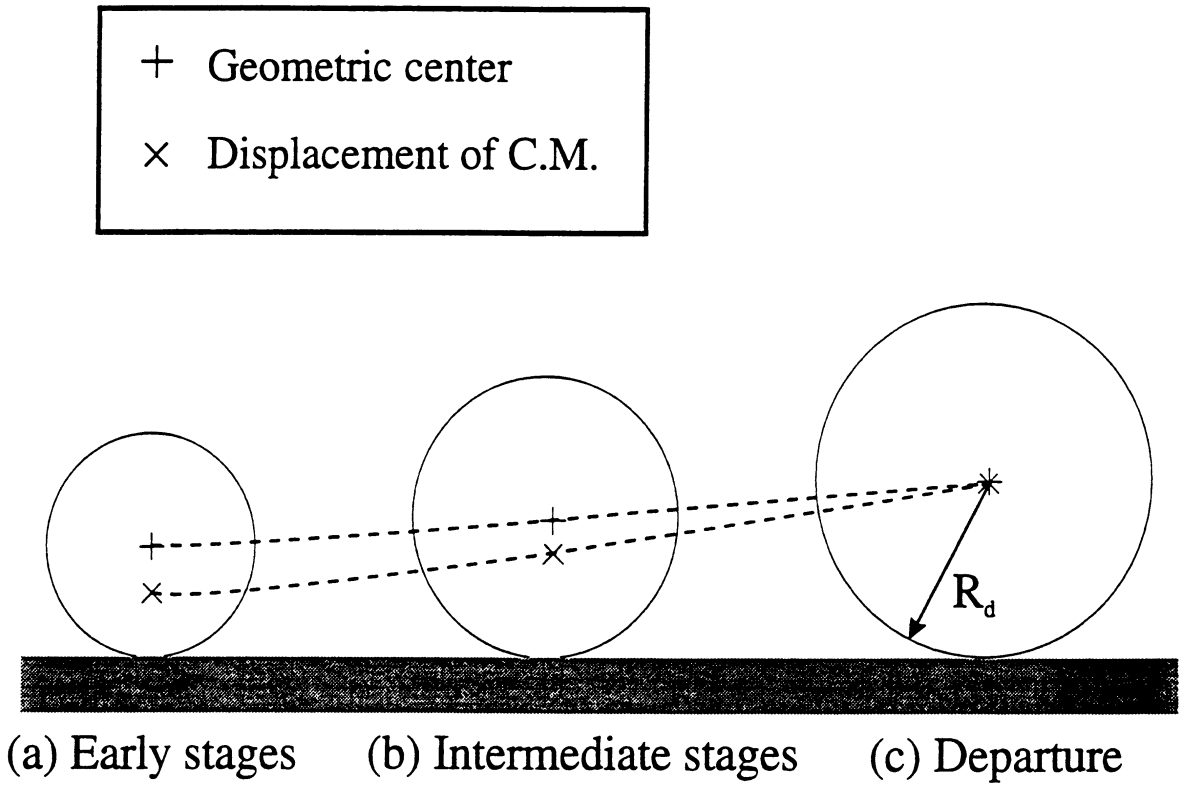

Figure 3.4. Illustration of the departure criterion used in the forced convection model

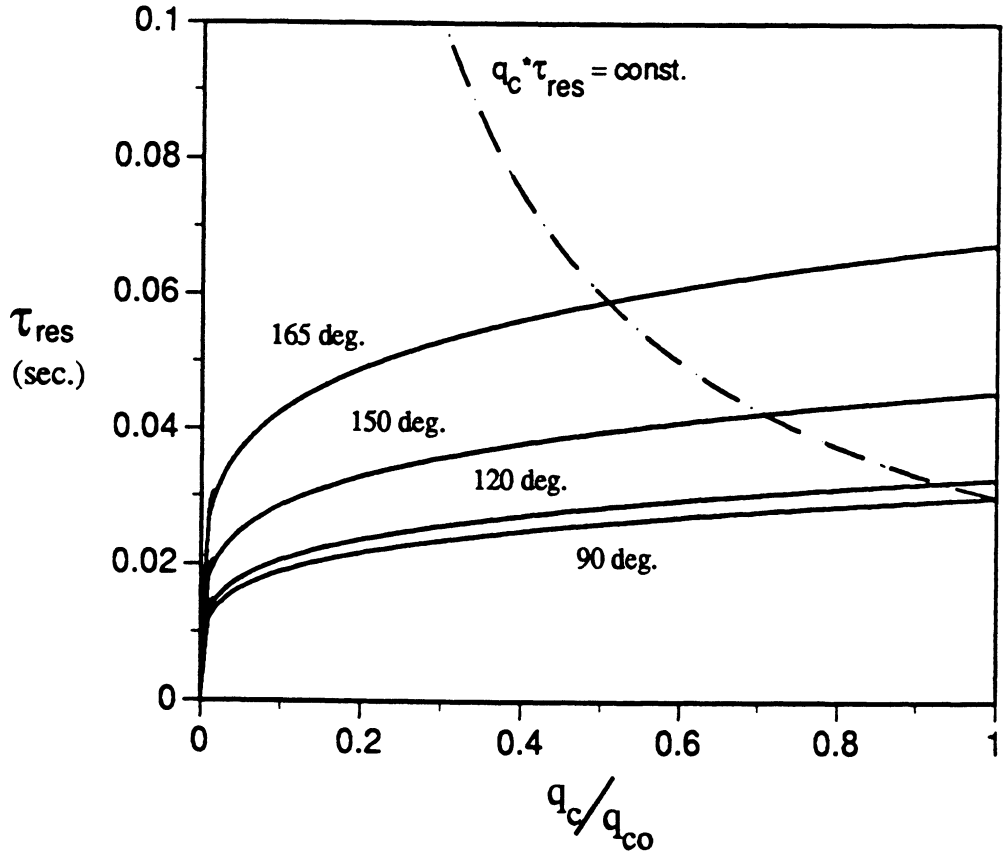

Figure 3.5. Graph demonstrating the solution method for the case of pool boiling

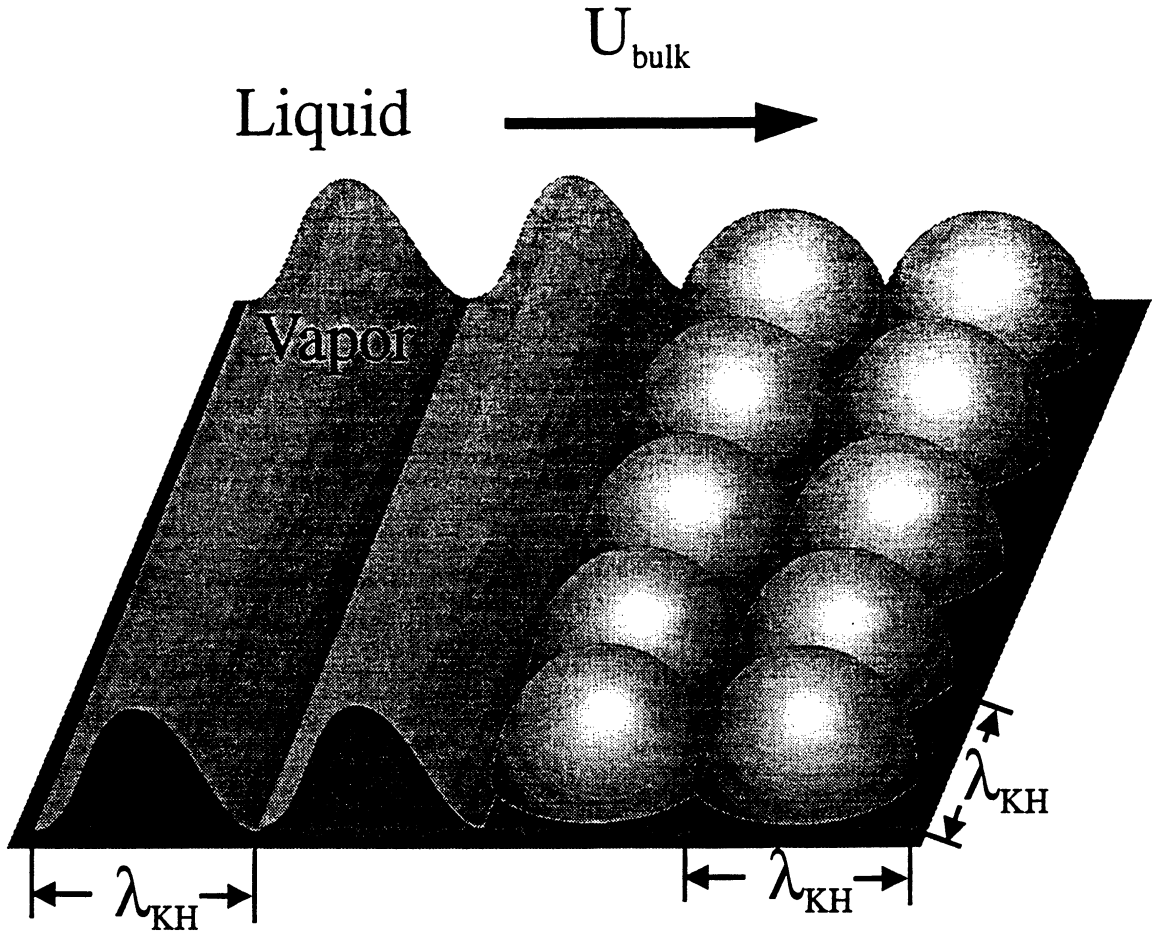

Figure 3.6. Illustration of the Kelvin-Helmholtz instability between the liquid and vapor phases in microgravity

CHAPTER 4

DESCRIPTION OF THE EXPERIMENTAL APPARATUS AND PROCEDURES

The experimental investigation with the forced convection loop consisted of three basic components:

(1) Measurements of the CHF using the metal surface

(2) Hot wire anemometer measurements of boiling near the CHF

(3) High-speed photographs of boiling near the CHF on semi-transparent gold film heater surfaces as well as on the metal heater surfaces

While each component relates to the primary objective of obtaining a better understanding of the CHF, the apparatus and procedures pertaining to each are quite distinct. This chapter gives a description of the apparatus as well as a description of the procedures used in the experimental investigation of the CHF.

4.1. Experimental Apparatus Description

A forced convection boiling loop was constructed to examine the relative influences of heater orientation and flow inertia on subcooled forced convection boiling at various levels of flow velocity, heat flux, and subcooling at different orientations relative to gravity. The heated sections are relatively short, and no attempt was made to introduce quality at the inlet to the test section, so only the subcooled bubbly flow regime was studied here. By rotating the loop to any position from 0 to 360 degrees about its axis, the component of the buoyancy force between ± 1 g relative to the direction of the flow was varied. Since future work in parabolic trajectory flights is anticipated, the flow

loop was designed according to the likely size and electrical constraints of the aircraft used for such missions.

The individual elements comprising the flow loop are described below, including the heater surfaces, the calibration equipment, the components relating to the hot wire anemometer, and the optical and photographic equipment.

4.1.1. Forced convection boiling loop

The forced convection boiling loop is shown schematically in Figure 4.1. The loop can be rotated about an axis near its center of gravity to provide any desired orientation of the heater surfaces in the test section relative to the direction of gravity, and consists of six basic components: the flow control system, the pressure control system, the temperature control system, the flow straightener and mixer, the test section, and the condenser-cooler system. The flow sections are constructed of stainless steel and aluminum, and are sealed from the environment by Buna-N and teflon seals. The integrity of the seals was checked regularly using a halogen leak detector, indicating a leakage rate of less than 0.5 ounces of freon per year. Moreover, leakage of air into the loop was prevented by continuously maintaining a positive pressure difference between the inside of the loop and the surroundings.

The features of each component are discussed in detail in the following sections. Some components were modified during the course of the experimental study, although their basic functions remained the same. Each of these modifications is noted in the description below.

4.1.1.1. Flow control system

A block diagram of the flow control system is given in Figure 4.2. The system was designed to maintain a steady flow rate to within approximately ± 2 percent of the desired set point through a proportional-integral-derivative (PID) control scheme. Closed loop control of the flow rate was achieved through feedback from a turbine flowmeter. The system components were altered from their original configuration to increase the maximum flow capacity from about 7 liters/min. to over 11 liters/min. and to incorporate a more contemporary digital control scheme. The range of flow rates reasonably obtainable with the original system was approximately 1 to 7 liters/min., while a range of about 2 to 11 liters/min. was possible with the modified system. An optional bypass loop was established about the pump so as to permit it to operate at higher speeds at lower flow rates, which lessened the flow fluctuations at the lower flow limits.

The original system components consisted of a 0.125-hp sealless centrifugal pump (Gorman-Rupp Industries, Model 14520-3) which was controlled by a 0 to 12 VDC analog circuit. Feedback to the control was achieved through a turbine flowmeter (Halliburton, Catalog No. MP7) with a linear range of 1.1 to 11 liters/min. The conditioned frequency output from the flowmeter was displayed on a pulse counter (Hewlett-Packard Universal Counter, Model 5316B), which was recorded and later converted to the corresponding flow rate using the flowmeter calibration curve given in Appendix B.3.

A schematic diagram of the modified control system is given in Figure 4.3, along with a more detailed diagram of the turbine flowmeter signal conditioner in Figure D.1 in Appendix D. In the modified system, the smaller pump was replaced by a 0.5-hp magnetically-coupled centrifugal pump (Liquiflo, Model 62FS33MCD), and the analog control was replaced by a 90 VDC maximum output digital controller (Dart Controls, Model MD30P) with an LED display of the set point and feedback signals. To

accomodate the increased flow rate of the pump, a larger flowmeter (Halliburton turbine flowmeter, Cat. No. LR21617) was added in parallel with the other flowmeter, so as to extend the linear feedback range to flow rates up to 28.5 liters/min. The calibration curve for the larger flowmeter is also provided in Appendix B.3.

4.1.1.2. Pressure control system

The pressure control system is shown schematically in Figure 4.4, with the corresponding block diagram given in Figure 4.5. The system was designed to maintain the pressure at the inlet to the test section within ±0.34 kPa (± 0.05 psi) of the desired set point by means of a pneumatically-controlled stainless steel bellows. The original analog control circuit was replaced by a digital control unit (Honeywell UDC 3000, Model DC300K-T-0B0-31-0000-0), although the control scheme was not changed.

As represented in the block diagram, the controller receives the requested setpoint and compares it to the measured pressure feedback signal. It then gives a command to the pneumatic valves which either admit or vent air from the outer side of the bellows. The bellows is then displaced slightly until pressure equilibrium is established between the test fluid on the inside and the air on the outside. As is shown in the diagram, the controller sends out two control signals. The first is the on/off 12VDC signal given to the bellows vent and fill solenoid valves (Kip, Inc., valve no. 0141010), which are triggered when the pressure deviation exceeds a predetermined threshold level, usually ± 5 kPa (±0.75 psi) from the setpoint. This increases the response to large changes in the pressure, given the relatively large volume of the bellows, which is 17.8 cm in diameter. The other control signal is the proportional-integral (PI) signal to the proportional valve, which vents air from the outer side of the bellows at a rate roughly proportional to the input voltage over its linear range of about 1.2 to 2.0 VDC. To keep the proportional valve in its linear operating range, air is admitted to the outer side of the bellows at a

nearly constant rate through a manually-set needle valve, which balances the steady flow rate through the proportional valve. Additionally, the proportional valve receives a sinusoidal dither signal aliased with the command signal to eliminate steady state errors in the pressure due to friction hysteresis in the valve.

Feedback to the pressure controller is from a diaphragm-type pressure transducer (Heise, model 623), which has a linear operating range from 0 to 207 kPa (0 to 30 psia) and a sensitivity of 0.010 kPa (0.002 psi). Details of the calibration of the pressure transducer are given in Appendix B.4. With this sensor, the closed loop control is able to maintain the pressure in the flow loop within approximately ±0.34 kPa of the requested setpoint, corresponding to a ±0.12 °C deviation in the saturation temperature.

4.1.1.3. Temperature control system

A schematic representation of the system used to control the inlet temperature to the test section is shown in Figure 4.6, along with its corresponding block diagram in Figure 4.7. The system was designed to maintain the inlet temperature to within ±0.12 °C of the requested setpoint by exchanging heat with the hot water reservoir at a controlled rate. The primary components of the system include the controller, the hot water reservoir and pump, two throttling valves, two heat exchangers and a thermocouple.

As indicated in the block diagram, the controller (Omega CN9000) receives the manually requested test section inlet temperature and compares it to the actual measured temperature, then puts out a signal to the motor driving one of the throttling valves according to its PID algorithm. The valve throttles the hot water pumped from the reservoir by a 110 VAC JABSCO Model 18560-0000 pump through the larger of the two preheaters, while the other valve is manually set to throttle the hot water to the smaller secondary preheater at a fixed rate. The net amount of heat transferred to the test fluid in the preheaters is then balanced against the heat removed or added elsewhere in the system

to bring the liquid at the inlet to the test section to the desired steady operating temperature.

The preheaters are single-pass tube-in-shell counterflow heat exchangers constructed of stainless steel. The larger preheater contains thirty five tubes, each 0.953 cm OD by 0.693 cm ID by 40.64 cm long, while the smaller preheater is identical, except having only thirteen tubes. The hot water is on the shell side, while the test fluid is on the tube side. The reservoir from which the hot water is drawn, is maintained at a nearly constant temperature by an Omega controller (Model CN9000) which powers a 2 kW AC cartridge heater, and which receives feedback through an RTD located in the reservoir.

4.1.1.4. Flow straightener-mixer section

The flow straightener-mixer section, depicted in Figure 4.8, is located just upstream of the test section, and was designed to yield a nearly isothermal, fully-developed flow at the inlet to the test section. In order to break up any jets or large eddies in the flow, a tightly-packed bed of 1.3 cm (0.5 in.) diameter spherical marbles was placed in the straight section exiting the preheaters, which also serves to even out the temperature of the test fluid through enhanced mixing. Following the marbles, the flow passes through a 90-degree bend with turning vanes to mitigate the effects of secondary flow patterns in the bend. Finally, the flow passes through a series of high-density wire mesh screens before entering the transition section preceding the test section.

4.1.1.5. Test section

The test section consists of a straight rectangular duct, 10 cm (4.25 in.) wide by 35.6 cm (14.0 in.) long, with various heights of 0.32, 1.27, and 2.54 cm (0.125, 0.5 and 1.0 in.) available with different sections, and is designed to accommodate as many as

three pairs of heater surfaces. A typical test section is illustrated in Figure 4.9, showing the pressure transducer, thermocouple and RTD connections at the inlet, as well as the six possible heater positions. Windows of optical grade quartz are placed on the sides and opposite the heater surfaces, which allow for both transverse and overhead views of the surfaces during operation.

The transition from the flow straightener section to the test section is through a 25.4 cm-long tapered section designed to avoid flow separation as the 2.54 cm duct height is gradually reduced to the test section height. Additionally, the entire section is insulated from the surroundings to reduce any temperature gradients at the duct walls and hence in the flow prior to entering the test section.

4.1.1.6. Condenser-cooler system

The condenser-cooler system, illustrated in Figure 4.10, is designed to condense the vapor leaving the test section and to subcool the liquid sufficiently to prevent cavitation in the main pump. Excess latent heat produced in the test section can be removed by circulating cold water through the coils of an auxiliary condenser located immediately following the test section, thereby permitting high heat flux tests at lower subcoolings. Ideally, the minimum amount of energy is removed to accomplish these objectives, since most of the energy extracted here must be replaced subsequently in the preheaters following the pump.

The test fluid exiting the test section enters the auxiliary condenser section, which consists of a coiled stainless steel tube (0.47 cm O.D. by 0.28 cm I.D.) through which cold tap water can be circulated, if necessary. A series of three multiple tube counterflow heat exchangers immediately follows, each consisting of thirteen 0.953 cm O.D. by 0.693 cm I. D. by 33.0 cm long stainless steel tubes. Water is circulated from the shell side of

the heat exchangers to the spiraled coils contained in the cold water reservoir by means of a small DC pump (Gorman-Rupp Industries, Model 14520-3), whose speed was controlled so as to subcool the liquid entering the main pump and avoid cavitation. The cold water reservoir is cooled by a constant flow of building utility water over the outside of the copper coils, providing a sink for the energy removed in the heat exchangers.

4.1.1.7. Thermocouples

Chromel-constantan (Type E) teflon-sheathed thermocouples with ungrounded junctions are used for measuring the liquid temperature at the inlet to the test section. The thermocouple measuring junctions were produced by welding the 30-gage wires together to form a 0.51 ± 0.13 mm (0.020 ± 0.005 in.) bead. As described in Appendix B.5, twenty sample sections of wire originating from the same spool were calibrated against a platinum resistance thermometer, yielding a single calibration curve for all of the thermocouples with relatively little variability. The accuracy of the temperature measurement as determined by the calibration, including the use of an ice junction as a reference, was approximately ± 0.02°C. For convenience, though, the internal calibration for Type E thermocouples in the MRL datalogger was used, since it agreed within ± 0.1°C with the calibration using the platinum resistance thermometer.

The chromel-constantan thermocouples located in the flow loop were placed in Omega (Type SMP) subminiature thermocouple connectors mounted on a control panel which rotated with the flow loop. The shielded thermocouple wires were extended from the control panel to the thermocouple reference junction, contained in a Dewar of crushed ice and water. Shielded copper wires were then used as an extension from the ice junction to the terminals of the data acquisition system.

4.1.1.8. Test Fluid

R113 was chosen as the test fluid, due to familiarity considerations as well as its desirability as a fluid representative of those to be used in future microgravity heat transfer applications. Historically, R113 has been used to model coolant systems in Pressurized Water Reactors (PWRs), since its thermodynamic properties at near standard temperature and pressure are similar to those of water at high pressures. Its boiling point of 47.6 °C at atmospheric pressure is relatively close to ambient room temperature, which minimizes the energy which must be supplied to the temperature control system during the experiments. Although the physical properties of R113 vary considerably with temperature (but not with pressure), this effect was minimized by holding the temperature at the test section inlet constant for all subcoolings and varying the pressure accordingly. In addition, R113 is electrically non-conductive, which permitted the use of the gold film resistance heaters and improved the performance of the hot wire anemometers.

The purity of the R113 was assured through distillation and degassing to avoid variations in the saturation properties of the fluid and to eliminate most artificial nucleation sites. Vapor pressure measurements performed on some of the batches of the R113 verified the effectiveness of these procedures. Utilizing the degassing apparatus illustrated in Figure 4.11, the R113 was first distilled, removing high-boiling-point substances such as oils and solids, then passed through a molecular sieve of synthetic silico aluminate zeolite with an effective pore size of 4 Å, which filters out the heavier gaseous components, including the water and carbon dioxide. The R113 was then frozen on a series of fins whose base was cooled by a reservoir of liquid nitrogen, while the air was pumped away simultaneously by a vacuum pump. The frozen R113 remaining on the fins was subsequently melted and transferred to a pressure vessel.

4.1.2. Test surfaces

Two types of heating surfaces were used for the experimental work, one which consists of high-conductivity copper body heated from below, the other which is a thin gold film on a quartz substrate. Because of the difference in the manner in which the surfaces are heated, the two types provide distinctly different surface heating conditions. Both types have rectangular heating surfaces identical in size, 19 by 38 mm (0.75 by 1.5 inches), and are cylindrical in shape so that they may be rotated and thus oriented in two different aspect ratios relative to the flow direction. The heating surfaces are flat to maintain a constant orientation between the body force and the heater surface and to eliminate any curvature effects associated with the solid-liquid-vapor interface.

4.1.2.1. High heat flux copper surfaces

The type of metal heater surface illustrated in Figure 4.12 has been used previously with success for quasi-steady boiling experiments, and is somewhat representative of materials found in engineering applications. The unit shown is designed to provide heat flux levels up to 80 W/cm^2 at the heated surface by the use of a cylindrical copper body heated by three cartridge heaters in its base and insulated on all other sides. Because of its large heat capacity and high thermal conductivity, the heater yields a nearly uniform temperature at the boiling surface. Three chromel-constantan (type E) thermocouples are placed at precise locations beneath one another in the straight section leading to the boiling surface so that the surface heat flux and temperature can be calculated. A smooth copper foil 0.1 mm (0.004 in.) thick is soldered over the top surface so as to prevent boiling at the crevices around the surface perimeter and in grooves on the

surface produced by machining. The surface was then electroplated with gold so as to give surface energy characteristics nearly identical to those of the gold film heaters.

4.1.2.2. Gold film surfaces

The second type of heating surface consists of a thin semi-transparent gold film on a quartz substrate, illustrated in Figure 4.13, and was used primarily for photographic purposes. Electrical energy is dissipated evenly in the film, which is nominally 400 Å thick, providing a nearly uniform heat flux over the heating surface. This contrasts with the metal heater, which gives a uniform temperature on the surface. In addition to its utility as a heater, the resistance versus temperature characteristics of the gold film allow it to be used as a resistance thermometer, although the measurements give only the mean temperature integrated over the entire surface. The transparency of the quartz and the gold film makes it possible to photograph the boiling processes on the surface from below, giving an unobstructed view of the boiling processes at the surface itself.

4.1.2.3. Heater controller system

The power to the metal heaters was controlled manually through a variable AC power supply, which was adjusted manually to the desired voltage across the heater terminals.

The voltage across the thin gold film heaters is controlled by an analog circuit, shown schematically in Figure D.3 in Appendix D, which maintained a nominally constant surface heat flux. A block diagram of the heater system is given in Figure 4.14, showing the P-I controller receiving the difference of the requested and actual output voltages, and then giving the appropriate signal to the power transistors to drive the

heater. The power transistors have a maximum output of approximately 500 W at 12.5 Amps.

4.1.2.4. Heater power measurement circuit and shutdown relay

A schematic of the power circuit for the metal heater is given in Figure 4.15. The current through the heater was measured directly with a 0 to 5 Amp inductance meter in series with the heater, while the voltage across the heater terminals was displayed on a Keithley Model 196 digital multimeter.

A schematic of the circuit for the gold film heaters is given in Figure 4.16. With the knife switch in one position, the +5 VDC power supply is used in series with a calibrated shunt (Leeds & Northrup, Cat. 8070) of resistance 10.0100 Ω ± 0.0005 Ω at 25 °F for the single point calibration. With the knife switch in the other position, a calibrated shunt of resistance 0.016314 Ω ± 0.000002 Ω from 75 to 105 °F is placed in series with the heater for measuring the current, while the potential across the heater is measured directly by the MRL datalogger.

A heater shutdown relay is also indicated in Figures 4.15 and 4.16. If the measured surface temperature of either the metal heater or the gold film heater exceeds 110 °C, a relay in the MRL datalogger triggers an external mechanical relay to open the heater circuit as a precaution against damaging the heater surface.

4.1.3. Data acquistion systems

An Esterline Angus Multipoint Recorder/Logger (MRL) (Serial No. 88200030), a 48-channel multiple microprocessor-based, user-programmable data acquisition system was used to monitor the operation of the flow loop and to make test measurements. The analog input channels have a range of ± 1 mV to ± 60 V DC, with a 20 MΩ input

impedance for the 0 to 1 V inputs, 1MΩ for higher input levels. The reported measurement accuracy was ±0.25% of the internal measurement span, although a calibration test using a Keithley multimeter (Model 196) as a reference proved the actual performance to be slightly better: ± 0.05 mV for the 100 mV range and ± 3.0 mV for the 20 V range.

The MRL was programmed to measure the thermocouple voltages, the pressure transducer output voltage, the gold film heater voltage and shunt voltage, and then perform the necessary mathematical manipulations to display the measurements in the desired form. The MRL displayed various loop temperatures, heater temperatures and heat flux levels, and the system pressure on both an LED display and a hard-copy trend report. The MRL also has up to eighteen 2 amp, 24VDC alarm relay outputs, two of which were programmed to trigger the heater shutdown relays when the calculated heater temperatures exceeded a specified level.

The calibration of the heater surfaces and the thermocouples was monitored by a Campbell Scientific Co. CR7X datalogger (serial no. 1448). The CR7X is a programmable digital measuring and controlling device which can record data over eight different ranges, from ± 1.5 mV (within ± 50 nanovolts) to ± 5 V (within ± 166 mV). Several tests were conducted by Ervin (1991) to evaluate the performance of the CR7X, showing the accuracy to be within at least ± 0.6 mV over the 15 mV and 50 mV ranges, which are commonly specified for the heater and thermocouple calibrations. Data can be acquired at two different speeds, the slower one with a 16.66 ms integration time (a rate of 60 Hz), the faster one with a 250 microsecond integration time (a rate of 4 kHz).

The hot wire anemometer output was recorded by the DATAQ Instruments, Inc. Codas (version 5.04) PC-based high-speed data aquisition system. The system consists of software run from a 386DX-25 PC with an analog-to-digital interface. The analog-to-digital converter has 12-bit resolution (1 part in 4096), with a conversion time of 20 microsecond, including acquisition, and a throughput of 1 Hz to 50 MHz. The Codas

system can receive up to sixteen single-ended (or eight differential) -2.5 to 2.5 VDC analog inputs, and is capable of recording the data directly to the PC hard disk in a variety of formats while simultaneously displaying the scaled input channels in strip chart form on the PC monitor. The reported accuracy is ±0.01% of full scale, or ±0.25 mV, although a calibration using the CR7X datalogger as a reference determined the accuracy to be about ±1 mV. The jitter, i.e., the error arising from a non-uniform clock speed, is minimized through an onboard crystal controlled oscillator with a base frequency of 20 MHz.

4.1.4. Optical/photographic system

Figure 4.17 shows the optical setup used for obtaining two orthogonal views of the boiling occurring on the heater surface, with one view through the heater surface from below and the other from the side, both being perpendicular to the direction of flow. High speed photography at a rate of up to 1000 frames/second was achieved with the Kodak Ektapro 1000 Image System, recorded on a magnetic tape. The high framing rate necessitated the use of intense lighting, provided by 360 Watt incandescant bulbs powered by a variable 110 VAC supply. The infrared radiation from the bulbs is filtered with "cold mirrors" of special IR filtering glass, which then reflect the light to the imaging camera. In addition, translucent plastic or ground glass is used as shown to diffuse the light source to decrease the non-uniformity of the source.

4.1.5. Power supplies

A Sorensen DCR150-35 variable DC power supply provided the +24 VDC source used for the control circuitry. A transformer is then used to convert the 24VDC source to the +12 VDC and +36 VDC sources required. A Lambda Model LB-704-FMOV 0-60

VDC, 40Amp variable DC power supply was used to power the gold film heaters, while a variable AC transformer was used for driving the metal heaters. The ± 15 VDC and + 5VDC sources used for the controls and instrumentation are provided by an AC rectifier/transformer.

4.1.6. Hot wire anemometer

A hot wire anemometer is used to measure the transient and time-averaged motion of the liquid and vapor phases above the heater surface, providing adequate dynamic response with reasonable accuracy. Although the hot wire is an intrusive device, this effect was minimized by introducing the test probe and its support into the test section from downstream of the heater surface, as shown in Figure 4.18. The hot wire anemometer and the associated instrumentation are described below.

4.1.6.1. Measuring probe

The hot wire probe designed for the experiments is shown in Figure 4.19. The sensing wire is high purity platinum, and its temperature coefficient of resistance is assumed to be that of pure platinum and therefore reasonably constant over a broad range of temperatures. The wire is 25 microns (0.001 inches) in diameter by 1.3 mm (0.050 in.) long nominal, and is soldered to the tapered ends of two 1.0 mm (0.040 in.) diameter phosphor-bronze lead wires. To give support to the lead wires and to provide a means of attaching the probe to the lead screw mechanism, the lead wires pass through an electrically non-conductive composite material, and are epoxied in place. The probe is then firmly secured to the lead screw mechanism described below by means of a small cap screw running through the center of the composite body.

4.1.6.2. Lead screw mechanism

The lead screw mechanism used to displace the probe is illustrated in Figure 4.20, and provides a means of displacing the probe in two orthogonal directions, one normal to the heater surface, the other in the direction of flow. The probe displacement is measured by two separate dial indicators, each with a range of 0.000 to 1.000 inches, marked in increments of 0.001 inches.

The movement in the direction perpendicular to the heater surface is achieved by the larger of the two lead screws shown in the figure. The mechanical displacement of the fine screw thread allows for the fine adjustment of the relative position of the hot wire probe normal to the surface. The displacement of the probe in the direction parallel to the surface is accomplished by a hydraulic link between the smaller lead screw and the link to which the probe is attached. The screw moves a piston at the top of the mechanism, which is hydraulically linked to another piston of equal diameter at the bottom through a tube filled with motor oil, which gives a displacement at the probe tip equal to that of the screw. The return motion of the lower piston is aided by a small load spring, which helps to reduce hysteresis errors induced by friction in the piston seals.

4.1.6.3. Electrical control circuit

The current passing through the hot wire is controlled electrically by the circuit shown schematically in Figure D.4 in Appendix D. The circuit functions to maintain a constant current through the hot wire despite changes in load resistance resulting from fluctuations in the rate of heat transfer from the hot wire. The advantage of operating in constant current mode versus the more conventional constant temperature mode is that the voltage across the hot wire increases as it enters a vapor mass, giving superior

sensitivity to the detection of the vapor phase relative to a probe operated at a constant temperature. By Ohm's Law, with the current maintained constant:

$$\Delta E(t) = \bar{I}R(t) \tag{4.1}$$

The fluctuations in the measured voltage across the probe will therefore be proportional to the fluctuations in resistance, which is in turn proportional to the fluctuations in the mean temperature of the heated wire. The sensed output from the probe is first sent through an analog anti-aliasing filter, designed with a cutoff frequency of approximately 1000 Hz and a rolloff of 60 dB/decade. This acts as a barrier against externally-imposed electrical noise and random spikes. Next, the DC portion of the signal is subtracted, while the remaining fluctuating portion is amplified by a factor of two hundred. The resulting output to the data acquisition system then constitute the filtered and amplified hot wire voltage fluctuations.

4.2. Experimental Procedures

4.2.1. Flow loop filling procedure

Precautions are taken during the filling of the flow loop to avoid contact between the purified R113 and the air, preventing contamination of the fluid with air. After draining the previous charge of R113 from the loop, the integrity of the seals is checked by pressurizing the loop with air and monitoring any leakage of the residual R113 to the surroundings using a halogen leak detector. The loop is then depressurized, and a vacuum pump connected to evacuate the entire flow loop and filling apparatus over the course of approximately four hours. During the evacuation, the R113 source tank is heated by infrared lamps to bring its vapor pressure to approximately 3 to 5 psi above atmospheric pressure, and the tank is situated above the flow loop to also provide a

positive hydrostatic pressure difference during filling. When the vacuum in the system is measured as less than 100 microinches of Hg, the vacuum pump is closed off, and the filling tank is opened to the system until the loop is completely filled. The loop is then immediately disconnected from the filling system and pressurized to prevent possible leakage of air into the loop.

4.2.2. Quasi-steady heat flux measurements

Measurements of the surface heat flux with the metal heater were conducted under quasi-steady conditions in which the orientation of the heater surface, the bulk flow velocity and bulk subcooling were varied. Prior to the commencement of testing, the flow loop was operated for approximately four hours to reach thermal equilibrium at the desired operating condition.

At the beginning of the tests, boiling was initiated on the metal heater surface by raising the power on the heater surface to a level well above the steady limit for natural convection. Boiling inception was customarily marked by a direct transition to film boiling on the surface, similar to what was previously observed by Okuyama and Iida (1991) for boiling inception with stepwise heating at high superheat levels with R113 and liquid nitrogen. Quasi-steady nucleate boiling was then established by removing power to the heater to allow the quenching of the surface, then reapplying the power once rewetting was observed through a sharp drop in the measured surface temperature. Once a steady operating condition was attained, the temperature measurements from the three thermocouples leading to the heater surface are recorded manually, as is the voltage across the heater terminals, the measured current, the test section inlet temperature and pressure and the turbine flowmeter reading. The voltage across the heater is then increased incrementally, and the conditions recorded as before when the heating surface has reached a quasi-steady operating temperature. When a sharp rise in the surface

temperature is observed with a unit incremental rise in the heater power, the transition to film boiling is assumed to occur, and the last recorded steady state operating condition is used to calculate the CHF. All CHF measurements are repeated, some of them several times, to verify their reproducibility. The CHF measurements were duplicated, within some estimated uncertainty, although the accompanying superheat sometimes varied a few degrees, possibly as a result of changing nucleation patterns on the heater surfaces over time.

The experiments were performed at various heating surface orientations ranging from 0 to 360 degrees. The orientation of the heater surface is defined in this work with respect to the horizontal facing upward position in Figure 4.21. The flow direction is indicated by the arrows, and orientations intermediate to those shown in the figure are defined by the counterclockwise rotation. Using this convention, vertical with upflow corresponds to $\theta = 90$ degrees, horizontal facing downward to $\theta = 180$ degrees, and vertical with downflow to $\theta = 270$ degrees. The direction of the buoyancy force relative to both the imposed flow velocity and the heater surface changes with orientation, and is responsible for the effects to be demonstrated in the next chapter.

4.2.3. Data reduction

The measurements collected in the CHF experiments using the metal heater surfaces and thin gold film heater surfaces were reduced using a Microsoft Excel worksheet, yielding the results tabulated in Appendix A. The specific algorithms used are detailed below.

4.2.3.1. Average surface heat flux

The average surface heat flux for the metal heater was calculated from the First Law:

$$q''_{surf} = \frac{1}{A_{surf}}\left(\dot{P}_{gen} - \dot{Q}_{loss}\right) \qquad (4.2)$$

The total power input to the heaters is determined from the measurements of the voltage and current, while the heat loss to the surroundings is estimated from the measured base temperature using Eqn.(B.5) in Appendix B. With the uncertainties in the loss calibration along with the uncertainty in the measured heater power, the estimated surface heat flux is accurate to within about ± 1.5 W/cm^2. Further elaboration on the uncertainty is given in Appendix C.1.

The surface heat flux for the gold film heaters is also determined using Eqn. (4.2), assuming the peripheral heat losses to be negligible compared to the total power input. The power input to the heaters is determined from the measured voltage and current. The uncertainty in the calculated surface heat flux due to peripheral heat losses and uncertainties in the measured voltage and current is about ± 3 %. A more detailed analysis of the uncertainty is given in Appendix C.3.

4.2.3.2. Heater surface temperature

Through repeated trials during the calibration of the metal heater surfaces, an estimate of the metal heater surface temperature from a linear extrapolation of the two thermocouples closest to the surface was determined to be reasonably accurate. The first thermocouple lay 1.3 mm below the heater surface, while the second was 9.5 mm below that. Using a linear extrapolation, the uncertainty in the calculated surface temperature is

about ± 0.9 °C, given the tolerance in the size and position of the holes into which the thermocouples were placed and the uncertainty in the measured temperatures.

The spatial mean temperature of the gold film heaters is estimated from the measured heater surface resistance, determined from the measured voltage and current. Using the temperature versus resistance characteristic determined from the gold film calibration in Appendix B.2, the thin film heater temperature is calculated. As a result of uncertainties in the heater calibration and in the measured voltage and current values, the estimated uncertainty in the mean surface temperature is approximately ± 1.0 °C.

4.2.3.3. Local bulk liquid subcooling

The local bulk liquid subcooling at the heater surface is calculated based on the pressure and temperature measured at the inlet to the test section. The subcooling is defined as the difference between the bulk liquid temperature and the saturation temperature, and a second-order polynomial is used to approximate the vapor pressure curve taken from Mastroianni, et al. (1978), as:

$$T_{sat} = 54.48 + 5.058P - 0.05208P^2 \qquad (4.3)$$

where the temperature is given in units of °F, and the absolute pressure in units of psia. The local pressure above the heater surface was then calculated by taking the pressure measured at the inlet to the test section and correcting it for the hydrostatic pressure difference between the pressure tap and the heater as:

$$P = P_{inlet} - \rho_l g H \sin\theta \qquad (4.4)$$

Here, H is the measured distance between the pressure tap and the heater, and θ is the heater surface orientation angle. Given some relatively small error introduced through the use of Eqns. (4.3) and (4.4), along with the uncertainty in the measured pressure of $\pm$ 0.14 kPa, and the uncertainty in the bulk inlet temperature of about $\pm$ 0.12 °C, the total uncertainty in the calculated local bulk subcooling is approximately $\pm$ 0.2 °C. A more detailed analysis of the uncertainty in the subcooling is given in Appendix C.4.

4.2.4. Hot wire anemometer measurements

The analog output from the hot wire circuit was sampled at a rate of 400 Hz, meaning that events at 200 Hz or higher are not able to be characterized. The natural frequency of the hot wire probe was measured at about 70 Hz, which further narrowed the measurable frequency band. Each sampled data record, generally about thirty seconds long, was then downloaded to the signal analysis software on the PC, where two main operations were performed on it. First, a spectral analysis was performed to determine the dominant frequencies present in the recorded time series. Next, a digital filter with a cutoff frequency of 100 Hz was employed, and the time series was then differentiated to identify the high rates of change corresponding to the passage of vapor bubbles over the hot wire probe. A more detailed discussion of the digital signal processing techniques used is given in Appendix B.1. The power spectrum and the differentiated signal were then processed by a FORTRAN-77 code "VOID.FOR", listed at the conclusion of Appendix B, to calculate the mean bubble frequency and the average void fraction.

4.2.4.1. Peak bubble frequency

The power spectrum data were analyzed to determine the mean frequency, with the spectral density representing the weighting function for the average. The uncertainty in the peak, or mean frequency was estimated by determining the frequency band where the relative amplitude of the frequency component drops at least ten percent relative to the peak frequency component. The estimated uncertainty in the peak frequency ranged from about ± 0.2 Hz for heater orientations with a slight angle of inclination relative to 180° to almost ± 2.0 Hz for the vertical orientation. It will also be noted that the measured peak frequencies generally are 25 Hz or less, which is well within the dynamic range of the probe, determined in Appendix B.1.

4.2.4.2. Local void fraction

To calculate the void fraction, the code sets an upper and lower trigger level on the differentiated hot wire output, which is then used to generate an indicator function time series. When the rate of change exceeds the upper trigger level, the indicator function is set to 1, corresponding to the presence of vapor at the hot wire probe. When the rate of change falls below the lower trigger level, the indicator function returns to zero, signaling the presence of liquid at the probe. The void fraction is estimated, by averaging the indicator function series over time. A reasonable variation of the trigger levels set on the differentiated signal gives an approximate uncertainty in the estimated void fraction of about ± 10 %. A detailed discussion of the calibration of the void fraction measurements is given in Appendix B.1, while the uncertainty is computed in Appendix C.2.

4.2.4.3. Void fraction profiles

The void fraction profiles are generated by precisely positioning the probe above the boiling surface, with the position of the probe measured from a reference point directly on the surface. The void fraction profile to be presented below was determined at three different axial locations along the heater surface, 5.1 mm, 11.4 mm and 16.5 mm from the leading edge. Assuming the void fraction profile to be uniform over the width of the heater, the mean void fraction is obtained by integrating the temporally-averaged void fraction measured for two dimensions over the entire profile.

4.2.4.4. Bubble boundary layer thickness

The bubble boundary layer thickness was calculated by performing a spectral analysis on the hot wire data and observing the sharp decline in the peak value of the autospectrum with increasing distance away from the heater surface. This was simpler and possibly more accurate than determining the drop in the local void fraction with the distance from the surface, since the boiling on the hot wire gives erroneous results at low void fractions. After determining the local bubble boundary layer thicknesses for three axial positions on the heater surface, 5.1, 11.4 and 16.5 mm from the leading edge, the average bubble boundary layer thickness over the surface was calculated by integrating the parabolic curve fit through the three measured points. The uncertainty in the average

bubble boundary layer thickness is approximately ± 0.13 mm, based on the uncertainty of the locally measured values.

4.2.4.5. Mean bubble residence time

The mean bubble residence time is calculated by considering the motion of a series of bubbles on the surface, as in Figure 4.22. Assuming the bubbles to move at the same velocity, the time between successive bubbles is given by the distance between them divided by the velocity as:

$$t^* = \frac{X}{U_v} = \frac{1}{\bar{f}} \tag{4.5}$$

which is calculated from the measured peak bubble frequency. The fraction of the time interval between the bubbles during which the bubble is resident at a point over the surface, which is called the bubble residence time, is then expressed as:

$$\tau_{res} = \alpha t^* = \frac{\alpha}{\bar{f}} \tag{4.6}$$

The mean bubble residence time is calculated by dividing the temporally- and spatially-averaged value of the void fraction over the heater surface by the peak bubble frequency.

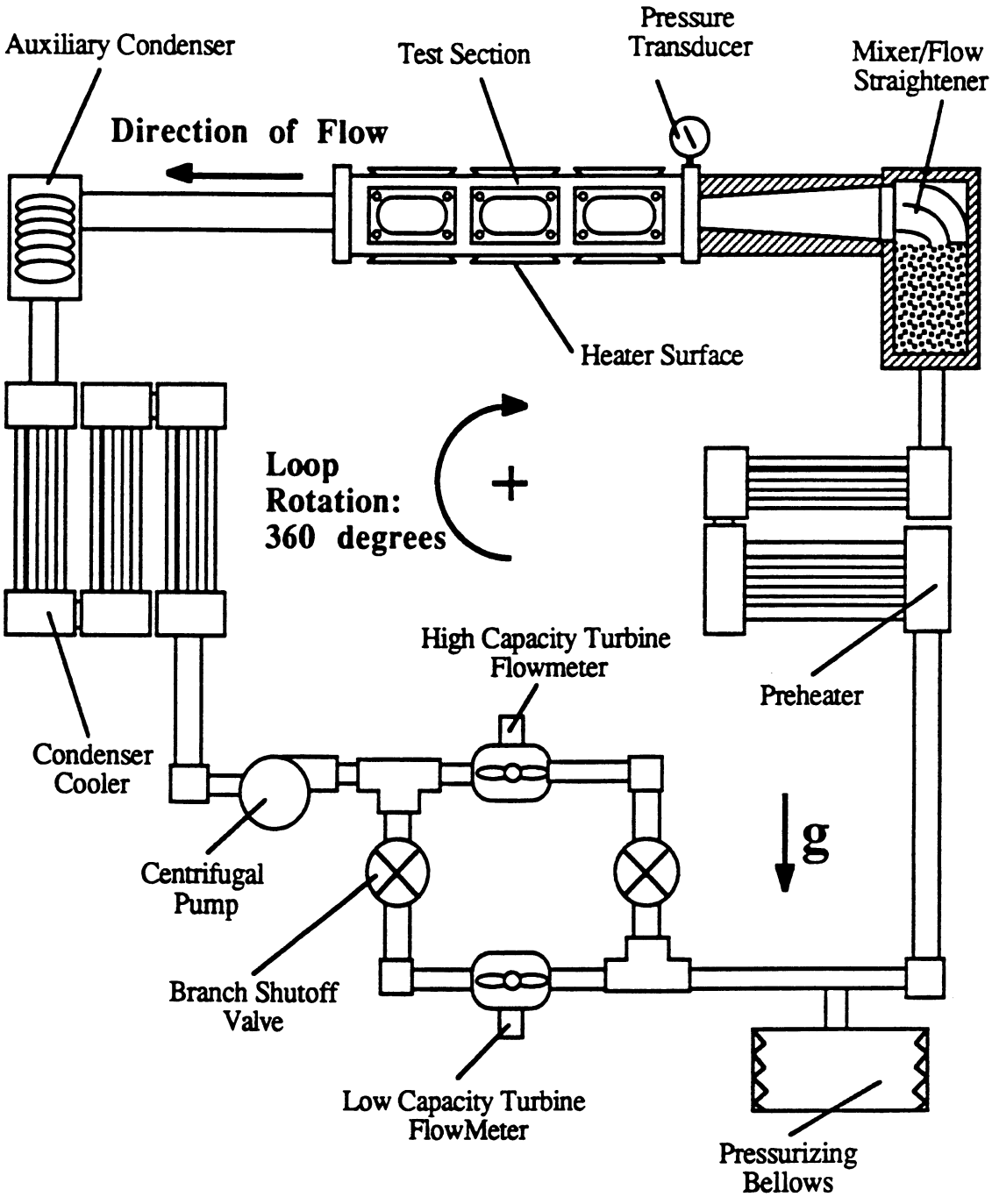

Figure 4.1. Schematic of the forced convection loop

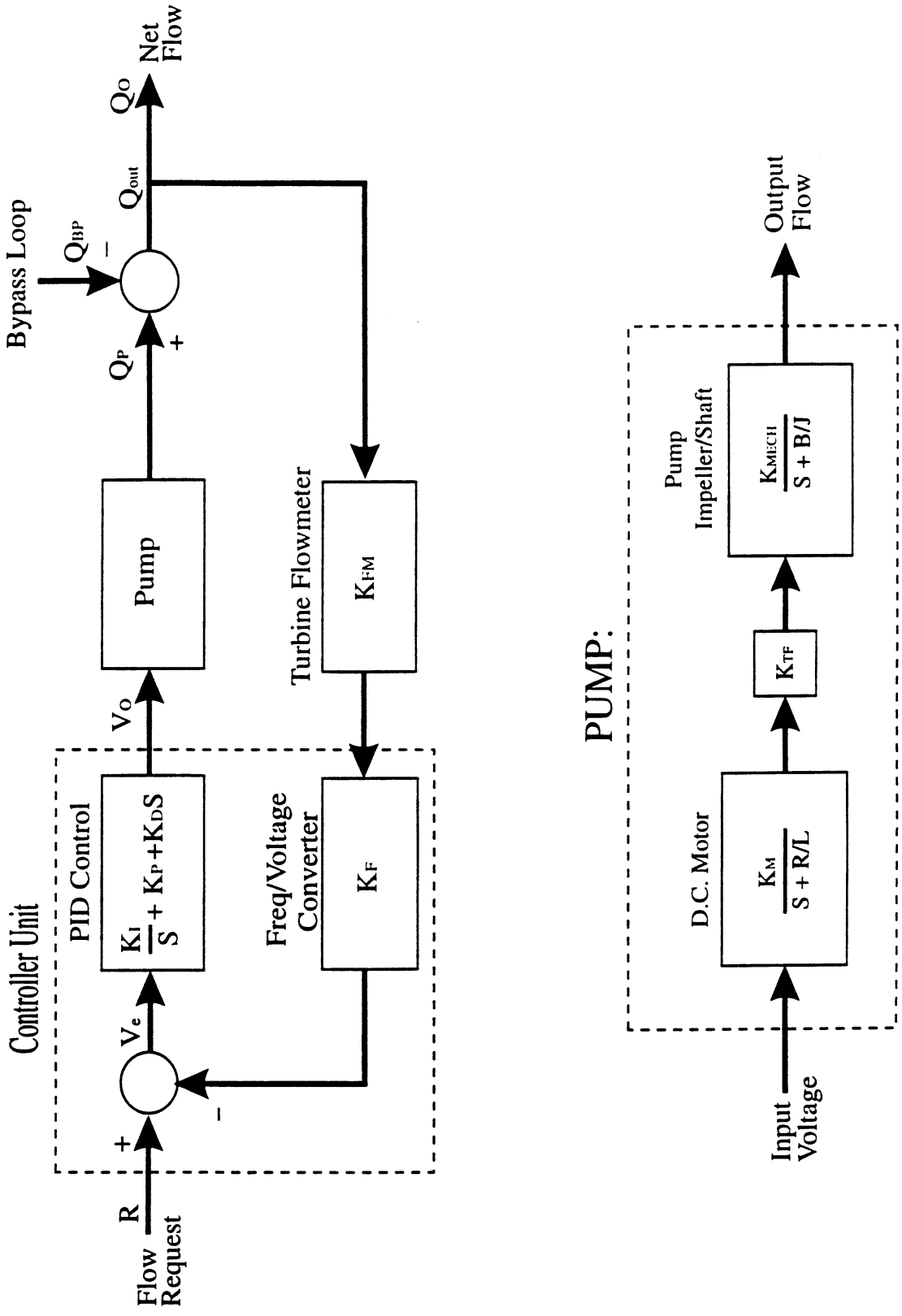

Figure 4.2. Block diagram representation of the flow control system

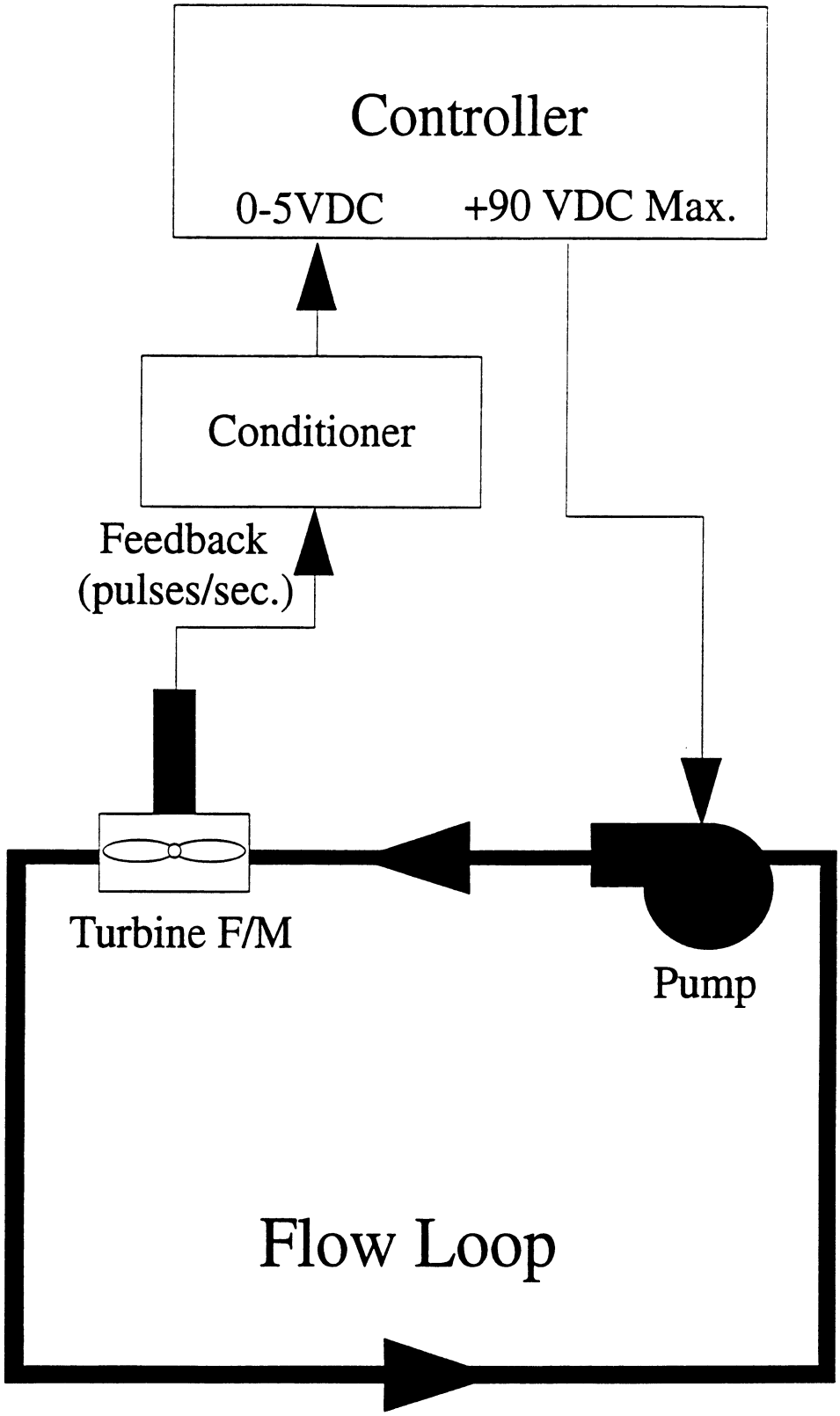

Figure 4.3. Schematic of the modified flow control system

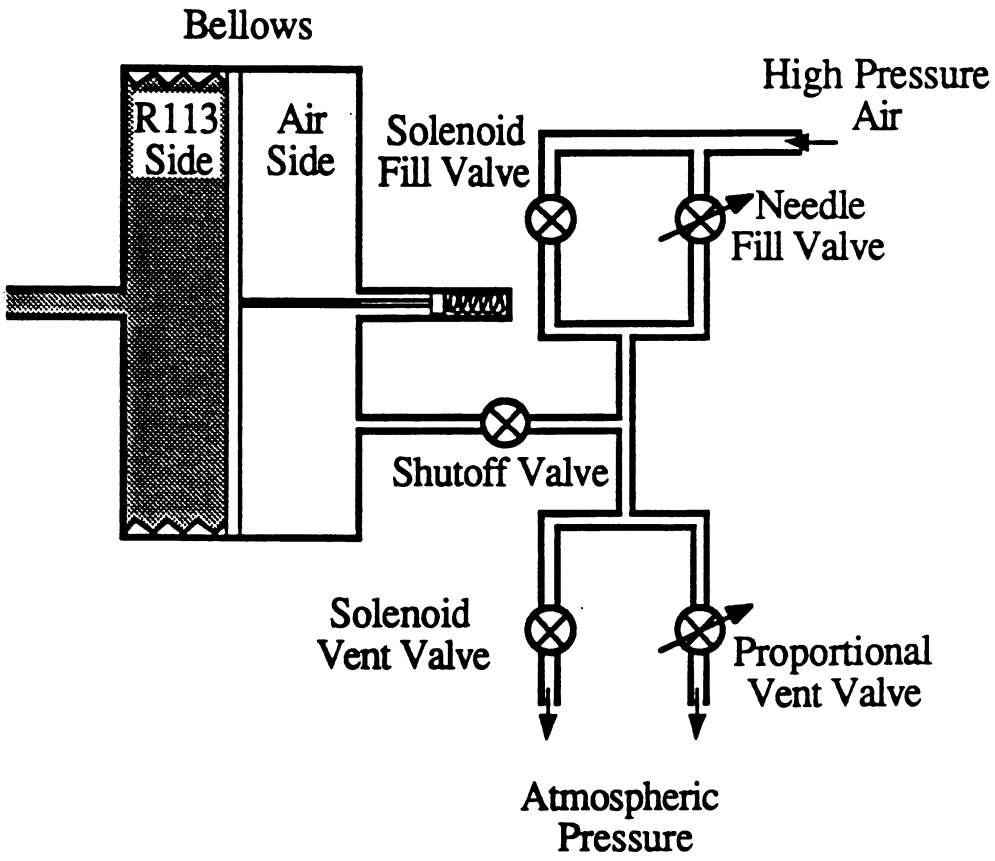

Figure 4.4. Schematic of the pressure control system

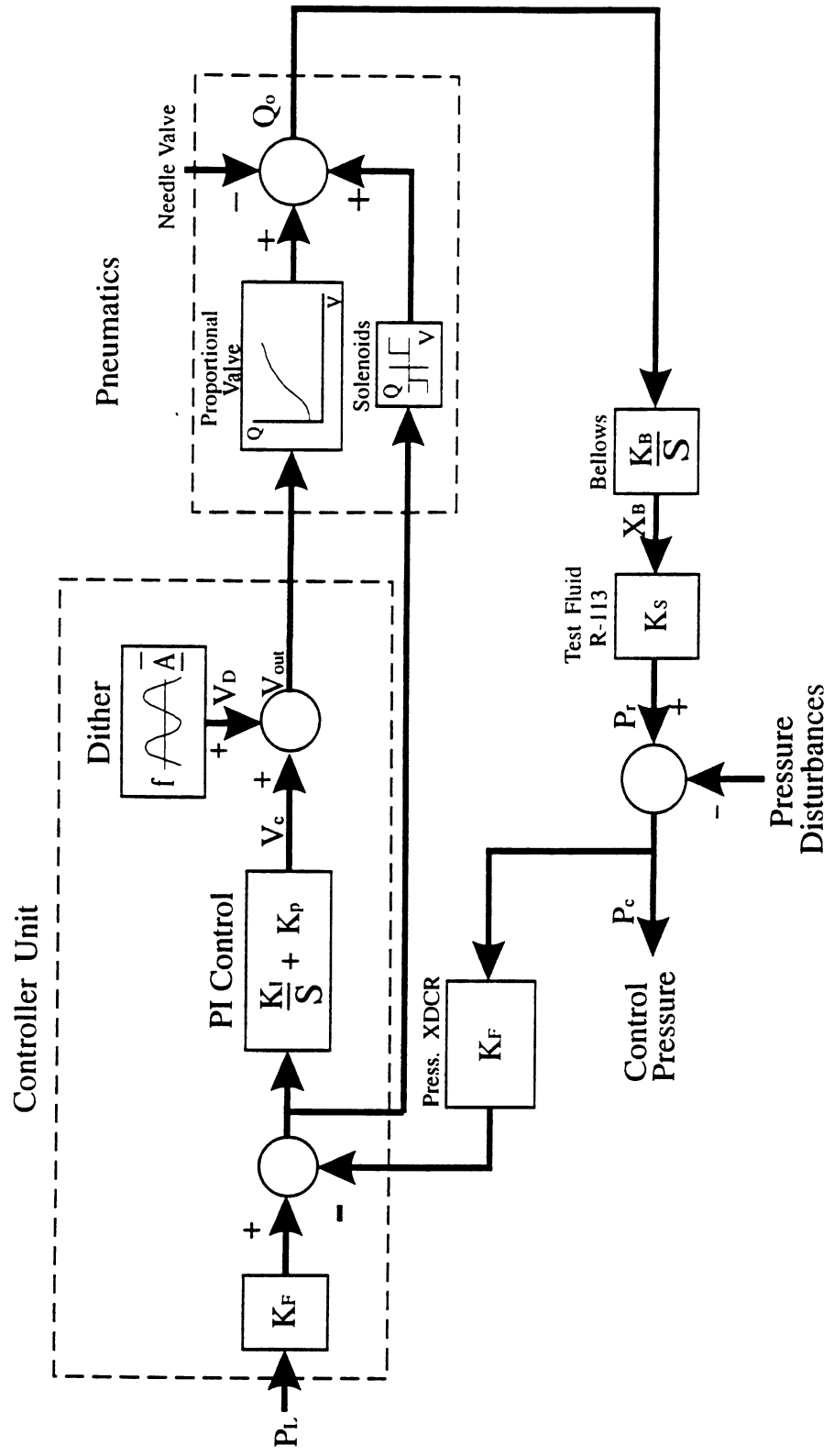

Figure 4.5. Block diagram representation of the pressure control system

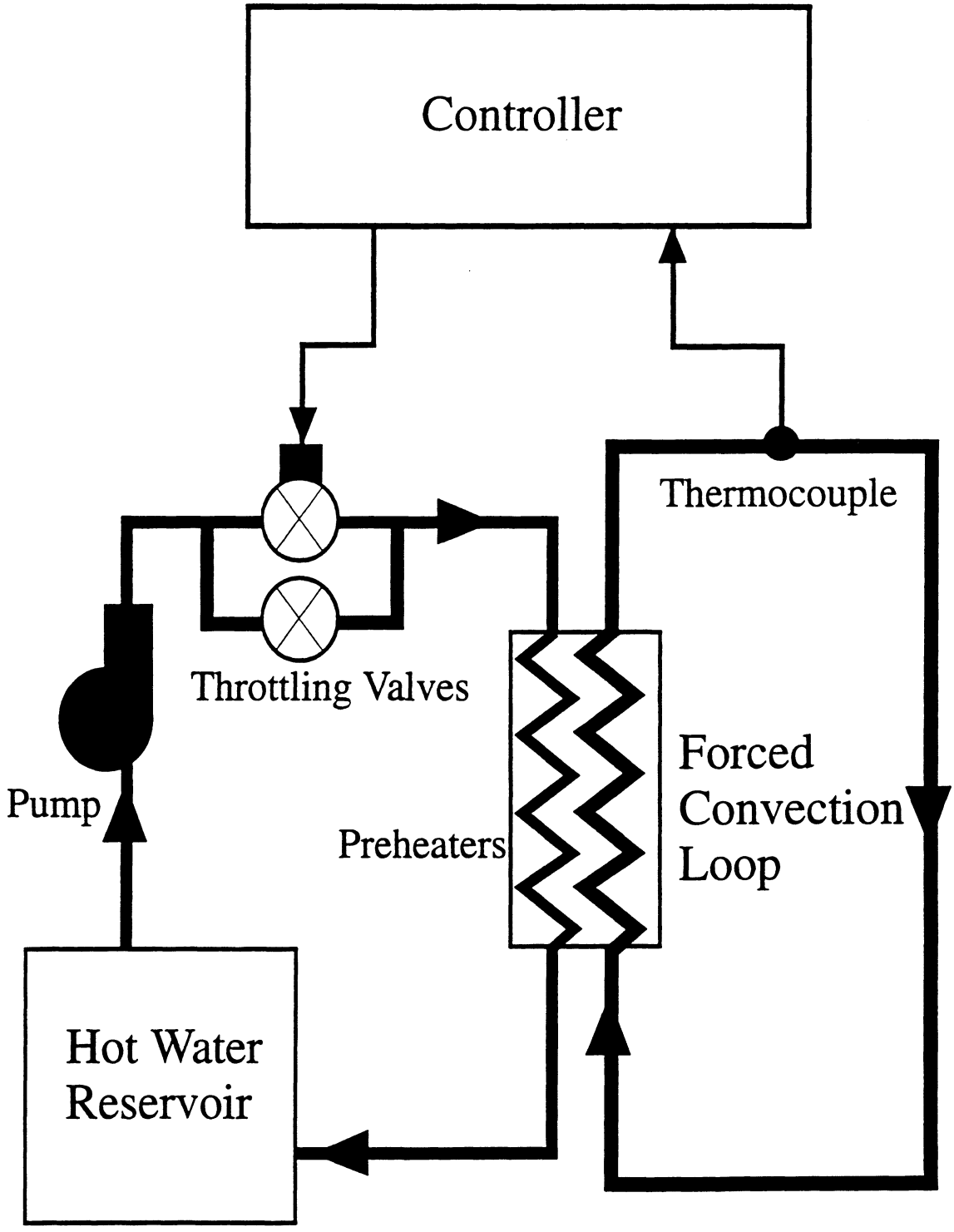

Figure 4.6. Schematic of the temperature control system

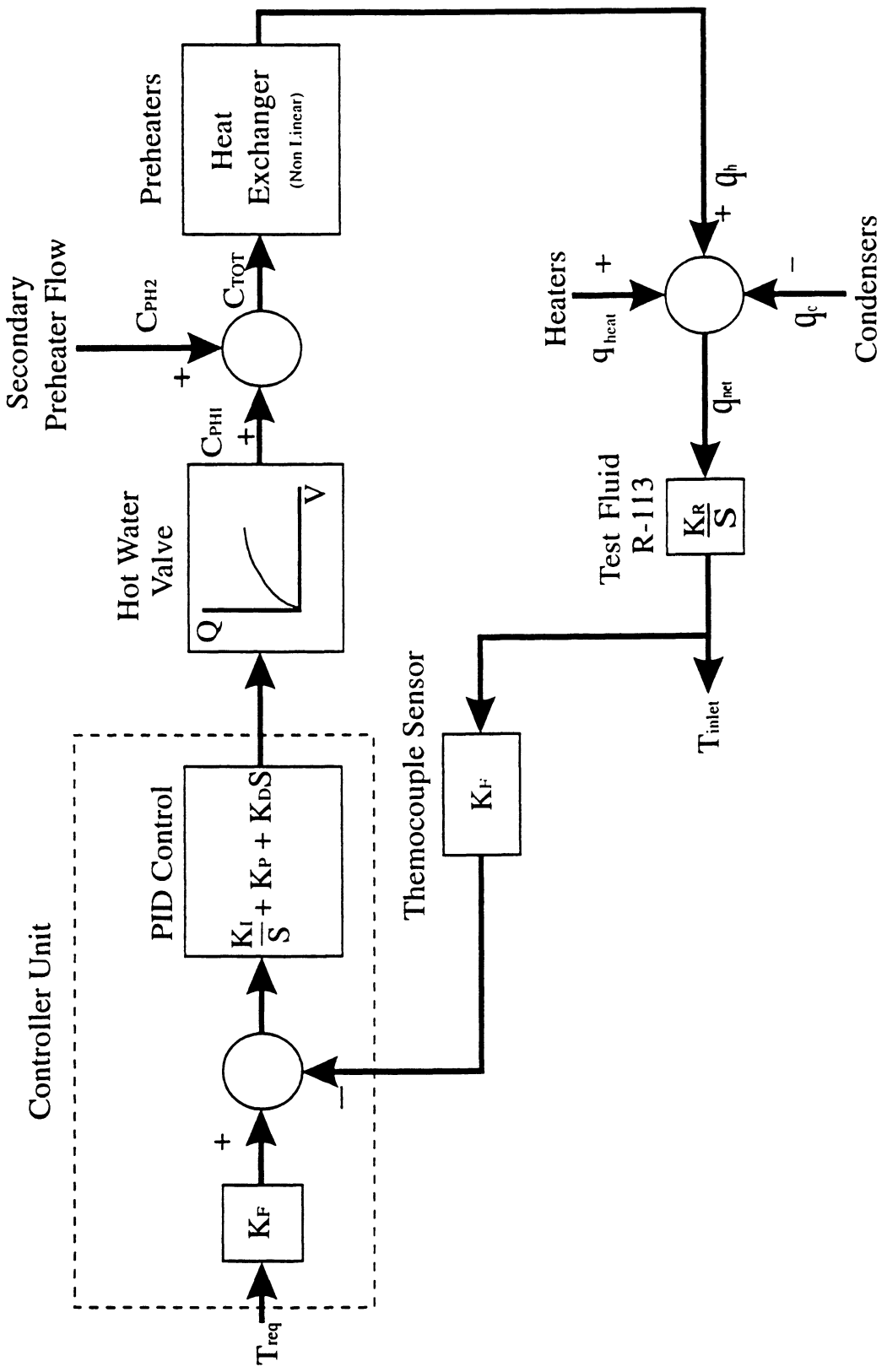

Figure 4.7. Block diagram representation of the temperature control system

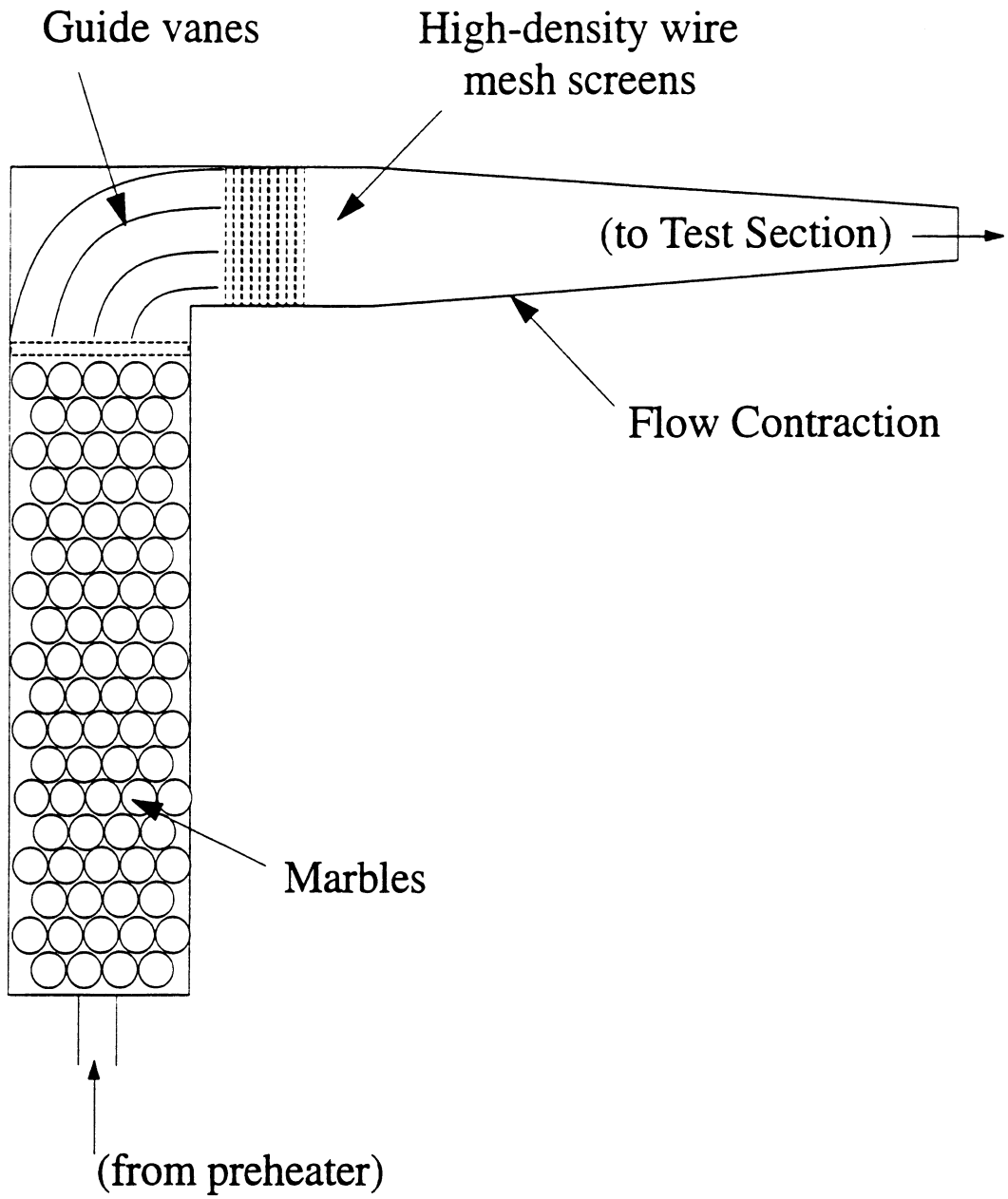

Figure 4.8. Illustration of the flow straightener-mixer section

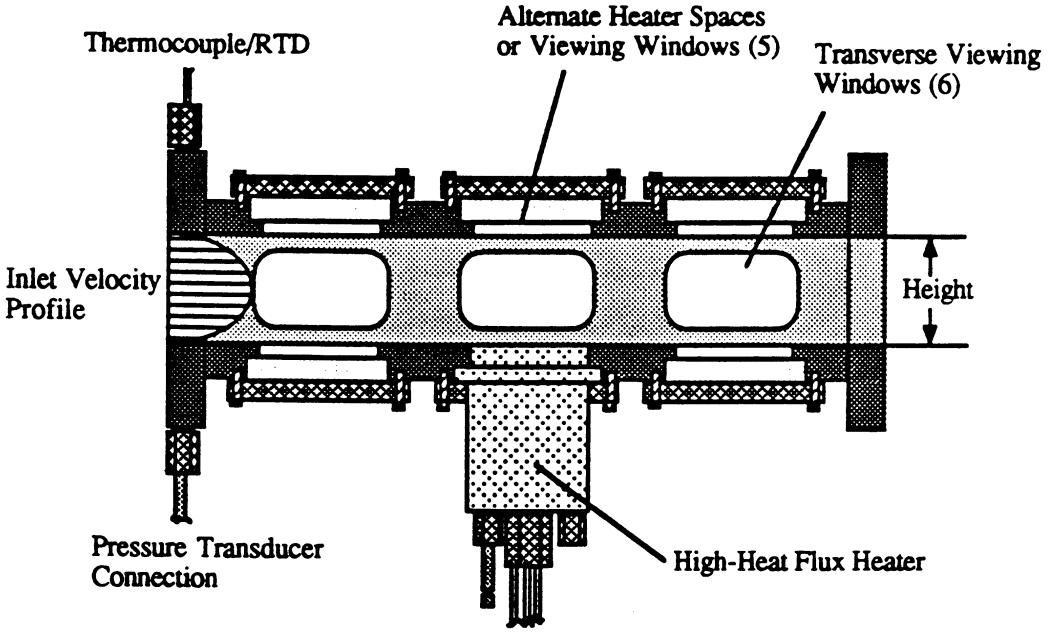

Figure 4.9. Illustration of the test section

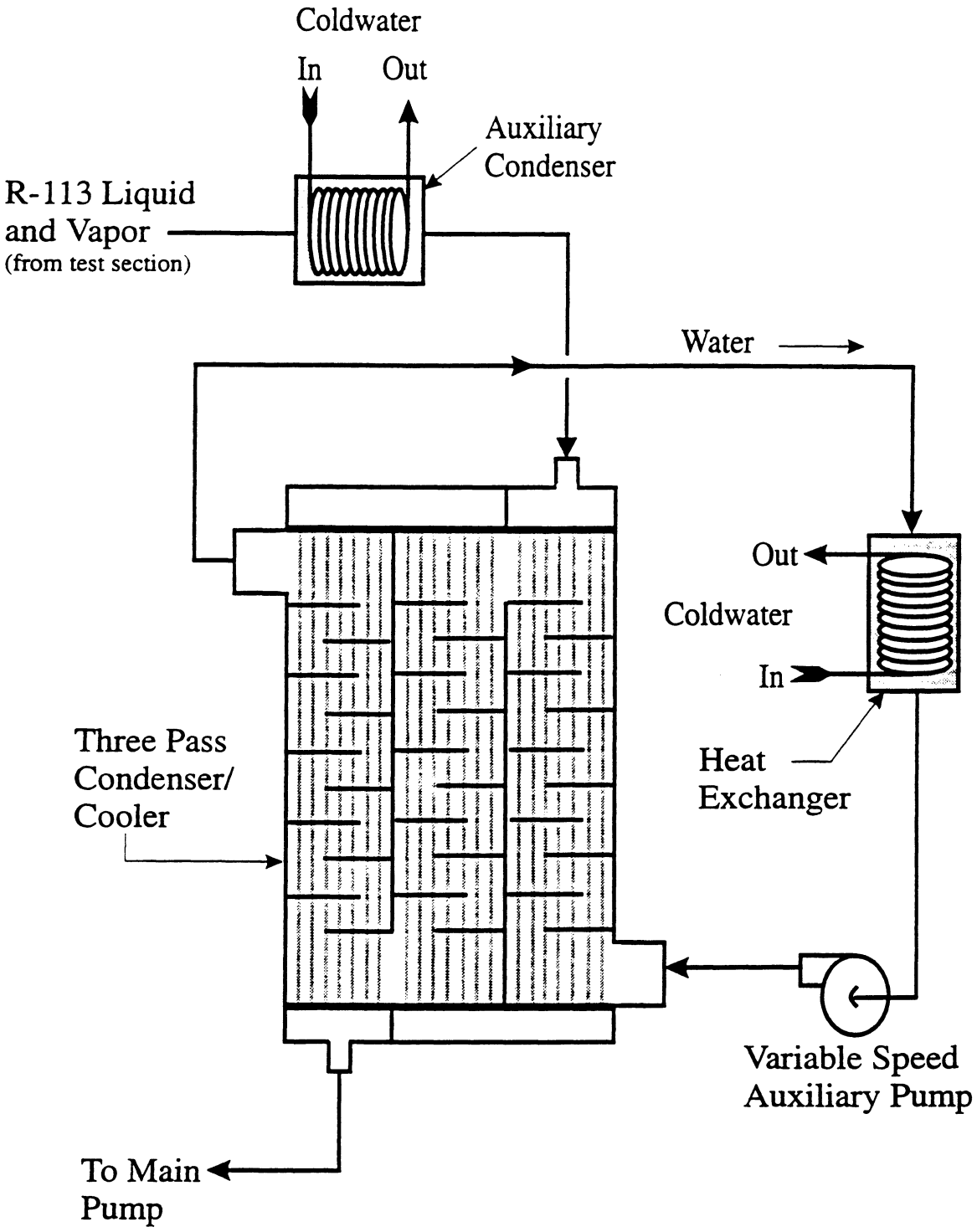

Figure 4.10. Illustration of the condenser-cooler section

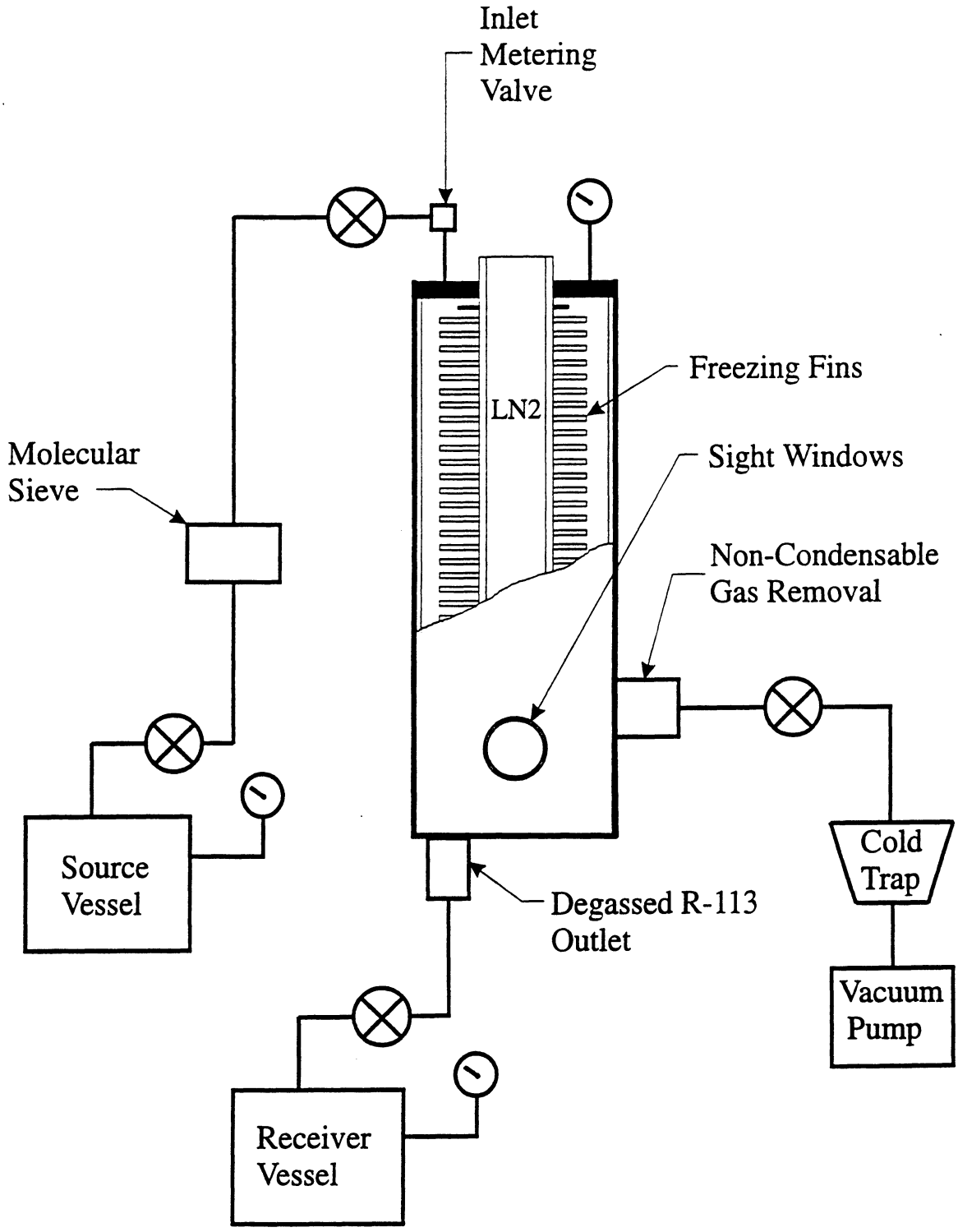

Figure 4.11. Illustration of the degassing apparatus

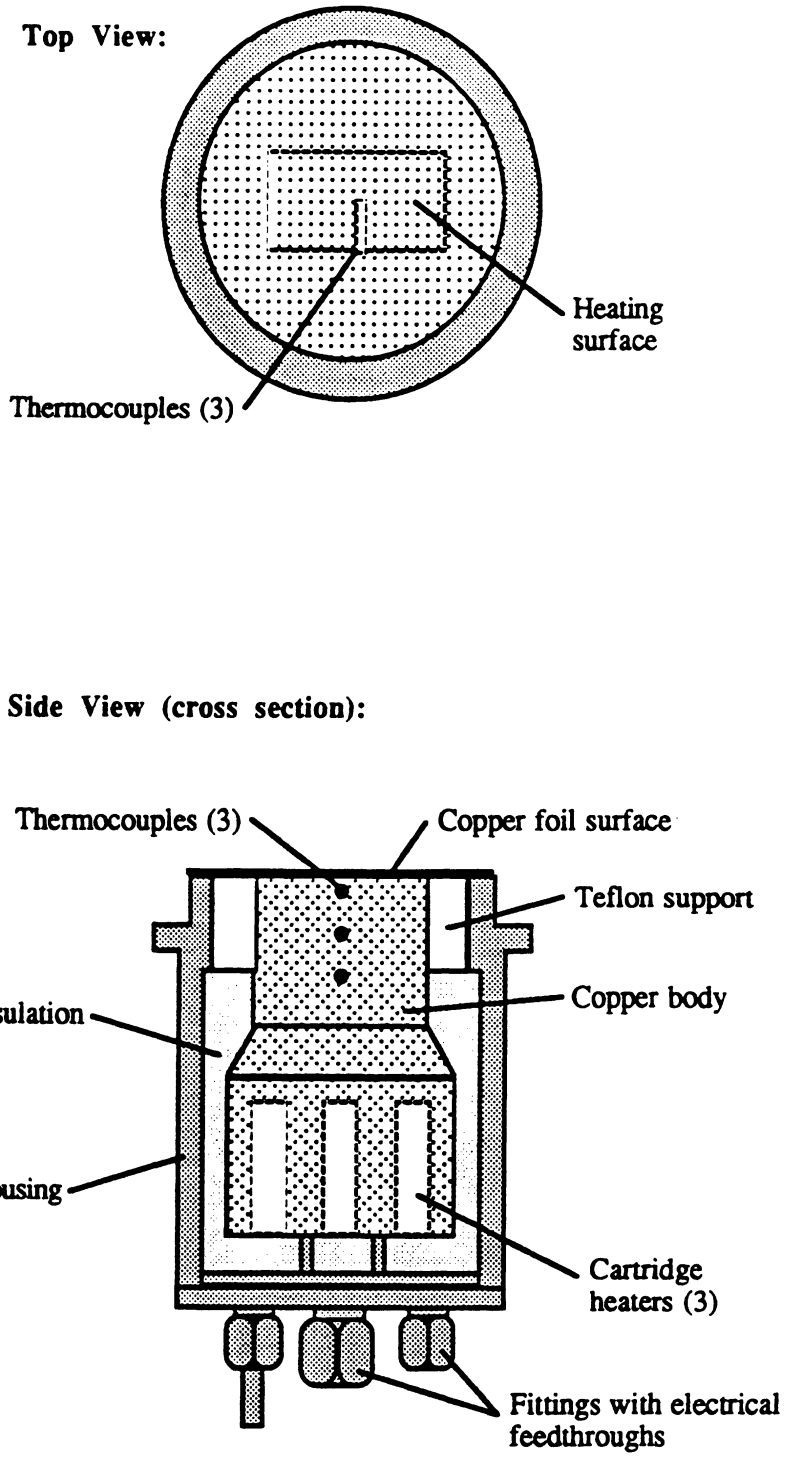

Figure 4.12. Illustration of the metal heater surface

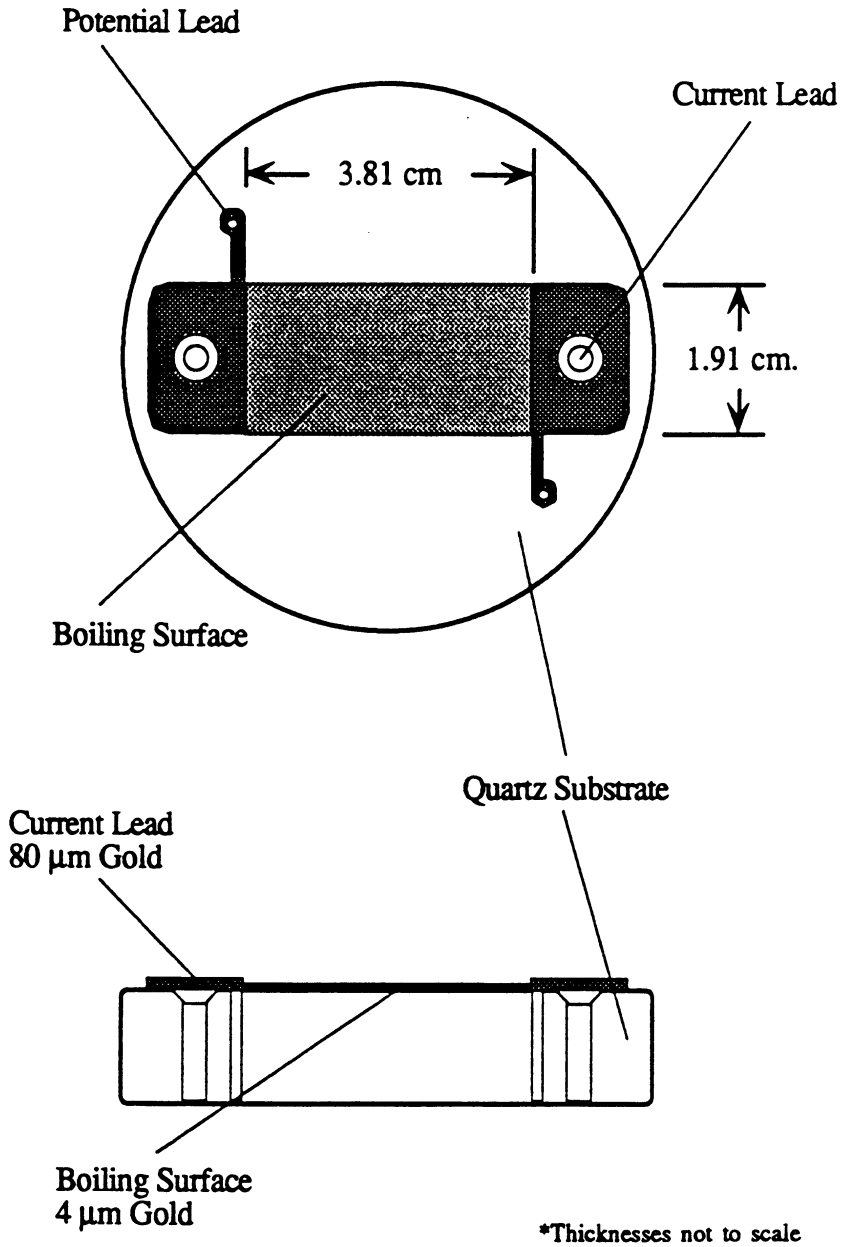

Figure 4.13. Illustration of gold film heater surface

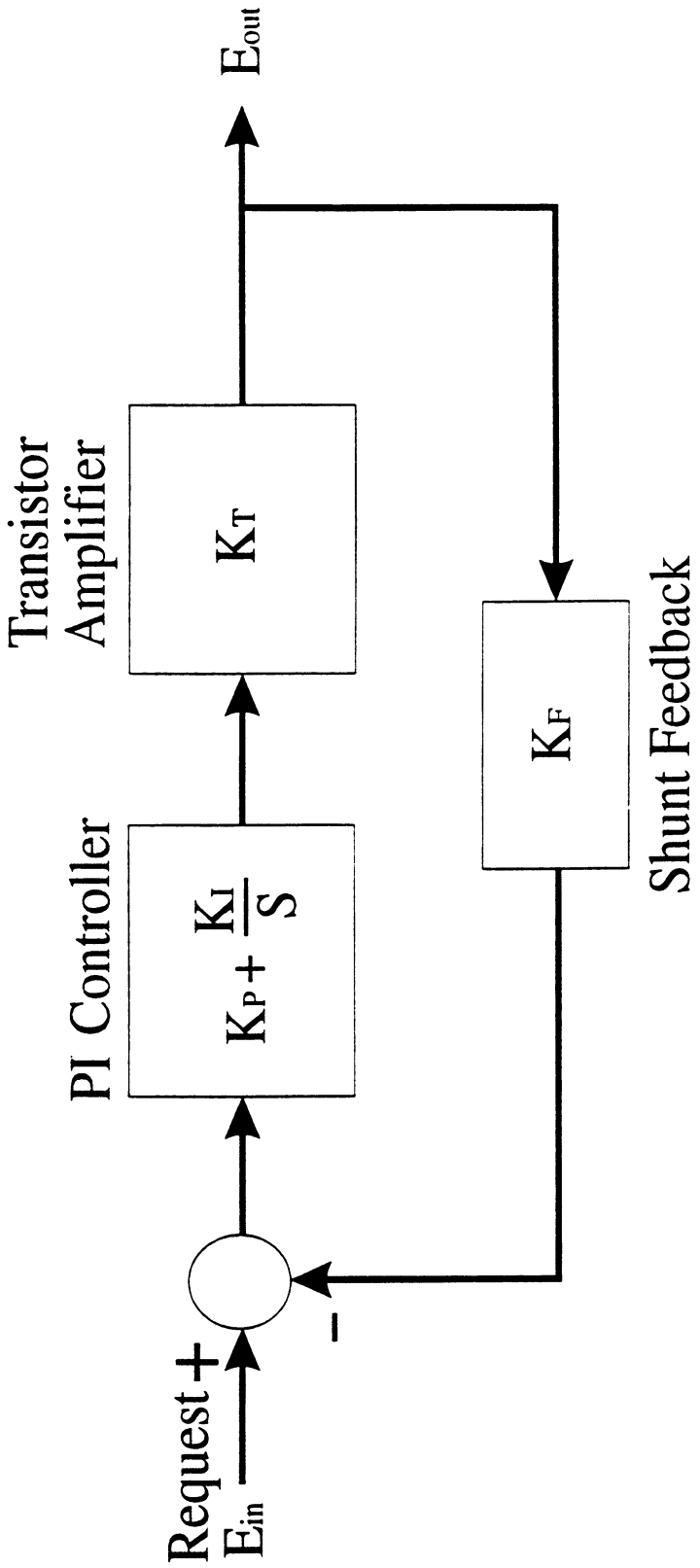

Figure 4.14. Block diagram representation of the heater control system

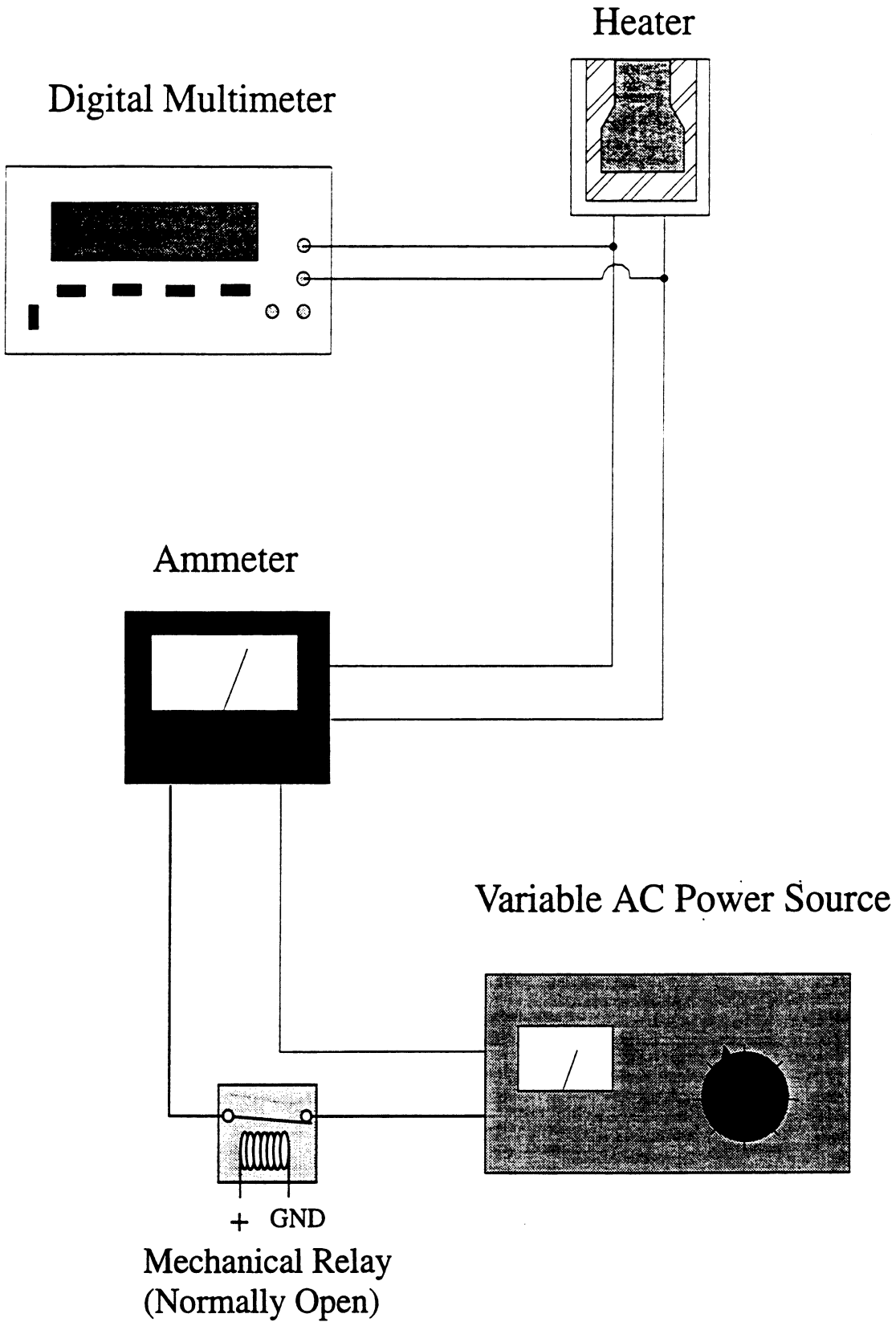

Figure 4.15. Schematic diagram of the power circuit driving the metal heater

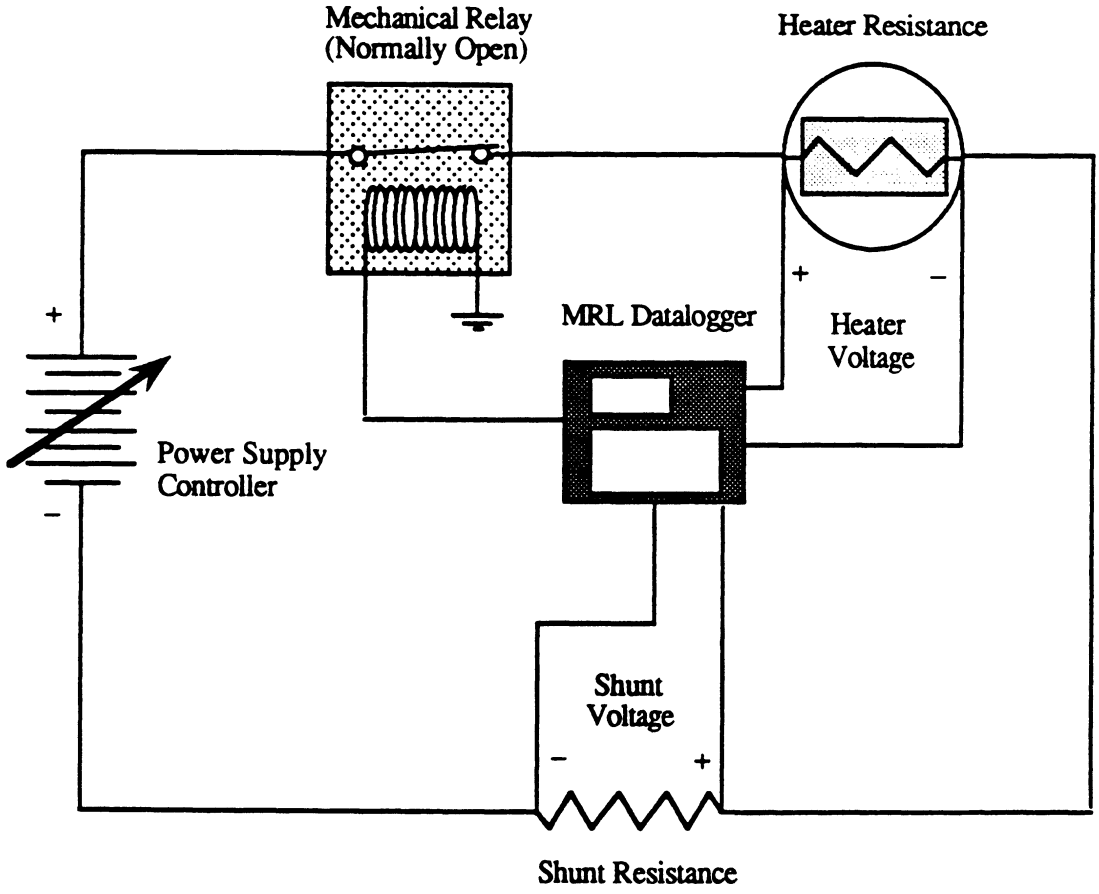

Figure 4.16. Schematic diagram of the power circuit driving the gold film heater

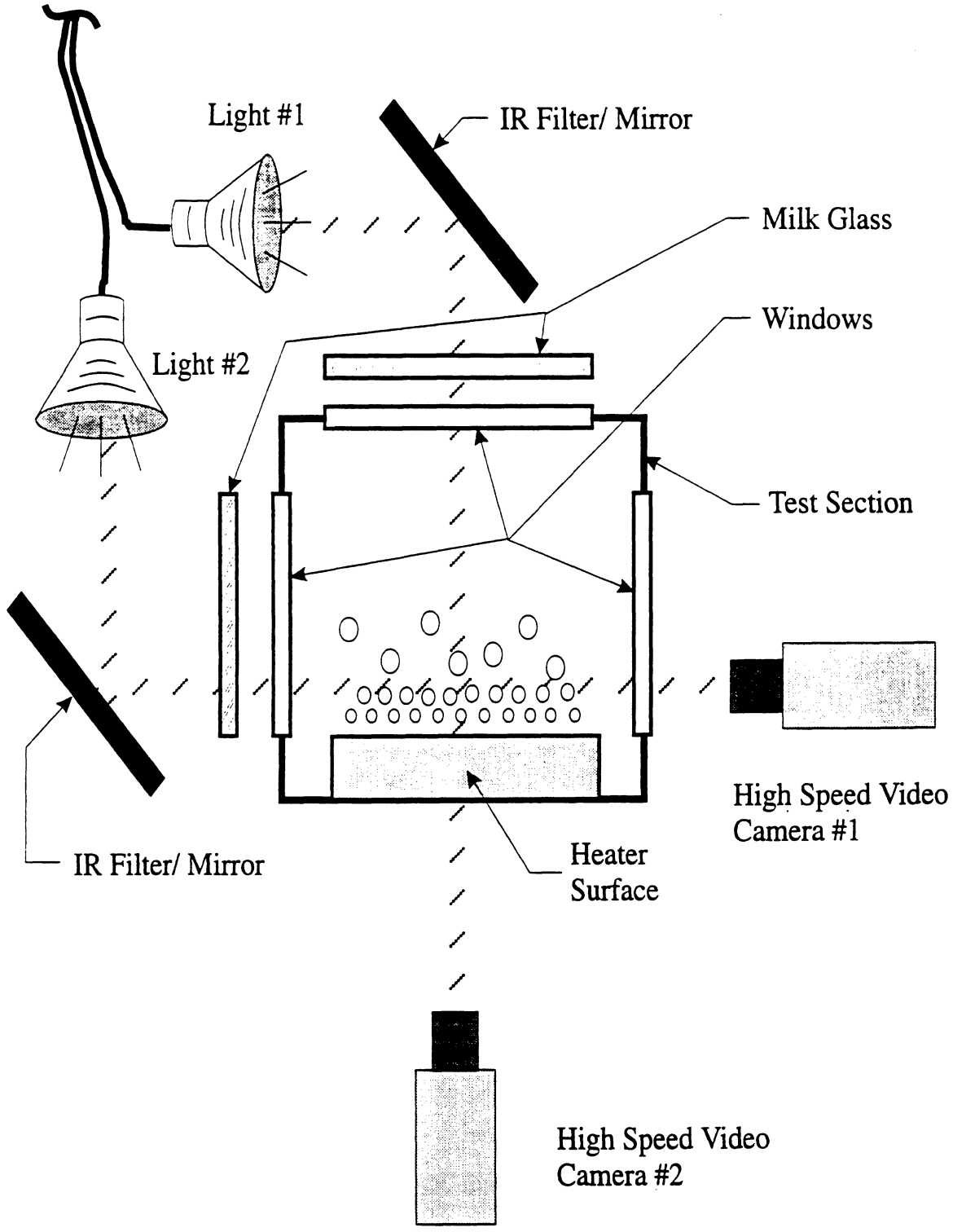

Figure 4.17. Illustration of the optical setup used with the high speed photography

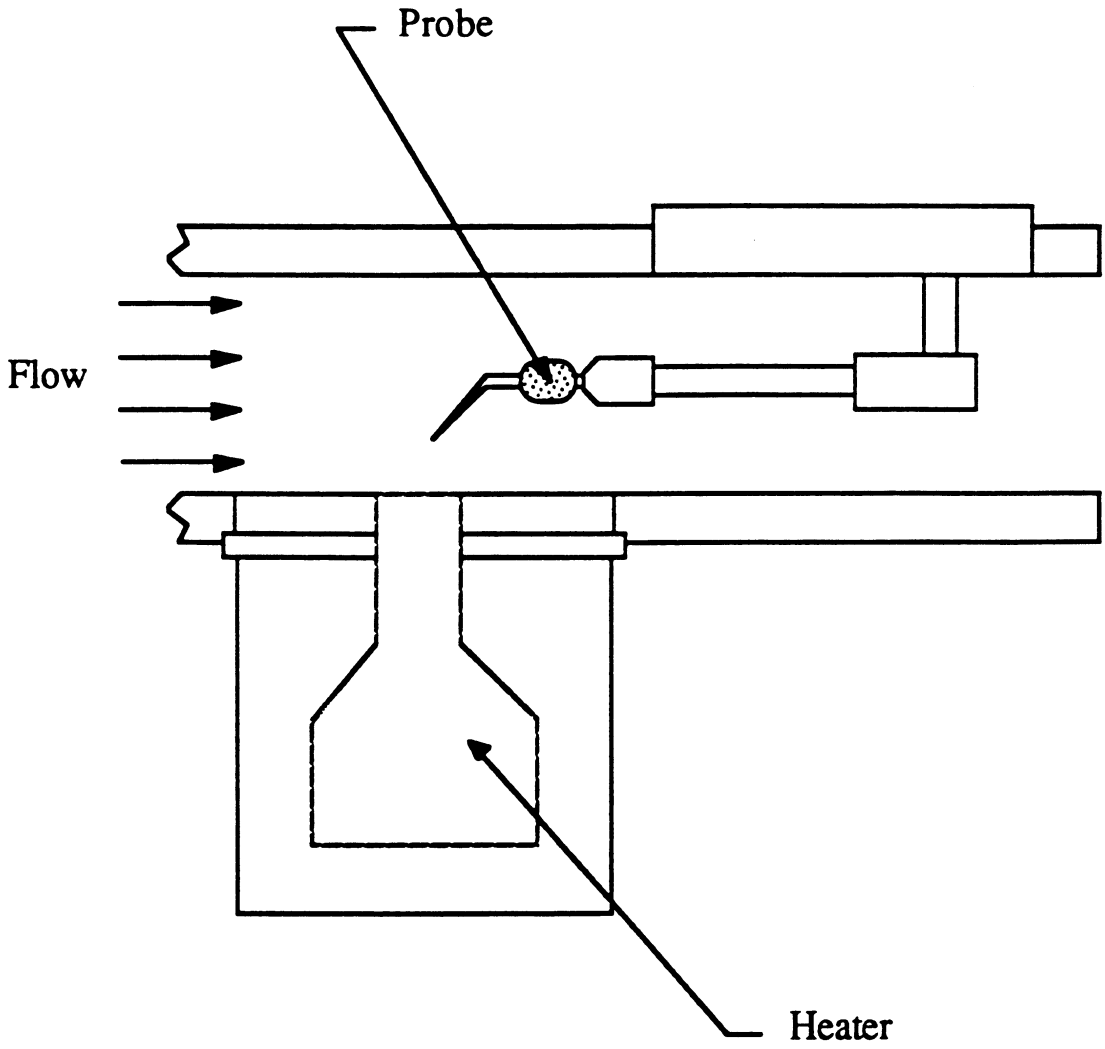

Figure 4.18. Illustration showing the placement of the hot wire apparatus in the test section

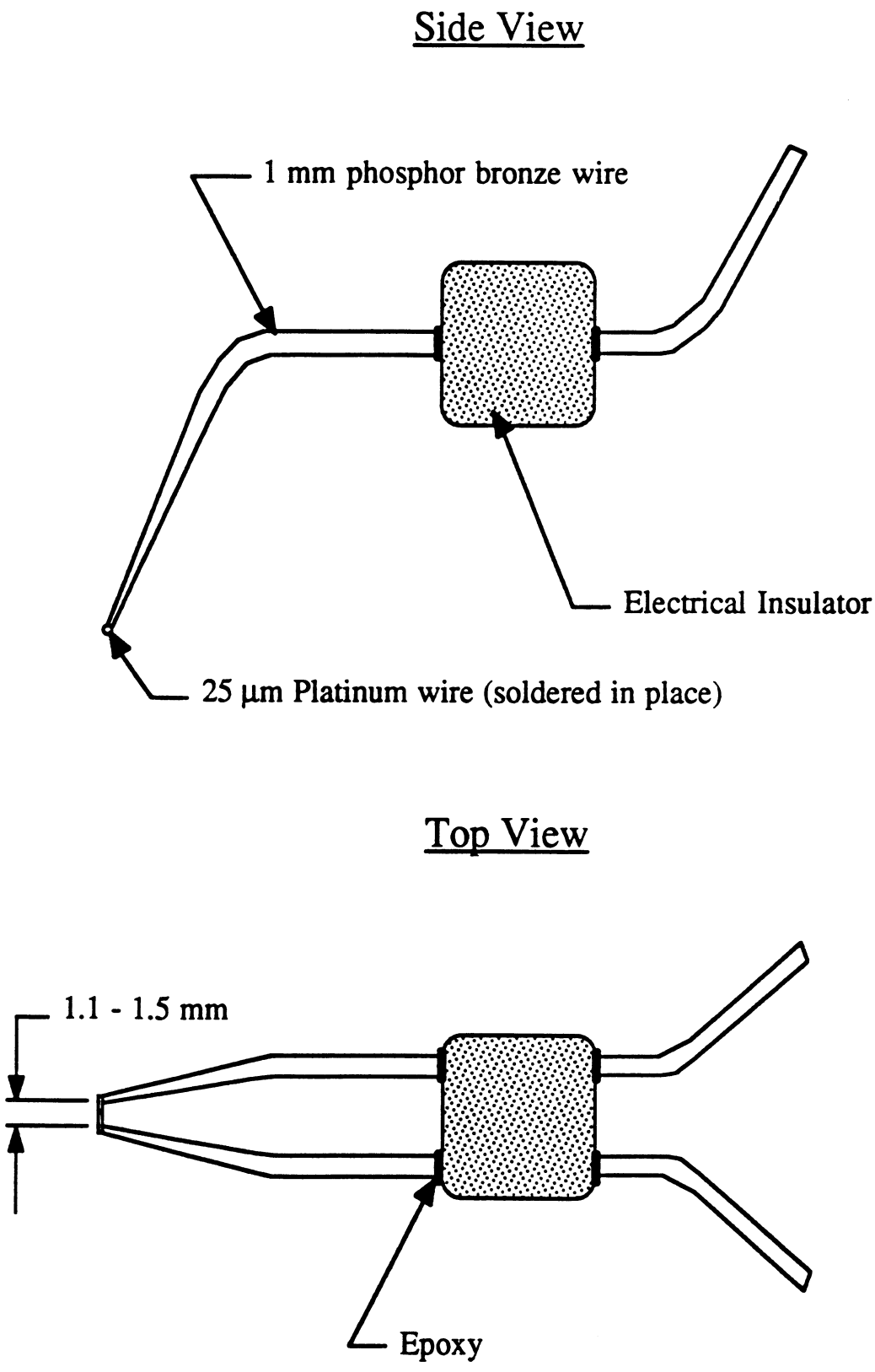

Figure 4.19. Illustration of the hot wire test probe

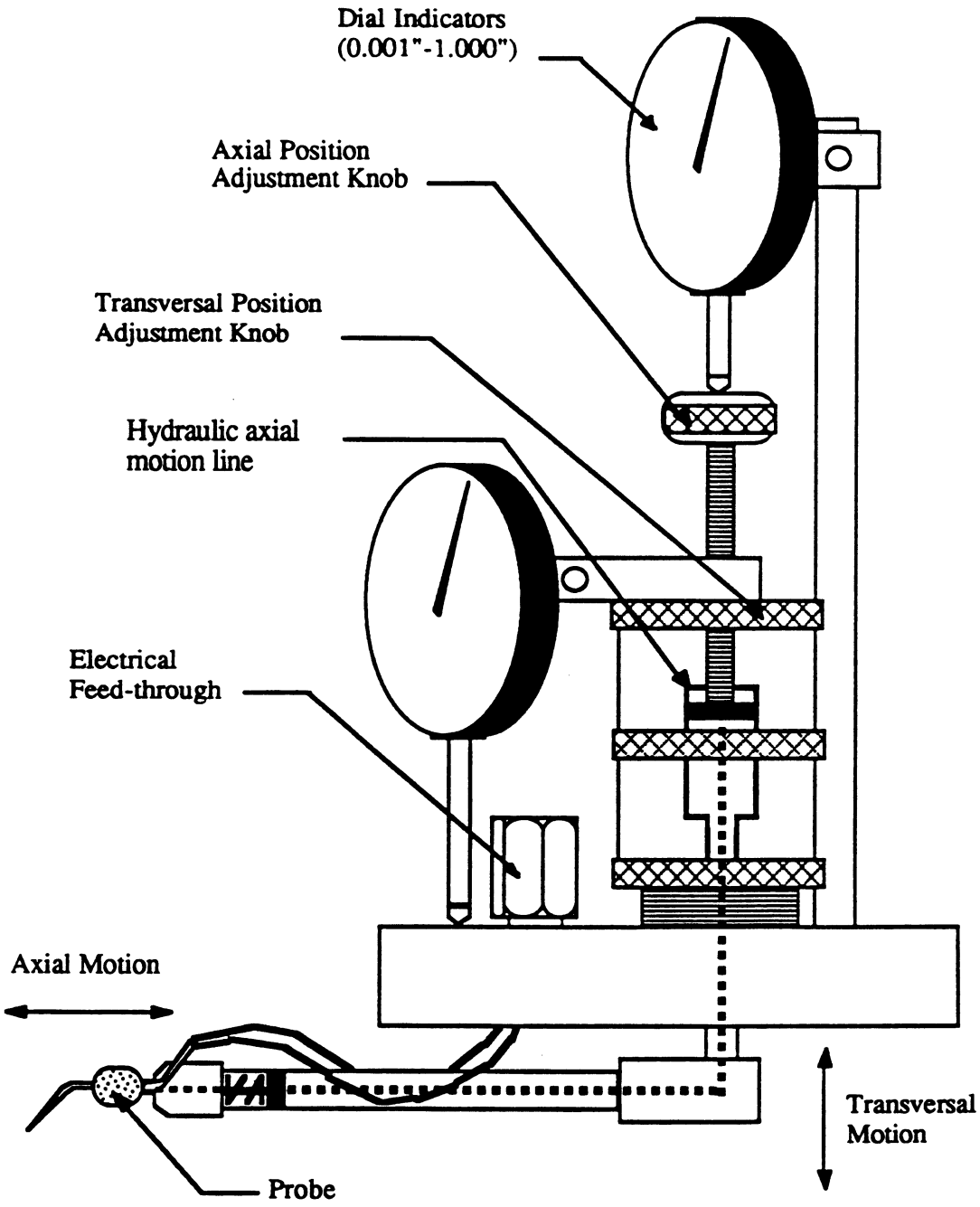

Figure 4.20. Illustration of lead screw displacement mechanism

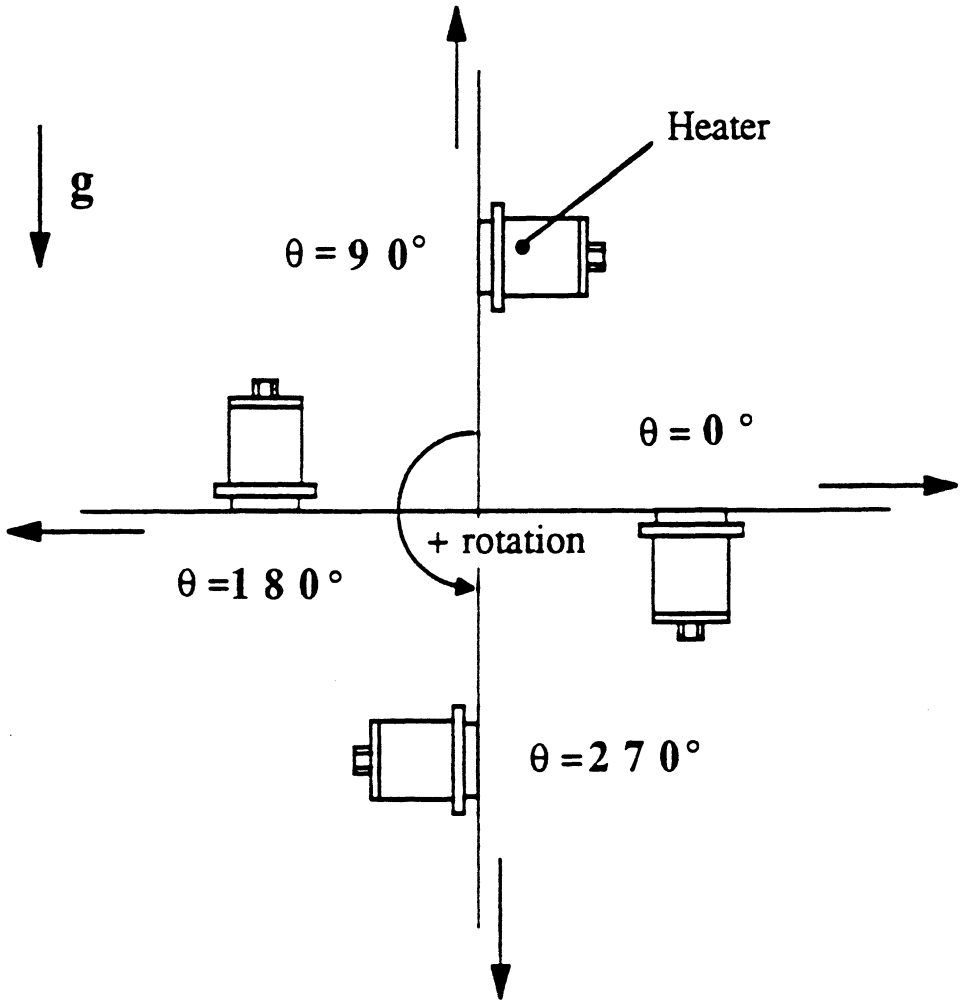

(Arrows indicate the direction of flow over the heating surface)

Figure 4.21. Diagram of the heater surface orientation designations

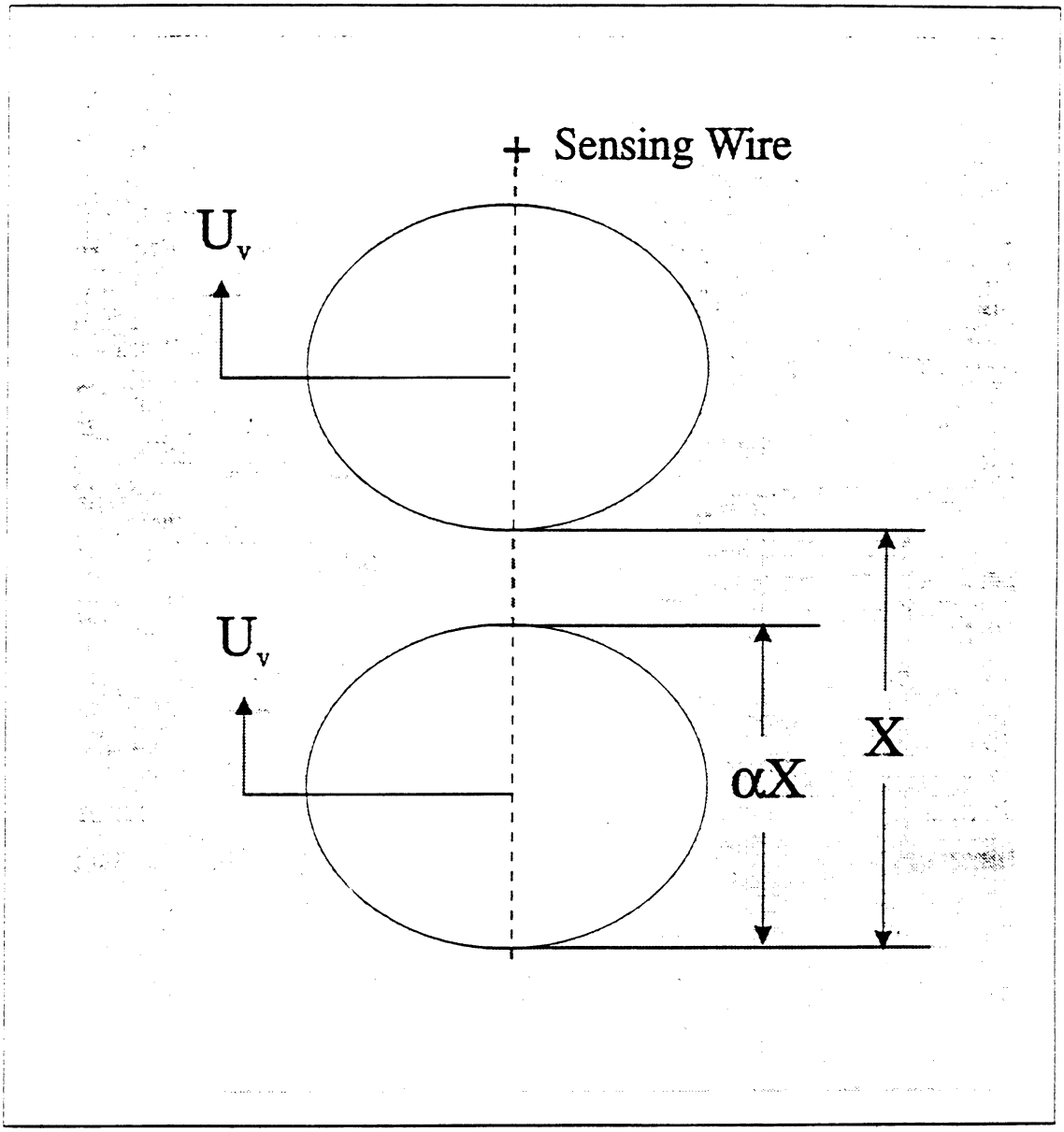

Figure 4.22. Illustration of the definition of the bubble residence time

CHAPTER 5

EXPERIMENTAL RESULTS

The experimental measurements obtained during the current study are presented below. The results consist primarily of measurements of the CHF at various flow velocities, subcoolings and heater surface orientations, and are presented in tabular form in Appendix A. These are compared with the results of the forced convection CHF (FCCHF) model described in Chapter 3. In addition, measurements using hot wire anemometry are presented, showing the behavior of the void fraction and bubble frequency above the metal heater surface for downward-facing heater orientations at various levels of subcooling and at a relatively low flow velocity. These measurements are accompanied finally by high speed photographs of boiling with both the metal and thin gold film heater surfaces.

The results are presented in dimensionless form, where appropriate, using normalization factors pertaining to low-velocity forced convection boiling. The CHF values are non-dimensionalized with respect to the correlation by Ivey and Morris (1962) for subcooled pool boiling:

$$q_{co} = q_z \left[1 + 0.102 \left(\rho_l / \rho_v \right)^{0.75} \frac{c_{pl} \Delta T_{sub}}{h_{fg}} \right] \tag{5.1}$$

where q_z is the CHF predicted for saturated pool boiling over an infinite flat plate by Zuber (1958) as follows:

$$q_z = \frac{\pi}{24} \rho_v h_{fg} \left[\sigma g (\rho_l - \rho_v) / \rho_v^2 \right]^{1/4} \tag{5.2}$$

The value for pool boiling is chosen as the reference for low-velocity forced convection boiling since the two regimes share many common features, including the relatively strong influence of buoyancy and surface tension forces. The variation of q_{co} with subcooling is shown for R113 in Figure 5.1. The CHF varies linearly with subcooling, except for a slight deviation due to changes in the fluid properties with changes in the saturation temperature. According to the experimental procedures described in Chapter 4, the subcooling is varied by increasing the system pressure, while maintaining a constant bulk liquid temperature. To distinguish the influence of the system pressure from that of the subcooling, the CHF for the saturated liquid case is also plotted in Figure 5.1 as a function of the subcooling. The subcooling in the ordinate corresponds to the system pressure level needed to raise the saturation temperature relative to the bulk liquid temperature at 49 °C. The difference between q_z and q_{co} at a given subcooling (or pressure) then represents the effect of subcooling independent of the pressure effect.

The influence of the flow velocity compared with that of the buoyancy acting on the vapor is given by the ratio of the buoyancy force to the flow inertia as:

$$\xi \equiv \frac{F_{buoy}}{F_{inertia}} \sim \frac{g(\rho_l - \rho_v)L_c}{\rho_l U_b^2} \tag{5.3}$$

The characteristic length in this case is the ratio of the volume of the bubble to its frontal area, which was assumed in the FCCHF model in Chapter 3 to be proportional to the unit bubble spacing for boiling at high heat flux levels. The Rayleigh-Taylor instability determines the bubble spacing, as in Eqn. (3.33), since the bubbles on the surface generally originate from a vapor blanket with a relatively high void concentration. Omitting proportionality constants, ξ is expressed as follows:

$$\xi = \frac{g(\rho_l - \rho_v)\sqrt{\frac{\sigma}{g(\rho_l - \rho_v)}}}{\rho_l U_b^2} = \sqrt{\frac{g(\rho_l - \rho_v)\sigma}{\rho_l^2 U_b^4}} \tag{5.4}$$

The values of ξ corresponding to R113 at the flow velocities used in the experiments are given in Table 5.1, and range from 6.57 at a bulk flow velocity of 4 cm/s to 0.03 at 55 cm/s. In terms of the terminal velocity of a deformable bubble rising under buoyancy in an inviscid, stagnant, infinite medium given by Harmathy (1960), ξ is proportional to the square of the ratio of the buoyant terminal velocity of a bubble to the bulk flow velocity. Where ξ is unity, therefore, the bubbles should tend to stagnate when the bulk flow

velocity is opposite the buoyant velocity. Also, where ξ is small, the flow velocity should dominate over the buoyancy effects, and vice-versa. In a study of the relative effects of flow inertia and buoyancy on heat transfer in nucleate boiling, Kirk (1992) obtained a dimensionless relation for the ratio of the buoyancy to inertia forces, termed the two-phase Richardson number, which is related to Eqn. (5.4) as follows:

$$Ri_{2\phi} = \frac{1}{2}\left[\sqrt{1 + c_0 \xi^2} - 1\right] \tag{5.5}$$

where c_0 is a constant. Eqns. (5.4) and (5.5) have similar utility in quantifying the relative effects of buoyancy compared to the flow inertia, which is of interest when considering the limit of microgravity, where both ξ and $Ri_{2\phi}$ approach zero.

The bubble residence times, calculated from hot wire measurements using Eqn. (4.6), are non-dimensionalized with respect to the bubble residence time τ_0 calculated for a vertical surface (θ = 90 deg.) in pool boiling from Eqn. (3.59) as:

$$\tau_0 = \left(9\pi \frac{\chi q_c}{\rho_v h_{fg}} \frac{\sigma}{g(\rho_l - \rho_v)}\right)^{\frac{1}{5}} \left[\frac{4}{g} \frac{\frac{19}{32}\rho_l + \rho_v}{\rho_l - \rho_v}\right]^{\frac{3}{5}} \tag{5.6}$$

As was stated in Chapter 3, this expression for τ_0 is independent of subcooling, and R113 at a saturation pressure of one atmosphere under Earth gravity, with χ_0 = 0.3, gives a value of τ_0 = 0.0307 seconds. Eqn. (5.6) is used as a reference for the bubble residence

time for the same reason that Eqn. (5.1) is used for the CHF. Both Eqns. (5.1) and (5.6) give representative values for pool boiling, which is similar in many ways to forced convection boiling at low flow velocities.

5.1. Relative effects of orientation and flow velocity on the CHF: comparison of the experimental measurements with the CHF model predictions

The heater surface orientations in the experimental results below are defined in Figure 4.21. In what follows, the term "upflow" refers to those heater surface orientations where the flow direction is the same as that of the buoyancy force component acting on the vapor parallel to the heater surface (0 deg. < θ < 180 deg.), while "downflow" refers to those orientations where the flow acts opposite the buoyancy (180 deg. < θ < 360 deg.). "Upward-facing" refers to heater orientations where the buoyancy force component on the vapor normal to the heater surface acts in the direction away from the surface (0 deg. < θ < 90 deg.; 270 deg. < θ < 360 deg.), while "downward-facing" refers to orientations where the buoyancy force acts against the surface (90 deg. < θ < 270 deg.).

5.1.1. Low flow velocities (4 cm/s and 8 cm/s)

Figures 5.2 and 5.3 show a comparison of the measured CHF with the FCCHF model predictions at various levels of subcooling at imposed flow velocities of 4 and 8

cm/s, respectively. The data exhibit very little effect due to the flow, being similar to pool boiling, as demonstrated by the nearly symmetric characteristic about the horizontal facing down position (θ = 180 deg.). ξ is relatively high for both of these cases (ξ = 6.57 for 4 cm/s, ξ = 1.64 for 8 cm/s), indicating a strong influence of buoyancy relative to flow inertia, which results in a drastic decrease in the CHF for the downward-facing orientations. As the horizontal down position is approached, the buoyancy component on the vapor normal to the surface becomes increasingly larger, while the buoyancy component parallel to the heater surface becomes correspondingly smaller. As a consequence, the vapor remains pinned to the surface in the downward facing orientations, and slides along parallel to the heater surface. Dryout occurs at exceedingly low heat flux levels in the horizontal down position, since the vapor is virtually stagnant above the surface due to the relatively small flow forces, and perhaps also due to the increase in surface tension forces arising from the increased perimetral area at the base of the characteristically large flattened bubbles. In contrast, the CHF in the upward-facing orientations is nearly constant, close to that for a horizontal surface in pool boiling.

The results in Figures 5.2 and 5.3 appear to exhibit a relationship between the motion of the vapor and the CHF. In the upward-facing orientations, where the vapor departs the surface freely, the CHF is relatively large and nearly independent of the orientation angle, while in the downward-facing orientations the motion of the vapor is expected to depend strongly on the magnitude of the buoyancy component parallel to the heater surface, and the CHF becomes comparatively small. At all of the heater surface orientations, the vapor generally formed large vapor slugs above the surface, which

appeared to cover the surface completely when viewed with the naked eye. A sequence of high speed photographs of a characteristically large bubble is shown in Figure 5.4 at 6 millisecond intervals during its growth and departure cycle, and reveal further details about the nature of the vapor. The photographs show the side view of a bubble growing on the metal heater surface at a high level of heat flux (q_{surf} = 30 W/cm^2) in the vertical upflow orientation (θ = 90 deg.), with an imposed flow velocity of 8 cm/s and 11.1 °C subcooling. The first frame identifies the bubble in its earlier stages of growth, where it appears to originate from the coalescence of a cluster of smaller bubbles. As time progresses, the bubble grows and accelerates along the heater surface under buoyancy and flow forces. Coalescence seems to play a significant role in the growth process, since individual bubbles are not easily distinguishable in the photographs; rather, the vapor on the surface appears to coalesce into larger, deformed masses. Assuming this process to be quasi-periodic, an extrapolation of the photographs over time gives a period between bubbles of about 0.042 seconds, corresponding to a rate of about 23 bubbles/second, which agrees resonably well with the peak frequency of 21 to 22 bubbles/second measured for vertical upflow at a flow velocity of 4 cm/s using a hot wire. From the high-speed photographs viewed from the top (not shown in the figure), using the heater length as a reference, the larger bubble sizes are estimated to be an average of between six and eight millimeters in diameter, which compares with a mean departure diameter of 7.7 millimeters predicted by the FCCHF model for similar conditions.

The residence times of the larger bubbles on the heater surface are calculated using Eqn. (4.6) based on the dominant bubble frequencies measured with the hot wire

anemometer, assuming that these correspond to the motion of the larger bubbles over the heater surface. As pointed out above, the CHF is relatively large and nearly independent of the orientation angle in the upward-facing orientations, where the vapor departs the surface freely, while the CHF becomes comparatively small in the downward-facing orientations, where the motion of the vapor depends strongly on the magnitude of the buoyancy force component parallel to the heater surface. The reciprocal of the measured bubble residence times above the heater surface at heat fluxes approaching the CHF are shown in Figure 5.5 in normalized form with respect to Eqn. (5.6), for various levels of subcooling and a flow velocity of 4 cm/s as a function of the heater surface orientation. The corresponding measured values of the CHF in dimensionless form are also included, and demonstrate a direct relationship between the CHF and the reciprocal of the bubble residence time, or, equivalently, that the product of the CHF and the bubble residence time is a constant. Thus, as the residence time becomes large, the CHF becomes small in inverse proportion, and vice-versa.

5.1.2. Intermediate flow velocities (18 cm/s and 25 cm/s)

The CHF measurements for 18 and 25 cm/s are given in Figures 5.6 and 5.7, respectively, at slightly higher flow velocities than in the previous figures, and demonstrate a slight but noticeable increase in the influence of the flow inertia. While the CHF in the upward-facing orientations exhibits only a small enhancement due to the increased flow velocity, the minimum value for the CHF in both of these velocities shifts

from the horizontal facing-downward orientation to a slightly inclined orientation, where the buoyancy of the vapor opposes the direction of the imposed flow. The resulting balance of buoyancy and drag produces a stagnation of the vapor on the heater surface, which increases the probability of the coalescence of neighboring bubbles into larger slugs which then blanket the surface and cause dryout. As with the lower flow velocities, the CHF in the upward facing orientations is nearly independent of orientation, and is virtually the same magnitude as in pool boiling over a horizontal surface. Moreover, the CHF now depends more strongly on the orientation of the buoyancy force in the downward-facing orientations, suggesting that the drag and lift forces on the vapor associated with the flow, by themselves, are still relatively small compared to the buoyancy force.

The effects of the flow forces predicted by the FCCHF model are clearly exhibited in Figure 5.6, in the vicinity of $\theta = 255$ deg. A slight crook in the predicted behavior arises due to the effect of the lift force, which becomes marginally greater than the buoyancy force normal to the surface, and aids in the removal of vapor from the surface. At higher flow velocities, such as in Figure 5.7, the lift force plays a stronger role in the vapor removal process over a wider range of orientations, and the change in curvature of the predicted CHF is not so obvious.

5.1.3. High flow velocities (32 cm/s, 45 cm/s and 55 cm/s)

The flow inertia generally dominates over the effects of buoyancy at the higher flow velocities, and the dependence of the CHF on the heater surface orientation becomes accordingly weaker. Figure 5.8 shows the dependence of the CHF on orientation for a bulk flow velocity of 32 cm/s compared with the FCCHF model prediction, indicated by the solid line. While the difference in the CHF between vertical upflow (θ = 90 deg.) and vertical downflow (θ = 270 deg.) is substantial, the dependence of the CHF on the orientation of the buoyancy force is significantly diminished relative to the flow, as evidenced by the relatively large increase in the minimum CHF at θ = 240 deg. The minimum CHF occurs where the vapor remains almost static due to the balance of the buoyancy and drag forces on the vapor, which results in dryout at relatively low heat flux levels. This phenomenon can be seen in the high speed photographs in Figure 5.9, which show the evolution of a dry spot on a thin gold film heater beneath a group of nearly stationary, coalescing bubbles at an orientation of θ = 225 deg., with a bulk flow velocity of 32 cm/s and 11.1 °C subcooling. Notwithstanding the effects of the thin gold film heater and substrate material on the surface heat flux and temperature distribution, and hence on the bubble sizes as compared with those for a metal heater, the photos demonstrate the formation of a dry spot on the heater surface, indicated by the light-colored area beneath the large vapor mass in frame (e). The smaller bubbles forming at the leading edge of the heater surface in frame (a), whose motion is more strongly affected by drag forces, move toward the trailing edge of the heater in frame (b). They

coalesce to form larger bubbles along the way, as can be seen in frames (c) and (d), which increases the relative magnitude of the buoyancy force opposing the drag force, and the vapor eventually stagnates to produce conditions conducive to dryout, as in frame (e).

Figure 5.10 shows the measured CHF versus orientation compared with the FCCHF model predictions for an imposed flow velocity of 45 cm/s, at various levels of subcooling. While the flow forces acting on the vapor were observed to dominate over the buoyancy at all heater surface orientations, the minimum measured CHF occurred at θ = 240 deg., instead of at the vertical downflow orientation (θ = 270 deg.), where the buoyancy component opposite the direction of the flow is a maximum. This illustrates the effect of the hydrodynamic lift force, which becomes more significant in downflow, where the velocity of the vapor relative to the bulk flow reaches a maximum, since the buoyancy of the vapor is opposite the direction of the bulk liquid velocity. This aids in the removal of the vapor from the heater surface when the buoyancy force component normal and towards the heater surface becomes comparatively small, as in the vicinity of the vertical downflow position. While the ratio of the buoyancy to the flow forces is small, as indicated by the value of ξ (ξ = 0.05 in Figure 5.10), the variation in the CHF with orientation is still substantial, although the difference between the minimum and maximum CHF is relatively modest compared to that under buoyancy-dominant flow conditions, as in Figures 5.2 and 5.3. Also, the departure of the CHF measurements at low subcoolings from the model predictions is a secondary effect related to the test section geometry, and is discussed later, in section 5.3.

Figure 5.11 compares the measured CHF versus orientation at 55 cm/s for subcoolings of 11.1 °C and 22.2 °C with the CHF model predictions. The relatively small variation in the CHF with orientation shows that the effects of buoyancy on the CHF are now largely insignificant relative to the flow inertia. Most of the data fall in a band roughly ± 20% wide about a mean value approximately 20% greater than the prediction for pool boiling over a horizontal surface given by Eqn. (5.1). As in Figure 5.10, the minimum CHF occurs near θ = 240 deg. instead of θ = 270 deg., indicating the influence of the hydrodynamic lift force in the motion of the vapor away from the surface.

5.2. The effects of the bulk liquid subcooling on the CHF

The effects of subcooling in the CHF measurements presented above are correlated using Eqn. (5.1). The correlation is not successful in all cases, however, as seen in the changes in the non-dimensionalized heat flux values under certain conditions of flow and orientation, given only a change in the subcooling. For very low flow velocities, as in Figures 5.2 and 5.3, the effect of subcooling appears to be uniformly well-correlated for all heater orientations, even the downward-facing ones. Whereas Eqn. (5.1) was initially intended to describe the effects of subcooling in pool boiling over upward-facing surfaces, the data presented here show its success in predicting the effects at low flow velocities as well. One reason for this success is that the void produced on the heater surface occupied only a small fraction of the total flow cross-sectional area of the larger test section used for these tests, resulting in negligible acceleration of the

surrounding liquid. Additionally, the flow rate of liquid in the flow loop was sufficiently high such that the change in the bulk temperature of the liquid at the inlet to the test section due to condensation of the vapor was small, despite the departure of the vapor from the surface opposite the direction of flow in the case of downflow. As an estimate of this effect, the maximum possible change in the inlet bulk temperature due to condensation upstream of the heater can be evaluated from the following expression:

$$\Delta T_{bulk} = \frac{\chi q''_{surf} A_s}{\dot{m} c_{pl}} \tag{5.7}$$

where χ is the latent heat fraction defined in Chapter 3. At typical levels of heat flux for these low flow rates, the calculated maximum bulk temperature change is less than 0.3 °C.

Significant departures from the subcooling correlation occurs at the higher flow velocities, as the interaction of the uncondensed vapor with the test section walls becomes increasingly important in determining the CHF. Because of this, the deviation from the CHF model predictions becomes greater, since the model only accounts for the effects of the subcooling on the rate of vapor generation at the surface. One such effect occurs under circumstances of downflow, in which the narrow (3.2 mm) test section height increases the likelihood of coalescence of the vapor into large bubbles, which depart against the direction of flow due to the relatively strong buoyancy force. As the vapor condenses in the oncoming bulk liquid and decreases in volume, the drag force becomes relatively large compared with the buoyancy force, causing the vapor to reverse direction

and recirculate over the heater surface. At higher levels of subcooling, however, the adverse effects of the recirculation on the CHF are mitigated by the high rate of condensation into the bulk liquid. The effects of void recirculation are seen most clearly at the higher flow velocities in Figures 5.10 and 5.11. While the CHF measurements at the highest level of subcooling generally are in good agreement with the model predictions, the effects of recirculation at the lower subcoolings result in significant deviations. These deviations are possibly worsened by the condensation of the vapor upstream of the heater surface, which effectively lowers the inlet subcooling and consequently decreases the CHF. These combined effects of lowered subcooling and downflow are particularly obvious at higher flow velocities than at lower ones, because the CHF levels in downflow are increased considerably with the higher velocity.

For cases where the velocity of the vapor resulting from buoyancy is large in comparison with the bulk flow velocity, i.e., where ξ is relatively large, the effects of void recirculation are not as prevalent. Instead, the acceleration of the bulk flow resulting from the production of vapor in the test section plays a role in enhancing the transport of vapor from the heater surface due to the associated increase in the drag and lift forces on the bubbles. In these cases the FCCHF model under-predicts the CHF, as is witnessed, for example, in Figure 5.6 at a flow velocity of 18 cm/s. In the vicinity of θ = 225 deg., where the surface is facing downward and inclined at 45 deg. relative to the horizontal down position, the normalized CHF at 22.2 °C subcooling is substantially less than that at the lower levels of subcooling. This behavior is more closely related to the geometry of the test section, however, and further discussion is therefore deferred to section 5.3.

The effects of the bulk liquid subcooling manifested by the changes in the CHF described above originate near the heater surface, where the subcooling affects the evaporation process. The measured void fraction profiles above a heater surface oriented at θ = 150 deg. are compared in Figure 5.12 for two different levels of subcooling. In Figure 5.12(a), the void profiles appear to diverge from a common value at the heater surface, and this is attributed to the increasing thickness of the bubble boundary layer downstream from the leading edge of the heater. A comparison with Figure 5.12(b), for the same orientation but at 11.1°C subcooling and a substantially higher heat flux level, nontheless shows similarities between the void fraction profiles, especially close to the heater surface. The void fraction at the wall, as extrapolated from the measured void fraction profiles, is shown for various heater orientations in Figure 5.13. While the void fraction conventionally denotes the volumetric concentration of the vapor phase, when applied to a thin region near the heater surface itself, the void fraction approximates the mean fraction of the heater surface area covered by vapor. Although the gradient in the measured void fraction near the surface appears to be large, the probe measurements are within 0.1 mm of the surface, which is of the order of the smallest bubble sizes. It should be noted in Figure 5.13 that although the void fraction at the heater surface is assumed to be spatially uniform, it fluctuates temporally at a rate related to the measured bubble frequency. The results in Figure 5.13 for the various subcoolings show that the void fraction at the heater surface at the onset of the CHF is relatively uninfluenced by large changes in subcooling, despite the sometimes considerable differences in the heat flux levels. Also, the values of the void fraction measured at the wall for the downward-

facing orientations are close to 0.5, which is approximately equal to the critical packing fraction for a collection of spherical bubbles (Bankoff, 1962). Exceeding this void concentration greatly increases the probability of coalescence of neighboring bubbles into larger slugs, which could result in dryout of the heater surface.

Further evidence of the effects of subcooling on the CHF is obtained from the volumetric rate of vapor generation at the surface, estimated from measurements of the void fraction, bubble frequency, and bubble boundary layer thickness as follows:

$$v' = \bar{f}\,\alpha\,\delta_{BL}A_s \tag{5.8}$$

A more complete derivation of Eqn. (5.8) is given in Appendix F. In Figure 5.14, The volumetric rate of vapor generation at the CHF computed from the hot wire measurements is plotted in Figure 5.14 for subcoolings of 5.6 °C, 11.1 °C, and 22.2 °C as a function of the heater surface orientation. The rates are virtually the same for the different subcoolings, despite the corresponding differences in the heat flux levels, which vary with subcooling nearly according to Eqn. (5.1).

5.3. The effects of the test section height on the CHF

The effects of the test section height are accounted for in the CHF model only through the change in the bulk velocity profile of the liquid near the wall with changing Reynolds number. As such, the effects related to the interaction of the vapor with the test

section wall opposite the heater surface produce deviations from the model predictions. First, the smaller test section height decreases the CHF under certain conditions of downflow by confining the vapor leaving the heater surface to a relatively narrow gap. The 3.2-mm test section height is smaller than many of the larger bubbles, such as those shown in Figure 5.4, and therefore counteracts the lift forces acting on the bubbles, increasing their residence time on the surface. This, in turn, also increases the probability of coalescence between neighboring vapor bubbles, which exacerbates the deleterious effects of void recirculation on the CHF discussed earlier. In cases where the lift force plays a substantial role in the removal of the vapor, as at the higher flow velocities, this effect is likely to produce significant deviations from the CHF model, as can be seen in Figures 5.10 and 5.11. Figure 5.15 shows the top view of a large vapor slug formed through recirculation and coalescence of vapor in the narrow test section height above the metal heater surface in the vertical downflow orientation at a flow velocity of 18 cm/s. The heater surface appears to have nearly dried out during the residence time of the overlying vapor mass, although boiling is clearly observed in a thin liquid film on the surface, as indicated in the figure. These apparent adverse effects of narrowing the test section height produce a measurable difference in the CHF. This is clearly demonstrated in Figure 5.16, in which the CHF is compared between a test section height of 3.2 mm and a test section height of 12.7 mm under similar conditions with a flow velocity of 12.5 cm/s. While the two compare favorably in cases of upflow, they deviate from each other in downflow. The local acceleration of the liquid over the heater surface is increased considerably more in the 3.2-mm test section due to the production of vapor than in the

12.7-mm test section. A quantitative measure of the acceleration of the flow in the test section due to the generation of the vapor may be obtained from the average cross-sectional area occupied by the vapor over the total cross sectional area of the test section:

$$\%A = \frac{w_{heater}\alpha\delta_{BL}}{A_{XC}} \tag{5.9}$$

where w_{heater} is the width of the heater, and α and δ_{BL} are the mean void fraction and bubble boundary layer thickness measured with the hot wire in the 25.4-mm test section. The cross-sectional area occupied by the vapor measured in the 25.4-mm test section is assumed to be approximately the same in the 12.7-mm and 3.2-mm test sections. For the 3.2-mm test section, then, the void occupies 21% of the cross-sectional area, while only 5% and 3% of the cross-sectional area for the 12.7-mm and 25.4-mm test sections, respectively.

5.4. The effects of heated length on the measured CHF

The effects on the CHF of increasing the heated surface length in the flow direction from 19 mm to 38 mm are shown in Figures 5.17, 5.18 and 5.19, for imposed flow velocities of 18 cm/s, 45 cm/s and 32 cm/s, respectively. In Figure 5.17, where the flow velocity was 18 cm/s and the subcooling 11.1 °C, the twofold increase in the heated length lowers the CHF by approximately 25%. Because of this, the value of E'' in the FCCHF model must be adjusted accordingly to fit the experimental data, yielding the

difference between the dashed curve (the CHF predicted for L_{heat} = 19 mm) and the solid curve (the CHF predicted for L_{heat} = 38 mm) in Figure 5.17. Despite the decrease in the local acceleration in the test section due to the decrease in the heater width, the CHF measurements for the heater orientations with downflow still fall well above the model predictions for L_{heat} = 38 mm given by the solid line. The unexpectedly low CHF measured for the horizontal upward orientation, meanwhile, is likely an anomaly resulting from the confining geometry of the test section. Figure 5.18 demonstrates the combined effects of subcooling and the increase in heated length for a flow velocity of 32 cm/s. In general, the CHF was approximately 75% of the CHF with the 19 mm heated length, although the downward facing orientations, particularly those with downflow, appear to be disproportionately affected. The increase in subcooling lessens the severity of the decrease in the CHF due to the longer heated length, and at 22.2 °C subcooling, the characteristic behavior of the CHF with orientation approaches the FCCHF model predictions. Figure 5.19 shows the effect of the increase in heated length for a relatively high flow velocity, 45 cm/s, at a subcooling of 11.1 °C. The downward facing orientations are disproportionately affected, as indicated by the departure from the FCCHF model, which does not account for the secondary effects of the heated length.

5.5. The variation of the bubble residence time with surface heat flux

The CHF model predicts that the residence time of the bubbles on the surface varies with the surface heat flux, such that the product of the heat flux and the bubble

residence time increases until it reaches the prescribed value used to denote the onset of the CHF. The experimental measurements presented below are compared with the model results to better evaluate the accuracy of the model predictions.

Figure 5.20 shows the measured peak bubble frequency as a function of the surface heat flux relative to the CHF. The bubble frequency is also expected to depend on the magnitude of buoyancy force component parallel to the heater surface, hence the differences in the measured frequency between the various heater orientations, most notably $\theta = 165$ deg. The bubble frequency increases somewhat modestly with increasing heat flux for all heater surface orientations, showing that the increase in the vapor generation rate associated with the rise in heat flux produces bubbles at a higher rate. At the same time, Figure 5.21 shows that the mean void fraction also rises with increasing surface heat flux, although not at as high of a rate as the measured bubble frequency. This result is consistent with that obtained by Carvalho and Bergles (1994), who also measured the void fraction as a function of the surface heat flux, determining that both the mean bubble size as well as the void fraction increased slightly with increasing heat flux. The ratio of the void fraction to the peak bubble frequency, i.e., the mean bubble residence time, is shown in dimensionless form as a function of the surface heat flux in Figure 5.22, and decreases slightly as a function of the surface heat flux. The model prediction, given by Eqn. (3.59), is indicated by the solid line, and increases slightly as a function of the surface heat flux due to the longer time required for the velocity due to buoyancy to reach the outward velocity of the bubble due to an increase in volume.

Figure 5.23 shows the product of the surface heat flux times the bubble residence time non-dimensionalized with respect to the product of the CHF and the bubble residence time at CHF (i.e., the product of Eqns. (5.1) and (5.6)) for pool boiling as a function of the ratio of the surface heat flux to the CHF. The model predictions given by Eqn. (3.60) are given by the solid line, and over-predict the characteristic slope of the data due to the predicted positive slope for the residence time in Figure 5.22. Generally, the data fall in the vicinity of the predicted curve, however, and the measured product of the heat flux and the residence time increases up to the onset of the CHF, as expected. The exception is the data for θ = 165 deg., where the measured value of E'' is about 50 % greater than the model predictions.

5.6. Effects of the heater substrate material on the CHF

The purpose of the experiments with the gold film heaters was to determine their suitability for investigating boiling at high heat fluxes photographically, viewing the process through the heater surface, with the main objective being to characterize the behavior of the large coalesced vapor masses which likely play a significant role in the mechanisms of dryout on the metal heater surfaces. In Figure 5.24, the measured CHF for the gold film heaters at two different heater orientations for a flow velocity of 4 cm/s is given as a function of the subcooling. The CHF values are non-dimensionalized with respect to Eqn. (5.1), and show a significant decrease in the CHF due to the thermal properties of the quartz substrate compared with those for the metal heater. The dashed

line in the figure indicates the predicted first hydrodynamic transition (Moissis and Berenson, 1963) at about 56 % of the CHF, where the vapor generated on the surface transforms from individual bubbles into the coalesced vapor structures typical at the higher heat flux levels. The CHF for the quartz substrate heaters does not increase with subcooling in accordance with Eqn. (5.1), either, and may be due to the prevalence of individual bubbles on the surface instead of coalesced vapor slugs normally present above the metal heaters at high heat fluxes. The high-speed photographs in Figure 5.25 illustrate this difference; the metal heater surface, viewed from the top in the first photograph for vertical downflow at 32 cm/s and 11.1 °C subcooling at the CHF, is covered with large, amorphous vapor slugs. In contrast, the gold film surface, viewed from below in the second photograph for the same flow conditions at the CHF, has a relatively sparse population of moderate-sized, individual bubbles. It may be further noted that neither photograph in Figure 5.25 shows evidence of the "vapor columns" customarily associated with the first hydrodynamic transitions.

5.7. The relation of the surface superheat to the CHF

Figure 5.26 shows the measured surface superheat for the metal heater as a function of the heater surface orientation for four different flow velocities at a fixed subcooling of 11.1 °C. At the two lower flow velocities, where buoyancy generally dominates and produces considerable changes in the CHF for the downward facing heater orientations, the surface superheat at the CHF remains virtually constant with orientation,

except in the cases where the CHF levels are low, near the horizontal down position. In these situations, small incremental changes in the heat flux produced large changes in the surface superheat. Therefore, while the uncertainty in the heat flux measurements may be only marginally uncertain, due to the subjective nature of identifying the "true" onset of dryout, the corresponding uncertainty in the heater surface superheat becomes comparatively large. However, this uncertainty is not so large as to explain the substantial change in the superheat shown in Figure 5.26 for these lower CHF levels. For the higher flow velocities, meanwhile, the variation in the surface superheat with orientation is somewhat greater than for the lower velocities, and appears to vary in direct proportion to the surface heat flux. The measured surface superheat does not vary greatly with subcooling, as demonstrated in Figure 5.27 for a flow velocity of 18 cm/s at three different levels of subcooling. For each subcooling level, the surface superheat at CHF was more or less constant at 22 °C, except for the cases of downflow, slightly inclined from the horizontal down orientation, where the CHF was relatively small. It should be noted in both Figures 5.26 and 5.27 that the measured surface superheat is much less than the predicted Leidenfrost superheat, given by Berenson (1961) as 69 °C and by Henry (1974) as 74 °C, implying that the surface is still able to be wetted by liquid at the onset of the CHF.

U_b (cm/s)	ξ (–)
4.0	6.57
8.0	1.64
12.5	0.67
18.0	0.32
25.4	0.16
32.0	0.10
45.0	0.05
55.0	0.03

Table 5.1. Values of ξ from Eqn. (5.4) as a function of the bulk flow velocity for R113 at T_{bulk} = 49 °C.

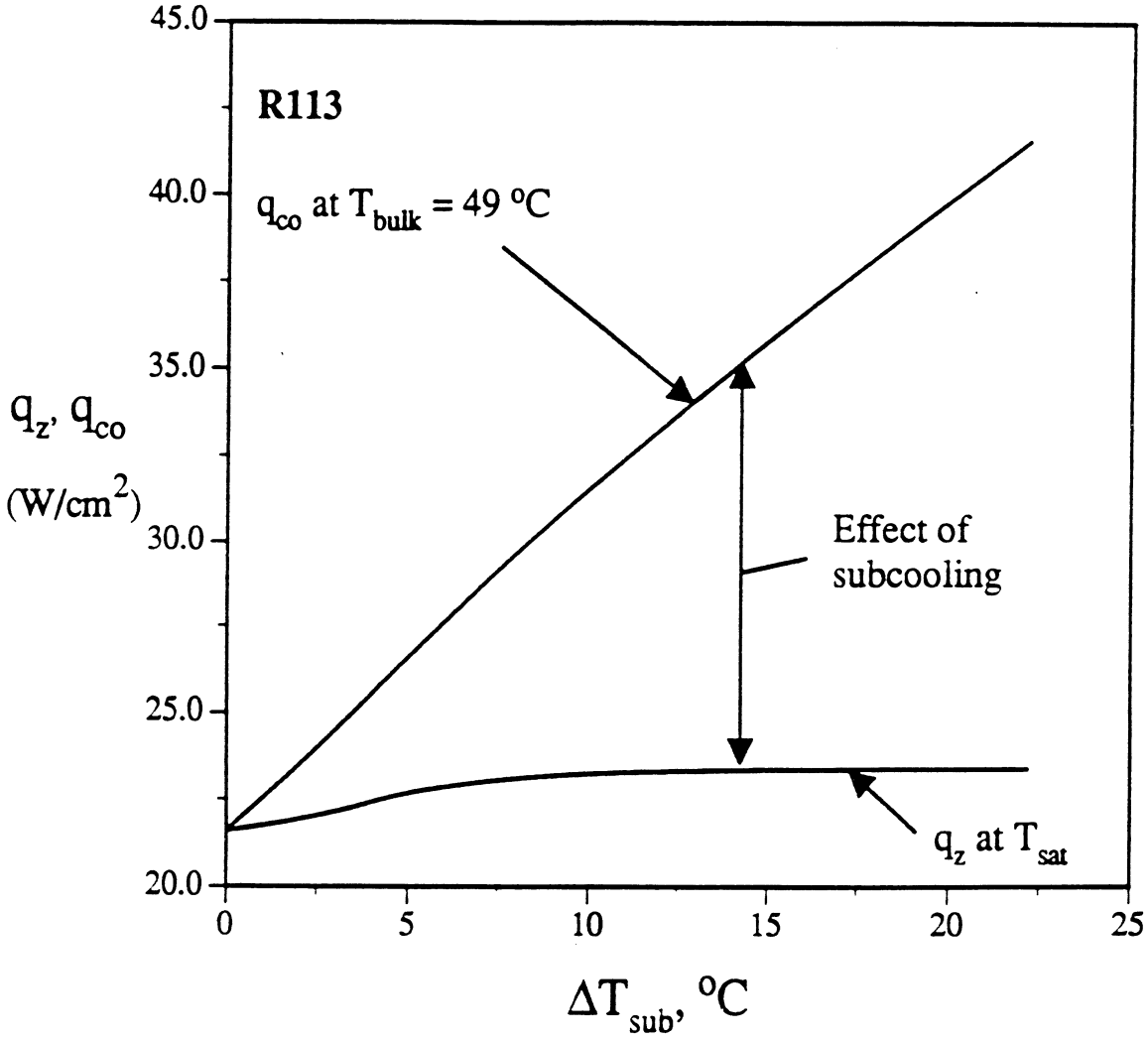

Figure 5.1. The CHF as a function of subcooling and pressure, from Eqns. (5.1) and (5.2)

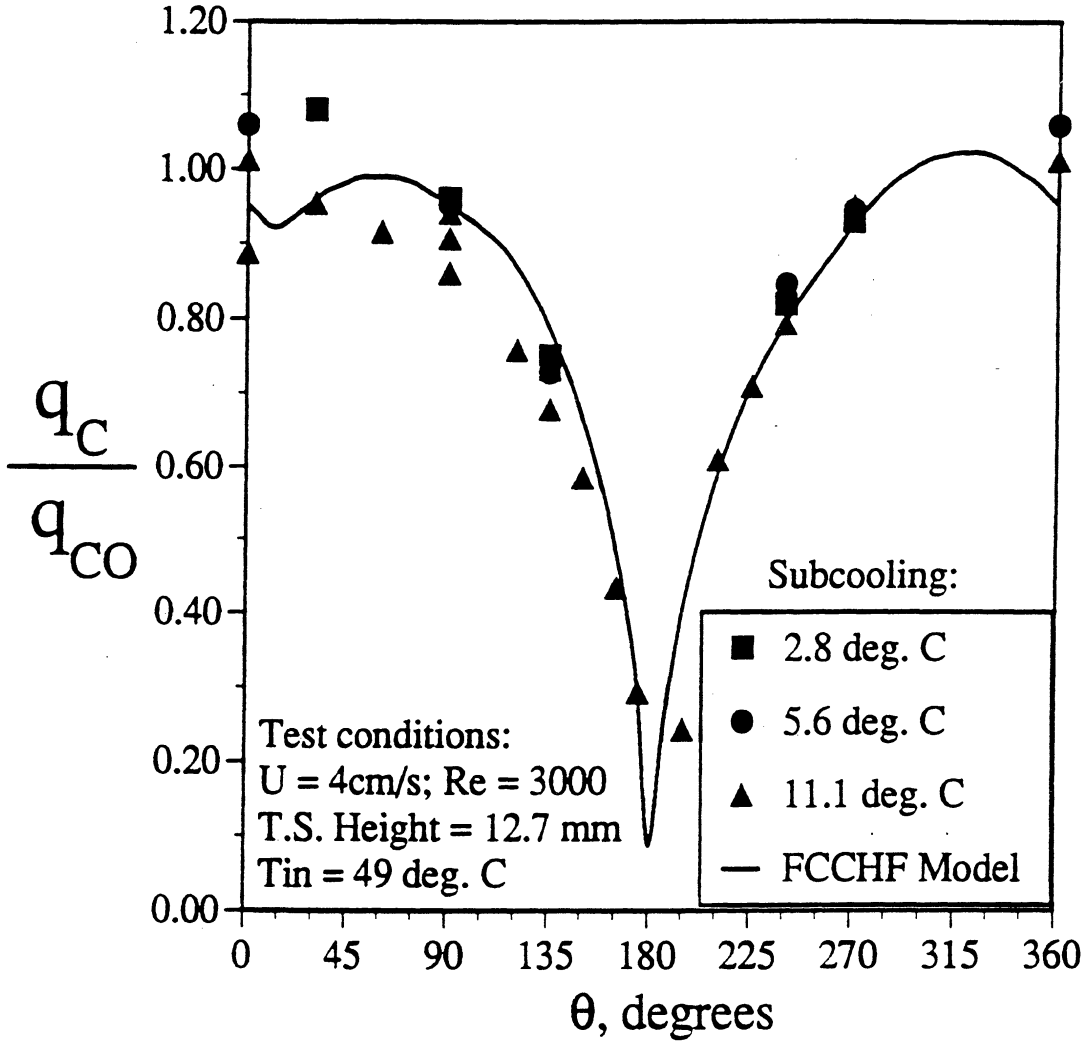

Figure 5.2. Comparision of the measured CHF with the FCCHF model predictions as a function of orientation, U_{bulk} = 4 cm/s.

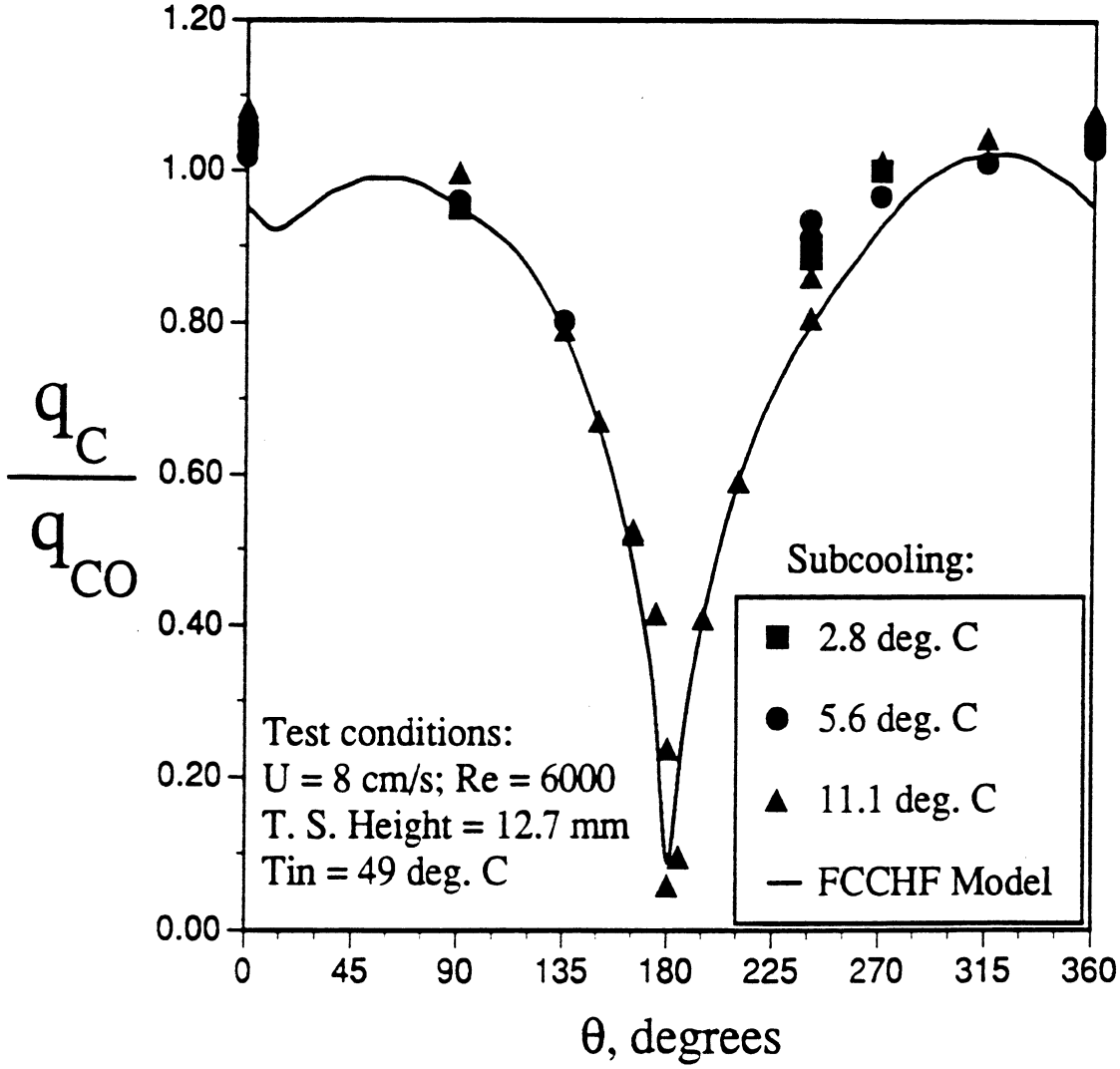

Figure 5.3. Comparision of the measured CHF with the FCCHF model predictions as a function of orientation, U_{bulk} = 8 cm/s.

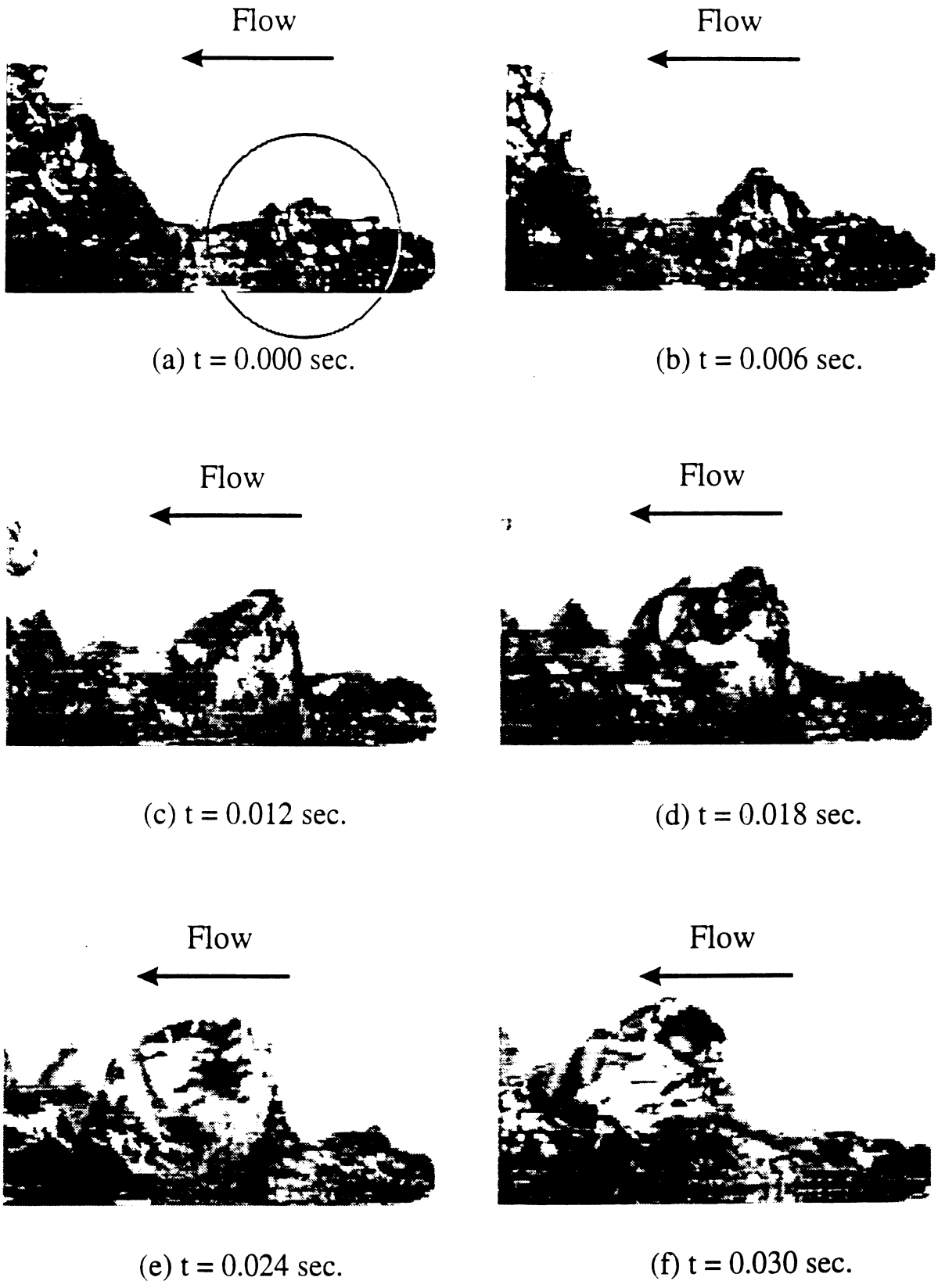

Figure 5.4. A typical large bubble shown at 6 millisecond intervals during its growth and departure cycle (side view of a metal heater surface); θ = 90 deg., q" = 30 W/cm^2, U_{bulk} = 8 cm/s, ΔT_{sub} = 11.1 °C, T_{bulk} = 49 °C.

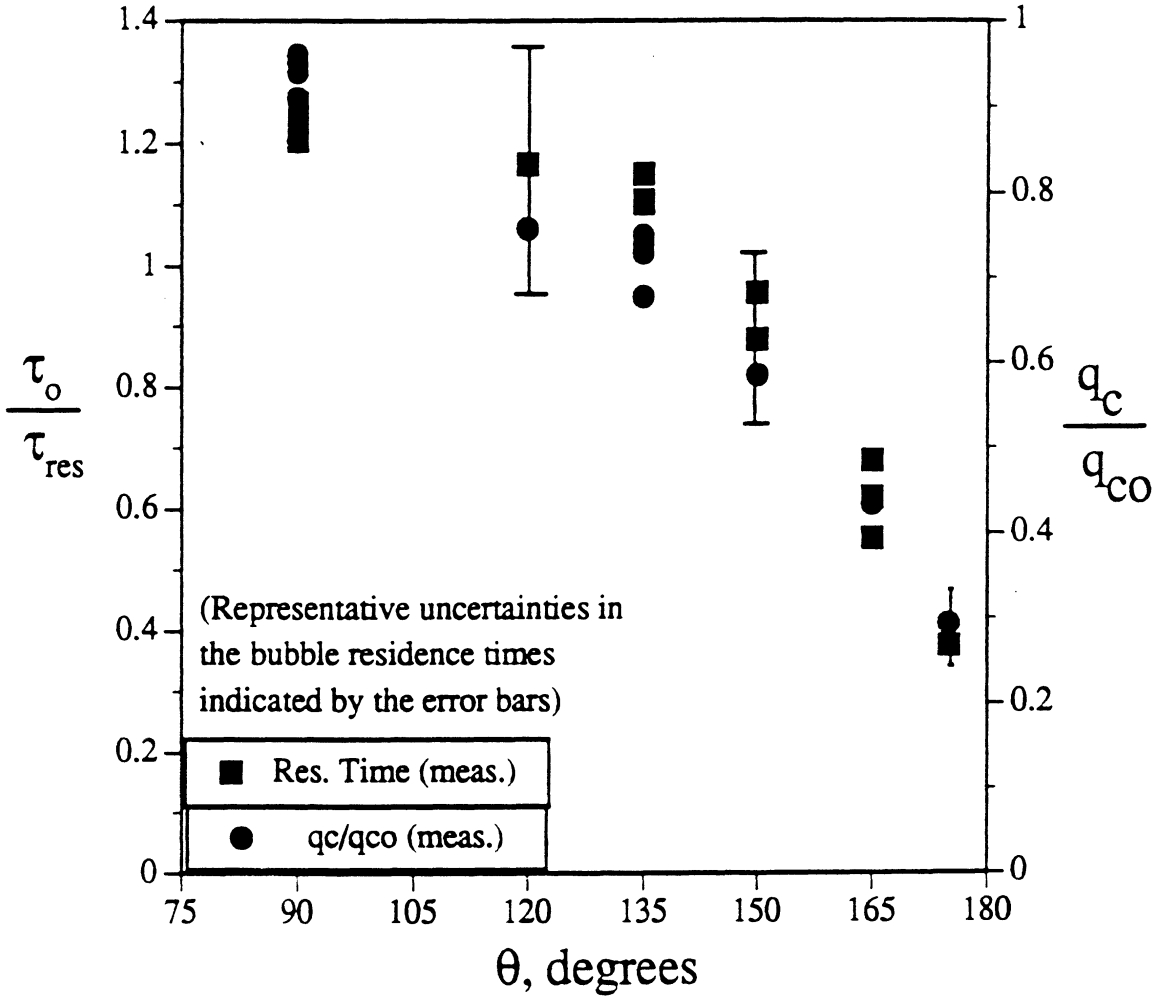

Figure 5.5. The reciprocal of the measured bubble residence time as a function of orientation compared with the corresponding CHF

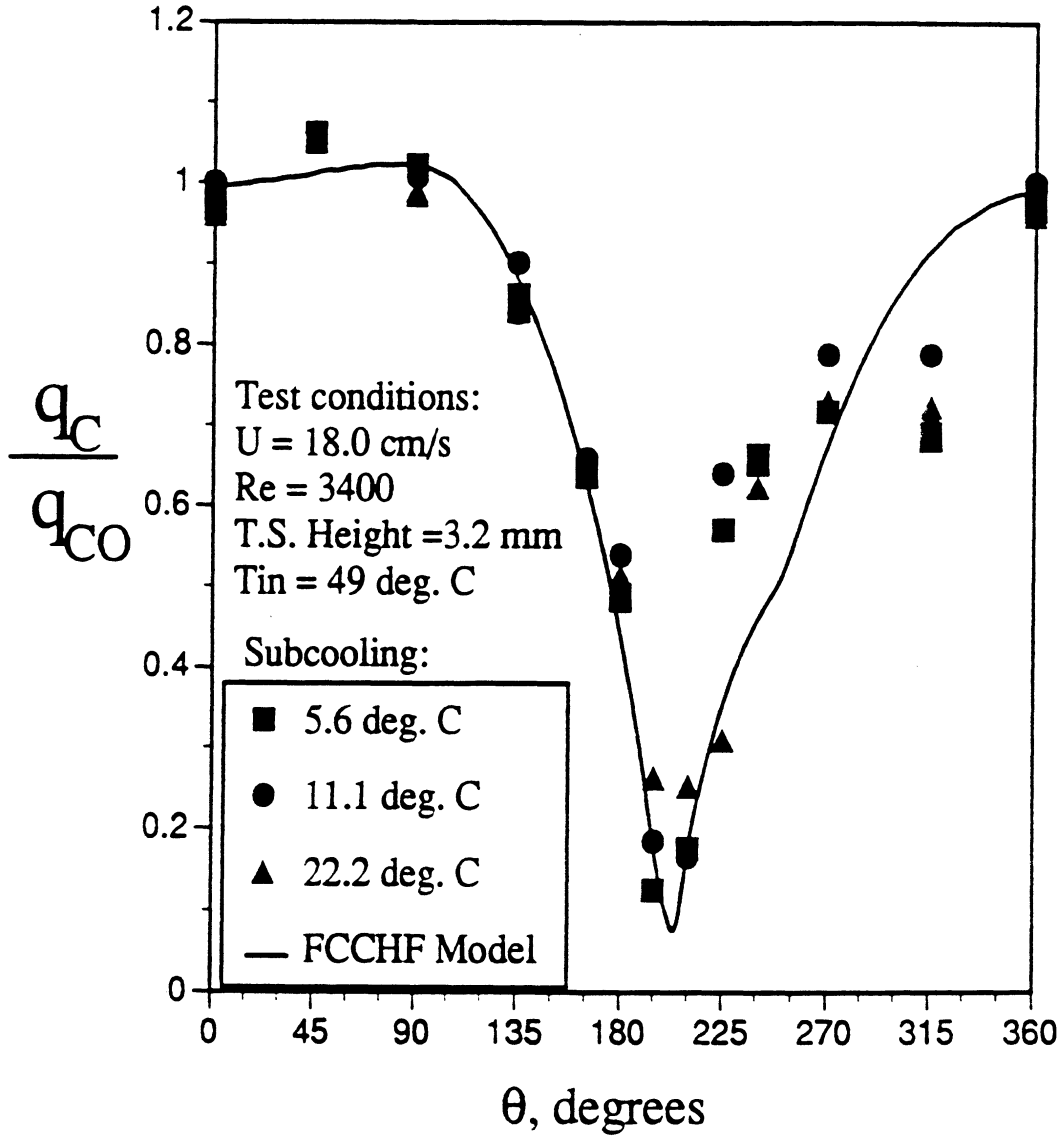

Figure 5.6. Comparision of the measured CHF with the FCCHF model predictions as a function of orientation, U_{bulk} = 18 cm/s.

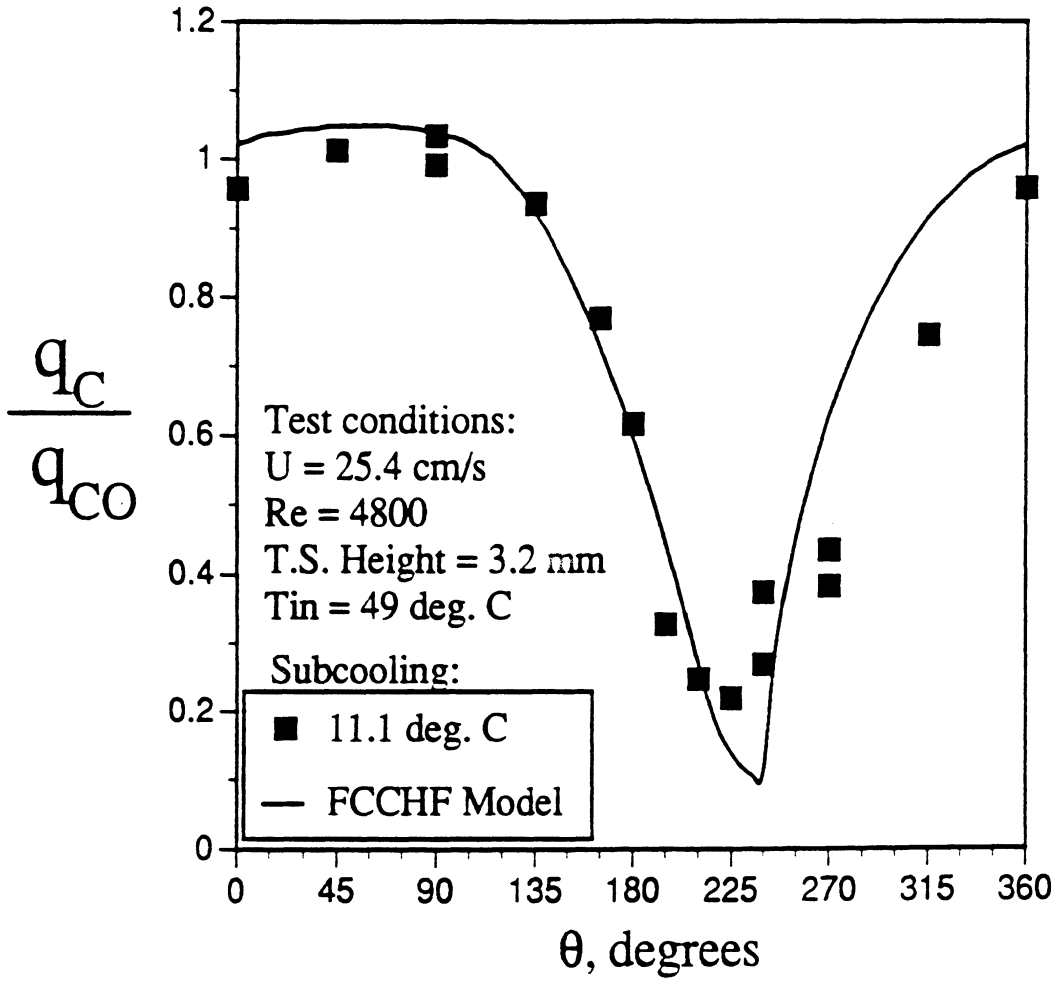

Figure 5.7. Comparision of the measured CHF with the FCCHF model predictions as a function of orientation, U_{bulk} = 25.4 cm/s.

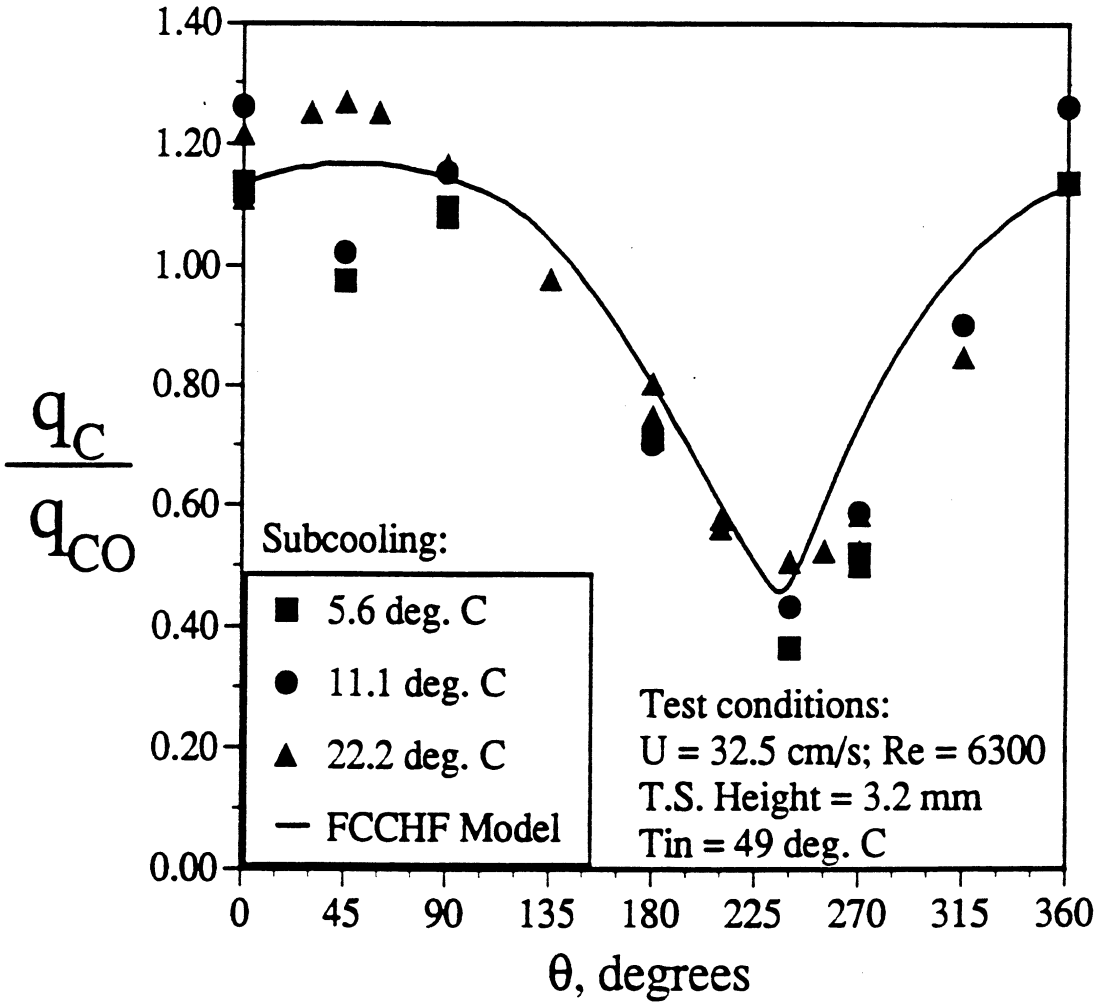

Figure 5.8. Comparision of the measured CHF with the FCCHF model predictions as a function of orientation, U_{bulk} = 32 cm/s.

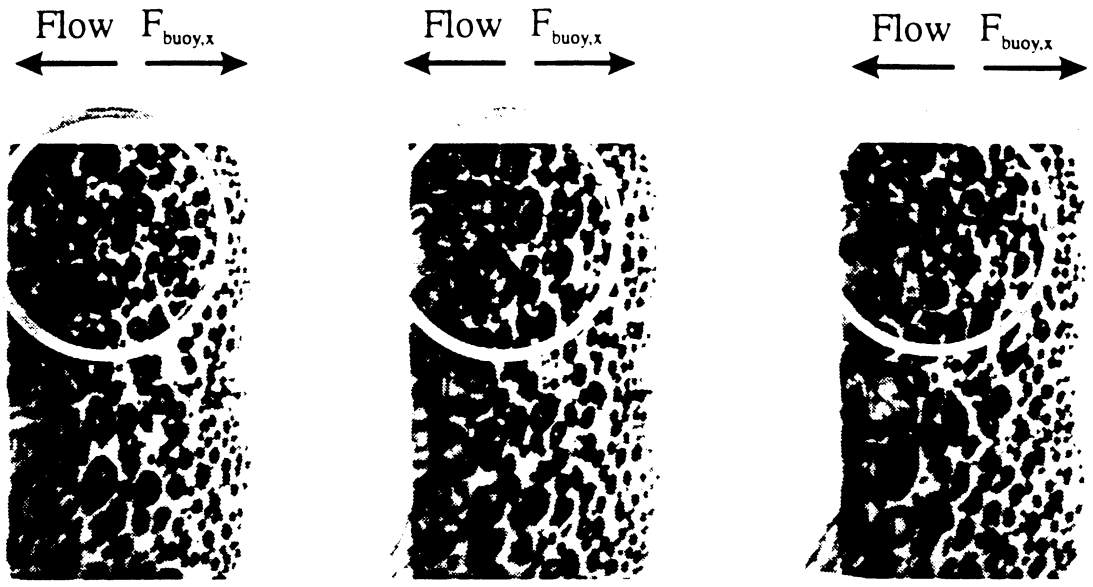

(a) t = 0.000 sec. (b) t = 0.010 sec. (c) t = 0.020 sec.

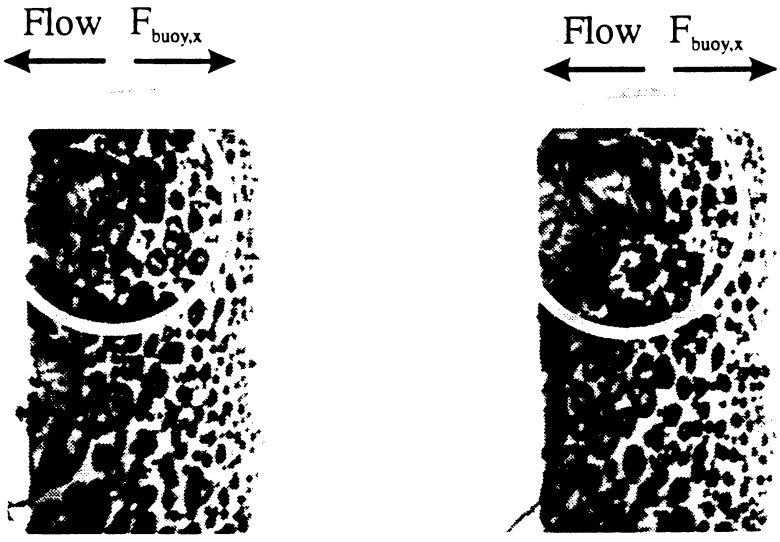

(d) t = 0.030 sec. (e) t = 0.040 sec.

Figure 5.9. The evolution of a dry spot on a thin gold film heater (view through the heater surface from below); θ = 225 deg., U_{bulk} = 32 cm/s, ΔT_{sub} = 11.1 °C.

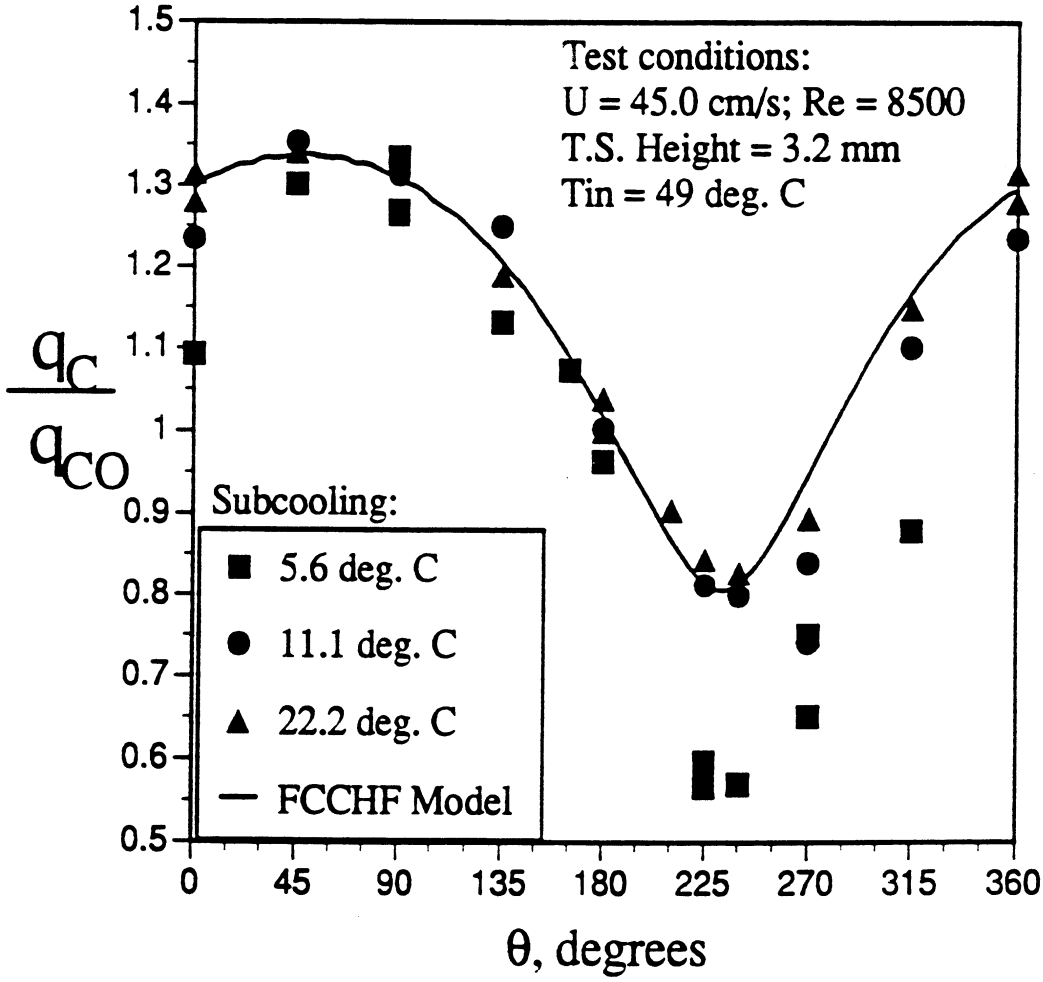

Figure 5.10. Comparision of the measured CHF with the FCCHF model predictions as a function of orientation, U_{bulk} = 45 cm/s.

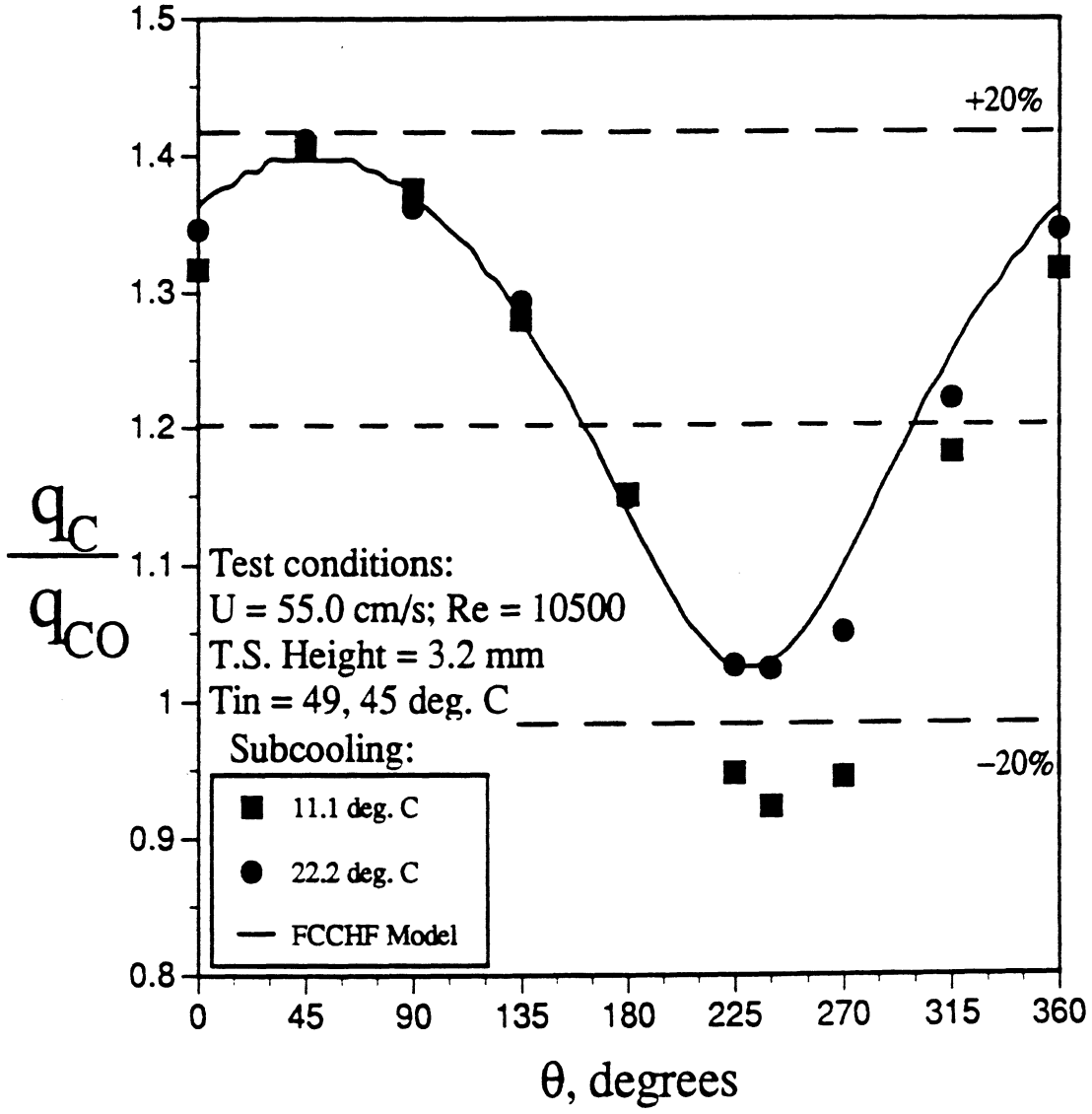

Figure 5.11. Comparision of the measured CHF with the FCCHF model predictions as a function of orientation, U_{bulk} = 55 cm/s.

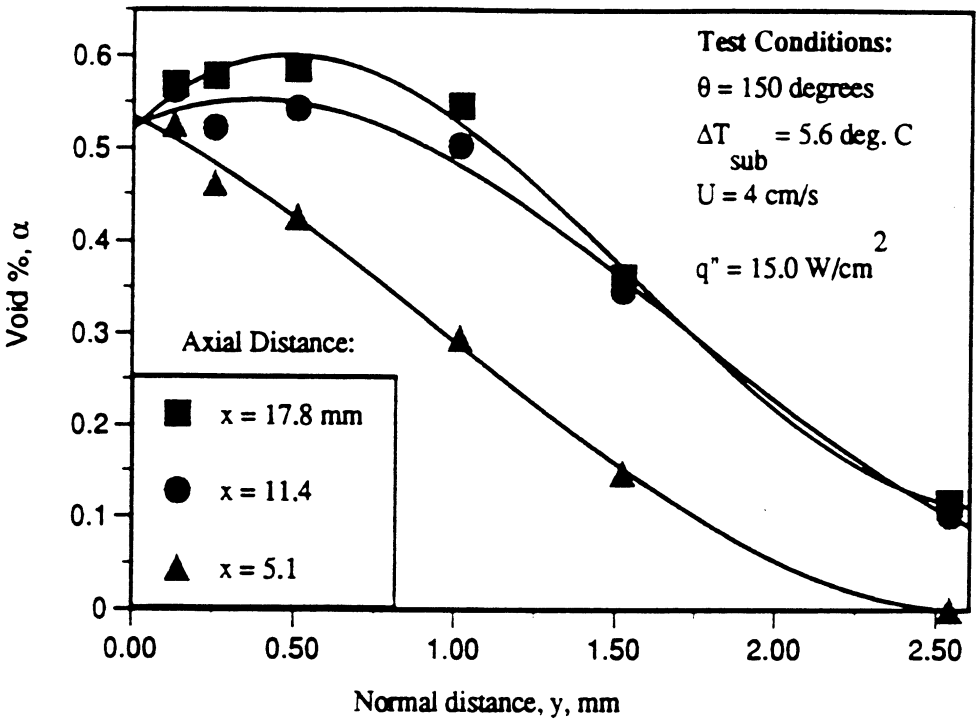

Figure 5.12(a). Void fraction profile at 5.6°C subcooling

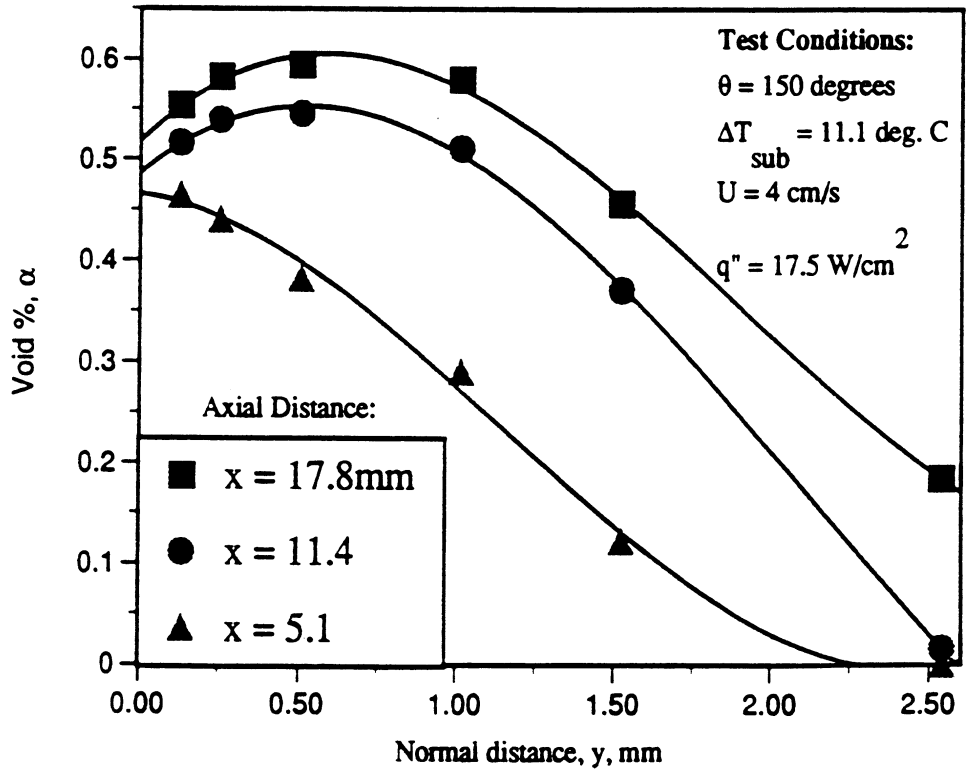

Figure 5.12(b). Void fraction profile at 11.1°C subcooling

Figure 5.12. Sample void fraction profiles over the metal heater surface for two different levels of subcooling, θ = 150 deg.

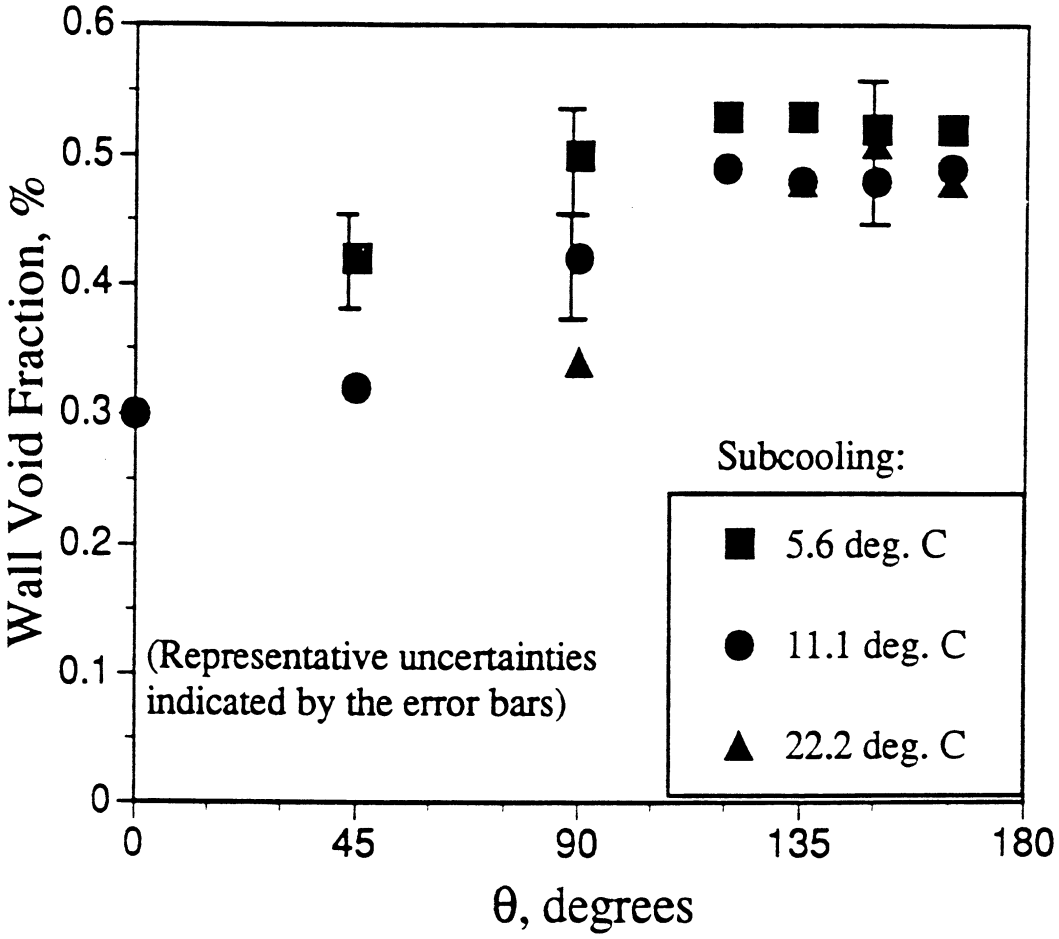

Figure 5.13. The measured void fraction extrapolated to the heater surface as a function of the heater surface orientation for various levels of subcooling.

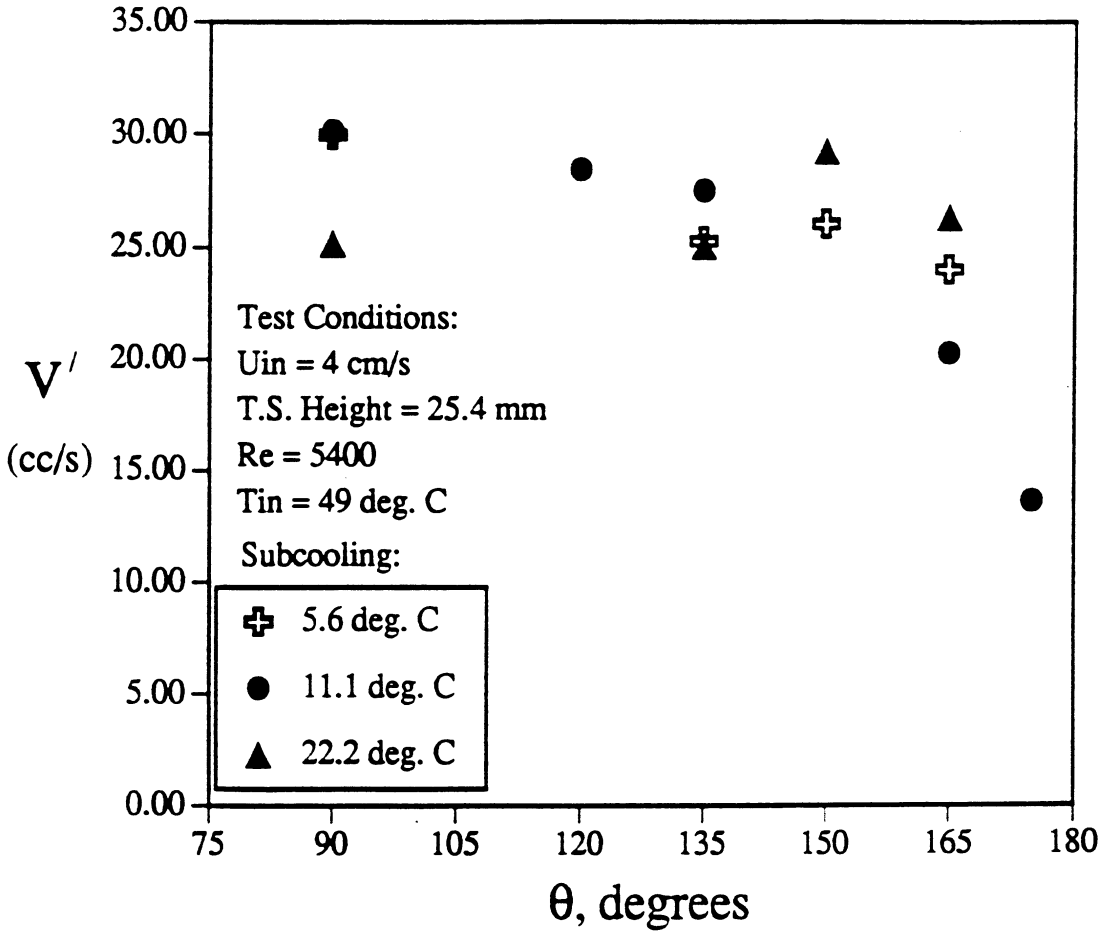

Figure 5.14. The measured volumetric rate of vapor generation as a function of the heater surface orientation for various levels of subcooling.

(a) t = 0.000 sec.

(b) t = 0.004 sec.

Figure 5.15. The top view of a large vapor slug above the metal heater surface, θ = 270 deg., U_{bulk} = 18 cm/s, ΔT_{sub} = 11.1 °C, T. S. height = 3.2 mm.

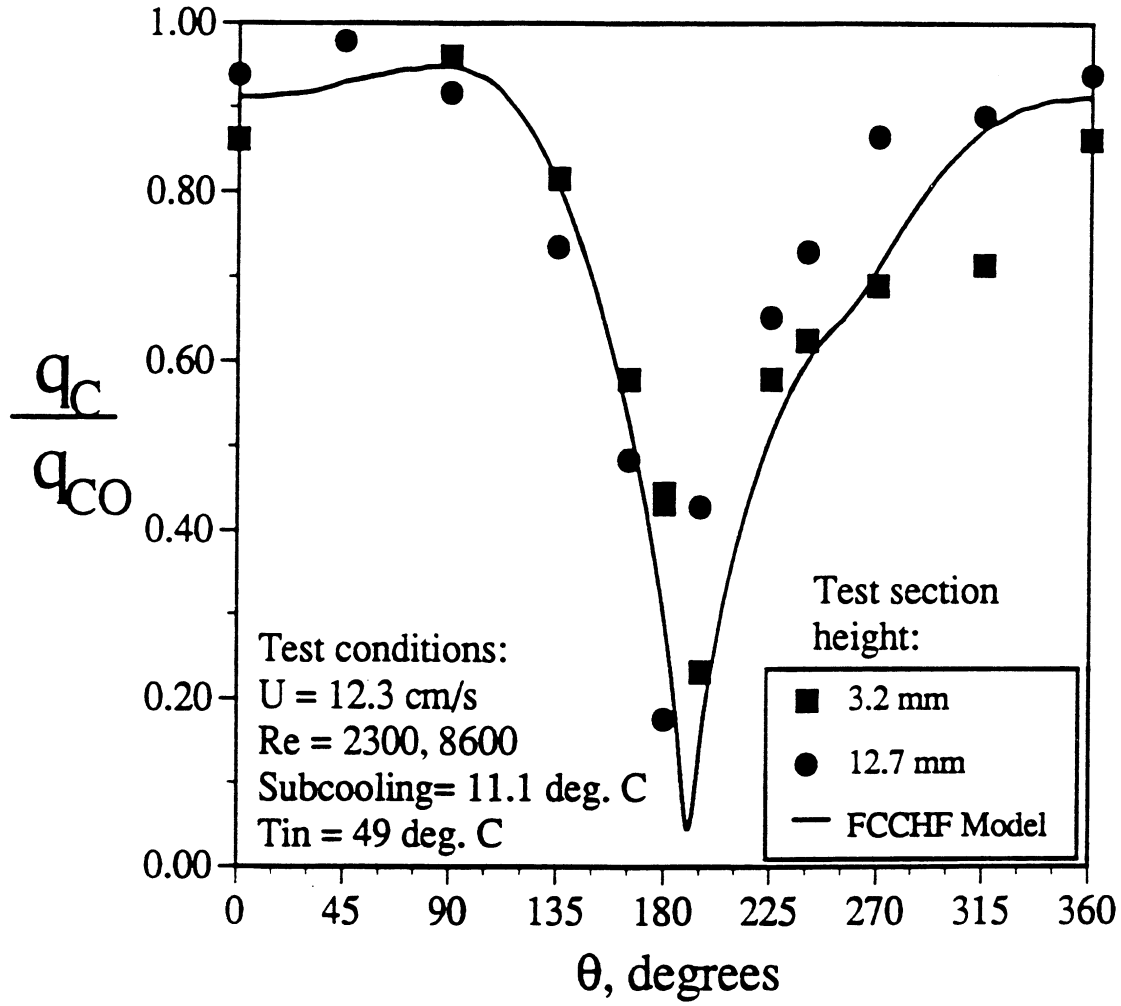

Figure 5.16. Comparison of the CHF versus orientation at U_{bulk} = 12.5 cm/s for test section heights of 3.2 mm and 12.7 mm.

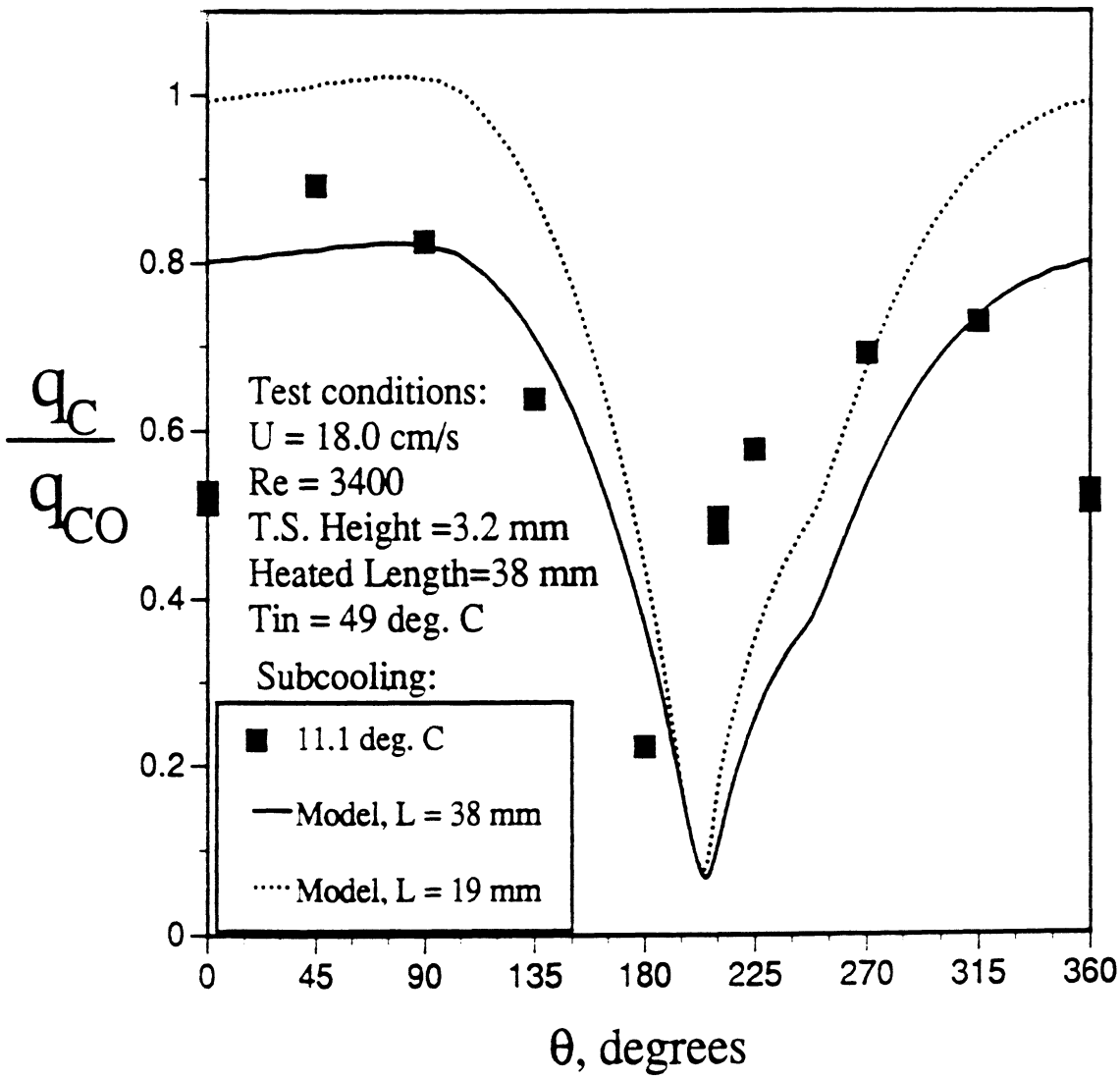

Figure 5.17. The effects of the heater length on the CHF versus orientation; ΔT_{sub} = 11.1 ^{o}C, U_{bulk} = 18 cm/s, L_{heat} = 38 mm.

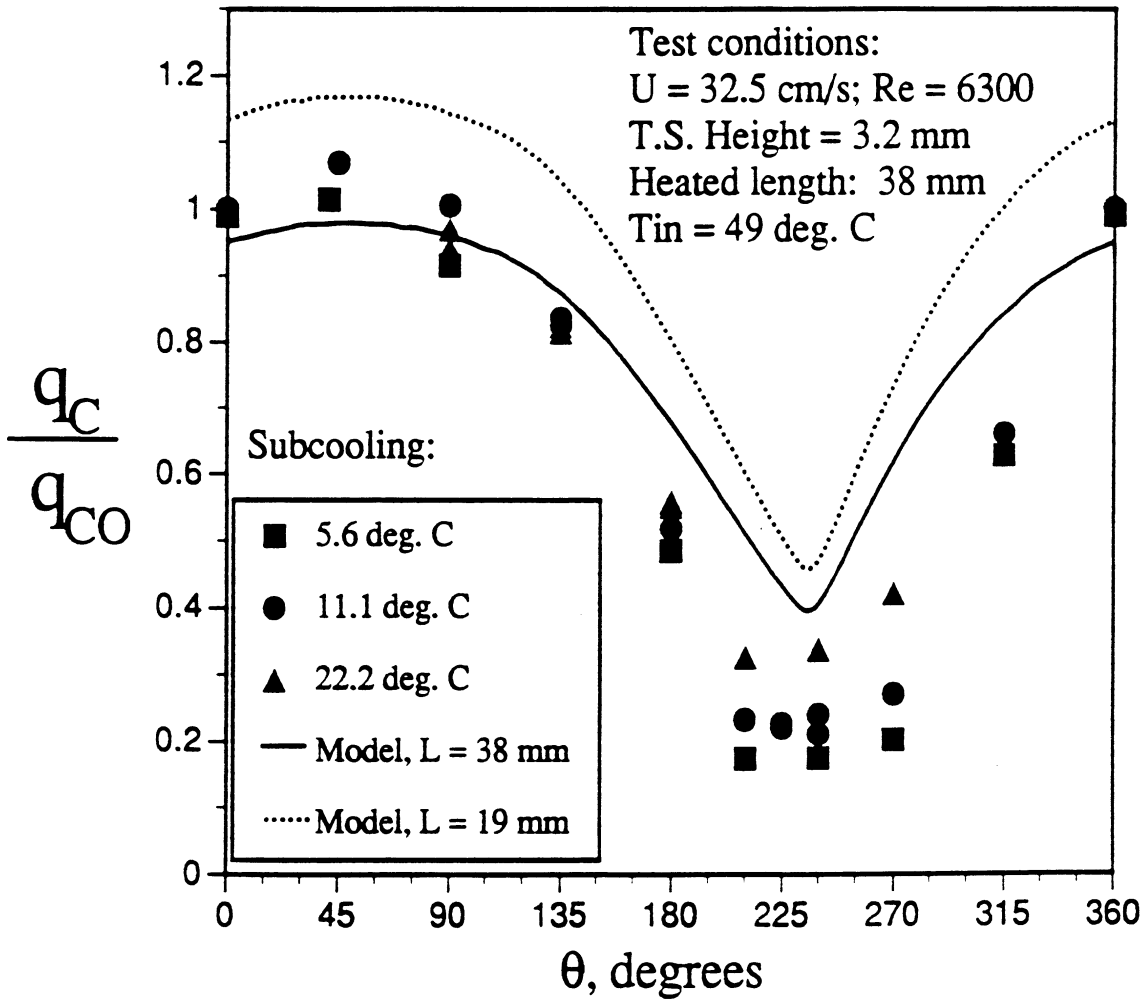

Figure 5.18. The effects of the heater length on the CHF versus orientation; U_{bulk} = 32 cm/s, L_{heat} = 38 mm.

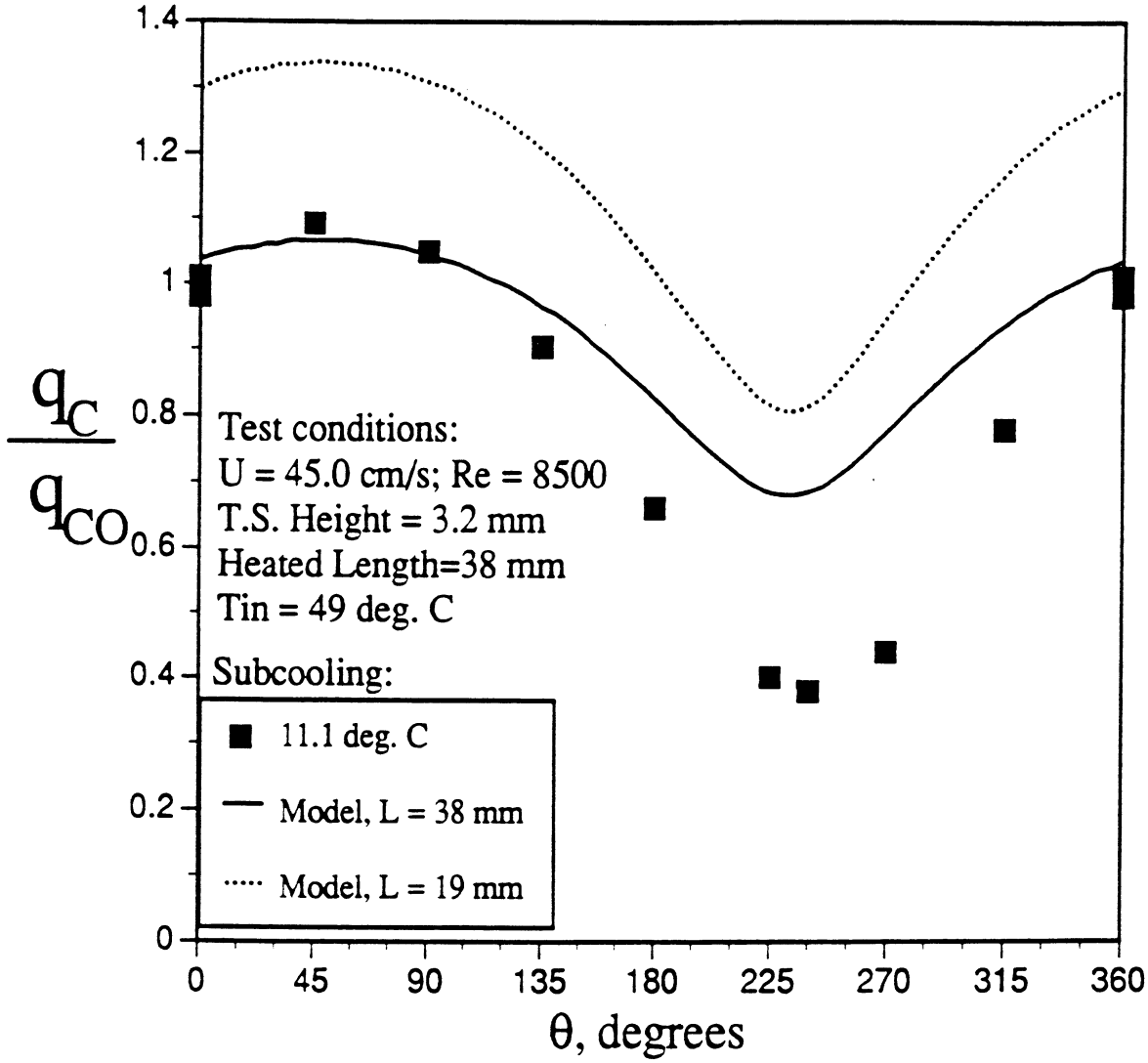

Figure 5.19. The effects of the heater length on the CHF versus orientation;

ΔT_{sub} = 11.1 ^{o}C, U_{bulk} = 45 cm/s, L_{heat} = 38 mm.

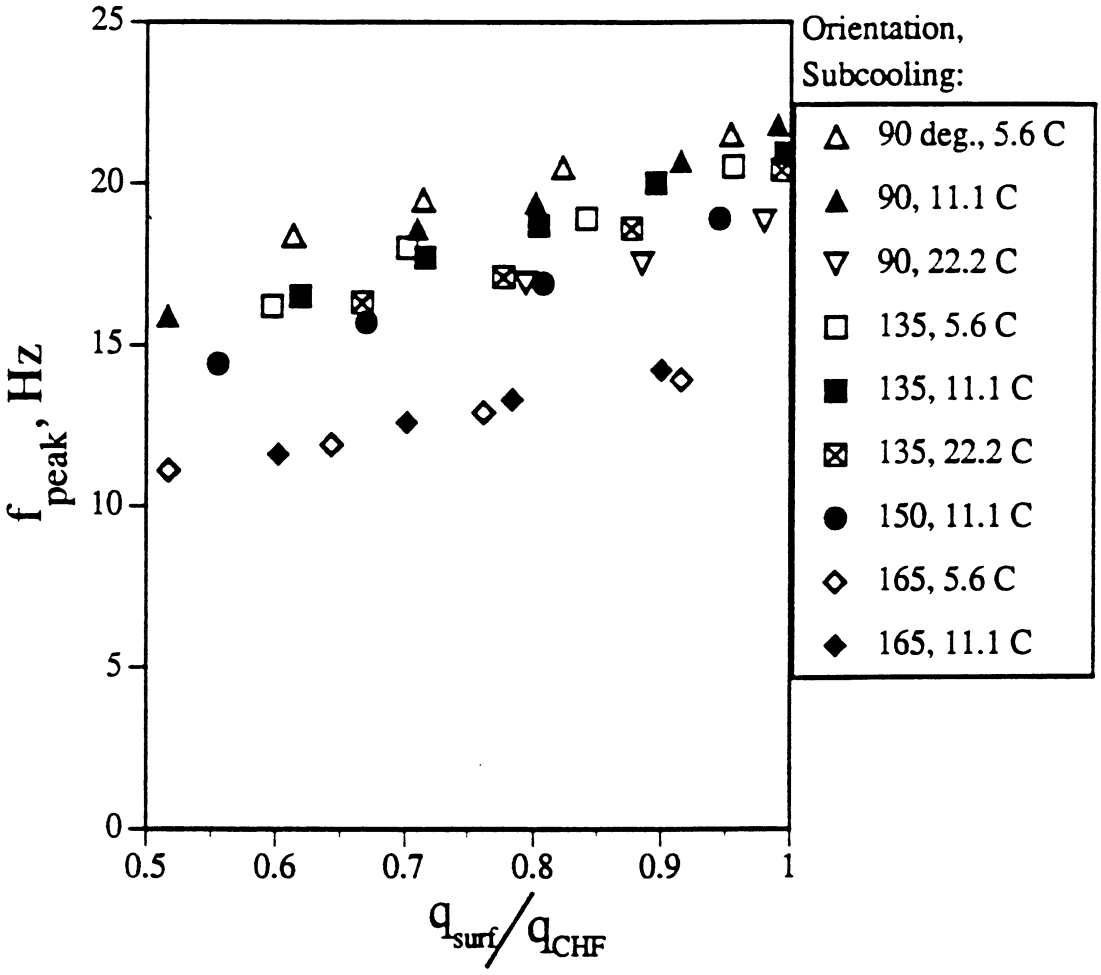

Figure 5.20. The measured peak bubble frequency as a function of the surface heat flux for a variety of heater orientations and subcoolings; U_{bulk} = 4 cm/s.

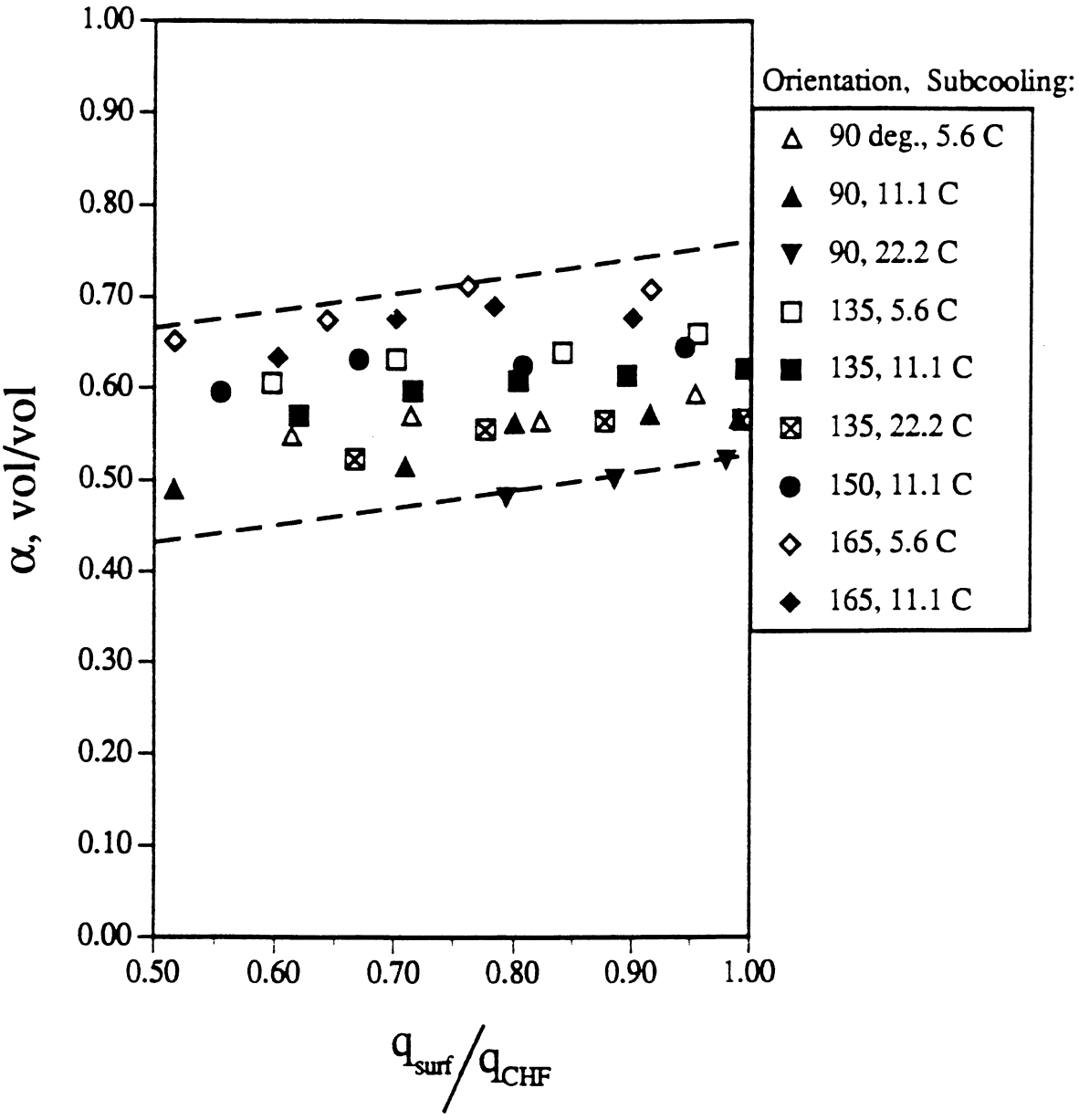

Figure 5.21. The measured mean void fraction as a function of the surface heat flux for a variety of heater surface orientations and subcoolings; U_{bulk} = 4 cm/s.

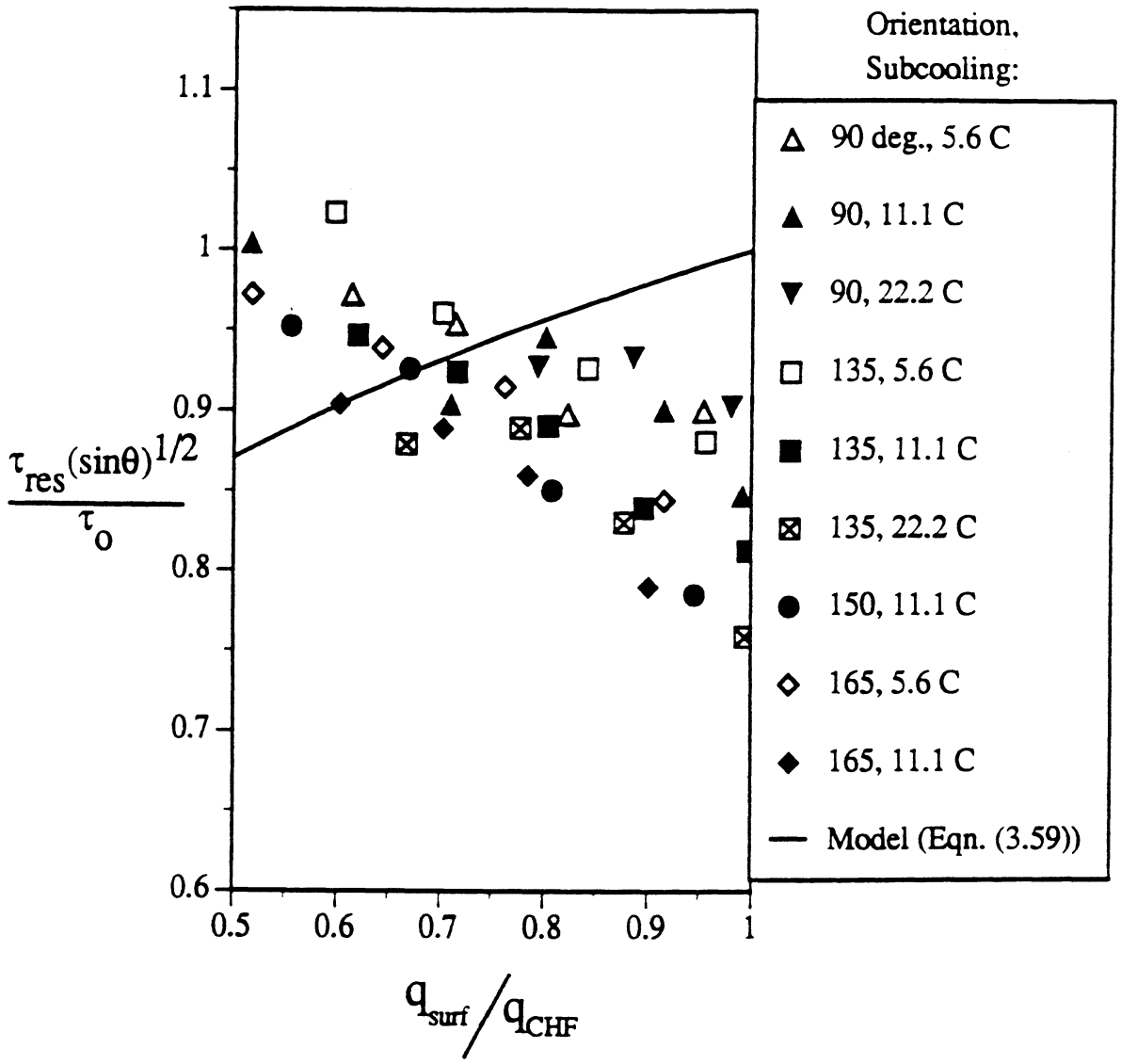

Figure 5.22. The mean bubble residence time as a function of the surface heat flux, shown in non-dimensional form for various heater surface orientations; U_{bulk} = 4 cm/s.

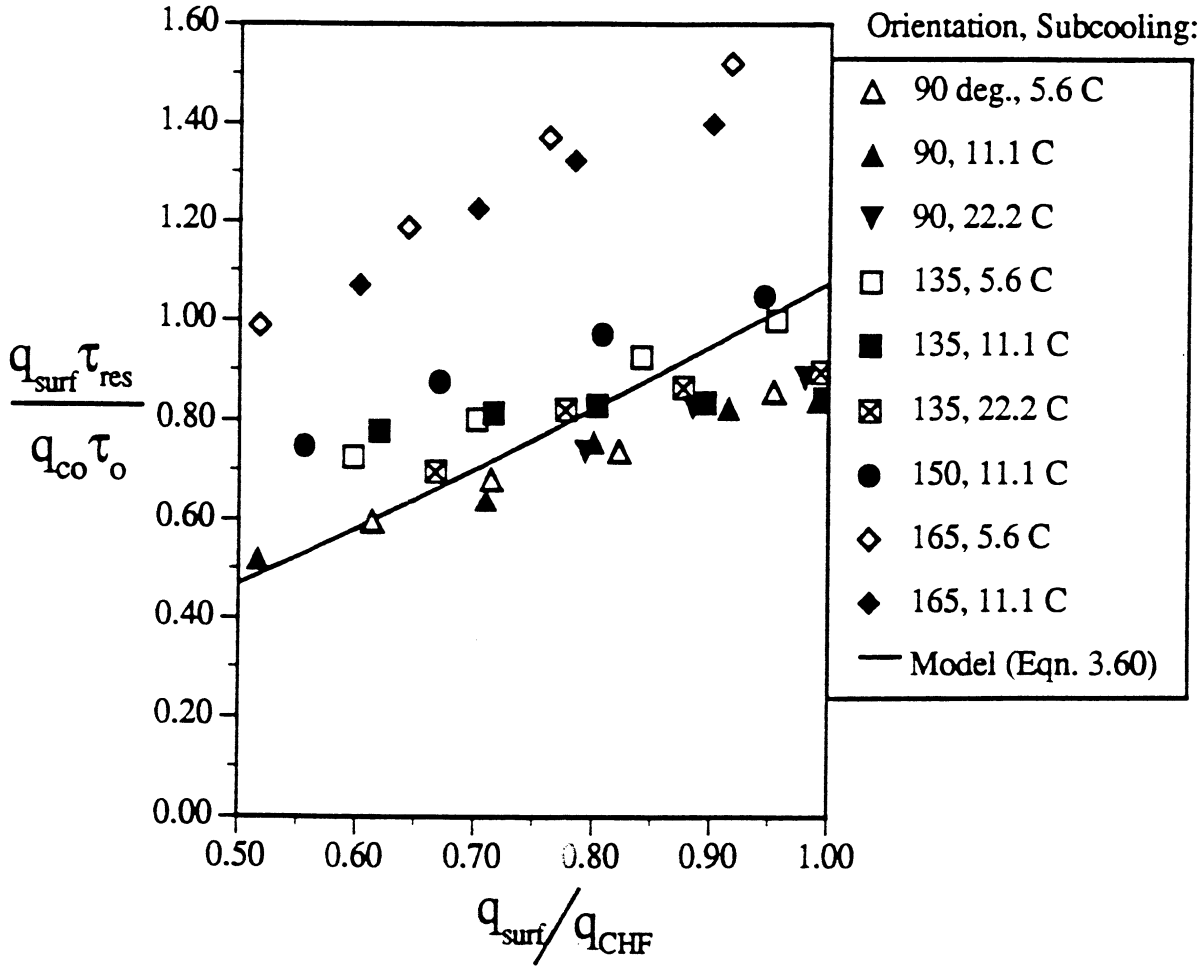

Figure 5.23. The product of the surface heat flux times the bubble residence time as a function of the surface heat flux, shown in non-dimensional form for various heater surface orientations; U_{bulk} = 4 cm/s.

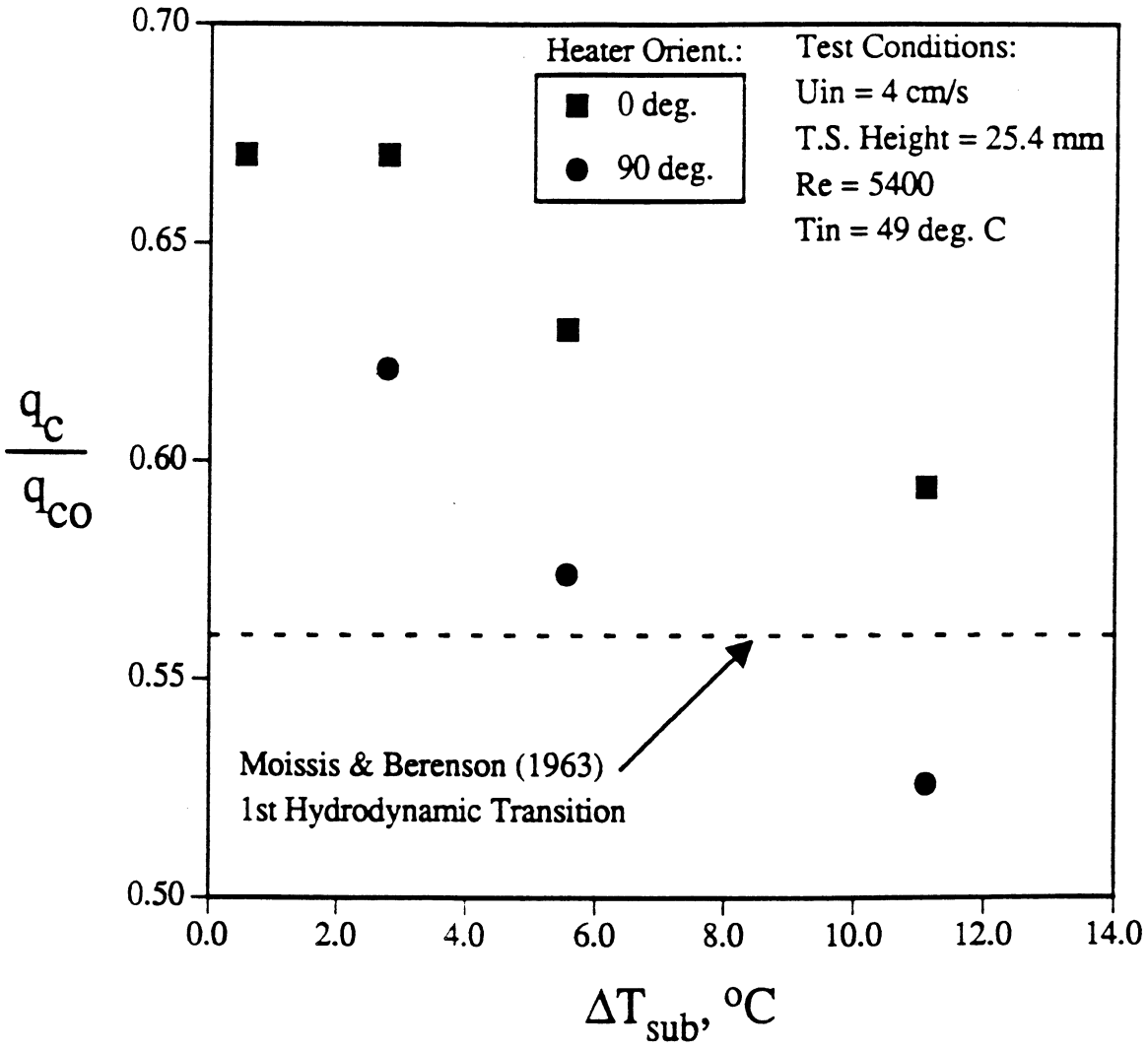

Figure 5.24. The measured CHF for the gold film heaters given for two heater orientations as a function of the subcooling.

Figure 5.25(a) Characteristic bubble sizes above the metal heater surface; θ = 270 deg., U_{bulk} = 32 cm/s, ΔT_{sub} = 11.1 °C, q" = 18.2 W/cm^2 (top view).

Figure 5.25(b) Characteristic bubble sizes above the gold film heater surface; θ = 270 deg., U_{bulk} = 32 cm/s, ΔT_{sub} = 11.1 °C, q" = 13.0 W/cm^2 (view from below).

Figure 5.25. Comparison of boiling over a metal heater surface with a gold film heater surface; θ = 270 deg., U_{bulk} = 32 cm/s, ΔT_{sub} = 11.1 °C.

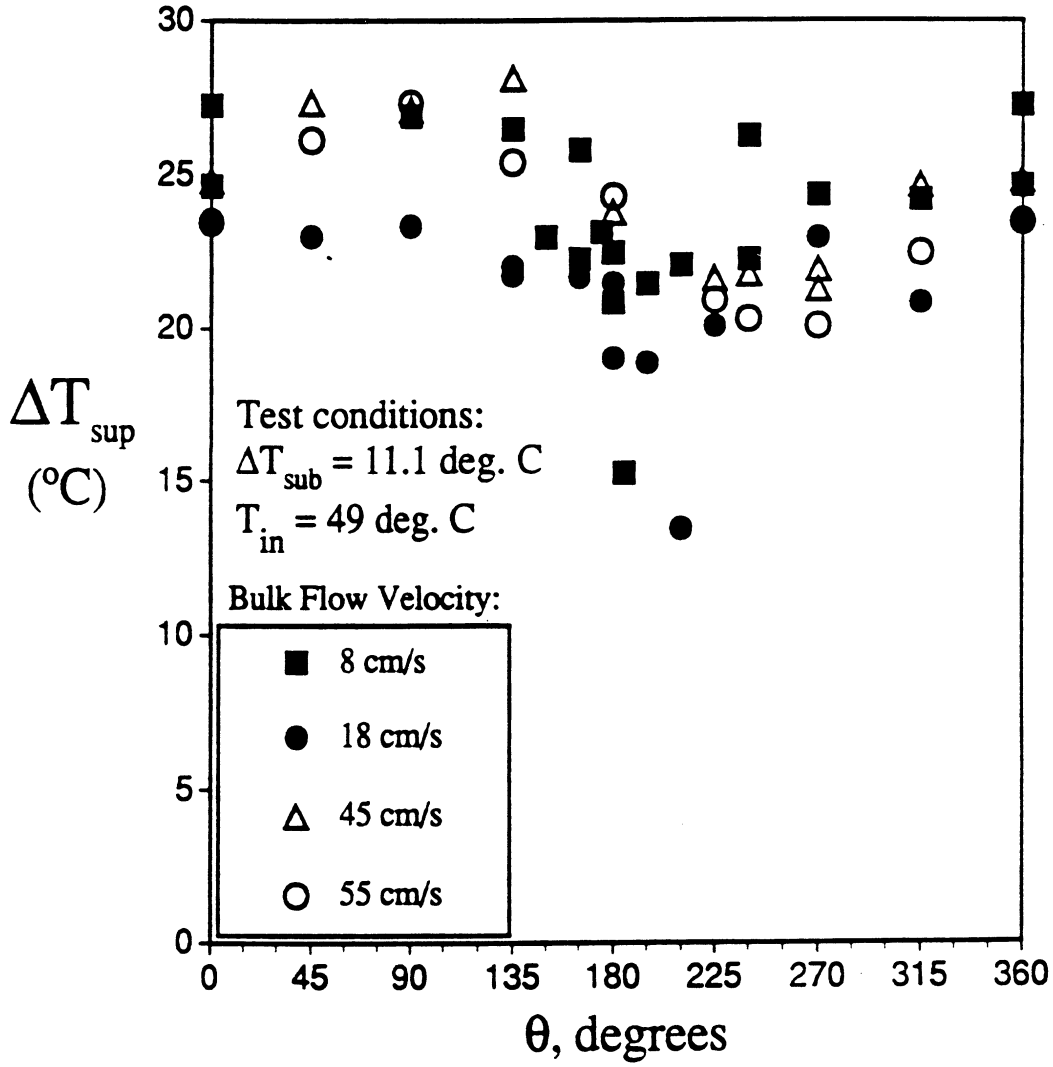

Figure 5.26. The measured surface superheat at CHF as a function of the heater surface orientation for various flow velocities;

ΔT_{sub}= 11.1°C (metal heater surface).

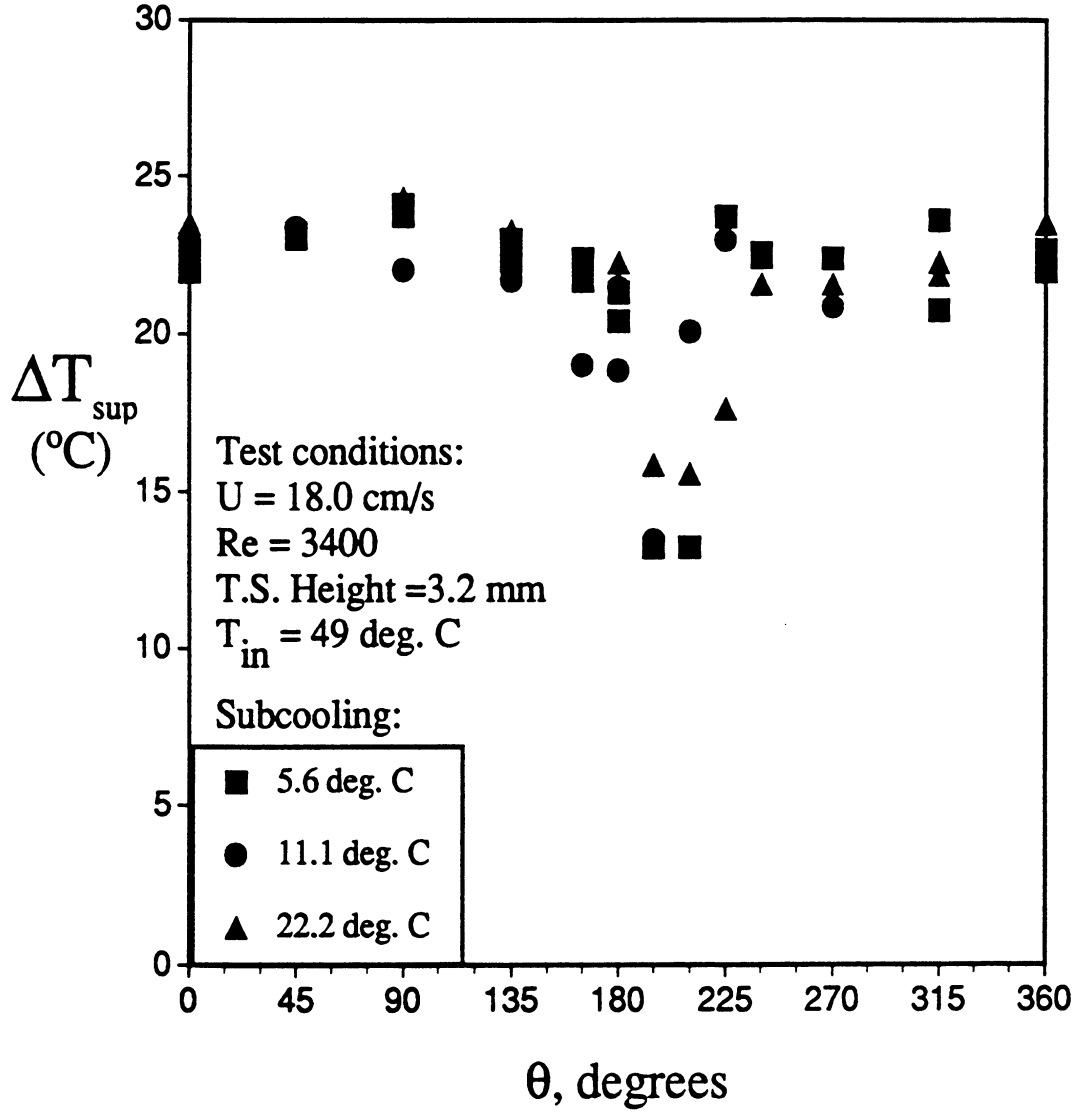

Figure 5.27. The measured surface superheat at CHF as a function of the heater surface orientation for various subcoolings; U_{bulk} = 18cm/s (metal heater surface).

CHAPTER 6

DISCUSSION AND CONCLUSIONS

6.1. The relative effects of flow inertia and buoyancy forces

The FCCHF model in Chapter 3 describes the motion of growing bubbles based on the action of buoyancy, drag and lift forces. The generally good agreement between the CHF measurements and the FCCHF model demonstrated in Chapter 5 suggests that the primary mechanisms of the CHF are therefore governed by these three main forces. The results in Chapter 5 also show that the secondary effects on the CHF resulting from the accumulation of vapor in the test section, not accounted for by the FCCHF model, arise consistently in downflow, where the buoyancy and flow forces nearly balance. At a flow velocity of 18 cm/s, for example, significant departure from the model can be seen in Figure 5.6 in the case of downflow, where the velocity of the vapor induced by buoyancy opposes the direction of the imposed flow. The FCCHF model predictions for the ratio of the buoyancy force parallel to the heater surface to the drag force acting on the vapor bubbles at the moment of departure is given as a function of the heater surface orientation in Figure 6.1 for a flow velocity of 18 cm/s. The small deviations appearing in the curve are attributable to the rather coarse convergence criteria used in the model.

The figure shows that for downflow, the buoyancy force component parallel to the heater surface is similar in magnitude and opposite in sign to the drag force, indicating the tendency of the vapor to stagnate above the heater surface and thus to cause the departure from the CHF model seen in Figure 5.6. Moreover, this near-balance of buoyancy and drag causes the CHF to be particularly sensitive to marginal increases in the drag force in the downflow orientations resulting from the acceleration of the liquid in the test section, which can also be observed in Figure 5.6. The ratio of the buoyancy force component normal to the heater surface to the lift force is shown along the ordinate on the right in Figure 6.1 as a function of orientation. The lift does not exceed the buoyancy holding the vapor to the surface except at orientations close to the vertical downflow position, and otherwise does not play a very substantial role in the vapor removal process at this relatively low flow velocity. The flow forces become more significant as the flow velocity is increased to 32 cm/s, and Figure 6.2 shows that the buoyancy force is generally the same order of magnitude as the drag force. For the upflow orientations, where the buoyancy and drag forces act in the same direction, the residence time of the vapor bubbles is relatively short. In the downflow orientations, on the other hand, where these forces act opposite each other and are roughly the same magnitude, the motion of the vapor above the heater surface is consequently sluggish. This greatly increases the probability of coalescence of the bubbles near the heater surface, resulting in the void recirculation phenomenon described in Chapter 5, which has a considerable effect on the CHF at lower subcoolings. As the flow velocity is increased further to 55 cm/s, the influence of the buoyancy force on the CHF is greatly diminished, as demonstrated in

Figure 5.11 by the relatively small variation in the CHF with orientation. Accordingly, Figure 6.3 shows that the relative influence of the buoyancy compared to the drag and lift forces acting on the bubbles is also small at a flow velocity of 55 cm/s. The ratio of the separate buoyancy force components to the drag and lift forces appear nearly as perfect sine and cosine waves, since the effect of the buoyancy force on the relative velocity between the liquid and vapor phases, and hence on the drag and lift forces, is almost negligible. Figure 6.3 also shows that the FCCHF model predicts a significant effect of the lift force in the processes of vapor removal at the higher flow velocities. Since obtaining the higher flow velocities in the laboratory necessitated the use of the narrow (3.2 mm) test section, the lift force is sometimes counteracted by the reaction of the vapor against the opposite wall of the test section, which causes the departure from the FCCHF model predictions observed in Figures 5.10 and 5.11 in Chapter 5.

The relative effects of buoyancy and flow forces on the CHF are demonstrated in Figure 6.4 through a comparison of the CHF measured for vertical upflow and vertical downflow at various flow velocities. The effects of the flow relative to buoyancy forces are expressed using the parameter ξ, defined in Chapter 5 as the ratio of buoyancy to flow inertia. An apparent transition point separating the inertia-dependent and inertia-independent flow regimes is indicated in Figure 6.4, arising where the bulk flow velocity is equal to the buoyant terminal velocity of bubbles rising in a stagnant medium, given by Harmathy (1960) as:

$$U_\infty = 1.53\sqrt{\frac{g(\rho_l - \rho_v)\sigma}{\rho_l^2}} \tag{6.1}$$

Combining Eqn. (6.1) with Eqn. (5.4), ξ can be expressed in terms of the ratio of the buoyant terminal velocity to the bulk flow velocity as follows:

$$\xi^{\frac{1}{2}} = 0.65\left(\frac{U_\infty}{U_b}\right) \tag{6.2}$$

Therefore, the transition point indicated by the vertical line in Figure 6.4 is the point where the bulk flow velocity overtakes the motion of the vapor induced by buoyancy, and marks the onset of the effects of the bulk flow velocity. For bulk flow velocities less than the buoyant terminal velocity ($\xi^{1/2}>0.65$), the CHF measured for both vertical orientations approaches the prediction for pool boiling over vertical surfaces given by Lienhard and Dhir (1973), indicating little effect of the bulk flow. For bulk flow velocities in the range of the buoyant terminal velocity ($\xi^{1/2}\approx 0.65$), the flow force opposing the buoyancy in the downflow orientation results in a significant decrease in the CHF compared with upflow. For much higher bulk flow velocities ($\xi^{1/2}<<0.65$), the CHF measured for the two vertical orientations converges, as buoyancy effects become almost negligible. As a result, the CHF values approach the predictions by Mudawar and Maddox (1989) for a 12.7 mm square heater surface in vertical upflow of FC-72 with negligible buoyancy effects, given by:

$$\frac{q_c}{q_{co}} = 1.229\xi^{\frac{1}{2}}\left(\frac{\rho_l}{\rho_v}\right)^{0.152}\left(\frac{L_{heat}}{D_H}\right)^{0.043}\left(\frac{\sigma}{\rho_l U_b^2 L_{heat}}\right)^{0.348} \tag{6.3}$$

6.2. The effects of the flow velocity common to all orientations: the correlation of E''

The effects of the flow velocity on the parameter E'', which is a constant for all heater orientations for a given set of flow conditions, were presented in terms of the non-dimensional parameters Φ and Ca in Chapter 3, given by Eqns. (3.51) and (3.54), respectively. A plot of Φ is given in Figure 6.5 as a function of Ca for a variety of flow conditions, evaluated using the values of E'' which yield the best fit to the experimental data presented in Chapter 5. The corresponding values of Ca and Φ correlate with each other approximately according to:

$$\Phi = 0.018Ca^{0.2} \tag{6.4}$$

Given this relationship, the parameter E'' decreases slightly with increasing flow velocity, although the data in Chapter 5 show the CHF generally increasing at the higher flow rates. A contradiction with the experimental data and with other studies of forced convection boiling (e.g., Yilmaz and Westwater, 1980) is avoided, however, since the

increasingly short bubble residence times at the higher flow velocities lowers the value for E''.

The effects of the heater length on E'' were correlated empirically in Eqn. (3.51), yielding a dependence of the CHF on the heater length to the minus-0.4 power. This result is based on data for only two heater lengths, however, both of which are relatively short, on the order of only one to five bubble diameters. The effect of the hydraulic diameter of the test section as predicted by Eqn. (6.4), on the other hand, is so slight as to be negligible. This appears to be corroborated by the comparison of the CHF data in Figure 5.16 for two different test section heights but the same flow velocity and subcooling, notwithstanding the secondary effects of the test section height previously discussed.

6.3. Assessment of the FCCHF model accuracy

Figure 6.6 shows the dimensionless comparison between the measured CHF and the FCCHF model for various bulk flow conditions and heater orientations. When presented in this fashion the data points which deviate most from the model are emphasized, in contrast to the manner in which these same data were presented in Chapter 5. While most of the values fall within the ± 30 % tolerance indicated, a few points, mostly those for downflow conditions, deviate more substantially. This does not significantly diminish the overall accuracy of the model, however, whose RMS error is estimated at ± 10 %.

6.4. Comparison of the FCCHF model results with previous works

Previous studies of the effects of orientation on the CHF exist which demonstrate behavior similar to that shown by the data in Chapter 5, and, likewise, similar to the predictions made by the FCCHF model. A survey of these results is given below.

6.4.1. Previous works in pool boiling

While previous studies of heater orientation effects in pool boiling do not specifically relate to the results presented in Chapter 5, they demonstrate the salient effects of orientation on the CHF in the absence of an imposed flow which are similar to the effects observed at very low flow velocities. Figure 6.7 shows the CHF data for various heater orientations presented in previous works, compared with a pool boiling CHF model presented in an earlier work (Brusstar and Merte, 1994), given by:

$$q_c = \begin{cases} q_{co} & 0^o \le \theta \le 90^o \\ q_{co}|\sin\theta|^{1/2} & 90^o \le \theta \le 270^o \\ q_{co} & 270^o \le \theta \le 360^o \end{cases} \qquad (6.5)$$

This is nearly equivalent to the forced convection CHF model in the limit of no imposed flow velocity. The data generally follow the trends observed in forced convection at low

flow velocities demonstrated in Figures 5.2 and 5.3, except in the horizontal down position. While the model predicts the CHF in the horizontal down position to be close to zero, the measured CHF results reported by Guo and El-Genk (1992) and Ishigai, et al. (1961) for saturated water, and by Merte (1990) for saturated LN_2 and LH_2 ranged from about 0.15-0.60 of the pool boiling CHF for horizontal upward facing surfaces. In each of these cases, however, the experimental configurations permitted an escape path for the vapor about the heater surface periphery, which gave results considerably higher than what would otherwise be expected for an infinite flat plate. Indeed, Ishigai, et al. (1961) varied the size of the heated surface relative to the unheated peripheral area and determined that the CHF decreased as the heater surface became proportionately smaller. At the other heater orientations, the data by Guo and El-Genk (1992) depart from the model at higher measured CHF levels, likely due to the transient quenching process used to measure the CHF. The results of Vishnev, et al. (1976) for steady heating of LH_2 also show significant departure from the model predictions in the downward-facing domain, although the accuracy of these measurements is difficult to assess from the information reported.

6.4.2. Previous works in forced convection boiling

Relatively few studies of the effects of heater orientation on the CHF forced convection boiling exist which may be compared with the results at low flow velocities given in Chapter 5. Among the few comparable studies, most examine the difference in

the CHF between the cases of vertical upflow and downflow, making observations similar to those noted in the previous chapter. Papell (1967), in a study of the effects of upflow and downflow on the CHF of saturated LN_2 in vertical heated tubes, found the CHF at relatively low flow velocities to be substantially reduced in downflow due to the stagnation of the vapor in the vicinity of the heater surface. An earlier photographic study of the CHF in vertical upflow and downflow by Simoneau and Simon (1966) confirms this observation. In Table 6.1, the CHF measurements by Papell (1967) at flow velocities of 30.5 cm/s and 61.0 cm/s are compared with the predictions of the FCCHF model, with a single value of E'' adjusted suitably to best fit the data. The CHF measured in the vertical downflow orientation is somewhat lower than the model predictions, likely as a result of the relatively long length to diameter ratio of the heated tube (1.3 cm dia. by 30.5 cm long). The results for upflow and downflow in Table 6.1 are nonetheless consistent with those obtained for R113 in Figures 5.8 and 5.11 for similar values of ξ, approximately equivalent to flow velocities of 32 cm/s and 55 cm/s. Other studies of upflow and downflow on the CHF include Mishima and Nishihara (1985) for the boiling of saturated water in a rectangular channel. While the results reported in the study are qualitatively similar to those given in other works, the flooding in the test section during the downflow tests prevented adequate control over the bulk flow velocity, and therefore no meaningful comparison can be made with the FCCHF model.

A more comprehensive study of the effects of heater orientation on the CHF in forced convection boiling was performed by Gersey and Mudawar (1992, 1993) for an in-line array of small heater surfaces with FC-72 as the working fluid. The minimum CHF

measured among the nine heater surfaces in the array is compared with the FCCHF model in Figure 6.8 for a flow velocity of 13 cm/s and a subcooling of 36 °C. The predicted behavior is similar to that observed for R113 in Figures 5.6 and 5.16 for flow velocities of 18 cm/s and 12.5 cm/s, respectively, due to the correspondingly similar value of ξ (ξ = 0.47) under these conditions. The minimum CHF measured for a flow velocity of 50 cm/s (ξ = 0.03) and 36 °C subcooling are compared with the FCCHF model predictions in Figure 6.9. While the model successfully predicts the qualitative trends in the CHF, the deviations from the model predictions are far greater than those observed in Figure 5.11 for similar flow conditions (U_{bulk} = 55 cm/s, ξ = 0.03). The departure from the model predictions observed in Figures 6.8 and 6.9 stem from the relatively small flow channel cross sectional area (20 mm by 5 mm) used by Gersey and Mudawar (1992, 1993). Under circumstances of downflow, the coalescence of vapor reportedly resulted in phase stratification and the appearance of elongated bubbles several centimeters in length in the test section. Further, the minimum CHF occurred at various positions in the heater array for different flow conditions, and it is uncertain how the CHF for a single chip in the array would behave. At the higher levels of subcooling, however, such as that shown in Figures 6.8 and 6.9, Gersey and Mudawar (1993) noted that the differences in the CHF between the different heater surfaces were relatively small, and the agreement between the FCCHF model and the data is therefore somewhat better than would otherwise be expected.

6.5. The role of the large bubbles in the CHF mechanisms

The motion of the large bubbles is the focus of the FCCHF model, since previous experimental studies of the CHF (Katto and Yokoya, 1968) have indicated the importance of the large bubbles in determining the CHF. First, while resident on the heater surface, these large bubbles obstruct the flow of liquid to the surface necessary to sustain the relatively high rates of evaporation. An exaggerated example of this effect can be seen in Figure 5.15 in the high-speed photographs of a large coalesced vapor slug hovering above the heater surface in the test section. Second, even in the absence of confining test section geometry, large bubbles still significantly influence the onset of CHF due to their role in the formation of dry spots on the surface, as was observed in the photographic study of boiling at high heat fluxes by Kirby and Westwater (1965). In the photographs of a heater surface from below during pool boiling of water at high heat flux, the growth of the large bubbles was observed to be somewhat different from the smaller ones, forming as a result of the evaporation of a thin liquid layer existing beneath the bubbles adjacent to the heater surface. The large bubbles were found to be responsible for the majority of the dry areas on the heater surface due to the evaporation of the liquid on the relatively large surface area they occupy, and hence play a more significant role in the mechanisms of dryout.

In previous studies characterizing the departure frequency of bubbles on a heater surface (Jakob, 1958; McFadden and Grassman, 1962), the larger bubbles are generally found to depart at a lower frequency, and therefore have longer residence times on the

heater surface. Jakob (1958) observed from bubbles leaving individual nucleation sites that the bubble frequency was inversely proportional to the bubble diameter. McFadden and Grassman (1962) used a dimensional analysis to correlate experimental data for water and other fluids, modifying Jakob's (1958) result to obtain:

$$f = \frac{const.}{D_b^{1/2}} \tag{6.6}$$

for a given set of conditions in pool boiling. Similar to the predictions of the FCCHF model, these models essentially suggest that among the various sizes of bubbles forming on the surface, the larger bubbles have correspondingly lower departure frequencies. The FCCHF model, however, assumes that the bubble sizes increase with increasing heat flux level, which may not actually be the case. The bubble frequency measurements in Figure 5.20 show that the large bubbles depart more frequently with increasing heat flux, but visual observations, along with the void fraction measurements in Figure 5.21 imply that the bubble size does not increase at the same rate. As a result, the measured bubble residence times in Figure 5.22 decrease slightly with increasing heat flux, contrary to the results of the FCCHF model. Despite this discrepancy, the model still appears to predict the behavior of the larger bubbles reasonably accurately. The significance of predicting the motion of the larger bubbles is demonstrated by the inverse relationship between the bubble residence time and the CHF first observed qualitatively by Katto and Yokoya (1968) and then by measurement of the bubble residence time at the CHF given in Figure 5.5. The slower, larger bubbles set the upper limit to the rate of vapor removal from the

surface, while simultaneously restricting the rate of inflow of the liquid from the bulk region, and thereby play a dominant role in establishing the CHF.

6.6. The effect of subcooling on the CHF

The effects of subcooling exhibited by the data in Chapter 5 can be attributed to two different mechanisms. Zuber et al. (1961) modeled the effect by considering the condensation of the vapor into the surrounding liquid as it leaves the heated surface. Kutateladze (1963) developed instead a correlation similar to Eqn. (5.1) based on the amount of sensible energy required to bring the liquid on the surface to the saturated state. Regardless of whether the vapor is produced and then quickly condensed, or whether more energy is required to produce the vapor, the net effect of the subcooling on the volumetric rate of vapor generation at the heater surface would be the same as that observed in Figure 5.14, where the rate of vapor generation was found to be nearly independent of the subcooling. On the other hand, the measurements of the void fraction at the wall in Figure 5.13 show that very close to the heater surface, the relative concentration of the liquid and vapor phases at the CHF are also the same for the different subcooling levels, indicating similar rates of vapor production at the surface. This suggests that the primary effect of subcooling is to suppress the rate of evaporation, and thus there is reasonable correlation with Eqn. (5.1), which is based on this principle. Moreover, the suppression of vapor production at the surface may be further enhanced with the longer heater dimension in the direction of flow, since the secondary flow per

unit length from the sides of the heater surface inward should be increased. As a result, the effects of the heater length on the CHF are not as pronounced at the higher levels of subcooling.

The secondary effects of subcooling identified in Chapter 5 arise increasingly as the rate of condensation into the bulk liquid is reduced at lower subcoolings. The effects of vapor recirculation are reduced drastically at high levels of subcooling, since the vapor departing the heater surface condenses rapidly into the bulk liquid. Also, the interference of the test section walls with the departure of the vapor at higher flow velocities is reduced with increasing subcoolings, as can be seen in Figures 5.10 and 5.11 for flow velocities of 45 cm/s and 55 cm/s. Since most of the condensation of the vapor occurs on the top of the bubbles, the height of the bubbles is smaller at higher subcoolings, yielding additional clearance between the bubble and the opposite wall of the test section and alleviating the interference.

6.7. The significance of the surface superheat to the CHF

Figure 5.27 demonstrated that the heater surface superheat at the CHF was largely independent of subcooling. Also, the results presented in Figures 5.26 showed the surface superheat to vary by a relatively small amount over a wide range of CHF levels at the higher flow velocities, and by a greater amount at the lower flow velocities. At the higher flow velocities, where the force ratios in Figures 6.2 and 6.3 demonstrate that the departure of the vapor is governed by flow forces in a manner common to all orientations,

the surface superheat does not vary greatly with orientation. At lower flow velocities, where the bubbles depart the surface freely under buoyancy at some orientations, and slide along the heater surface at others, the variation in the superheat with orientation is substantial. A discussion of these observed effects is given below.

While most models of the CHF assume the latent heat transport to dominate the heat transfer at high heat fluxes (Haramura and Katto, 1983; Zuber, 1958), the model presented in Chapter 3 assumes that the latent heat transport comprises a net fraction of a mere 20 to 30 percent of the total heat flux, based on measurements presented in Appendix F. Although this assumption, expressed in Eqn. (3.31), appears to adequately describe the net rate of vapor production, it lends no insight into the actual heat transfer mechanisms at the superheated surface that bring this about. A description of the relationship between the heater surface superheat and the surface heat flux at high heat flux levels has been attempted by several authors, although these invariably assume that all of the energy leaving the heater surface eventually goes into evaporation. Bhat, et al. (1983a), Pasamehmetoglu, et al. (1990) and Dhir and Tung (1988) assume unsteady conduction from an isothermal heater surface into an adjacent thin liquid macrolayer. An illustration comparing the assumed behavior of the liquid and vapor for these macrolayer evaporation models with a representation of the actual behavior observed in Chapter 5 is given in Figure 6.10. The macrolayer models assume that all heat transfer takes place through a uniform, thin liquid film on the surface, at a rate estimated by:

$$q_{surf} \cong k \frac{\left(T_{wall} - T_{sat}\right)}{\delta(t)} \tag{6.7}$$

which neglects real effects such as the localized dry areas and the wetting angle, β, at the triple interface. The predicted surface superheat for a given heat flux based on the macrolayer theory therefore relies heavily on the assumed liquid layer thickness, δ. Although many attempts have been made to measure δ (Bhat, et al., 1983b; Rajvanshi, et al., 1992), this is not realistically possible, since δ does not correspond to any physical quantity, but instead represents the net effect of a number of different modes of heat transfer acting together. Therefore, while the macrolayer evaporation models can be adjusted suitably to predict individual cases, the actual heat transfer modes must be considered to predict the relationship between the surface heat flux and superheat in the general case.

The surface superheat for an isothermal heater surface is the combined result of three primary interdependent (therefore non-superimposable) heat transfer modes illustrated in Figure 6.10(b):

1. Conduction heat transfer to the thin liquid regions
2. Convection to the dry areas on the heater
3. Convection to the liquid outside of the thin film regions.

The first of these modes is a highly efficient means of transferring large amounts of heat at relatively low levels of superheat (Bankoff, 1990), while the remaining two are comparatively poor at transporting heat energy from the surface. As a result, the heat transfer to the thin liquid regions dominates the overall heat transfer coefficient. During the transient growth of a single bubble on the heater surface, where the thin liquid regions

evaporate to give rise to dry spots, the relative significance of these basic heat transfer modes changes. With many bubbles at various stages of growth covering the heater surface, the surface superheat therefore represents the statistical average of the local behavior of individual bubbles.

The thin liquid film regions on the heater surface are established beneath the bubbles by the wetting angle, β, as illustrated in Figure 6.10(b). Assuming the upper surface of the thin films to be in thermal equilibrium with the vapor inside the bubble, and further assuming one-dimensionality, the local rate of heat conduction from the superheated wall into the film is approximately determined by the local thickness of the film as:

$$q_{local} \approx k \frac{(T_{wall} - T_{sat})}{\delta_{local}} \tag{6.8}$$

Factors affecting the wetting angle, including the heater surface orientation and the flow velocity, will therefore affect the rate of evaporation heat transfer and hence the average surface superheat. The effects of the wetting angle on heat transfer beneath bubbles sliding over a heater surface was calculated by Tsung-Chang and Bankoff (1990), yielding approximately a twofold enhancement in the latent heat transport compared with a static bubble growing on the surface. The effects of this enhancement can be seen in the downward facing heater orientations at lower flow velocities, where the larger, flattened bubbles sliding on the heater surface provide an increase in the thin film area, as illustrated in Figure 6.11(a). This enhancement in the thin film area explains the increase

in the measured value of E'' in Figure 5.23 for U_{bulk} = 4 cm/s and a heater orientation of θ = 165 deg., since a greater amount of liquid must be evaporated in this configuration during the bubble residence time to produce a dry spot on the heater surface of sufficient size to trigger the CHF. It further explains the increase in the measured values of the latent heat fraction, χ, presented in Appendix F for the same flow velocity and heater orientation, which are substantially higher than the average value measured for the other heater orientations. The net effect of the increase in latent heat transport is also observed in Figures 5.26 and 5.27 for U_{bulk} = 18 cm/s in the downward facing orientations, where the prevalence of the more efficient evaporation heat transfer beneath the sliding bubbles decreases the average surface superheat. Conversely, at the higher flow rates, the lift force acting on the vapor increases its contact angle with the surface and thereby reduces the enhancement in latent heat transport of the sliding bubbles, as illustrated in Figure 6.11(b). As a result, the rate of latent heat transport varies little with orientation, and therefore the measured surface superheat for the higher flow velocities shown in Figure 5.26 is nearly independent of orientation. In addition the rate of evaporation on the heater surface at the CHF is a strong function of the liquid subcooling, as was discussed earlier. The decrease in the latent heat fraction, χ, with increasing subcooling estimated by Eqn. (3.31), combined with the corresponding increase in the CHF, is offset by the change in the saturation temperature of the bulk liquid. As a result, the measured superheat values in Figure 5.27 appear to be independent of subcooling.

As the thin liquid film regions are depleted through evaporation, dry areas form on the heater surface, which greatly diminish the local rate of heat transfer due to the

relatively poor transport properties of the vapor. Previous studies of boiling at high heat flux levels near the CHF (Torikai, et al., 1991; Dhuga and Winterton, 1985) have clearly demonstrated the existence of dry spots in significant proportion to the total heater surface area on the heater surface at heat flux levels approaching the CHF. In the present study, the measurements of the void fraction extrapolated to the heater surface in Figure 5.13 show that nearly one half of the metal heater surface was dry at the onset of the CHF. The formation of dry spots explains the reduction in the CHF observed for the gold film on quartz heater surface seen in Figure 5.24. While the smaller, sparser bubbles on the gold film surface seen in Figure 5.25 likely indicate that a smaller portion of the surface is dry compared with that observed beneath the large bubbles on the metal heater, the CHF is significantly lower for the gold film heater due to inability of the quartz substrate material to attenuate the temperature fluctuations beneath a localized dry area through thermal diffusion. Carvalho and Bergles (1992) demonstrated the effects of the heater surface material on the CHF, correlating the measured CHF values with the heater material property $\sqrt{k\rho c}$, based on the solution of the transient heat diffusion equation for the portion of the heater temporarily covered by a vapor patch. For the gold film on quartz heater surface, whose $\sqrt{k\rho c}$ value is nearly two orders of magnitude smaller than that of the copper heater surface, the CHF is a function primarily of the local transient evaporation and dryout processes, since the thermal diffusion properties of the quartz substrate are such that a uniform surface temperature is not maintained during these processes. The local formation of dry patches is not as important in determining the CHF

for the metal heater surfaces, but detracts substantially from the spatially-averaged heat transfer coefficient, and hence tends to raise the surface superheat.

The single phase convection to the liquid outside of the thin liquid regions partly determines the net rate of evaporation from the heater surface, since the superheat energy contained in the liquid is used in the evaporation occurring at the liquid-vapor interface. The primary mechanism of single phase convection is probably the microconvective "pumping" action of bubbles leaving the surface postulated by Engelberg-Forster and Greif (1959), combined with the action of the sliding bubbles in stripping the thermal layer, observed by Tong, et al. (1988). While the significance of these single phase modes diminishes in importance at higher levels of heat flux, they play a key role in sustaining the change of phase on the surface, and therefore can have a significant indirect effect on the surface superheat.

6.8. Predictions of the CHF in microgravity

The CHF in microgravity predicted by the FCCHF model modified according to section 3.5 in Chapter 3 is compared with the CHF measured for vertical upflow under 1g in Figure 6.12 at various bulk flow velocities. Vertical upflow is similar to forced convection in microgravity in that the lift force is the only external force on the vapor acting normal to the heater surface in both cases, and at flow velocities exceeding the buoyant terminal velocity in vertical upflow, the drag force also acts in the direction of the imposed flow. As a result, the CHF predicted for microgravity at higher flow

velocities approaches that measured for vertical upflow. In contrast, the predicted CHF in microgravity is much lower than in vertical upflow for flow velocities lower than the buoyant terminal velocity under 1g, since the flow forces acting by themselves are not as effective as buoyancy in removing the vapor from the heater surface. The microgravity predictions are also compared in Figure 6.12 with the correlation by Mudawar and Maddox (1989) given in Eqn. (6.3) above, rewritten as follows:

$$\frac{q_c}{q_{co}} = 0.161 \frac{\rho_v h_{fg} U_b}{q_z|_{1G}} \left(\frac{\rho_l}{\rho_v}\right)^{0.652} \left(\frac{L_{heat}}{D_H}\right)^{0.043} \left(\frac{\sigma}{\rho_l U_b^2 L_{heat}}\right)^{0.348} \tag{6.9}$$

The accuracy of the FCCHF model predictions for microgravity is uncertain at this point, given the absence of any experimental data, although the results appear to be reasonable when compared with the vertical upflow data at high flow velocities and with the buoyancy-independent correlation for forced convection boiling given above.

The differences in behavior observed between microgravity and 1g at high heat flux levels are noteworthy. In pool boiling in microgravity, Merte, et al. (1994) showed that dryout occurred over a substantial fraction of the heater surface at low heat flux levels immediately on boiling inception; the change of phase was sustained without a large surface temperature excursion during the relatively short tests of the space flight experiments up to this point, likely as a result of the substantial thin liquid film regions existing at the periphery of the dry areas. Also, Balasubramaniam (1987) predicted a significant effect of thermocapillary forces on the motion of bubbles in the presence of an

imposed temperature gradient in the absence of buoyancy. With flow boiling in microgravity, however, the molecular transport within the bubbles will tend to reduce the temperature gradient over the bubble surface, as will the agitation and turbulent mixing in the liquid surrounding the bubbles. The thermocapillary effects may further be reduced due to the relatively large size of the bubbles, which reduces the magnitude of the surface tension gradient tangent to the bubble surface. While conjectural, the differences in the heat transfer mechanisms between 1g and microgravity must somehow be accounted for in order to improve the first-order CHF predictions given here.

6.9. Conclusions

1. The success of the forced convection CHF model in correlating the experimental data confirms the importance of the buoyancy, drag and lift forces in the vapor removal processes. The rate of vapor removal, in turn, determines the CHF through the inverse relationship between the bubble residence time and the CHF. This relationship between the bubble residence time and the CHF was measured at low flow velocities, and was successfully applied to higher flow velocities in the FCCHF model. The relationship suggests that a constant quantity of energy leaves the heater surface during the bubble residence time, which triggers the onset of the CHF.

2. As may be expected, the dependence of the CHF on the heater surface orientation diminishes with increasing flow velocity. A dimensionless parameter, ξ, was

introduced to describe the effect of the buoyancy force relative to the inertia of the imposed flow, and showed a transition from inertia-independent and inertia-dependent regimes at the point where the bulk flow velocity reaches the buoyant terminal velocity of the vapor, at $\xi = 0.43$. For lower flow velocities ($\xi > 0.43$), the CHF is close to that expected for pool boiling. As the flow velocity increases, the relative influence of buoyancy decreases, and the CHF eventually becomes independent of heater orientation, and for $\xi = 0.03$ corresponding to $U_{bulk} = 55$ cm/s, the CHF varied by only ± 20 % with orientation.

3. The primary effect of the bulk liquid subcooling is to suppress the rate of vapor generation at the heater surface by increasing the amount of energy necessary to bring the liquid on the surface to the saturated state. Secondary effects of the subcooling result from the rate of condensation of the vapor leaving the heater surface into the bulk liquid; at lower levels of subcooling, where the rate of condensation is lowered, the effects of void recirculation, interference of the test section walls and acceleration of the bulk liquid generally influence the CHF adversely, and vice-versa.

4. The large bubbles which form at high levels of heat flux play a significant role in determining the CHF, primarily since they occupy a relatively large portion of the heater surface area and have relatively long growth periods. The FCCHF model, which relates the motion of the large bubbles to the CHF, successfully predicts the CHF under most flow conditions.

5. The heater surface superheat, which represents the combined effects of evaporation, dryout, and single phase convection, varies with the heater surface orientation, although not to the same extent as does the CHF. The variation in the superheat with the heater surface orientation is attributable primarily to changes in the rate of latent heat transport, and diminishes with increasing flow velocity.

6. The CHF predicted for forced convection in microgravity is comparable to that for vertical upflow under 1g for bulk flow velocities exceeding the buoyant terminal velocity of the vapor in pool boiling. For low flow velocities, however, the CHF for microgravity is generally much lower than in the presence of buoyancy, as the flow forces acting on the vapor are rather unsubstantial.

6.10. Recommendations for future study

The next anticipated phase of the forced convection boiling program is testing in microgravity. In order to define the scope and magnitude of the tests effectively, a better understanding of the primary forces and dominant heat transfer mechanisms which likely will be present in microgravity must be obtained through testing in the laboratory under 1g . Further studies should include the following:

1. A study to determine the relationship between the surface superheat and the surface heat flux near the CHF. This would entail studying the relative contributions of the various modes of heat transfer discussed above in section 6.7. Also, the factors affecting the thickness of the thin liquid regions, including the buoyancy and flow forces, should be studied. A generalized method of predicting the dry area fraction has been proposed by Liaw and Dhir (1989) based on the wetting angle of bubbles forming on the surface. Combining this model with the effects of the wetting angle in determining the thickness of the thin liquid regions, the surface superheat can possibly be determined explicitly. Aside from a few studies (Jawurek, 1969; Voutsinos and Judd, 1975), little work has been devoted to examining the transient thickness of the liquid layer beneath growing bubbles, despite its importance to the heat transfer in boiling at high levels of heat flux. Combined with the equations of motion for the vapor and liquid phases used successfully in the FCCHF model in the present work, a relationship between the surface superheat and the CHF would lend explicit closure in lieu of the more empirical methods currently used.

2. A more detailed study of the effects of the heater surface material on the CHF, as it can lend further insight into the nature of the local behavior of the CHF. This should include measurements of the local dry area fraction, either photographically, through local surface temperature measurements or with a localized void fraction probe, accompanied by a study of the rewetting process. The localized behavior, including the transient conduction in the solid heater substrate material, can then be integrated to predict the

global behavior of the surface temperature, and is essential to a model of the surface superheat at high levels of heat flux.

The studies identified above not only would lend insight into the behavior of the CHF in microgravity, but would also enhance the understanding of the mechanisms of the CHF at 1g.

U_{bulk} (cm/s)	ξ (-)	CHF (vertical upflow) (W/cm^2)		CHF (vert. downflow) (W/cm^2)	
		Measured	Predicted	Measured	Predicted
30.5	0.11	20.4	20.4	10.6	12.5
61.0	0.03	21.3	21.0	14.7	17.6

Table 6.1. Comparison of the CHF obtained by Papell (1967) with the FCCHF model.

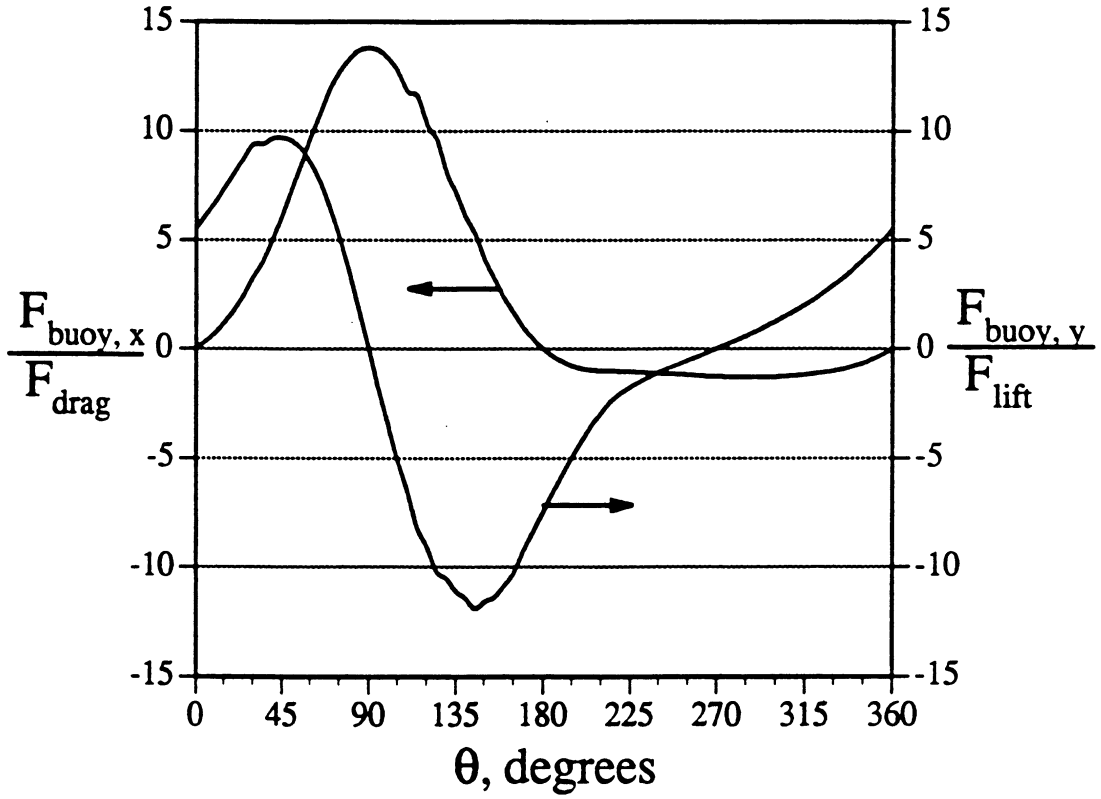

Figure 6.1. FCCHF model predictions for the ratio of the buoyancy force components parallel and normal to the heater surface acting on a bubble at departure compared with the respective drag and lift forces; U_{Bulk}=18cm/s

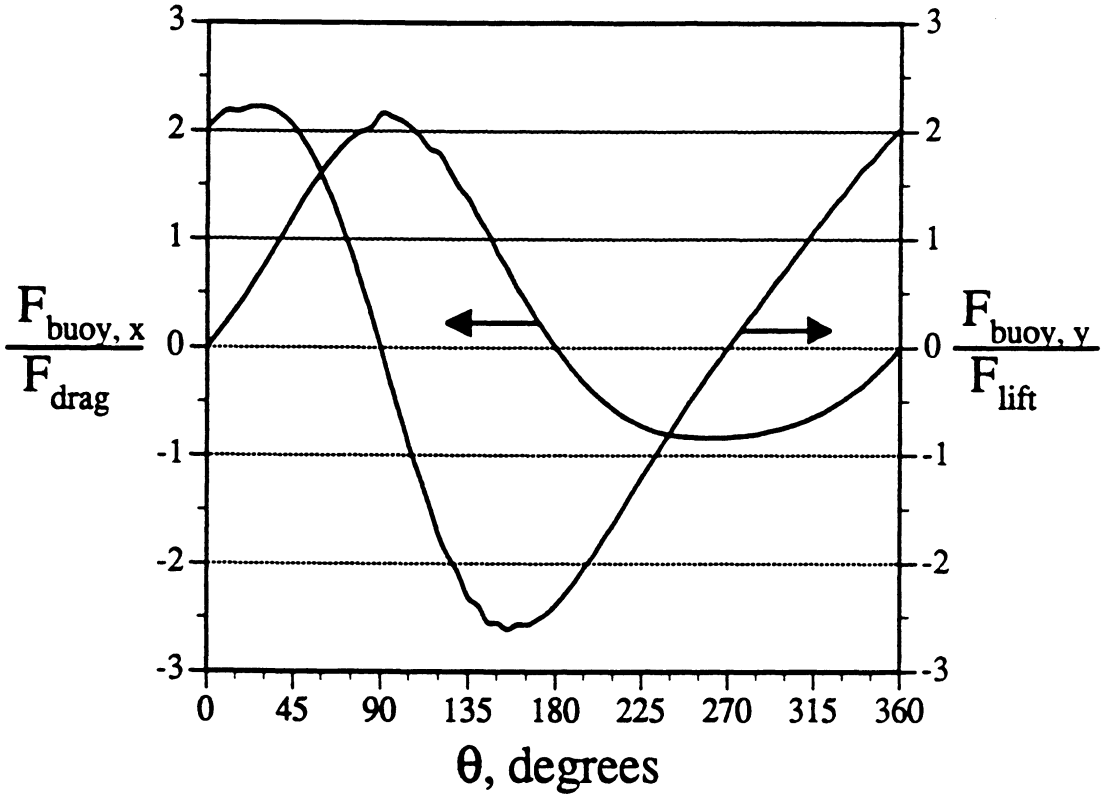

Figure 6.2. FCCHF model predictions for the ratio of the buoyancy force components parallel and normal to the heater surface acting on a bubble at departure compared with the respective drag and lift forces; U_{Bulk}=32cm/s

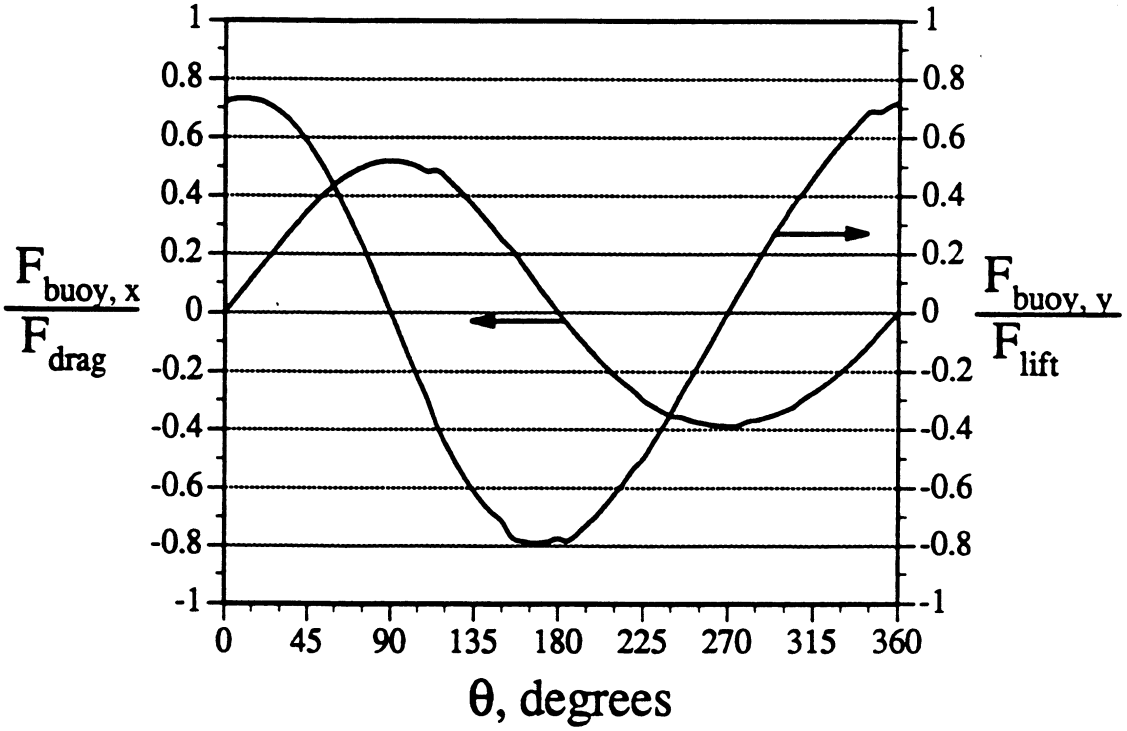

Figure 6.3. FCCHF model predictions for the ratio of the buoyancy force components parallel and normal to the heater surface acting on a bubble at departure compared with the respective drag and lift forces; U_{Bulk}=55cm/s

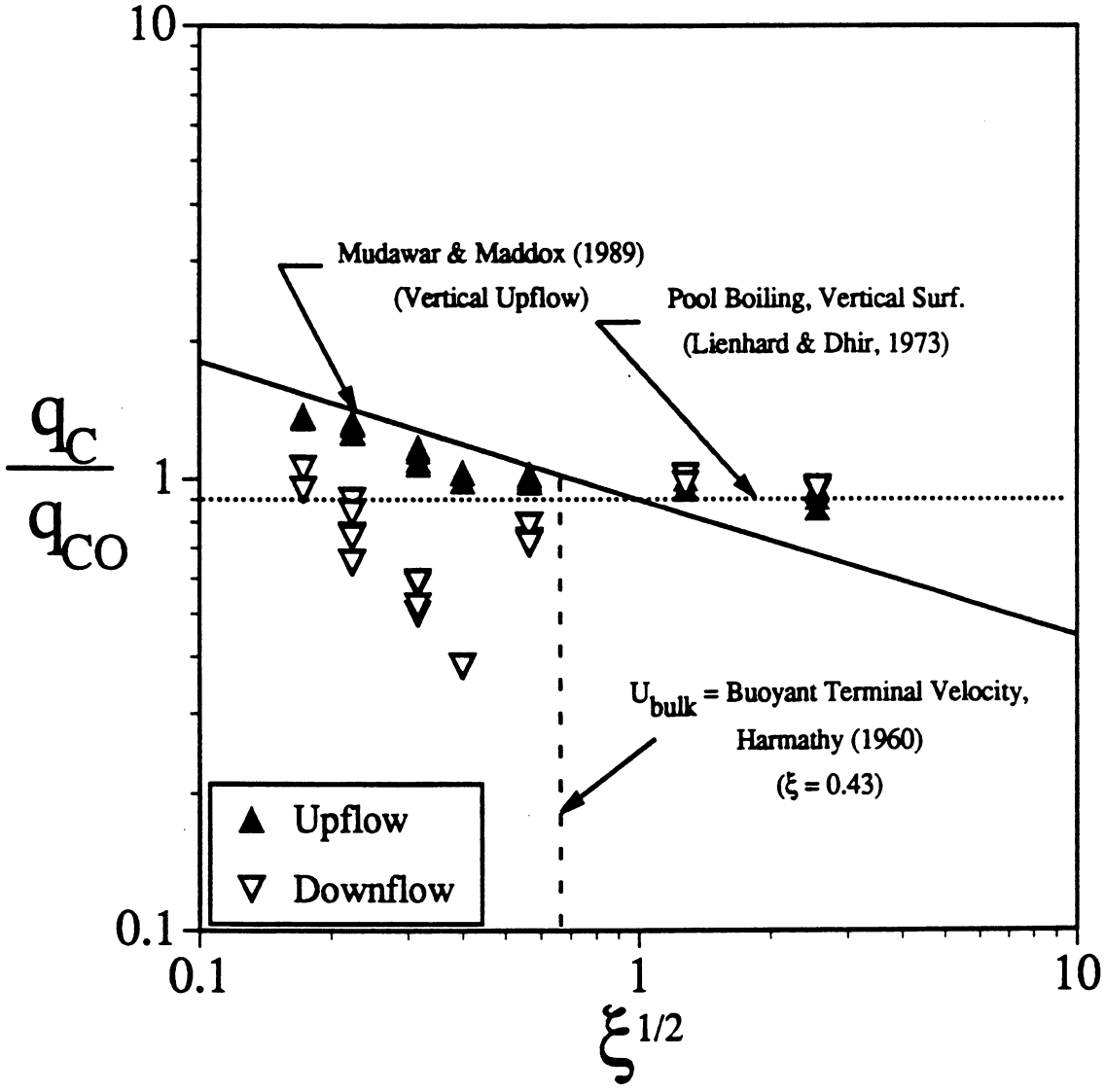

Figure 6.4. Relative effects of buoyancy and flow inertia on the CHF for vertical upflow and downflow

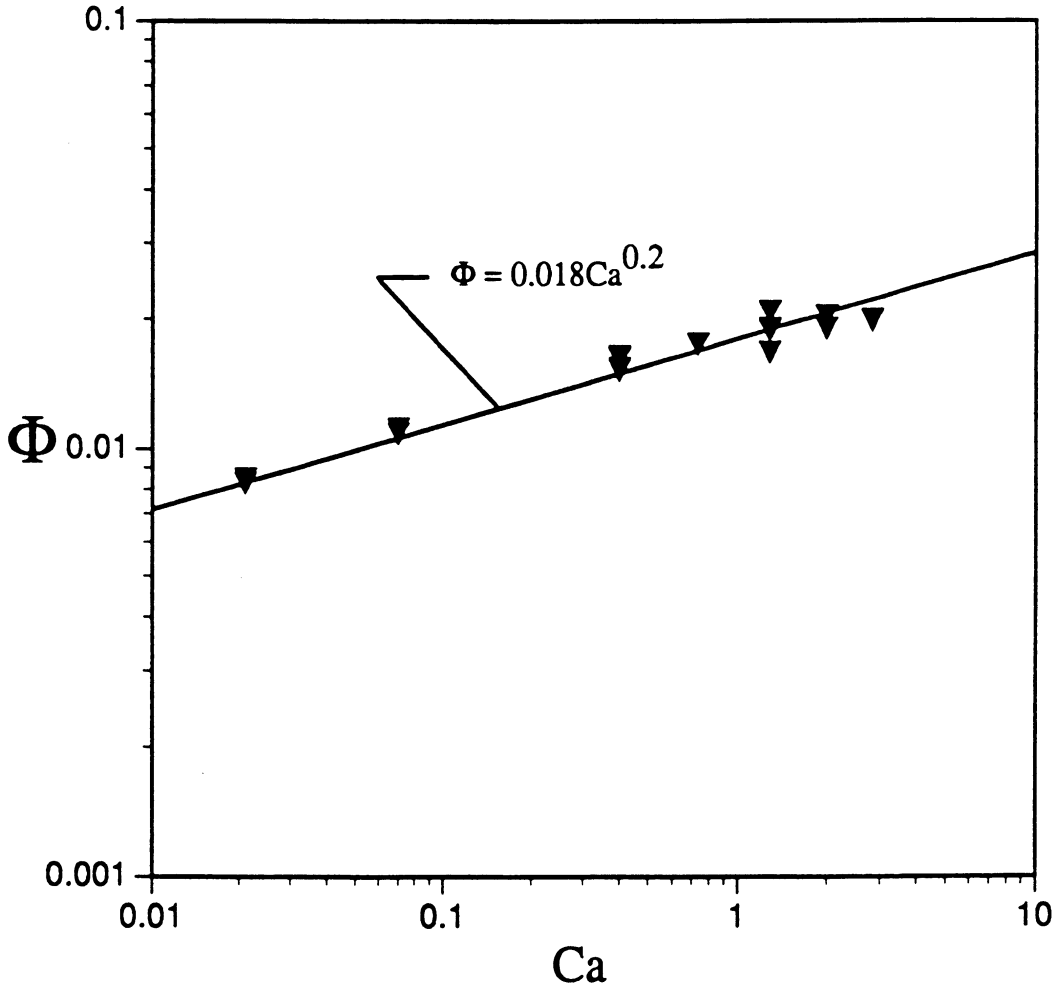

Figure 6.5. Graph of the correlation for E": Φ (Eqn. 3.51) as a function of Ca (Eqn. 3.54)

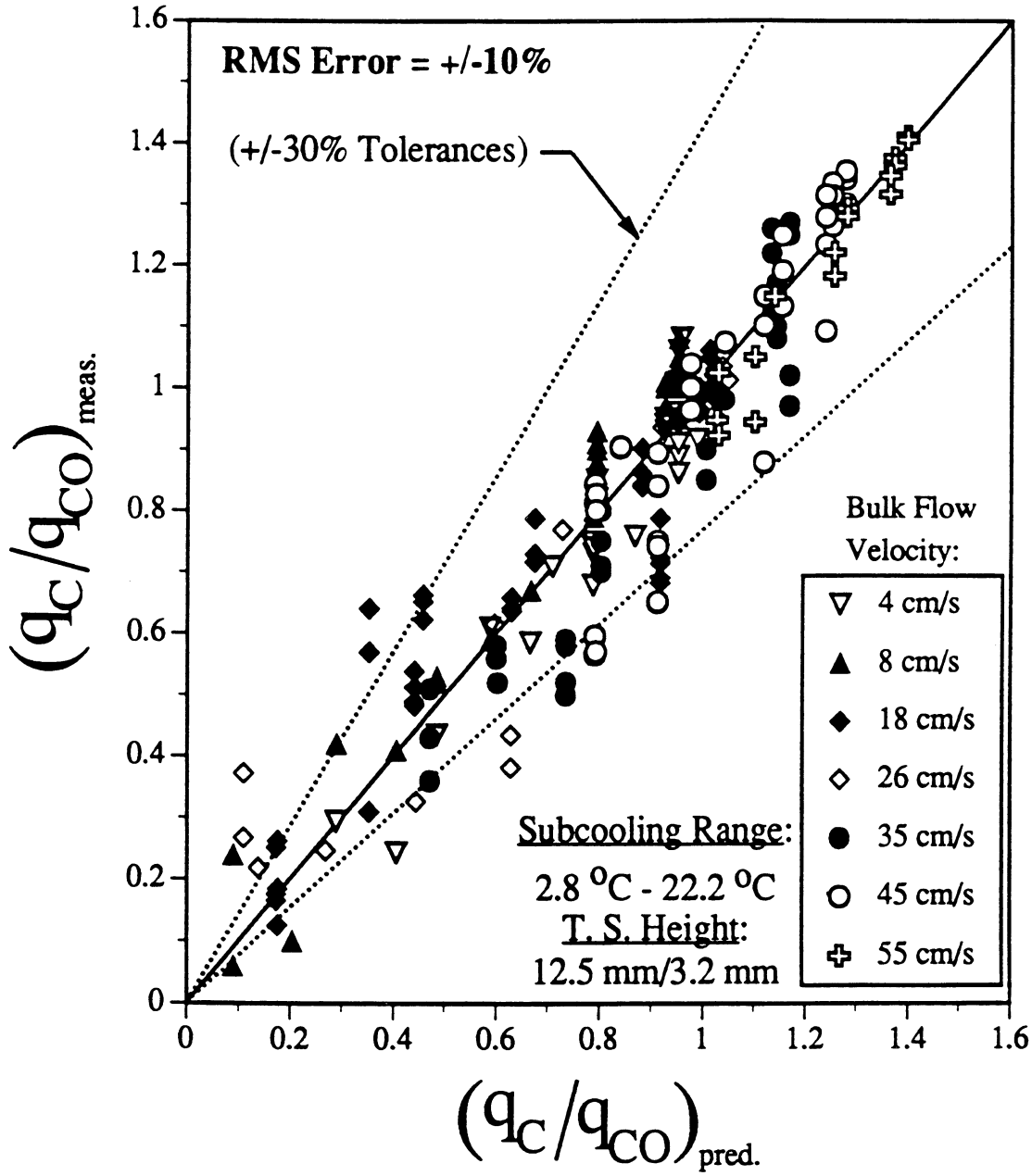

Figure 6.6. Comparison of the measured CHF with the FCCHF model predictions for various bulk flow conditions

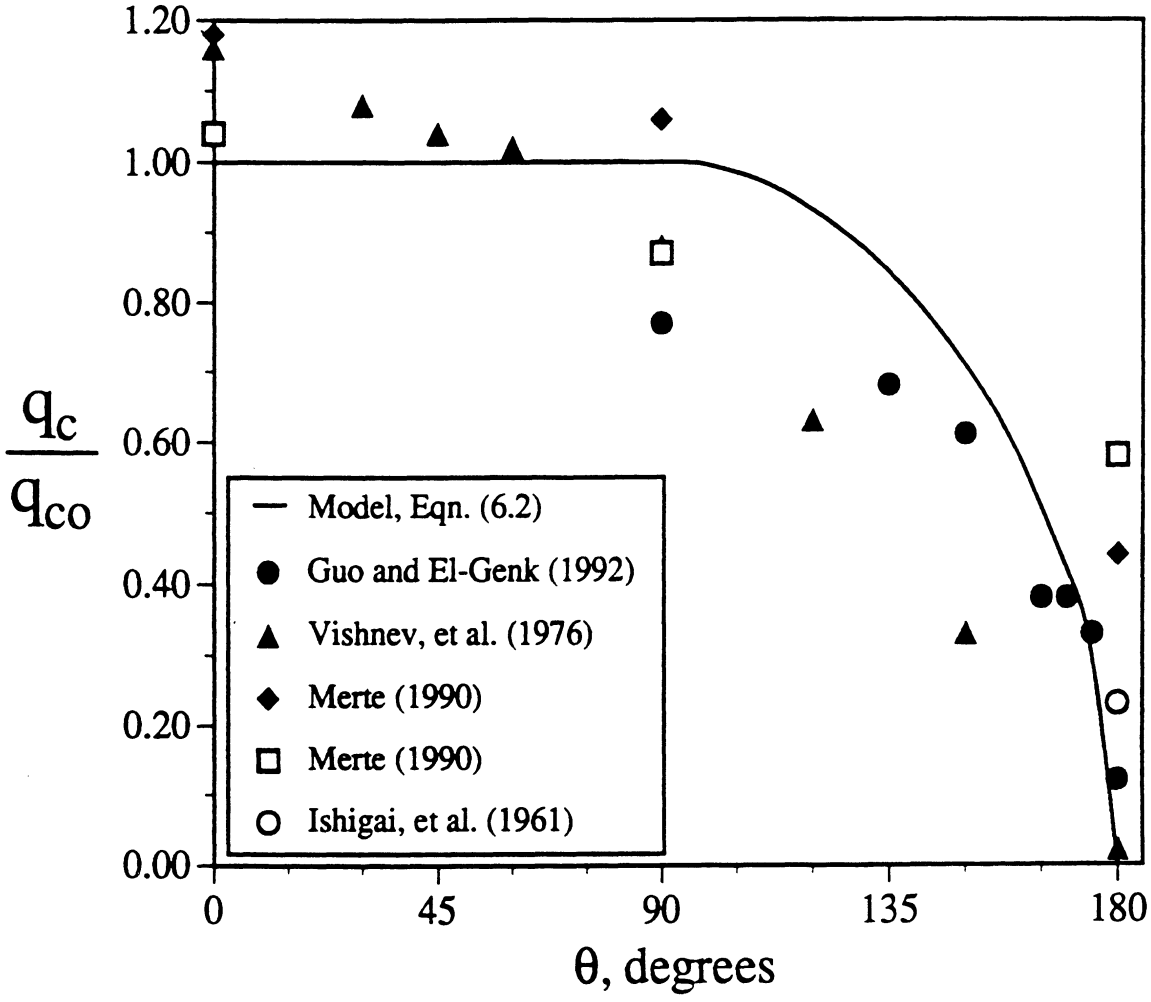

Figure 6.7. Comparison of pool boiling CHF data from previous works with a CHF model for pool boiling, Eqn. (6.2)

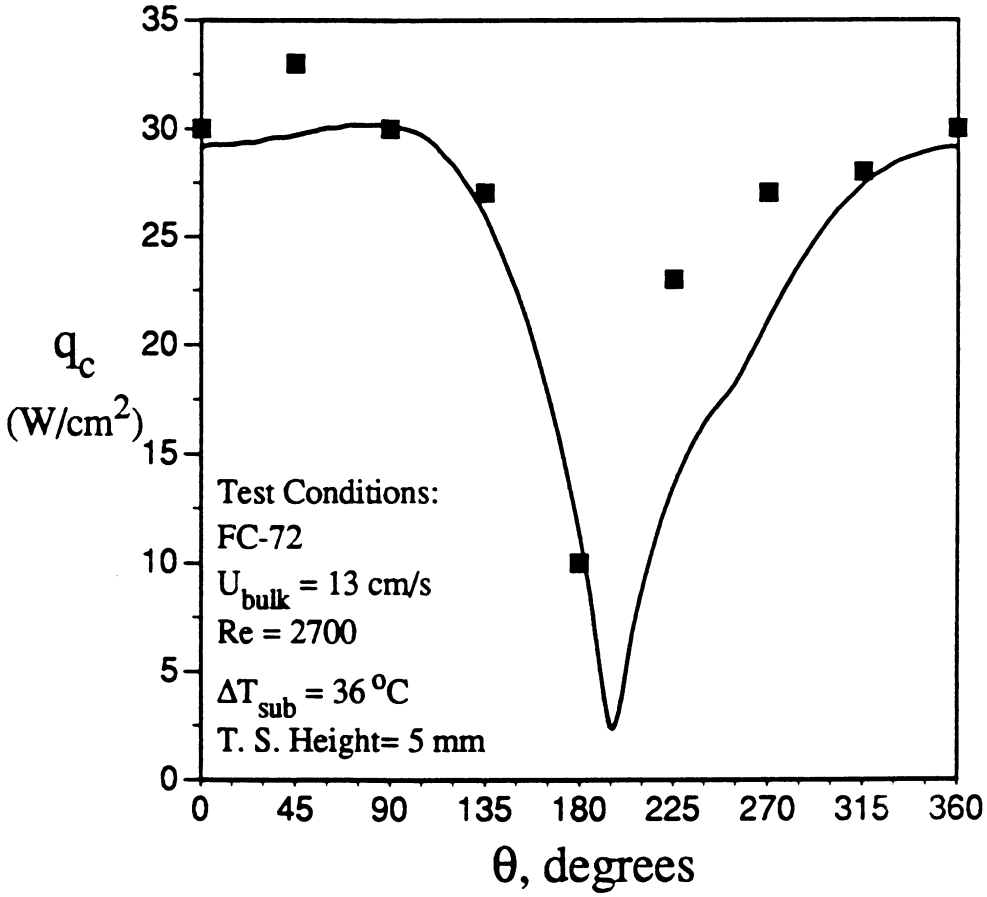

Figure 6.8. Comparision of the CHF measurements by Gersey and Mudawar (1992,1993) with the FCCHF model; FC-72, U_{Bulk}=13cm/s, ΔT_{Sub}=36° C

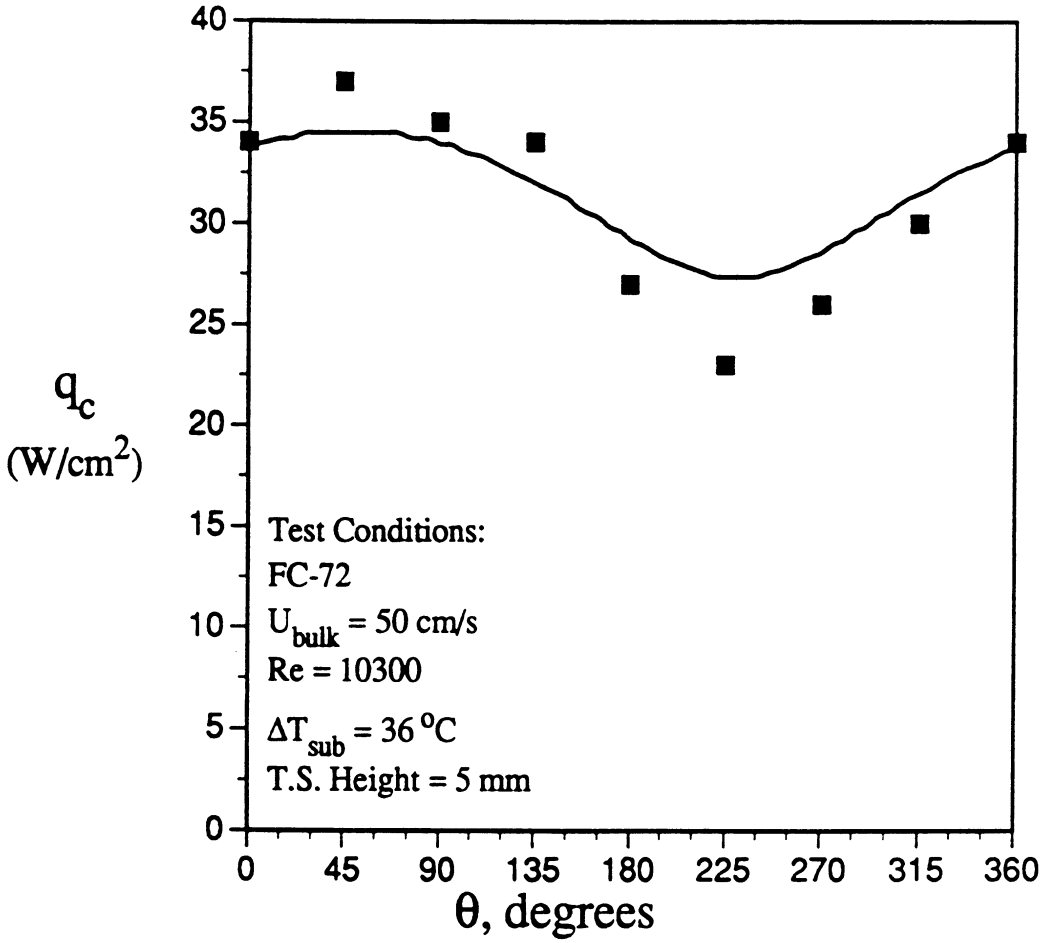

Figure 6.9. Comparision of the CHF measurements by Gersey and Mudawar (1992,1993) with the FCCHF model; FC-72, U_{Bulk}=50cm/s, ΔT_{Sub}=36^o C

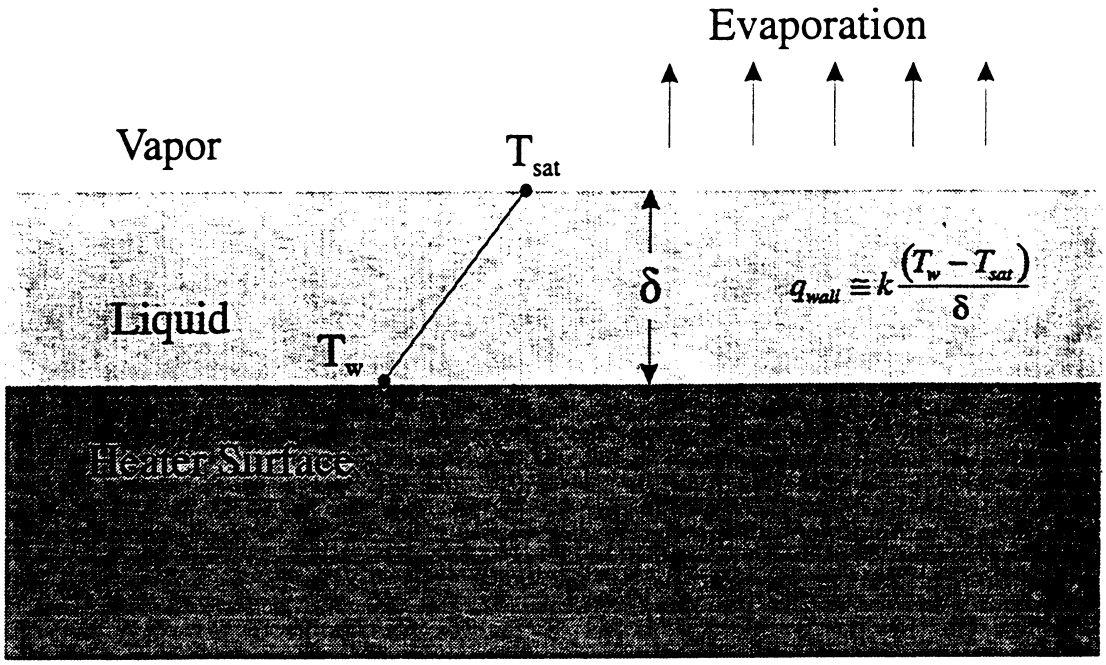

Figure 6.10(a). The assumed configuration in the macrolayer dryout models.

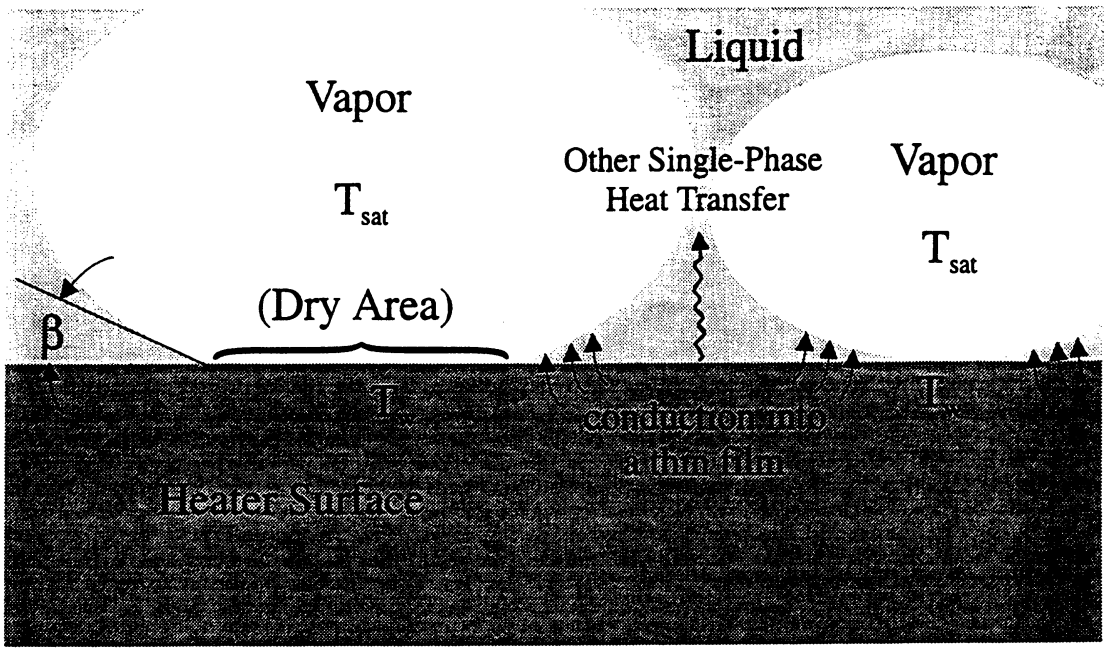

Figure 6.10(b). An illustration representing the actual behavior of the liquid and vapor on the heater surface.

Figure 6.10. Illustration comparing the assumptions made in the macrolayer dryout models with experimentally observed behavior.

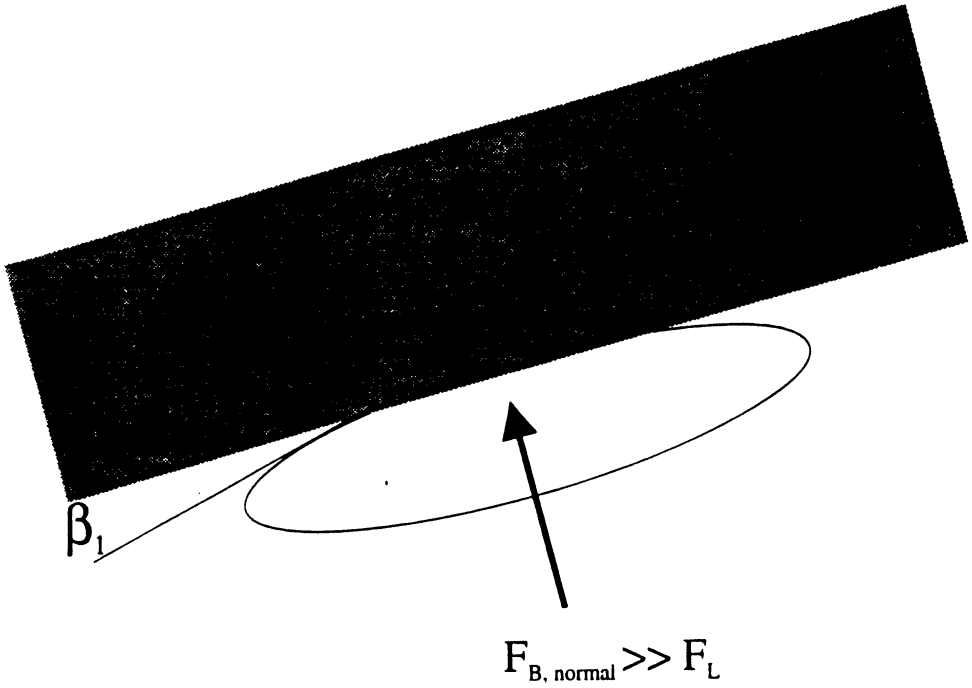

Figure 6.11(a). A flattened, sliding bubble at low flow velocity.

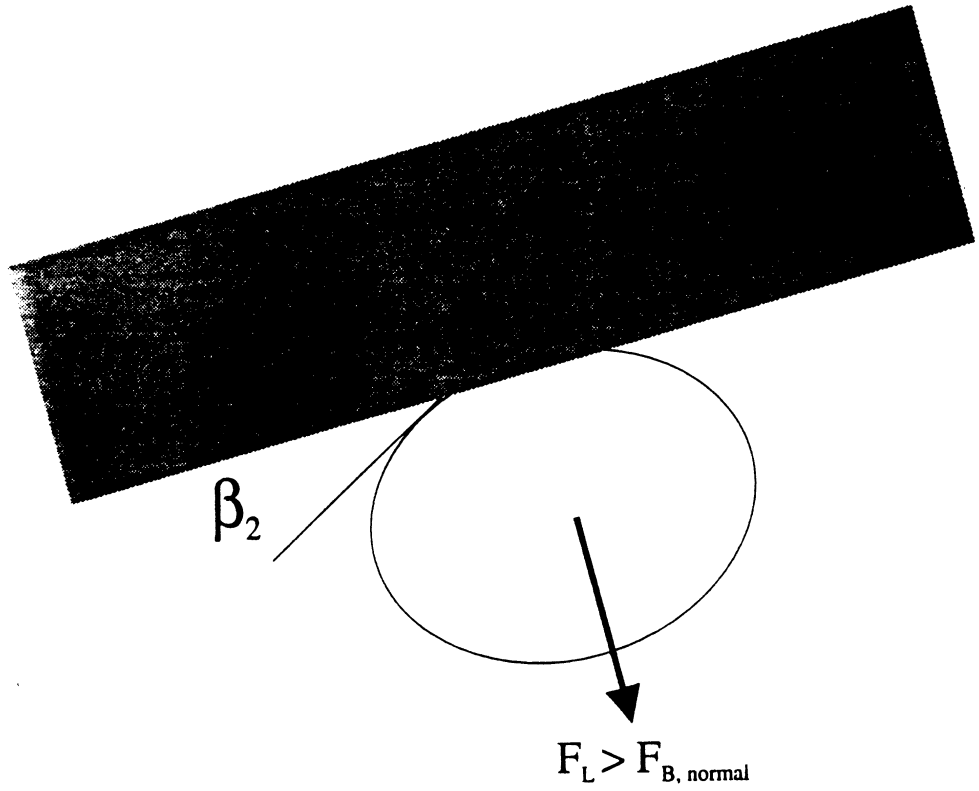

Figure 6.11(b). A bubble at high flow velocity.

Figure 6.11. Illustration of the effects of buoyancy and flow forces on the thickness of the thin liquid regions on the heater surface.

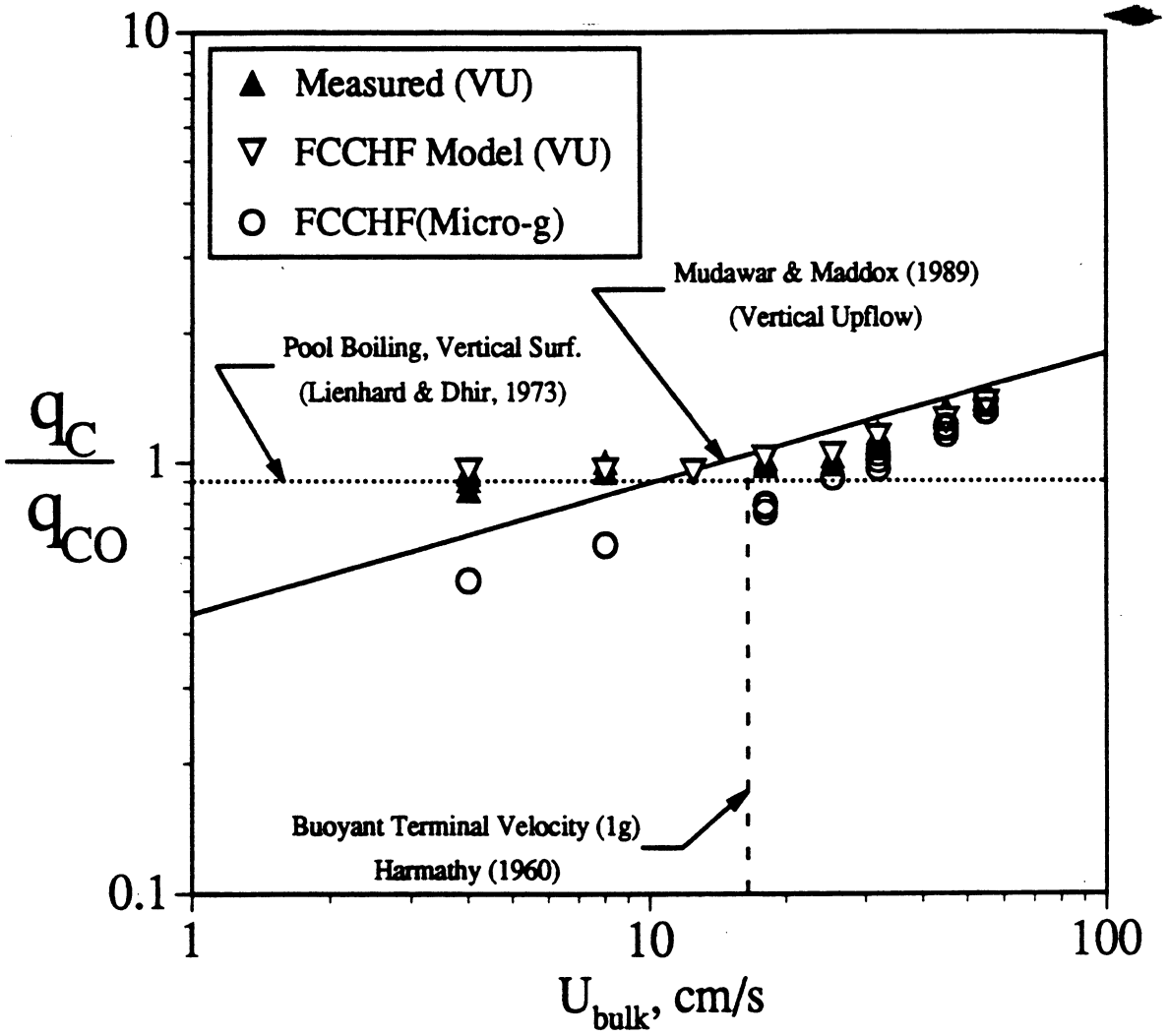

Figure 6.12. Predictions of the CHF as a function of the flow velocity in microgravity using the FCCHF model (ref. section 3.5) compared with the CHF for vertical upflow under 1g

APPENDIX A

CHF DATA TABLES

This appendix contains the measurements of the CHF in the forced convection loop, using both the metal and thin gold film heaters. The complete test matrix is given in Table A.1, listing the bulk flow conditions and the number of measurements for each condition. Next, the data are presented in three separate tables, as follows:

Table A.2. CHF measurements using the metal heater surfaces: shorter aspect ratio

Table A.3. CHF measurements using the metal heater surfaces: longer aspect ratio

Table A.4. CHF measurements using the gold film heater surfaces: shorter aspect ratio

The shorter aspect ratio denotes the shorter heated length parallel to the direction of the imposed flow, while the longer aspect ratio denotes the longer heated length parallel to the flow. The nomenclature used in the tables is defined as follows:

Orientation = heater surface orientation, as designated in Figure 4.21, in degrees

Q_{chf} = critical heat flux, W/cm^2

U_{in} = bulk velocity at the inlet to the test section, cm/s

T_{sup} = heater surface superheat, °C

T_{sub} = local bulk liquid subcooling at the leading edge of the heater, °C

T_{inlet} = bulk liquid temperature at the inlet to the test section, °C

Pressure = pressure at the leading edge of the heater, kPa

Re_{DH} = Reynolds number at the test section inlet based on the hydraulic diameter

T. S. Height = the height of the test section, millimeters

The data are sorted first based on the bulk flow velocity, in ascending order, then according to the bulk liquid subcooling, also in ascending order. The measurements at the different heater surface orientations are then given in ascending order.

Flow Velocity (cm/s)	Subcooling (°C)	Number of Data Points	Heated Length (mm)	Test Section Height (mm)
4	2.8	5	19.1	12.7
	5.6	6		
	11.1	20		
8	2.8	6	19.1	12.7
	5.6	11		
	11.1	9		
	11.1	8	19.1	3.2
12.5	11.1	11	19.1	3.2
	11.1	11	19.1	12.7
18	5.6	20	19.1	3.2
	11.1	13		
	22.2	13		
	11.1	11	38.1	
25.4	11.1	16	19.1	3.2
32	5.6	9	19.1	3.2
	11.1	19		
	22.2	18		
	5.6	8	38.1	3.2
	11.1	13		
	22.2	10		
45	5.6	13	19.1	3.2
	11.1	10		
	22.2	16		
	11.1	10	38.1	3.2
55	11.1	9	19.1	3.2
	22.2	13		

Table A.1(a). Matrix of CHF measurements using the copper heater surface.

Flow Velocity (cm/s)	Subcooling (°C)	Number of Data Points
2.5	2.8	2
	11.1	1
4	sat.	1
	2.8	3
	5.6	9
	11.1	9
12	11.1	2
32	5.6	8
	11.1	4

Table A.1(b). Matrix of CHF measurements using the gold film on quartz heater surface

Table A.2. CHF measurements using the metal heater surface: shorter aspect ratio

Orientation (degrees)	Q_{chf} (W/cm^2)	U_{in} (cm/s)	T_{sup} (° C)	T_{surf} (° C)	T_{sub} (° C)	T_{inlet} (° C)	Pressure (kPa)	Re_{DH} (-)	T. S. Height (mm)
30	26.2	3.8	25.7	77.8	1.3	50.9	118.1	2677	12.7
90	23.3	3.9	25.1	76.8	1.0	50.7	116.5	2685	12.7
135	18.3	3.8	24.8	76.7	1.0	50.9	117.3	2677	12.7
240	20.0	3.9	23.2	76.7	2.6	50.8	123.1	2694	12.7
270	22.7	3.9	22.8	76.2	2.5	50.9	122.8	2727	12.7
0	28.8	3.9	23.9	79.2	4.3	50.9	130.1	2694	12.7
90	25.9	3.8	25.8	80.2	3.6	50.8	126.7	2669	12.7
135	19.8	3.9	23.8	78.6	3.8	50.9	128.1	2694	12.7
135	20.1	3.8	24.1	78.7	4.1	50.6	127.6	2669	12.7
240	23.0	3.8	23.7	79.8	5.3	50.8	133.5	2669	12.7
270	25.7	3.8	23.3	79.4	5.2	50.9	133.4	2677	12.7
0	32.9	3.8	23.9	84.7	10.1	50.7	153.8	2677	12.7
90	29.5	3.8	23.7	83.8	8.8	51.3	150.8	2677	12.7
90	30.6	3.9	24.3	84.4	9.4	50.7	151.0	2694	12.7
135	23.8	3.9	23.3	83.3	9.2	50.8	150.5	2702	12.7
135	23.9	3.9	23.5	83.6	9.2	50.8	150.5	2710	12.7
240	26.7	3.9	23.1	84.2	10.4	50.8	155.7	2694	12.7
270	30.9	3.9	23.6	85.1	10.6	50.9	157.2	2694	12.7
0	28.9	3.4	20.2	80.3	10.6	49.4	150.5	2400	12.7
30	31.0	3.4	20.1	79.8	10.7	49.1	149.1	2373	12.7
60	29.8	3.4	20.1	80.0	10.9	49.1	150.1	2360	12.7
90	28.0	3.4	20.1	80.2	11.5	48.6	150.6	2400	12.7
120	24.6	3.4	19.9	79.9	10.9	49.2	150.7	2400	12.7
135	22.0	3.4	19.6	79.7	10.8	49.2	150.4	2373	12.7
150	19.0	3.4	19.7	79.8	11.0	49.1	150.5	2360	12.7
165	14.1	3.4	20.0	80.0	11.3	48.8	150.4	2386	12.7
175	9.5	3.5	19.8	79.8	11.8	48.2	150.3	2413	12.7
195	7.9	3.4	18.6	78.7	11.7	48.4	150.7	2360	12.7
210	19.8	3.4	18.8	79.6	12.5	48.3	154.0	2386	12.7

Orientation (degrees)	Q_{chf} (W/cm^2)	U_{in} (cm/s)	T_{sup} (° C)	T_{surf} (° C)	T_{sub} (° C)	T_{inlet} (° C)	Pressure (kPa)	Re_{DH} (-)	T. S. Height (mm)
225	23.0	3.4	19.2	80.1	12.2	48.6	154.1	2400	12.7
240	25.8	3.5	19.6	80.1	11.4	49.2	152.7	2413	12.7
0	25.4	7.9	25.0	77.6	1.8	50.8	119.9	5505	12.7
90	23.1	7.9	25.2	76.9	1.4	50.3	116.6	5514	12.7
240	21.5	8.2	22.9	76.2	2.5	50.8	122.4	5705	12.7
240	21.9	8.2	23.2	76.6	2.6	50.8	123.0	5680	12.7
270	24.3	8.0	25.0	78.5	2.6	50.9	123.2	5539	12.7
270	22.7	7.9	23.6	77.1	2.8	50.7	123.2	5530	12.7
0	28.0	8.3	31.0	86.3	4.6	50.7	130.4	5788	12.7
0	28.2	8.1	31.8	87.1	4.7	50.7	130.4	5647	12.7
0	27.7	8.1	25.2	80.5	4.7	50.7	130.7	5663	12.7
90	26.1	8.3	31.6	86.0	3.6	50.8	126.8	5796	12.7
135	21.8	8.1	30.7	85.6	4.0	50.9	128.8	5663	12.7
240	25.4	8.2	23.3	79.2	5.1	50.9	133.2	5680	12.7
240	23.2	8.2	22.8	78.7	5.2	50.8	133.2	5713	12.7
240	24.8	8.2	23.2	79.2	5.2	50.8	133.4	5680	12.7
240	23.1	8.1	23.1	79.2	5.3	50.8	133.6	5663	12.7
270	26.3	8.2	25.0	81.1	5.2	50.8	133.4	5705	12.7
315	27.5	8.2	25.3	81.2	4.9	50.9	132.6	5713	12.7
0	35.2	8.6	24.6	85.3	9.9	50.8	153.5	5963	12.7
0	35.0	8.3	27.2	88.1	10.1	50.8	154.2	5755	12.7
90	32.4	8.1	26.9	86.9	9.1	50.9	150.3	5663	12.7
135	25.7	8.2	26.4	86.7	9.4	50.9	151.6	5680	12.7
165	17.1	8.2	25.8	86.4	9.7	51.0	153.2	5680	12.7
180	1.9	8.1	22.4	83.2	10.1	50.7	154.0	5655	12.7
240	28.0	8.2	26.2	87.7	10.9	50.6	157.1	5738	12.7
270	32.9	8.3	24.3	85.8	11.2	50.3	156.8	5780	12.7
315	33.9	8.3	24.2	85.6	10.9	50.5	156.7	5771	12.7
150	21.8	7.3	22.9	81.2	9.3	48.9	142.5	1371	3.2
165	16.9	7.3	22.2	80.6	9.6	48.7	143.0	1371	3.2
175	13.5	7.3	23.1	81.7	9.6	48.9	144.0	1371	3.2

Orientation (degrees)	Q_{chf} (W/cm^2)	U_{in} (cm/s)	T_{sup} (° C)	T_{surf} (° C)	T_{sub} (° C)	T_{inlet} (° C)	Pressure (kPa)	Re_{DH} (-)	T. S. Height (mm)
180	7.7	7.2	20.8	79.3	9.4	49.2	143.9	1362	3.2
185	3.1	7.3	15.2	73.9	9.9	48.8	144.5	1371	3.2
195	13.3	7.3	21.4	80.2	9.6	49.1	144.8	1371	3.2
210	19.2	7.2	22.1	81.1	10.1	48.9	146.1	1362	3.2
240	26.2	7.2	22.2	81.6	10.4	48.9	147.2	1362	3.2
0	28.0	12.3	20.8	80.8	10.9	49.1	150.1	2319	3.2
90	31.2	12.2	20.6	80.7	11.4	48.7	150.8	2310	3.2
135	26.5	12.2	20.3	80.3	11.1	48.9	150.3	2310	3.2
165	18.8	12.2	18.5	78.4	10.8	49.1	149.9	2310	3.2
180	14.0	12.2	18.1	78.1	10.6	49.4	150.3	2310	3.2
180	14.4	12.2	18.7	78.6	10.9	49.1	150.2	2310	3.2
195	7.5	12.3	14.9	74.9	11.9	48.2	150.7	2319	3.2
225	18.8	12.3	20.1	80.2	10.7	49.3	150.5	2319	3.2
240	20.3	12.2	18.7	79.0	11.6	48.7	151.5	2310	3.2
270	22.4	12.2	19.2	79.2	11.9	48.1	150.6	2301	3.2
315	23.2	12.3	20.2	80.1	10.9	49.1	150.0	2319	3.2
0	30.5	12.3	19.4	79.4	10.9	49.1	150.3	8536	12.7
45	31.8	12.3	19.7	79.9	11.1	49.1	151.0	8576	12.7
90	29.8	12.3	20.0	80.1	11.2	48.9	150.4	8576	12.7
135	23.9	12.3	19.5	79.6	11.2	48.8	150.5	8589	12.7
165	15.7	12.3	19.1	79.1	10.6	49.4	150.2	8562	12.7
180	5.7	12.3	15.7	75.6	11.4	48.5	149.8	8523	12.7
195	13.9	12.3	19.4	79.4	11.0	49.0	150.3	8576	12.7
225	21.2	12.4	18.9	79.0	11.1	49.1	150.7	8615	12.7
240	23.7	12.3	18.3	78.2	11.0	48.9	149.8	8576	12.7
270	28.1	12.3	19.7	79.7	10.9	49.2	150.5	8549	12.7
315	28.9	12.3	18.9	79.0	11.1	49.0	150.6	8549	12.7
0	26.3	18.1	21.9	75.4	4.4	49.1	123.2	3421	3.2
0	26.9	18.1	22.6	76.1	4.5	48.9	123.1	3421	3.2
45	28.5	18.2	23.0	75.8	3.9	48.9	120.9	3439	3.2
45	28.8	18.4	23.2	76.1	3.9	48.9	121.0	3466	3.2

Orientation (degrees)	Q_{chf} (W/cm^2)	U_{in} (cm/s)	T_{sup} (° C)	T_{surf} (° C)	T_{sub} (° C)	T_{inlet} (° C)	Pressure (kPa)	Re_{DH} (-)	T. S. Height (mm)
90	27.8	18.2	24.1	76.6	3.8	48.8	119.7	3439	3.2
90	27.8	18.2	23.7	76.3	4.0	48.6	119.9	3430	3.2
135	22.9	17.9	22.3	75.2	4.1	48.9	121.0	3376	3.2
135	23.4	18.2	22.9	75.8	4.1	48.8	120.9	3439	3.2
165	17.3	18.1	22.3	75.6	4.3	48.9	122.5	3421	3.2
165	17.5	18.1	21.7	75.0	4.4	48.9	122.6	3421	3.2
180	13.1	18.3	20.4	73.8	4.7	48.8	123.2	3457	3.2
180	13.3	18.0	21.3	74.8	4.8	48.8	123.7	3394	3.2
195	3.4	18.0	13.2	66.9	4.8	48.9	124.2	3403	3.2
210	4.8	18.0	13.2	67.1	5.3	48.6	124.8	3394	3.2
225	15.5	18.1	23.7	77.8	5.1	49.0	125.8	3412	3.2
240	17.7	17.9	22.4	76.4	5.1	49.0	125.5	3385	3.2
240	18.0	18.0	22.5	76.8	5.4	48.9	126.3	3394	3.2
270	19.5	18.1	22.3	76.6	5.5	48.8	126.3	3412	3.2
315	18.8	18.0	23.6	77.7	5.1	49.0	125.6	3394	3.2
315	18.5	18.0	20.7	74.8	5.2	48.9	125.7	3403	3.2
0	32.5	18.3	23.6	82.2	10.3	48.3	144.3	3448	3.2
45	34.5	18.2	23.0	81.2	9.4	48.8	142.3	3430	3.2
90	32.7	17.8	23.3	81.1	8.8	48.9	140.3	3367	3.2
135	27.3	17.9	22.0	79.9	9.1	48.8	141.2	3385	3.2
135	29.3	17.9	21.7	80.0	9.4	48.9	142.7	3385	3.2
165	21.4	18.2	21.7	80.1	9.4	49.0	143.2	3439	3.2
180	15.8	18.1	19.0	77.7	9.7	49.0	144.3	3421	3.2
180	17.5	18.1	21.4	80.2	9.7	49.0	144.8	3412	3.2
195	6.0	18.3	18.8	77.6	9.8	49.0	145.0	3457	3.2
210	5.4	18.1	13.4	72.6	10.2	48.8	146.2	3412	3.2
225	20.8	17.8	20.1	79.2	10.2	49.1	146.8	3367	3.2
270	25.6	18.1	22.9	82.4	10.3	49.1	147.6	3421	3.2
315	25.6	18.0	20.8	80.0	10.4	48.8	146.6	3403	3.2
90	41.1	18.0	24.3	89.2	19.9	45.1	173.7	3394	3.2
90	40.9	18.0	23.9	88.9	19.9	45.1	174.1	3394	3.2

Orientation (degrees)	Q_{chf} (W/cm^2)	U_{in} (cm/s)	T_{sup} (° C)	T_{surf} (° C)	T_{sub} (° C)	T_{inlet} (° C)	Pressure (kPa)	Re_{DH} (-)	T. S. Height (mm)
135	35.2	18.0	23.2	88.4	20.1	45.1	174.9	3394	3.2
0	40.9	18.1	23.4	89.0	20.3	45.3	177.0	3421	3.2
0	39.9	18.1	22.2	87.8	20.4	45.2	177.2	3421	3.2
180	21.3	18.1	22.2	87.8	20.4	45.2	177.3	3412	3.2
195	10.9	18.1	15.8	81.6	20.5	45.3	178.0	3421	3.2
210	10.5	18.0	15.6	81.5	20.9	44.9	178.7	3403	3.2
315	30.1	18.2	22.2	88.2	20.9	45.1	179.4	3430	3.2
315	29.7	18.2	21.8	87.9	21.2	44.9	179.6	3430	3.2
240	25.9	18.1	21.6	87.7	21.2	44.9	179.8	3412	3.2
225	12.9	18.4	17.6	83.7	21.6	44.6	179.8	3466	3.2
270	30.4	18.2	21.6	87.8	21.7	44.6	180.7	3430	3.2
0	31.1	25.4	17.8	77.8	11.6	48.5	150.5	4798	3.2
45	32.9	25.5	17.7	77.7	11.0	49.1	150.5	4812	3.2
90	33.6	25.3	23.9	81.6	8.7	49.1	140.5	4776	3.2
90	32.2	25.3	17.8	78.0	11.3	48.9	150.9	4783	3.2
135	30.4	25.4	23.8	81.9	9.3	48.7	141.9	4803	3.2
165	25.0	25.5	22.9	81.3	9.7	48.7	143.3	4821	3.2
180	20.0	25.4	22.8	81.4	9.6	49.0	144.1	4794	3.2
195	10.6	25.5	20.6	79.4	10.1	48.8	145.1	4812	3.2
210	8.0	25.4	18.2	77.2	10.1	48.9	146.0	4803	3.2
225	7.1	25.1	16.2	75.4	10.3	48.9	146.8	4749	3.2
240	7.9	25.4	19.7	79.0	10.4	48.9	147.4	4803	3.2
240	8.7	25.4	17.7	77.0	10.6	48.8	147.3	4803	3.2
240	12.1	25.5	14.6	74.7	11.6	48.6	151.0	4812	3.2
270	12.4	25.5	21.0	80.3	10.6	48.7	147.2	4821	3.2
270	14.1	25.6	15.0	75.1	11.4	48.6	150.4	4826	3.2
315	24.2	25.5	16.8	76.9	11.2	48.9	150.7	4812	3.2
0	30.5	34.1	28.4	83.3	4.7	50.2	129.0	6438	3.2
0	30.9	34.3	29.7	84.6	4.8	50.2	129.0	6483	3.2
45	26.5	33.2	39.1	93.7	3.7	50.9	127.7	6266	3.2
90	29.4	32.8	35.7	90.4	4.0	50.8	128.3	6203	3.2

Orientation (degrees)	Q_{chf} (W/cm^2)	U_{in} (cm/s)	T_{sup} (° C)	T_{surf} (° C)	T_{sub} (° C)	T_{inlet} (° C)	Pressure (kPa)	Re_{DH} (-)	T. S. Height (mm)
90	29.8	32.8	36.9	91.7	4.3	50.5	128.5	6203	3.2
180	19.3	32.8	34.2	89.8	5.1	50.6	131.7	6203	3.2
240	9.9	33.6	28.9	84.7	4.9	50.8	132.4	6338	3.2
270	13.6	33.8	27.2	82.8	4.8	50.9	131.9	6374	3.2
270	14.1	33.7	28.2	84.0	4.9	50.9	132.3	6356	3.2
0	38.3	33.1	33.7	94.4	9.9	50.8	153.8	6257	3.2
0	37.2	33.1	33.6	94.4	10.0	50.8	154.0	6248	3.2
0	41.0	34.3	29.0	90.4	10.6	50.8	156.7	6483	3.2
45	33.2	33.2	41.4	101.6	9.3	50.8	150.9	6266	3.2
90	34.0	32.4	22.3	80.2	8.1	49.8	141.2	6122	3.2
90	36.2	32.5	24.1	82.1	8.9	49.1	141.4	6131	3.2
90	35.8	33.5	34.4	94.4	9.1	50.9	150.2	6320	3.2
90	37.5	33.6	37.4	97.4	9.2	50.8	150.3	6338	3.2
135	31.8	33.2	23.7	81.7	9.4	48.6	141.7	6266	3.2
135	29.3	34.6	37.0	97.6	9.7	50.8	152.7	6537	3.2
165	27.2	33.2	23.1	81.5	9.4	49.1	143.5	6275	3.2
180	22.8	34.7	34.1	95.0	10.1	50.8	154.2	6546	3.2
195	19.8	33.1	22.7	81.6	9.8	49.1	145.3	6257	3.2
240	14.1	34.3	32.2	93.6	10.7	50.8	156.7	6483	3.2
270	18.5	32.9	28.3	89.8	10.7	50.8	157.0	6221	3.2
270	19.1	33.4	29.3	90.8	10.7	50.8	157.2	6302	3.2
270	18.4	32.7	27.9	89.3	10.7	50.8	157.0	6176	3.2
270	18.4	33.1	28.2	89.7	10.7	50.8	157.1	6248	3.2
315	28.9	34.5	35.8	97.2	10.7	50.8	156.8	6519	3.2
0	47.3	33.3	23.8	89.2	19.7	45.7	176.3	6293	3.2
0	46.2	34.1	27.3	92.9	19.8	45.7	177.1	6447	3.2
0	50.6	33.9	26.4	91.9	20.1	45.4	176.6	6411	3.2
0	44.1	34.4	23.8	89.2	20.2	45.2	175.9	6492	3.2
30	52.1	34.2	29.4	94.7	20.3	45.0	175.4	6465	3.2
45	52.8	33.9	27.0	92.1	19.8	45.3	174.5	6402	3.2
60	52.1	34.3	29.8	94.8	20.4	44.6	173.8	6483	3.2

Orientation (degrees)	Q_{chf} (W/cm^2)	U_{in} (cm/s)	T_{sup} (° C)	T_{surf} (° C)	T_{sub} (° C)	T_{inlet} (° C)	Pressure (kPa)	Re_{DH} (-)	T. S. Height (mm)
90	48.5	34.0	26.5	91.3	18.4	46.5	173.4	6420	3.2
135	40.7	34.1	26.9	92.0	18.6	46.5	174.6	6438	3.2
180	33.4	34.2	25.2	90.9	21.3	44.4	177.6	6456	3.2
180	31.1	34.1	22.1	87.7	21.3	44.3	177.2	6438	3.2
210	23.4	34.4	24.2	90.2	21.6	44.3	179.0	6501	3.2
210	24.0	34.4	23.6	89.5	21.9	44.1	178.9	6492	3.2
240	21.1	34.4	23.3	89.5	22.2	44.0	180.0	6492	3.2
255	21.8	34.1	24.5	90.7	21.9	44.3	180.4	6447	3.2
270	21.8	33.4	17.6	83.6	21.1	44.9	179.1	6302	3.2
270	24.3	34.4	22.9	89.2	22.2	44.1	180.8	6501	3.2
315	35.3	34.3	23.9	89.6	20.4	45.3	178.0	6483	3.2
0	29.7	45.2	27.1	81.5	5.4	48.9	126.6	8528	3.2
45	35.4	45.1	33.6	87.9	6.1	48.3	126.7	8513	3.2
90	34.5	45.0	33.7	88.1	5.7	48.7	126.8	8499	3.2
90	36.3	45.0	28.2	82.5	5.8	48.4	126.4	8499	3.2
135	30.8	44.9	31.1	84.9	4.9	48.9	124.4	8485	3.2
165	29.2	45.0	31.7	85.9	5.7	48.6	126.2	8499	3.2
180	26.2	45.2	29.4	83.8	5.7	48.7	126.8	8542	3.2
225	15.4	45.2	18.9	73.0	5.3	48.8	125.6	8542	3.2
225	16.2	45.0	19.8	74.3	6.0	48.5	127.3	8499	3.2
240	15.5	45.2	18.9	73.4	5.8	48.7	127.1	8542	3.2
270	20.4	45.2	21.4	76.0	5.5	49.0	127.3	8528	3.2
270	17.7	45.0	20.3	74.7	5.7	48.7	126.9	8499	3.2
315	23.9	44.9	24.1	78.6	5.1	49.4	127.3	8471	3.2
0	40.1	45.2	24.8	84.8	11.2	48.8	150.3	8542	3.2
45	44.0	45.0	27.3	87.4	11.3	48.7	150.5	8499	3.2
90	42.7	45.2	27.1	87.2	11.7	48.4	150.8	8528	3.2
135	40.6	45.2	28.1	88.2	11.6	48.6	150.8	8528	3.2
180	32.6	45.2	23.8	83.8	11.0	49.1	150.5	8542	3.2
225	26.4	45.0	21.6	81.7	11.1	49.0	150.6	8499	3.2
240	26.0	45.2	21.8	82.4	11.9	48.7	153.2	8528	3.2

Orientation (degrees)	Q_{chf} (W/cm^2)	U_{in} (cm/s)	T_{sup} (° C)	T_{surf} (° C)	T_{sub} (° C)	T_{inlet} (° C)	Pressure (kPa)	Re_{DH} (-)	T. S. Height (mm)
270	27.3	45.0	21.9	82.0	11.0	49.1	150.5	8499	3.2
270	24.1	45.0	21.3	81.3	11.3	48.7	150.4	8499	3.2
315	35.8	44.9	24.7	84.7	11.1	48.9	150.6	8471	3.2
0	53.2	45.0	21.4	89.7	22.0	46.3	192.0	8499	3.2
0	53.3	45.1	21.6	89.9	22.2	46.2	192.2	8513	3.2
0	54.7	45.2	22.9	91.2	22.2	46.1	192.1	8528	3.2
45	52.3	45.1	18.1	86.5	22.1	46.3	192.9	8513	3.2
45	55.8	45.1	22.2	90.7	22.3	46.1	192.5	8513	3.2
90	52.6	45.0	20.7	89.1	22.3	46.1	192.4	8499	3.2
135	46.8	45.0	17.4	85.8	22.3	46.1	192.2	8499	3.2
135	49.5	45.1	20.8	89.1	22.3	46.1	192.3	8513	3.2
180	43.2	45.1	21.2	89.6	22.3	46.1	192.2	8513	3.2
180	41.6	45.2	20.2	88.6	22.3	46.1	192.3	8528	3.2
210	37.6	44.9	20.4	88.8	22.2	46.2	192.4	8485	3.2
225	35.1	44.9	18.9	87.4	22.3	46.2	193.1	8485	3.2
225	35.4	45.0	16.1	84.5	22.4	46.0	192.6	8499	3.2
240	34.4	45.3	18.8	87.2	22.2	46.2	192.3	8556	3.2
270	37.2	45.1	19.3	87.7	22.3	46.1	192.5	8513	3.2
315	47.8	45.1	21.2	89.5	22.3	46.1	192.3	8513	3.2
315	45.5	45.2	17.3	85.7	22.3	46.1	192.8	8528	3.2
0	42.8	55.0	23.4	83.5	11.3	48.8	150.8	10378	3.2
45	45.7	55.1	26.1	86.2	11.3	48.7	150.3	10407	3.2
90	44.7	55.2	27.3	87.3	11.2	48.9	150.4	10421	3.2
135	41.6	55.0	25.4	85.4	11.2	48.9	150.4	10393	3.2
180	37.4	55.1	24.3	84.3	11.2	48.8	150.3	10407	3.2
225	30.8	55.0	20.9	80.9	11.0	49.0	150.3	10393	3.2
240	30.0	55.0	20.3	80.3	11.1	49.0	150.4	10393	3.2
270	30.7	55.2	20.1	80.1	10.9	49.1	150.3	10421	3.2
315	38.4	54.9	22.4	82.4	11.2	48.8	150.3	10364	3.2
0	56.0	54.9	21.5	89.8	22.2	46.2	192.2	10364	3.2
45	58.7	55.1	22.3	90.6	22.2	46.2	192.2	10407	3.2

Orientation (degrees)	Q_{chf} (W/cm^2)	U_{in} (cm/s)	T_{sup} (° C)	T_{surf} (° C)	T_{sub} (° C)	T_{inlet} (° C)	Pressure (kPa)	Re_{DH} (-)	T. S. Height (mm)
45	56.3	54.8	18.6	86.9	22.5	45.9	192.2	10350	3.2
90	56.7	55.0	21.8	90.2	22.1	46.3	192.4	10378	3.2
135	53.8	55.0	21.8	90.2	22.3	46.1	192.3	10378	3.2
135	51.7	54.9	18.4	86.8	22.4	45.9	192.5	10364	3.2
180	47.8	55.2	20.8	89.2	22.1	46.2	192.2	10421	3.2
225	42.7	54.9	20.1	88.5	22.2	46.2	192.5	10364	3.2
225	41.9	55.1	17.3	85.6	22.5	45.8	192.0	10407	3.2
240	42.6	55.0	20.3	88.7	22.3	46.1	192.4	10378	3.2
270	43.7	55.0	20.2	88.6	22.3	46.1	192.2	10378	3.2
315	50.2	54.9	18.0	86.3	22.3	46.0	192.2	10364	3.2
315	50.8	55.0	20.9	89.3	22.3	46.1	192.6	10393	3.2

Table A.3. CHF measurements using the metal heater surfaces: longer aspect ratio

Orientation (degrees)	Q_{chf} (W/cm^2)	U_{in} (cm/s)	T_{sup} (° C)	T_{surf} (° C)	T_{sub} (° C)	T_{inlet} (° C)	Pressure (kPa)	Re_{DH} (-)	T. S. Height (mm)
0	17.1	18.1	19.6	79.5	11.2	48.7	149.8	3417	3.2
0	16.7	18.1	19.1	79.1	11.3	48.7	150.3	3417	3.2
45	29.0	18.1	21.3	81.3	10.9	49.1	150.1	3417	3.2
90	26.9	18.2	20.9	80.9	10.9	49.1	150.3	3445	3.2
135	20.7	18.2	19.8	79.9	10.9	49.2	150.7	3431	3.2
180	7.2	18.2	19.1	79.1	10.9	49.1	150.2	3431	3.2
210	15.5	18.0	19.2	79.2	11.4	48.6	150.3	3403	3.2
210	16.1	18.2	19.7	79.7	11.3	48.8	150.4	3431	3.2
225	18.7	18.1	20.0	80.1	11.2	48.9	150.5	3417	3.2
270	22.5	18.2	19.7	79.7	10.7	49.3	150.2	3431	3.2
315	23.7	18.0	20.4	80.4	11.4	48.6	150.3	3403	3.2
0	26.9	32.9	25.0	78.3	4.7	48.7	122.8	6221	3.2
41	27.6	33.0	24.6	77.4	3.9	48.9	120.5	6239	3.2
90	24.9	33.2	25.1	77.6	3.3	49.2	119.5	6275	3.2
180	13.2	33.2	23.4	76.8	4.4	48.9	122.8	6266	3.2
210	4.7	33.1	17.6	71.3	4.9	48.9	124.4	6257	3.2
240	4.8	33.4	17.8	71.9	5.4	48.7	125.5	6302	3.2
270	5.5	32.9	18.3	72.6	5.5	48.7	126.0	6221	3.2
315	17.1	33.3	22.9	76.8	5.3	48.7	125.0	6284	3.2
0	32.5	33.2	24.6	83.3	9.8	48.9	144.5	6266	3.2
45	34.8	32.9	25.5	83.7	8.7	49.5	142.2	6221	3.2
90	32.7	33.0	25.1	82.8	9.2	48.6	140.6	6230	3.2
135	27.2	32.8	24.6	82.6	9.2	48.9	141.8	6203	3.2
135	26.8	32.9	23.9	82.2	9.2	49.1	142.5	6212	3.2
180	16.8	32.7	22.9	81.6	10.4	48.3	144.4	6167	3.2
210	7.6	33.2	17.8	76.9	10.1	48.9	146.2	6266	3.2
225	7.4	33.2	17.9	77.0	10.1	49.0	146.3	6266	3.2
225	7.1	33.2	17.8	76.9	10.2	48.9	146.3	6266	3.2
240	6.8	33.2	20.4	79.8	10.2	49.2	147.4	6275	3.2

Orientation (degrees)	Q_{chf} (W/cm^2)	U_{in} (cm/s)	T_{sup} (° C)	T_{surf} (° C)	T_{sub} (° C)	T_{inlet} (° C)	Pressure (kPa)	Re_{DH} (-)	T. S. Height (mm)
240	7.8	33.2	17.9	77.2	10.2	49.0	146.9	6275	3.2
270	8.8	32.9	19.9	79.3	10.3	49.1	147.6	6212	3.2
315	21.5	32.8	23.4	82.5	10.3	48.8	146.3	6185	3.2
0	41.9	33.3	25.4	89.4	20.5	43.4	168.7	6293	3.2
90	40.4	33.5	25.3	88.7	19.8	43.6	166.1	6329	3.2
90	39.2	32.8	23.7	88.6	19.8	45.1	173.6	6185	3.2
135	34.3	33.0	24.3	87.8	20.2	43.3	166.6	6230	3.2
135	33.9	33.0	24.3	87.8	20.2	43.3	166.6	6239	3.2
180	23.2	33.1	24.1	88.1	20.8	43.1	168.7	6248	3.2
180	22.9	33.0	23.4	87.4	20.9	43.1	169.2	6239	3.2
210	13.5	33.0	19.8	84.1	20.9	43.3	170.3	6239	3.2
240	14.0	33.0	21.1	85.7	21.1	43.4	171.8	6239	3.2
270	17.5	33.0	21.3	86.1	21.2	43.6	172.9	6230	3.2
0	32.8	45.1	20.6	80.5	11.1	48.8	150.1	8513	3.2
0	31.8	45.1	20.1	80.0	11.2	48.8	150.1	8513	3.2
45	35.5	45.0	20.9	80.9	11.1	48.9	150.3	8499	3.2
90	34.1	45.0	21.1	81.1	11.2	48.9	150.5	8499	3.2
135	29.3	45.1	20.0	80.0	11.4	48.6	150.1	8513	3.2
180	21.5	45.0	18.6	78.6	11.1	48.9	150.5	8499	3.2
225	13.0	44.9	16.8	76.9	11.6	48.6	150.8	8471	3.2
240	12.3	45.0	16.6	76.7	11.2	48.9	150.8	8499	3.2
270	14.3	45.0	19.3	79.3	11.0	49.1	150.5	8499	3.2
315	25.3	45.1	19.7	79.7	11.3	48.7	150.4	8513	3.2

Table A.4. CHF measurements using the gold film heater surfaces: shorter aspect ratio

Orientation (degrees)	Q_{chf} (W/cm^2)	U_{in} (cm/s)	T_{sup} (° C)	T_{surf} (° C)	T_{sub} (° C)	T_{inlet} (° C)	Pressure (kPa)	Re_{DH} (-)	T. S. Height (mm)
0	15.4	2.8	42.6	94.1	2.3	49.2	115.7	3581	25.4
0	15.9	2.8	42.3	93.8	2.3	49.2	115.8	3566	25.4
0	19.3	2.2	39.9	100.1	10.2	49.9	150.9	2828	25.4
0	14.8	4.1	40.9	90.2	0.4	48.8	107.3	5147	25.4
0	16.3	4.1	43.8	95.3	2.9	48.6	115.5	5139	25.4
0	15.5	4.1	42.3	93.7	2.9	48.5	115.5	5147	25.4
90	15.1	4.1	40.3	91.0	2.1	48.7	112.8	5177	25.4
0	17.2	4.1	40.4	94.9	5.6	49.0	127.5	5154	25.4
0	16.1	4.1	40.6	95.2	6.1	48.5	127.5	5139	25.4
90	15.6	4.1	38.6	92.1	4.5	49.1	123.5	5169	25.4
120	14.3	4.1	32.6	86.2	4.8	48.8	123.8	5139	25.4
135	13.1	4.1	33.7	87.4	4.8	49.0	124.4	5139	25.4
150	11.3	4.1	34.1	88.0	4.8	49.2	125.0	5162	25.4
150	11.2	4.1	34.7	88.7	4.8	49.2	125.3	5147	25.4
165	8.8	4.1	32.6	86.7	5.2	48.9	125.4	5101	25.4
165	9.1	4.1	33.8	88.0	5.3	48.9	126.1	5147	25.4
0	18.7	3.4	41.9	101.8	10.1	49.8	150.1	4243	25.4
0	19.3	3.4	41.2	101.4	10.5	49.7	151.0	4273	25.4
90	17.1	4.1	37.2	96.4	9.6	49.6	146.6	5177	25.4
120	15.2	4.1	33.3	92.7	10.3	49.1	147.5	5131	25.4
120	15.5	4.1	32.3	91.6	10.3	48.9	146.8	5124	25.4
135	14.2	4.1	32.4	91.8	10.6	48.8	147.6	5131	25.4
150	12.4	4.1	32.8	92.3	10.6	48.9	148.2	5124	25.4
165	9.8	4.1	32.1	91.8	10.8	48.9	148.9	5124	25.4
175	6.1	4.1	28.8	88.6	10.8	48.9	149.0	5109	25.4
0	18.2	11.4	31.7	91.8	12.0	48.1	150.6	2148	3.2
90	18.0	11.4	31.7	91.0	11.3	47.9	147.2	2148	3.2
0	16.9	33.2	31.4	85.8	4.7	49.7	127.0	6266	3.2
0	17.0	33.4	31.5	85.9	5.0	49.4	127.0	6302	3.2

Orientation (degrees)	Q_{chf} (W/cm^2)	U_{in} (cm/s)	T_{sup} (° C)	T_{surf} (° C)	T_{sub} (° C)	T_{inlet} (° C)	Pressure (kPa)	Re_{DH} (-)	T. S. Height (mm)
90	18.2	32.9	29.7	83.5	4.8	49.0	124.3	6221	3.2
90	18.3	33.6	30.5	84.2	4.8	48.9	124.1	6338	3.2
90	18.0	33.6	30.3	84.0	4.8	48.9	124.2	6338	3.2
180	12.6	32.9	30.9	85.4	5.2	49.3	127.2	6221	3.2
270	10.0	32.5	23.9	79.6	6.1	49.6	131.6	6131	3.2
270	10.3	32.9	24.1	79.5	6.2	49.2	130.8	6212	3.2
0	20.3	33.1	36.3	96.2	10.5	49.4	150.0	6248	3.2
90	20.9	33.4	35.1	94.5	10.1	49.4	147.8	6302	3.2
180	13.8	33.0	28.6	88.5	10.8	49.1	149.7	6239	3.2
270	13.3	33.0	28.2	89.1	12.2	48.8	154.5	6230	3.2

APPENDIX B

CALIBRATION PROCEDURES

The apparatus and procedures used in calibrating the hot wire anemometer, the heater surfaces, the turbine flowmeters, the pressure transducer and the thermocouples are described below.

B.1. Hot wire anemometer calibration

The hot wire anemometer was calibrated to determine its accuracy in measuring the bubble frequency and void fraction over the heated surface. The calibration was performed in a closed vessel containing air and R113, into which air bubbles were introduced, as illustrated in Figure B.1. The calibration consisted of three parts:

(1) Measurement of the step response of the hot wire to a change in the surrounding phase, to determine the usable bandwidth of the sensor.

(2) Calibration of the void fraction calculated from the sensor output.

(3) Calibration of the bubble frequency.

From the calibration, the uncertainty of the hot wire in determining the unsteady and stationary behavior of the vapor and liquid above the heater surface can be evaluated both qualitatively and quantitatively.

B.1.1. Hot wire step response measurement

The response of the hot wire to a step change in the phase of the surroundings was measured in a vessel containing R113 and air to determine the dynamic range of the sensor. Using the CODAS data acquisition system at a sampling rate of 1000 Hz, the time series of the voltage output from the probe was recorded while the hot wire was plunged rapidly in and out of the R113. The time constant of the probe was approximated from repeated measurements of the rise time of the voltage output during step transients. The measured time constant of the hot wire to a step change from liquid to air averaged over ten trials was 0.015 ± 0.003 seconds, while the time constant in going from air to liquid was an average of 0.003 ± 0.002 seconds. Using the slower time constant of a step change from a liquid to a gas as the upper limit to its performance, the dynamic range of the sensor extends out to about 56 Hz.

B.1.2. Void fraction calibration

Despite the finite time response of the hot wire, the transition of the hot wire passing from the liquid to the gas phase can be discerned, since it is generally characterized by a high rate of change in the probe output. The ideal probe response to a gas bubble is a square wave, as shown in Figure B.2, with the voltage rising as it enters the bubble and falling again as the bubble passes. With non-ideal effects such as boiling on the hot wire, turbulence in the bubble wake, stretching of the bubble due to surface tension, and the thermal lag of the probe in its surroundings, the hot wire output more closely resembles that illustrated in the figure. In the signal processing steps used to calculate the void fraction, the sampled hot wire signal, shown in Figure B.3(a) is

differentiated to identify the high rates of change, as shown in Figure B.3(b). Next, suitable upper and lower threshold levels are set on the differentiated signal which identify the transitions from liquid to vapor. The computer code VOID.FOR, given at the conclusion of Appendix B, uses these threshold levels to generate an indicator function time series, with "1" corresponding to the presence of vapor at the sensor, and "0" corresponding to the presence of liquid, as shown in Figure B.3(c). Therefore, when the time derivative of the hot wire output exceeds the established upper threshold, the code assumes the presence of a vapor bubble and assigns a value of "1" to the indicator function, and when the time derivative falls below the lower threshold, the code assumes the presence of liquid and assigns a "0". The generated indicator function series is then averaged over the entire data record to obtain a temporal average of the void fraction. The void fraction calculated using this method is compared in Figure B.4 with the void fraction measured simultaneously using high speed video. The calculated values are generally somewhat higher than those observed on video, due primarily to boiling on the heated wire, and to bubbles passing very close to the probe but not intercepting it. This is particularly true at small void fractions, where the bubbles are smaller relative to the hot wire length and the events are short in duration. Both of these effects result in smaller deflections in the output voltage output compared with those resulting when intercepting larger bubbles, and are often difficult to discern from the small deflections in the output which arise with boiling on the wire.

B.1.3. Peak frequency calibration

The peak frequency is determined from the peak in the power spectral density of the hot wire output. The results of the spectral analyses are compared in Figure B.5 with the average frequency observed visually from high speed photographs. The peak values in the power spectra, shown as the ordinate, were calculated using DADiSP signal processing software for data records approximately thirty seconds long. For the film analysis, the peak bubble frequency was estimated by counting the total number of bubbles passing over the hot wire over three time periods, each approximately one second in duration, then averaging the three results to obtain the value shown as the abscissa in Figure B.5. It should be noted that the measured peak bubble frequencies fall well below the limit to the dynamic range of the hot wire, determined in section B.1.1.

A second smaller peak sometimes appears in the power spectrum, as seen in Figure B.6, with the larger peak at the dominant frequency and the other smaller peak at exactly twice the dominant frequency. This arises from the response of the hot wire to bubbles spaced relatively far apart, as with orientations like the one shown in Figure B.6, which are close to the horizontal facing down position. The actual response of the hot wire to a series of bubbles, shown in Figure B.7, can be broken into two dominant frequency modes. The frequency component of larger amplitude corresponds to the bubble frequency, while the smaller component corresponds to the two dips in the probe response resulting from evaporation on the hot wire and the wake of the passing bubble. For each rise in the hot wire response due to the passing of a bubble, there are two smaller corresponding dips in the probe response, hence the smaller peak in the power spectrum at twice the peak bubble frequency.

B.2. Metal heater surface calibration

The metal heaters were calibrated to determine the heat loss to the surroundings as a function of the heater base temperature. The heater surface was placed facing upward in an open vessel containing stagnant air, with one thermocouple placed within one to two millimeters above the heater surface and another several centimeters away for measuring the bulk air temperature. Power was then supplied to the heater using a variable AC transformer, while the voltage across the heater and across a shunt resistor in series with it were measured directly using a digital multimeter. The thermocouple readings were recorded using the programmable Campbell recording device described earlier in section 4.1.3. The heater was allowed approximately three hours to reach steady state, at which time the measured air temperature and heater temperatures were recorded, as was the voltage across the heater and the current calculated from the voltage across the shunt. The test was then repeated at a slightly higher power increment.

The first law applied to the copper heater, with Joulean heat dissipation in the cartridge heaters gives:

$$\dot{P}_{gen} = q''_{surf} A_{surf} + \dot{Q}_{loss} \qquad \text{(B.1)}$$

The heat flux on the heater surface, q''_{surf} was estimated using a natural convection correlation given by Goldstein, et al. (1973) for a finite heated surface facing upward:

$$Nu_L = 0.54 Ra_L^{\frac{1}{4}} \qquad 10^4 \leq Ra_L \leq 10^7 \qquad \text{(B.2)}$$

The peripheral heater losses were then calculated by subtracting the surface heat transfer rate from the total power input to the heater. An empirical relation was then established

between the temperature at the base of the heater, in °C, and the heater losses, in Watts, based on the calibration curve shown in Figure B.8, as:

$$\dot{Q}_{loss} = 0.064(T_{base} - T_{surr}) - 1.13 \qquad \text{(B.3)}$$

The uncertainty in the loss measurements is perhaps as large as ± 50 %. For a typical value of the base temperature of about 105 °C, however, the uncertainty with such a loss equates to an uncertainty in the surface heat flux of only about ± 1 W/cm^2. Further details on the uncertainty in the calculated surface heat flux due to the losses is given in Appendix C.1.

B.3. Thin film heater calibration

As mentioned in Chapter 4, the linear characteristic of the resistance of the thin film heaters with temperature enables it to be used as a resistance thermometer. The resistance of the heater depends on many factors in addition to the temperature, however, including the heater geometry, film thickness, and manufacturing techniques. As such, each thin film heater must be individually calibrated to determine both the slope and intercept values of the linear characteristic of the film resistance with temperature, represented as follows:

$$R_{film} = a\left(T_{surf} - T_{ref}\right) + b \qquad \text{(B.4)}$$

The foundational work of Oker and Merte (1981) with thin gold film heaters determined that the slope, a, of the characteristic remains virtually constant with use over time, while the intercept, b, can shift with time and use. To determine the characteristic for an

individual thin film heater surface, the calibration consists of a one-time multiple-point calibration of the heater resistance versus temperature to determine the slope, and a single-point measurement of the heater resistance at room temperature performed periodically during testing to determine the intercept. These procedures are described below.

B.3.1. Calibration of the slope of the resistance versus temperature characteristic

The resistance of each gold film heater was determined individually for at least five different temperatures in the range of 20 °C to 90 °C to establish the slope of the resistance versus temperature characteristic. The calibration was done by placing the surface within a large copper vessel and immersing the vessel in a Colora (Model NB-35 640) constant temperature water bath to ensure uniformity of temperature throughout the test surface. At least three hours was allowed for the surface to reach thermal equilibrium with the vessel and the surrounding water bath before recording any measurements.

The electrical circuit used for the resistance measurements is given in Figure B.9. A 12 V battery supplied the DC power to the circuit. A variable resistor set at a nominal value of 800 Ω was used in series with the thin film heater such that the Joulean heat dissipation in the thin film would produce a negligible change in the film temperature, and hence in the measured film resistance. Also in series with the thin film heater was a calibrated shunt resistance of 3.776 Ω ± 0.001 Ω measured at 75 ° F, which was used to measure the current through the circuit. The resistance of the film is then calculated from the following expression:

$$R_{film} = \frac{\Delta V_{film}}{\Delta V_{shunt}} R_{shunt} \qquad \text{(B.5)}$$

B.3.2. Room temperature resistance measurements

The single point calibration circuit is given in Figure B.10. With the heater surface installed in the flow loop, and with the flow loop not yet in operation and nearly in thermal equilibrium with the room air, a small current is passed through the thin film in series with a shunt resistance of 10.0100 Ω ± 0.0005 Ω measured at 70 °F. By measuring the voltage drop across the film relative to that across the shunt resistance, the film resistance is determined from Eqn.(B.5). From the measured heater temperature, assumed equal to that measured at the inlet to the test section, the intercept value of the resistance versus temperature relationship is determined from Eqn. (B.4).

B.4. Flowmeter calibration

Two turbine flowmeters with different linear operating ranges were used in the experimental apparatus, with each calibrated using identical procedures. First, the flowmeter was connected downstream of a gate valve following a straight section of pipe, and then emptied into a container of known volume. The water was then passed through the flowmeter at different rates, and the output of the flowmeter in pulses per second was recorded as a function of the volume flow rate. The volume flow rate was determined from measurements of the volume of water collected divided by the elapsed time. The resulting calibration curve for the smaller capacity flowmeter is given in Figure B.11, along with that for the larger capacity flowmeter in Figure B.12.

The pressure transducer (Heise, ser. no. S6-6914) was calibrated previously using the procedures and apparatus described by both Kirk (1992) and Ervin (1991). The transducer was calibrated in three different orientations, horizontal, vertical up and vertical down, with only a small difference between the three results. The resulting calibration curve for the three orientations is given in Figure B.13. The original calibration, performed in 1988, was checked again in 1993 through measurements of atmospheric and vacuum pressure in the flow loop, using a calibrated mercury barometer accurate to within ± 0.01 inches Hg as a reference. The results are shown in Table B.1.

B.6. Thermocouple calibration

Twenty chromel-constantan (Type E) thermocouples originating from the same spool of 30 gage wire were calibrated against a platinum resistance thermometer (Leeds and Northrup, No. 8163, calibrated by the National Bureau of Standards) by Kirk (1992) and Ervin (1991) in a constant temperature water bath, in a manner similar to that described for the gold film heaters in section B.3.

For purposes of convenience, the internal chromel-constantan thermocouple calibration of the MRL data acquisition system was used instead of the calibration curve for the thermocouple measurements at the various locations in the flow loop. The thermocouple temperatures calculated using the internal MRL calibration compared with the measured curve within ± 0.1 °C over the range of the flow loop operating temperatures. Since this difference is much larger than the uncertainty of ± 0.02 °C associated with the individual thermocouple calibration, the uncertainty in the measured heater and fluid temperatures is ± 0.1 °C.

B.7. Computer Code "VOID.FOR" used for the hot wire data reduction

```
c    Program Title:  VOID.FOR
c    Program Objective:
c
c    (1) Calculates the mean void fraction based on a discrete time series.
c    The program converts the time series into a telegraph signal, 1 corresponding
c    to the presence of vapor, zero corresponding to the presence of liquid.
c    After the conversion, the series of 0's and 1's is averaged to yield
c    the time-averaged void fraction at a point.
c
c    (2)Calculates the average bubble frequency and std. dev.
c
c    (3)Widens the power spectrum band widths.
C
     implicit real*8 (a-h, o-z)
     character*18 datfil1, datfil2
c
     dimension deriv(20000), signal(20000), sigout(20000), power(20000)
     dimension fave(3000), amp(3000)
c
     open(5, file = 'c:\dsp\filinfo.dat')
c     FILINFO.DAT contains info such as the file length, sampling freq.,and the upper
c    and lower trigger levels (for the indicator signal generation),
c     spectral bandwidth, and standard normal area allowance(ref. Bendat, p. 523)....
     read(5,*, end = 999)n, fsamp, trighi, triglo, nwide, znorm
c
c    ...Next, open user-designated data input files...
     write(*,*)" Enter the name of the void fraction input file"
     read(*,100)datfil1
     open(6, file = datfil1)
c
     write(*,*)" Enter the name of the power spectrum input file"
     read(*,100)datfil2
     open(7, file = datfil2)
c
c    ...Open data output files...
     open(8, file = 'c:\dsp\void.out')
c
     open(9, file = 'c:\dsp\compar.out')
c
     read(6,150)(deriv(i),signal(i), i = 1, n)
c    Note: signal(i) is not used, except for later comparison purposes.
c
c    sigout(i) is the indicator function signal generated from the data
c    voidsum = sum of the indicator function signal
```

```
      sigout(1) = 0.d0
      voidsum = 0.d0
c
c     Compare the input raw data samples to the upper and lower trigger levels
      do 20 j = 2, n
        if(deriv(j) .ge. trighi)then
          sigout(j) = 1.d0
        elseif(deriv(j) .le. triglo .and. sigout(j-1) .eq. 1.d0)then
          sigout(j) = 0.d0
        else
          sigout(j) = sigout(j-1)
        endif
c
        voidsum = voidsum + sigout(j)
20    continue
        alpha = voidsum/dfloat(n)
c
c     ....Part II:  Power Spectrum manipulation....
c       i.  Spectral bandwidth is increased
c       ii.  Determines average freq. and std. dev. (1st and 2nd moments)
c
c     ...Limit frequency range of interest to between 0 and 50 Hz....
      nclip = (fsamp/50.0)/2
      nsp = n/2/nclip
      powsum = 0.d0
c
      do 30 k = 1, nsp
        read(7, 300)power(k)
        powsum = powsum + power(k)
30    continue
c
c     ...Subtract off the DC offset at f = 0...
      powsum = powsum - power(1)
c     ....Tau is the reciprocal of the current spectral band width...
      tau = dfloat(n)/fsamp
c
      fsum = 0.d0
      iflag1 = 0
      iflag2 = 0
c
c
      do 40 i = 2, nsp
        f = dfloat(i-1)/tau
        beta = power(i)/powsum
        fsum = fsum + beta
```

```
            if (fsum .ge. znorm .and. iflag1 .ne. 1)then
               iflag1 = 1
               fstd1 = f
            endif
            if (fsum .ge. 0.5 .and. iflag2 .ne. 1)then
               fmean = f
               iflag2 = 1
            endif
            if (fsum .ge. (1 - znorm))then
               fstd2 = f
               goto 5
            endif
40    continue
c
5     stddev = (dabs(fstd1 - fmean) + dabs(fstd2 - fmean))/2
c
      iband = 0
      fband = 0.d0
      avepow = 0.d0
      pmax = 0.d0
      fmax = 0.d0
c     ...Spectrum "smoothing" section...
      do 50 j = 2, nsp
         f = dfloat(j-1)/tau
         fband = fband + f
         avepow = avepow + power(j)
         if(j/nwide*nwide .eq. j)then
            iband = iband + 1
            fave(iband) = fband/dfloat(nwide)
            amp(iband) = avepow
            fband = 0.d0
            avepow = 0.d0
               if(amp(iband) .gt. pmax)then
                  pmax = amp(iband)
                  fmax = fave(iband)
               endif
         endif
c
50    continue
c
c
      write(8,400)alpha, fmean, stddev, fmax, pmax
c
c
      close(8)
```

```
c
c     write(*,*)" Enter the name of the smoothed spectrum output file"
c     read(*,100)outfil
      open(8, file = 'c:\dsp\psd.out')
c
      write(8,200)(fave(ipr),amp(ipr), ipr = 1, iband)
c
c     ....Compare the telegraph signal with the original signal...
      write(9,200)(signal(jpr), sigout(jpr), jpr = 1, int(fsamp))
c
999   write(*,*)"Program is finished"
c
100   format (a18)
150   format (2e20.8)
200   format (2f12.6)
300   format (e20.6)
400   format (' Time-averaged void fraction, ALPHA = ',f8.5//
     #    ' Calculated mean bubble frequency, FMEAN = ',f8.3/
     #    ' Calculated standard deviation, STDDEV = ', f8.4//
     #    ' Smoothed peak frequency, FMAX = ', f8.3/
     #    ' Smoothed peak amplitude, PMAX = ', f8.5)

      end
```

Transducer Reading (Volts)	Calculated pressure (psia)	Barometer Reading (psia)	Deviation (± psia)
2.3220	14.15	14.17	- 0.02
2.3650	14.41	14.39	+ 0.02
2.3390	14.25	14.25	0.00
-0.0480	0.06	0.09*	-0.03

Test dates: Feb. 12-16, 1993

*-Measured using a Heise pressure gage (uncertainty ± 0.025 psia)

Table B.1. Calibration check of Heise pressure transducer S6-6914

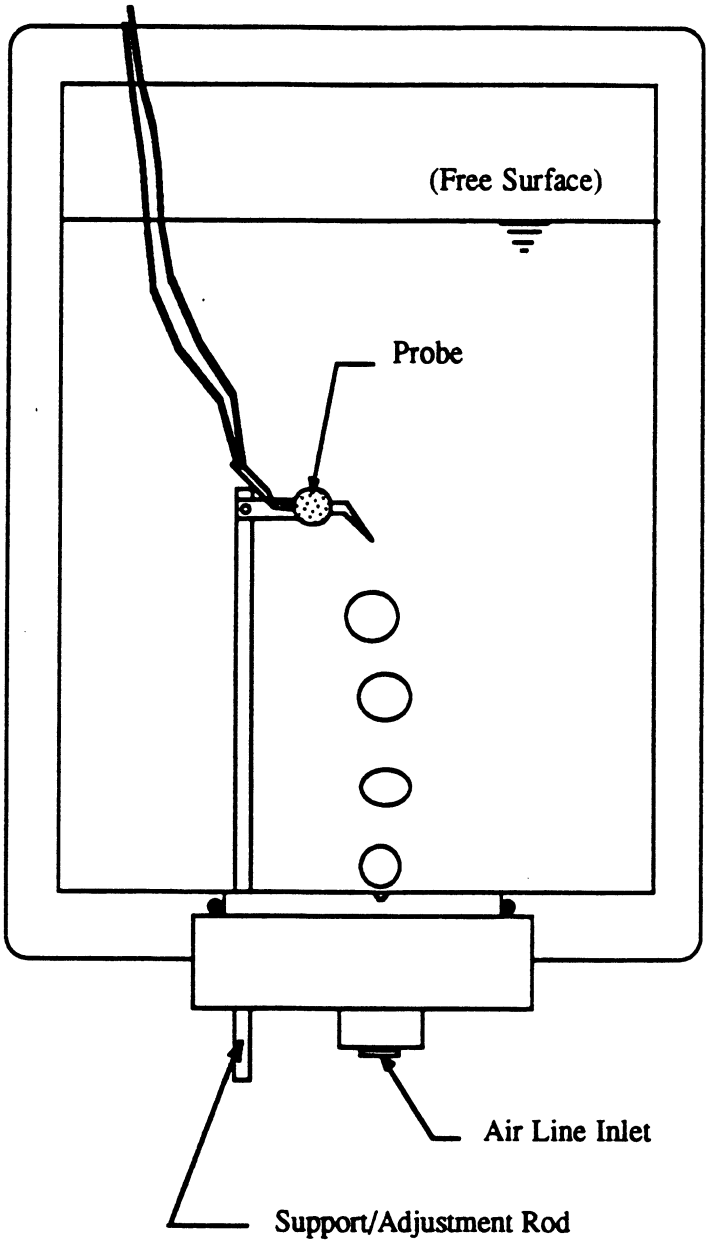

Figure B.1. Illustration of the test vessel used for the hot wire anemometer calibration.

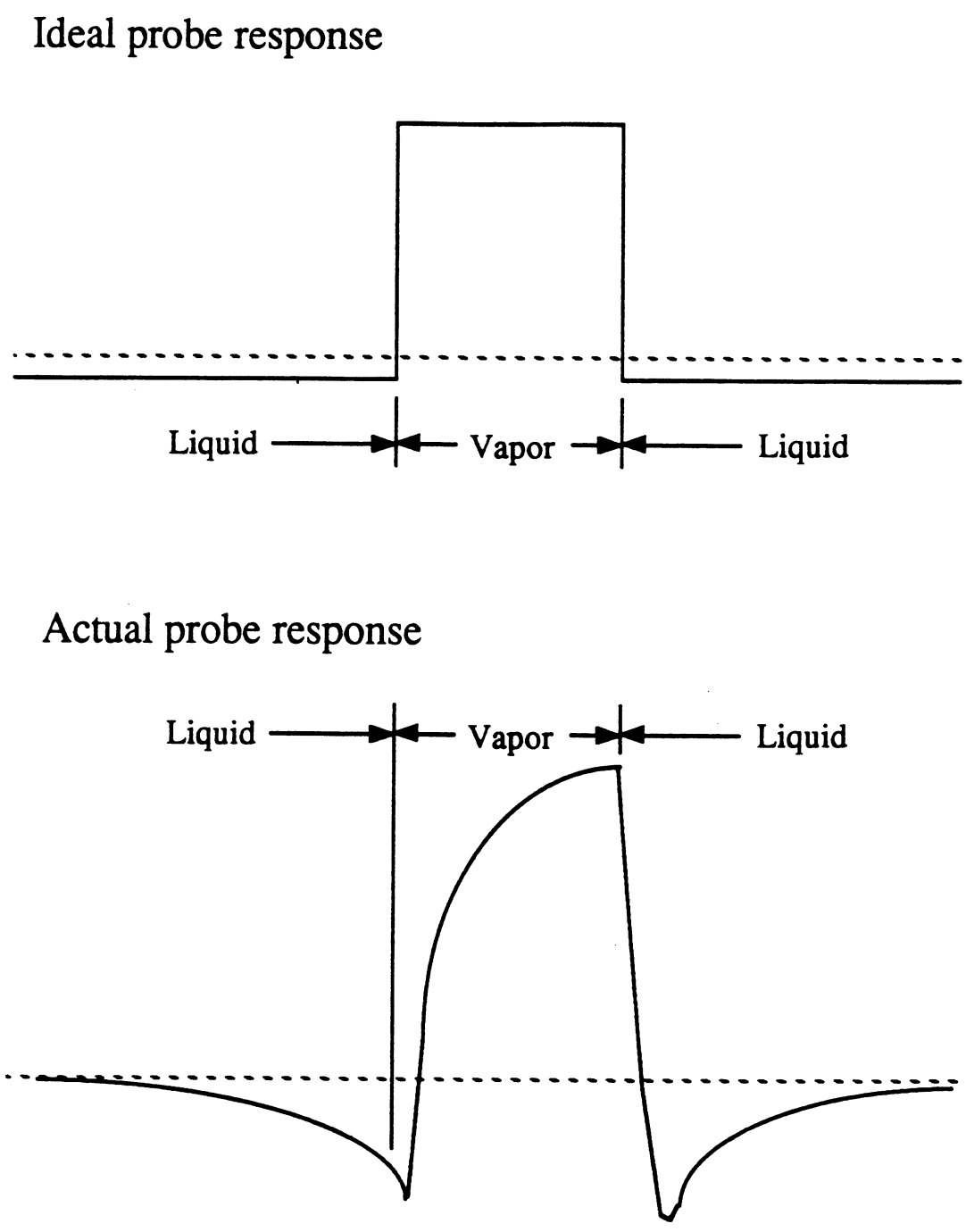

Figure B.2. Typical response of the hot wire anemometer to the passage of a bubble.

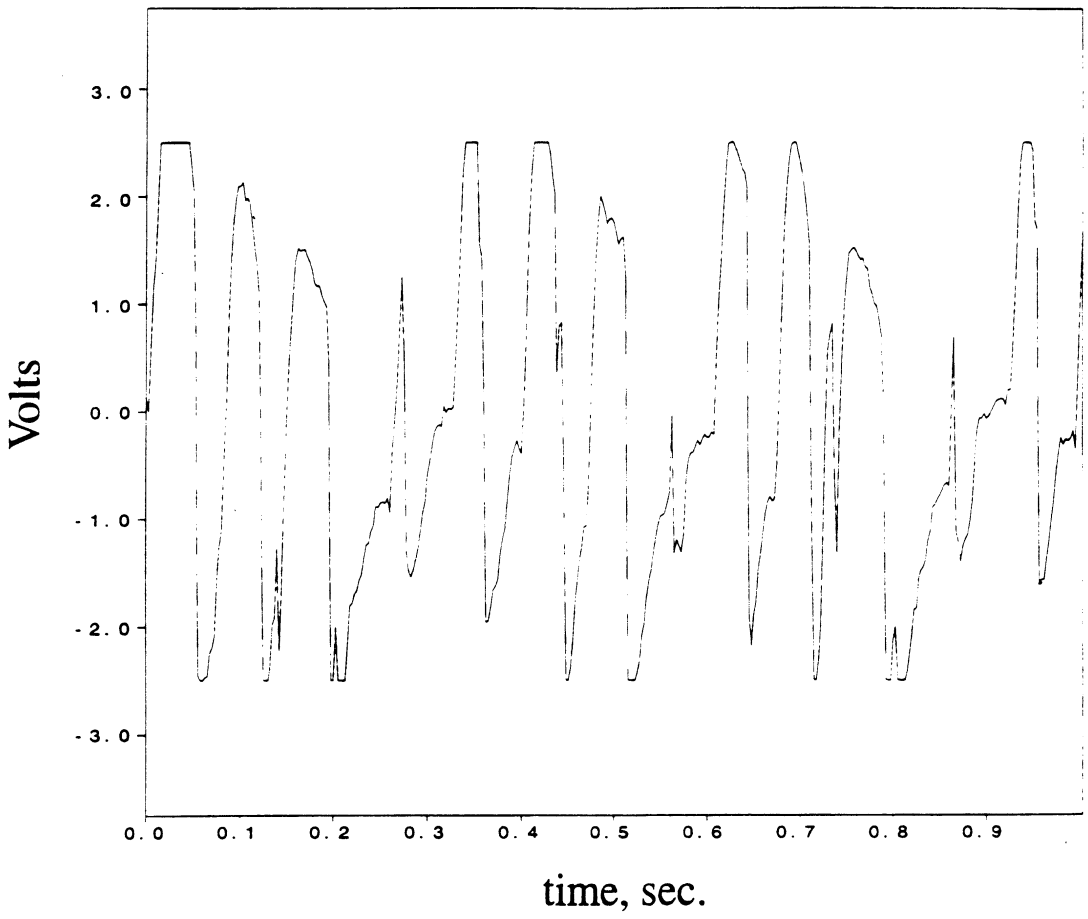

Figure B.3(a). Sampled output signal from the hot wire anemometer

Figure B.3. Example of the signal processing steps used to calculate the void fraction

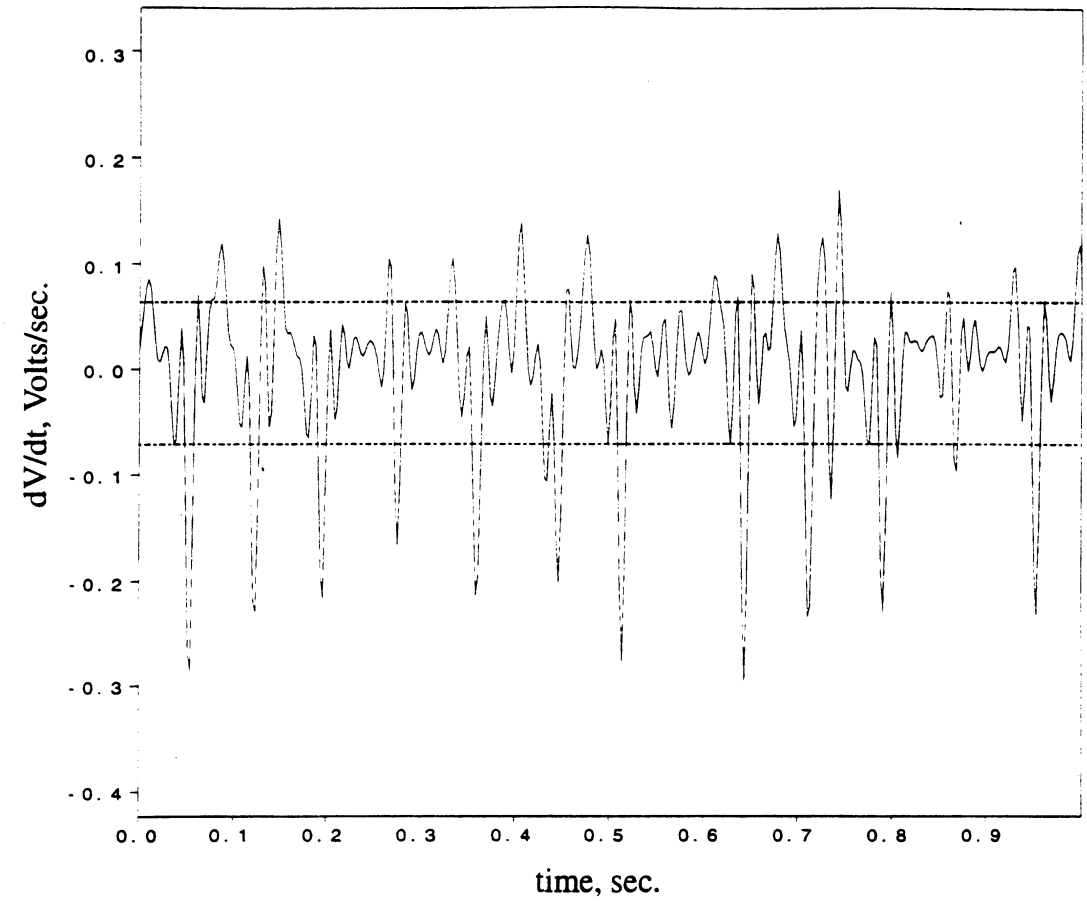

Figure B.3(b). Differentiation of the sampled hot wire signal

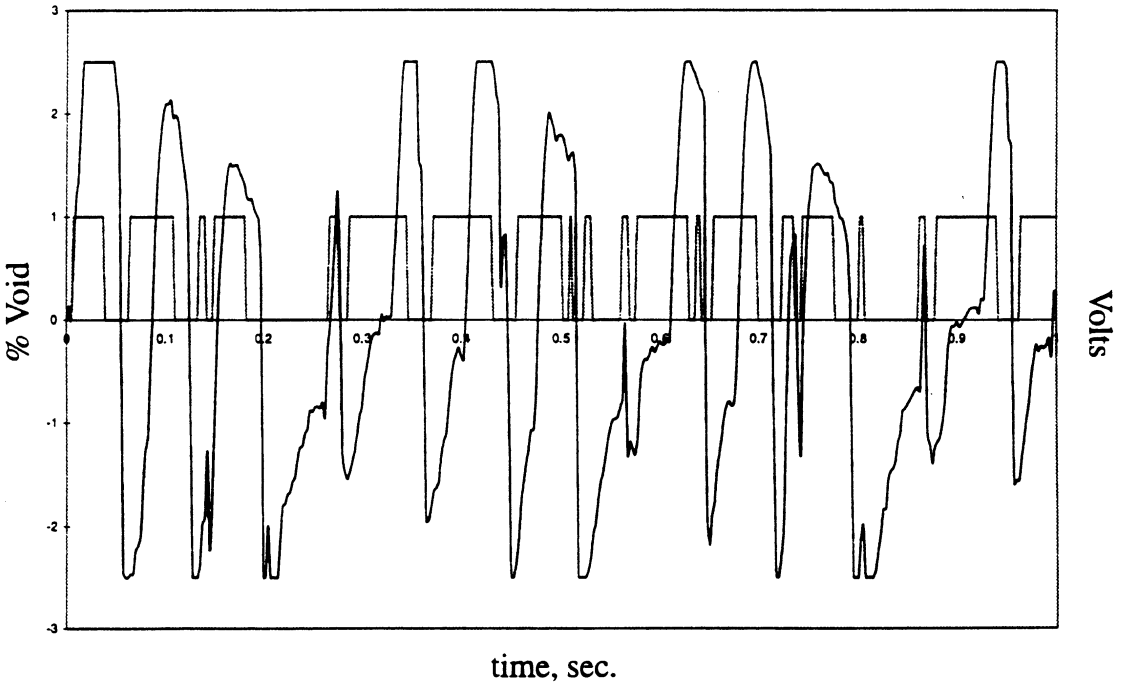

Figure B.3(c). Calculated indicator function signal compared with the original signal

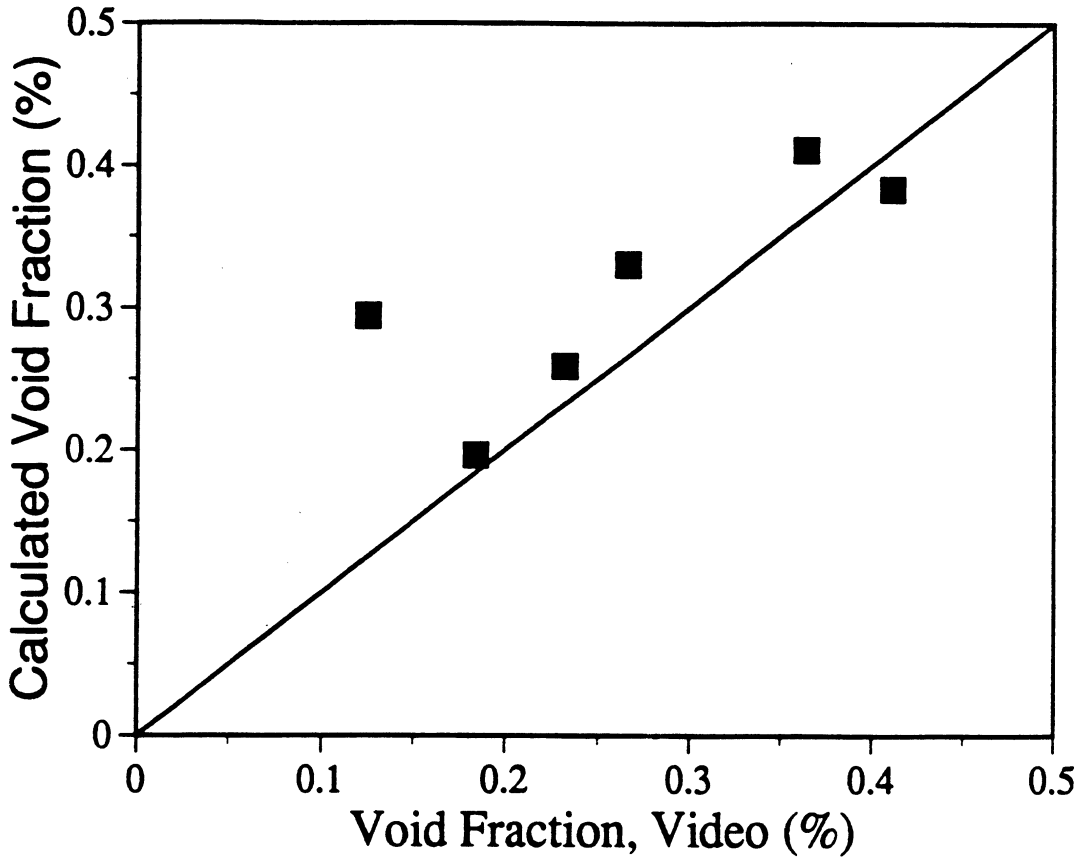

Figure B.4. Calibration of the void fraction measurements

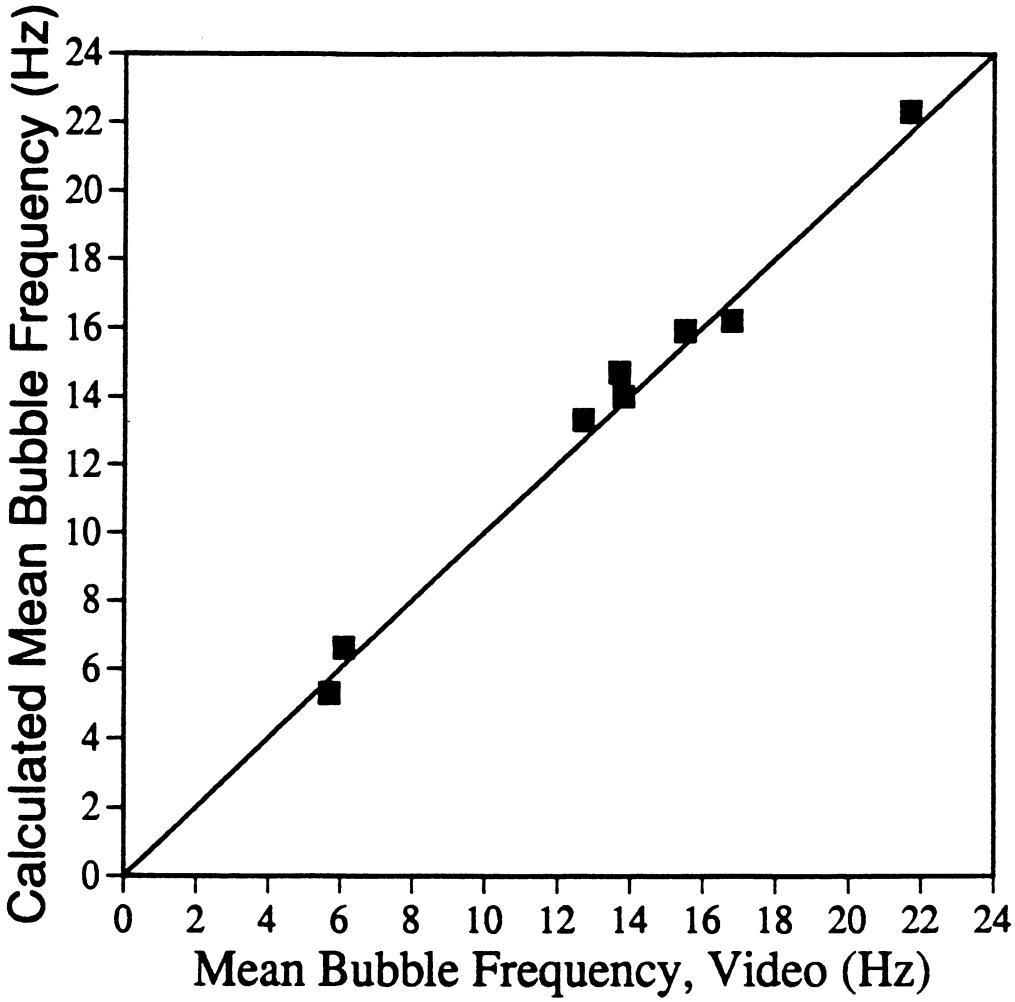

Figure B.5. Calibration of the peak bubble frequency measurements

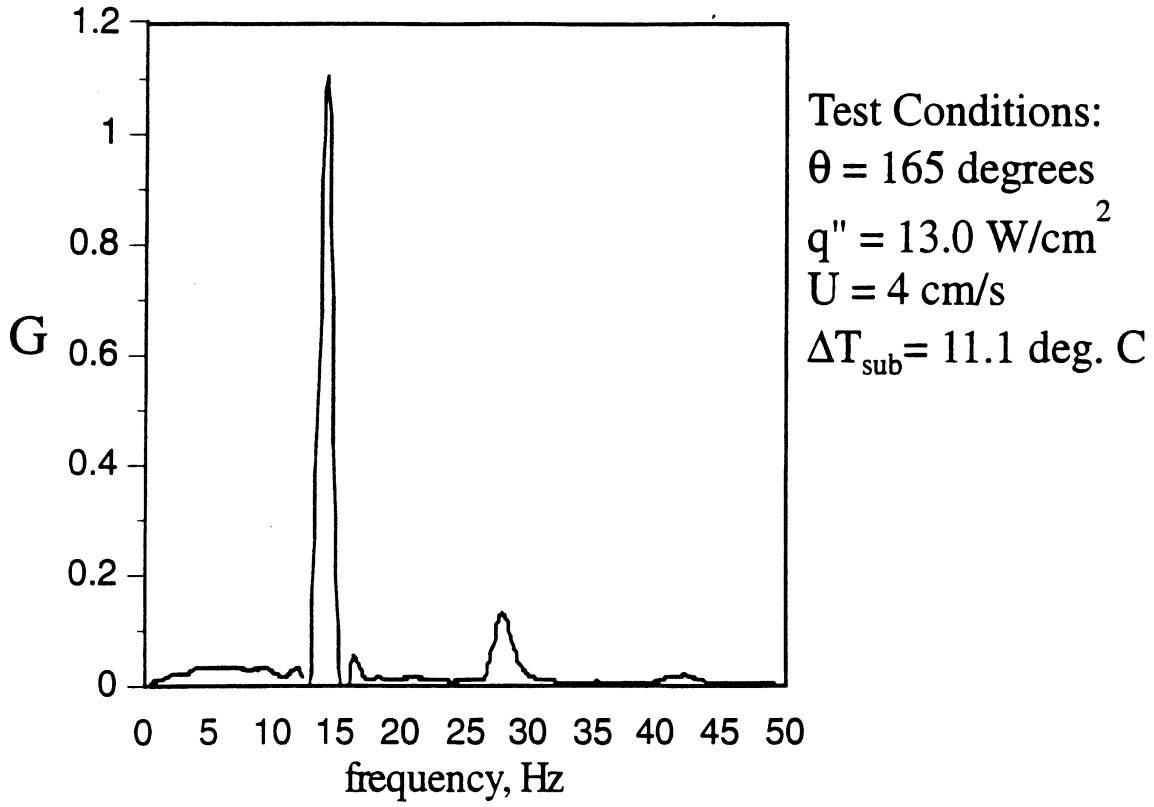

Figure B.6. Example of the autospectrum, showing a second peak frequency

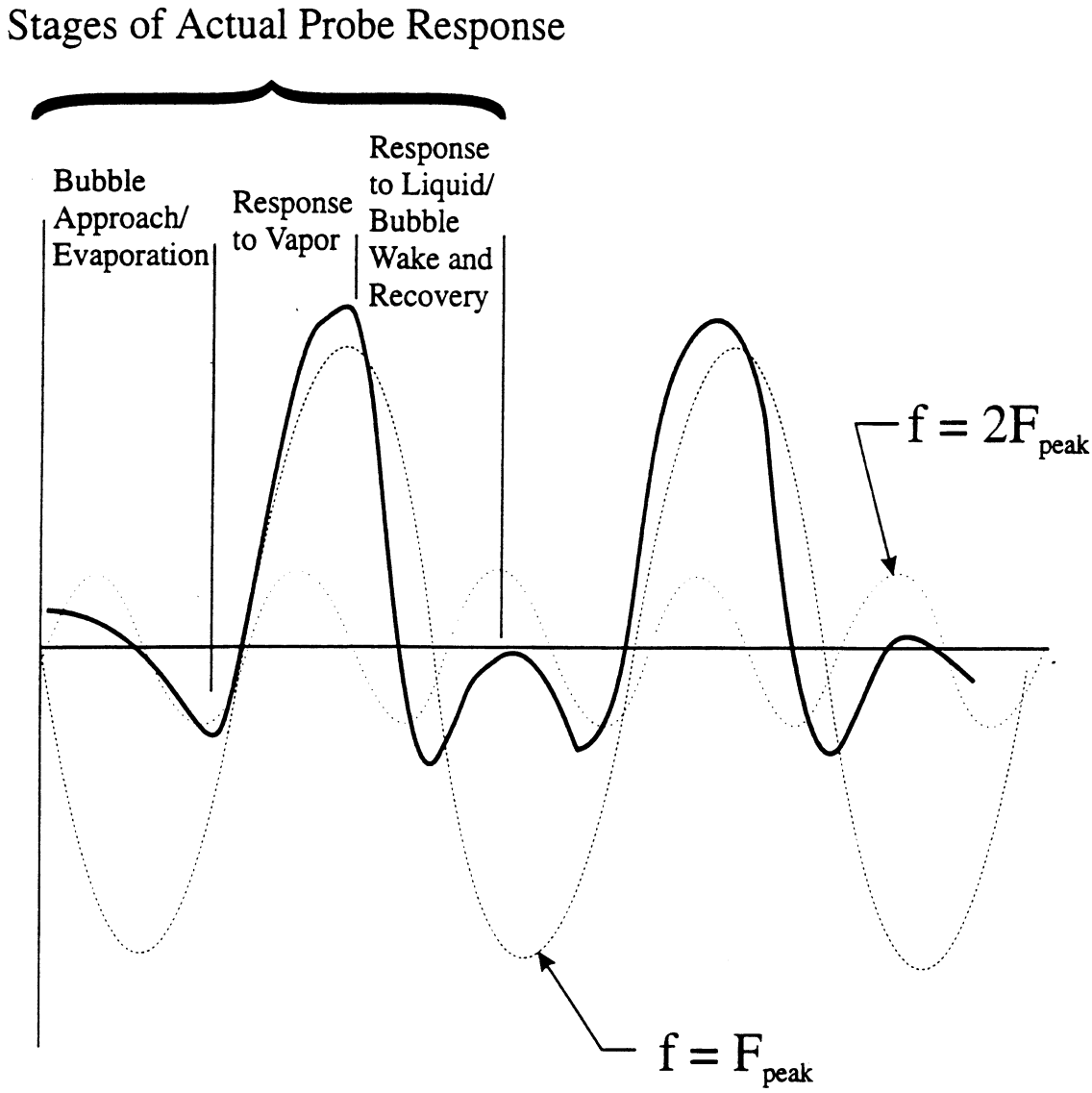

Figure B.7. Illustration showing two primary frequency modes in the hot wire output

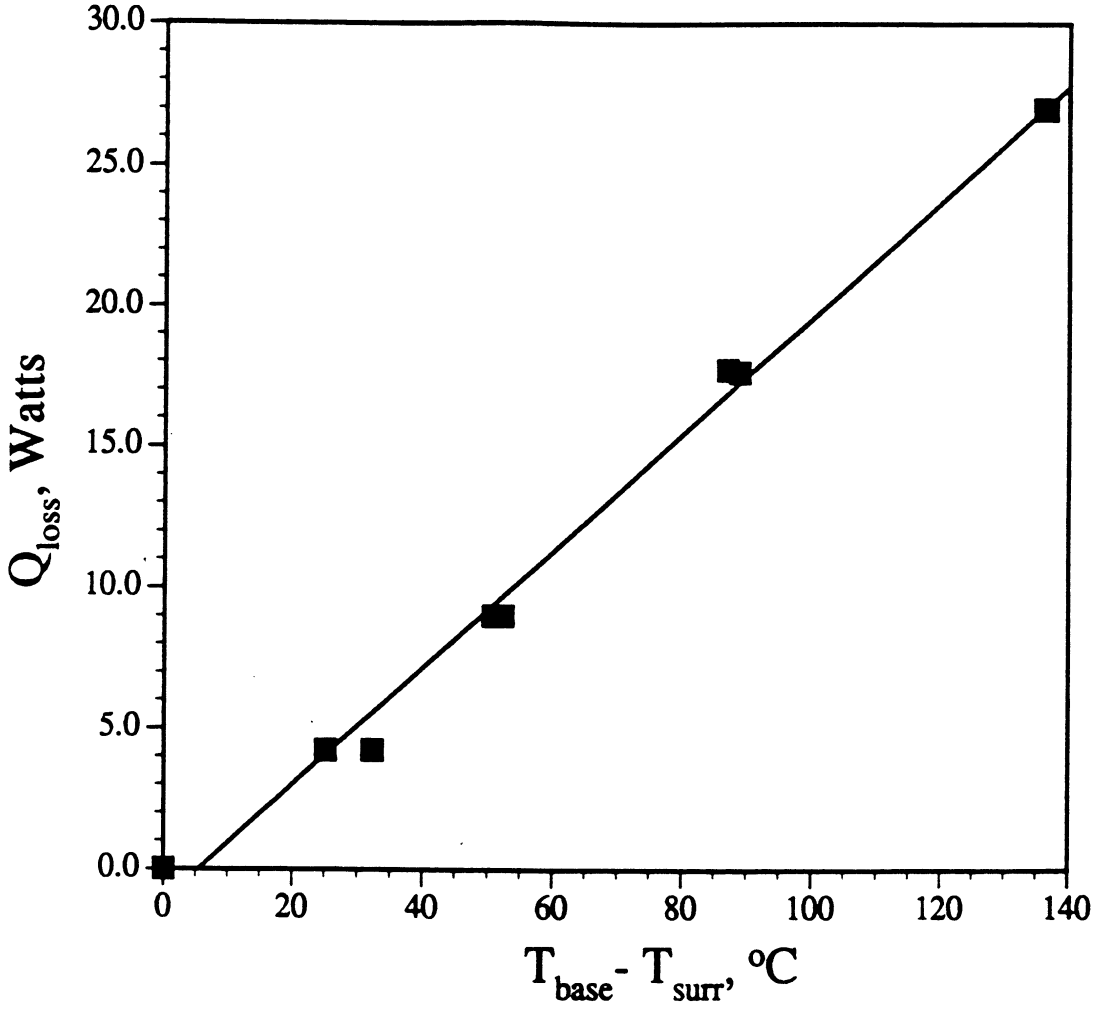

Figure B.8. Calibration curve for the metal heaters: peripheral heat loss versus base temperature difference

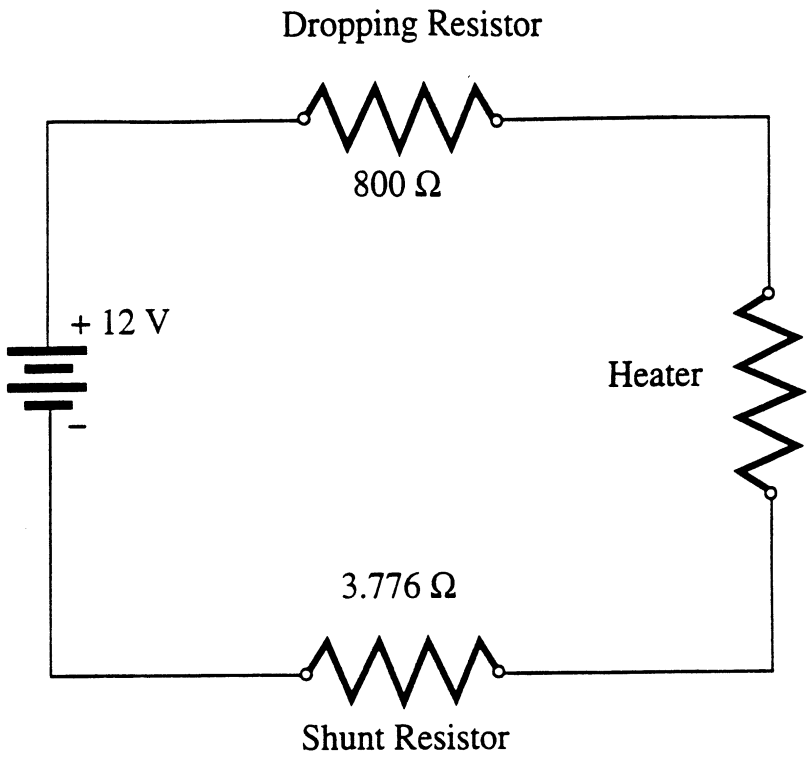

Figure B.9. Schematic of the electrical circuit used for the gold film heater calibration

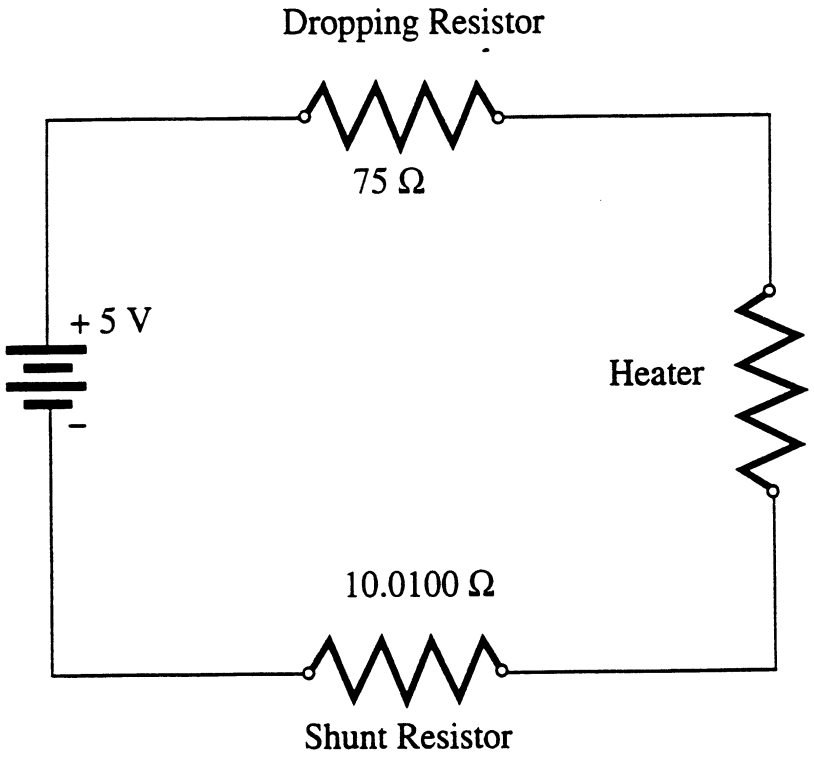

Figure B.10. Schematic of the electrical circuit used for the single-point calibration

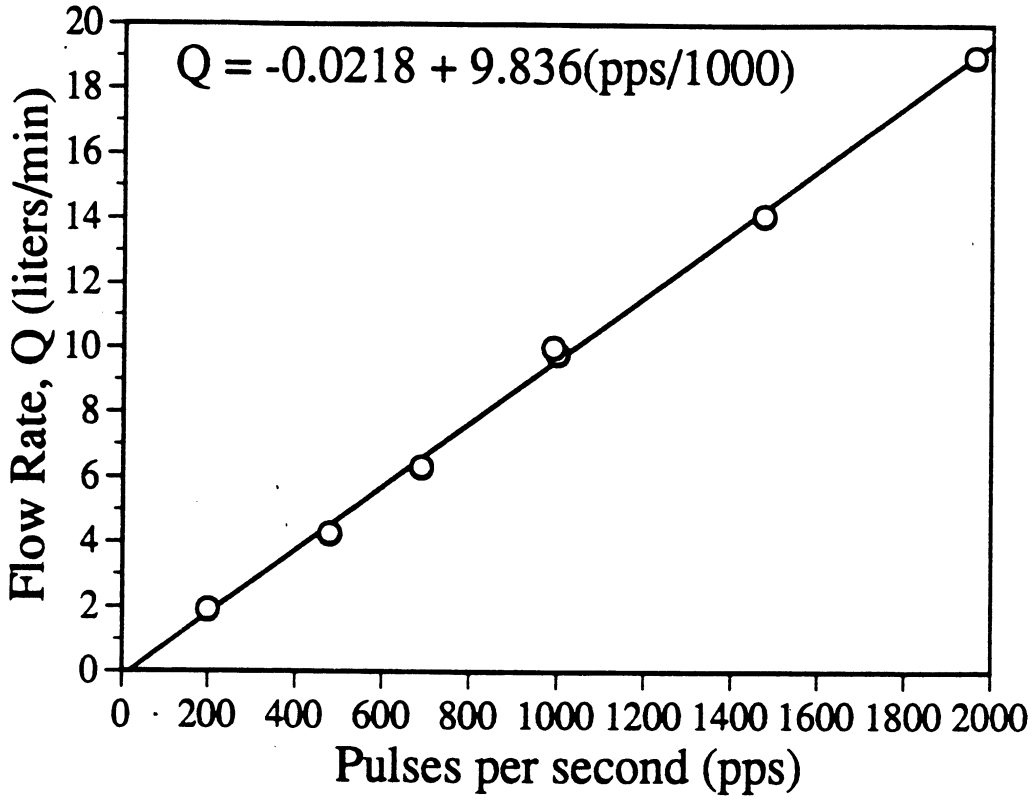

Figure B.11. Calibration curve for the lower capacity flowmeter

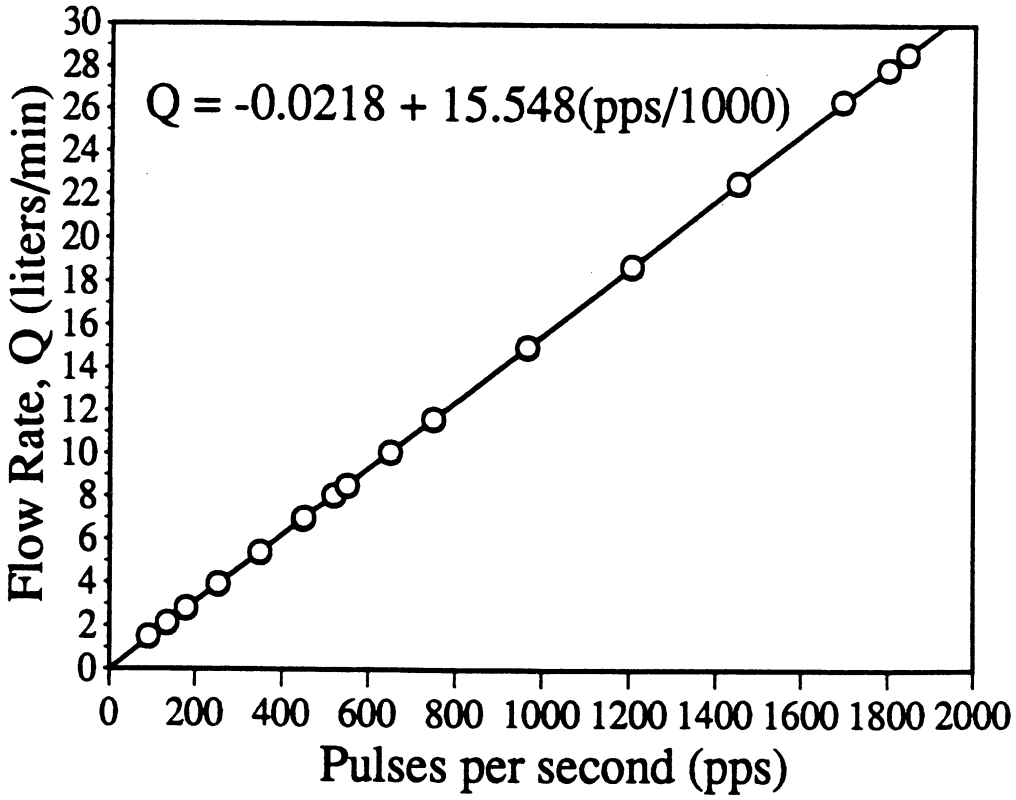

Figure B.12. Calibration curve for the higher capacity flowmeter

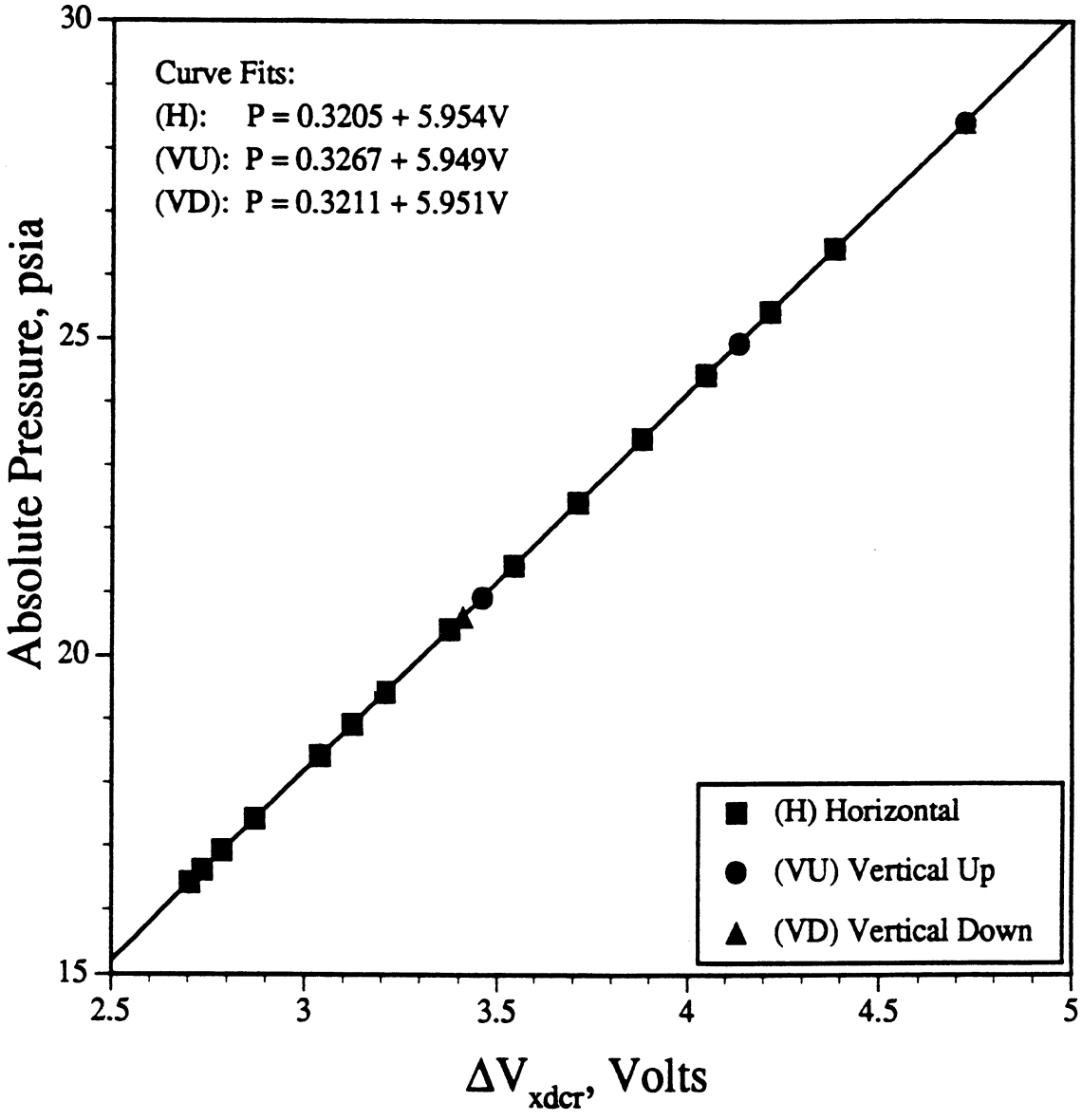

Figure B.13. Calibration curve for the pressure transducer (S6-6914)

APPENDIX C

UNCERTAINTY ANALYSIS

If a quantity, θ, depends on several measured quantities as follows:

$$\theta = f(a,\ b,\ c,\ \ldots) \qquad \text{(C.1)}$$

then the percent uncertainty in θ attributable to the uncertainty in a single measured quantity, a, can be expressed as:

$$\varepsilon_a = \frac{\delta\theta\big|_{b,c,\ldots}}{\theta} = \frac{1}{\theta}\delta\big(f(a+\delta a,\ b,\ c,\ \ldots)\big) \qquad \text{(C.2)}$$

where the δ denotes the perturbation, or uncertainty. If the uncertainty is not biased, and the respective uncertainties in the independent quanties a, b, c, etc. are random, then the average percent uncertainty in the measured mean value of θ can be expressed as the root mean square (rms) of the individual uncertainties as:

$$\varepsilon_T = \sqrt{\varepsilon_a^2 + \varepsilon_b^2 + \varepsilon_c^2 + \ldots} \qquad \text{(C.3)}$$

Using this method, the uncertainties in the experimental measurements are evaluated in the following sections.

C.1. Metal heater measurements

C.1.1. Surface heat flux

The surface heat flux is determined from the total power input minus the peripheral heat loss, according to Eqn. (4.2). The percent uncertainty in the surface heat flux can then be represented by:

$$\varepsilon_{q''} = \left(\varepsilon_A^2 + \varepsilon_{Pin}^2 + \varepsilon_{Qloss}^2\right)^{\frac{1}{2}} \qquad \text{(C.4)}$$

Since the heat flux relates inversely to the surface area, the percent uncertainty attributable to the surface area is expressed as follows:

$$\varepsilon_A = \left(1 + \frac{\delta A_s}{A_s}\right)^{-1} - 1 \approx \frac{\delta A_s}{A_s} \qquad \text{(C.5)}$$

The uncertainty in the surface area is about 0.1 cm^2 out of a mean total surface area of 7.25 cm^2. The percent uncertainty in the heat flux due to the uncertainty in the power input to the heater is given by:

$$\varepsilon_{Pin} = \frac{\delta \dot{P}_{in}}{q''_S A_S} \qquad \text{(C.6)}$$

where the uncertainty in the total power input depends on the uncertainties in the measured voltage and current as:

$$\delta \dot{P}_{in} = \dot{P}_{in}\left(\varepsilon_V^2 + \varepsilon_I^2\right)^{\frac{1}{2}} \qquad \text{(C.7)}$$

First, the uncertainty due to the voltage arises from the fluctuations in the output of the variable AC power supply, which are large compared to the uncertainties in the voltage measurement. Since the power is proportional to the voltage squared, the uncertainty associated with the fluctuations in the voltage are given by:

$$\varepsilon_V = \frac{2\delta V}{V} + \frac{(\delta V)^2}{V^2} \approx \frac{2\delta V}{V} \qquad \text{(C.8)}$$

The fluctuations in the voltage were usually ± 0.5 V or less. Second, the uncertainty in the total power input due to the uncertainty in the measured current is given by:

$$\varepsilon_I = \frac{\delta I}{I} \qquad \text{(C.9)}$$

The uncertainty in the ammeter reading is ± 0.02$\dot{5}$ amps. Eqn. (C.9) has a different form than Eqn. (C.8), since no corresponding uncertainty in the measured voltage results from the uncertainty in the current. The opposite is not true, however, given the nature of the uncertainty in the voltage.

The percent uncertainty in the surface heat flux due to the uncertainty in the peripheral heat loss, which generally makes up the largest part of the total uncertainty, is given by:

$$\varepsilon_{Qloss} = \frac{\delta \dot{Q}_{loss}}{q''_S A_S} \qquad \text{(C.10)}$$

The uncertainty in the peripheral heat loss depends on the percent uncertainty in the heat loss calibration

$$\delta \dot{Q}_{loss} = \dot{Q}_{loss}\, \varepsilon_{cal} \qquad \text{(C.11)}$$

The percent uncertainty in the calibrated heat loss was estimated to be about ± 50%.

The total uncertainty in the surface heat flux is calculated for two representative operating conditions in section C.1.3.

C.1.2. Surface temperature

The surface temperature was calculated from a linear extrapolation of the two thermocouple temperatures closest to the heater surface as follows:

$$T_{surf} = \frac{T_1 - T_2}{\Delta L_{1-2}} \Delta L_{1-surf} + T_1 \qquad \text{(C.12)}$$

The uncertainty in the heater surface temperature is therefore dependent on the uncertainties in the placement of the thermocouples and the uncertainty in the measured heater temperatures. The absolute uncertainty in the surface temperature is given by:

$$\delta T_{surf} = \left((\varepsilon_{L12} \Delta T_{12})^2 + (\varepsilon_{L1surf} \Delta T_{12})^2 + \delta T_1^2 + \delta T_2^2 \right)^{\frac{1}{2}} \qquad \text{(C.13)}$$

The uncertainty in the surface temperature due to the uncertainty in the placement of the thermocouples is represented in the first two terms on the right hand side. The magnitude of these two depends on the surface heat flux, as that affects the temperature difference between T_1 and T_2, ΔT_{12}. The uncertainty in the placement of the thermocouples is as follows:

$$\varepsilon_{L12} \approx \frac{\delta(\Delta L_{1-2})}{\Delta L_{1-2}} = \frac{0.018 \text{ inches}}{0.375 \text{ in.}} = 0.048 \qquad \text{(C.14)}$$

and

$$\varepsilon_{L1surf} = \frac{\delta(\Delta L_{1-surf})}{\Delta L_{1-surf}} = \frac{0.007 \text{ in.}}{0.050 \text{ in.}} = 0.140 \qquad \text{(C.15)}$$

The total uncertainty in the surface temperature for representative operating conditions is calculated in section C.1.3, given below.

C.1.3. Uncertainty calculations for two representative operating points of the metal heater

The uncertainty in the surface heat flux and surface temperature of the metal heater at two representative operating conditions, one at a relatively high heat flux, the other at a relatively low heat flux, is calculated as follows:

Case 1: Orientation = 175 deg.; U_{in} = 7.3 cm/s; ΔT_{sub} = 11.1 °C

ΔV_{heat} = 51.6 V ± 0.5 V

I_{heat} = 2.17 A ± 0.025 A

T_1 = 82.1 °C ± 0.12 °C

T_2 = 85.4 °C ± 0.12 °C

Q_{loss} = 13.6 W ± 6.8 W

q''_{surf} = 13.6 W/cm^2 ± 1.3 W/cm^2 (± 9.5 %)

T_{surf} = 81.7 °C ± 0.5 °C

Case 2: Orientation = 90 deg.; U_{in} = 32.5 cm/s; ΔT_{sub} = 11.1 °C

ΔV_{heat} = 81.5 V ± 0.5 V

I_{heat} = 3.45 A ± 0.025 A

T_1 = 83.2 °C ± 0.12 °C

T_2 = 91.9 °C ± 0.12 °C

Q_{loss} = 18.8 W ± 9.4 W

q''_{surf} = 36.2 W/cm^2 ± 1.7 W/cm^2 (± 4.8 %)

T_{surf} = 82.1 °C ± 1.3 °C

Taking the arithmetic average of the two results yields a mean uncertainty in the surface temperature of ± 0.9 °C, and a mean uncertainty in the surface heat flux of ± 1.5 W/cm^2

C.2. Hot wire measurements

C.2.1. Peak bubble frequency

The uncertainty in the peak bubble frequency was estimated by assuming an exponential distribution in the calculated power spectral density (psd) about the mean, or peak frequency. First, the peak frequency was calculated from a weighted average, using the psd as the weighting function. The psd distribution was then assumed to be centered about the peak value according to the following generalized expression:

$$\beta(f / F) = \beta_0 e^{-f/F} \qquad \text{(C.16)}$$

where β_0 is the peak value of the psd, and F is a characteristic frequency evaluated from the measured psd distribution. The uncertainty in the peak frequency was calculated by

determining the frequency component whose magnitude is at least 10% lower than the peak frequency component, or, equivalently, whose psd is 81% of the peak in the psd distribution. This is evaluated through an integration of the psd distribution.

The uncertainty in the peak frequency increases with increasing values of F, which is a function of the scatter in the psd about the peak value. For heater surface orientations close to the horizontal facing downward position, for example, the peak frequency is very sharply defined, and the associated uncertainty is on the order of ± 0.2 Hz. As the vertical orientation is approached, however, the scatter in the psd distribution increases, and the uncertainty is about ± 2.0 Hz.

C.2.2. Void Fraction

The uncertainty in the void fraction measurements arises from the subjectivity of establishing the upper and lower thresholds on the derivative of the hot wire output, which are used to differentiate the liquid and vapor phases. The uncertainty was quantified by varying the upper and lower thresholds a reasonable amount and evaluating the change in the calculated void fraction. A reasonable variation in the upper and lower thresholds was assumed to be ± 0.005 V/sec. In general, a variation in the lower threshold value produced a smaller change in the void fraction than a variation in the upper threshold, since the rates of change in the decreasing direction, when the probe reenters the liquid phase, are generally much greater than in the increasing direction. An analysis of twenty different data sets yielded an uncertainty of approximately ± 0.045, or ± 10 %.

C.3. Thin gold film heaters

A detailed uncertainty analysis of the measured heat flux and mean film temperature for the thin gold film heaters is given in Kirk (1992). The results of this analysis are summarized below.

C.3.1. Surface heat flux

The uncertainty in the mean heat flux arises from uncertainties in the measured voltage and current, in the heat loss estimates, and in the size of the heater. These factors produce a combined uncertainty of ± 0.24 W/cm^2. Since losses were neglected completely in the heat flux measurements given in Appendix A, Table A.3, an additional uncertainty of approximately + 0/- 0.5 W/cm^2 must be added to that, resulting in a total uncertainty of about + 0.24/- 0.74 W/cm^2 in the measured surface heat flux.

C.3.2. Mean film temperature

The uncertainty in the measured mean film temperature comes from the uncertainty in the calibration of the heater resistance, described in section B.3, and in the uncertainty in the data acquisition system. The combined uncertainties associated with the measurement of the voltage and current in the calibration produce an uncertainty in the measured temperature of approximately ± 0.4 °C. The uncertainty in the calculated resistance using the MRL datalogger adds an average of about ± 0.6 °C uncertainty to the total, giving a combined average uncertainty in the measured surface temperature of ± 1.0 °C.

C.4. Bulk liquid subcooling

The uncertainty in the bulk liquid subcooling is determined from the uncertainties in the pressure and temperature measured at the inlet to the test section. The uncertainty in the subcooling can be expressed as follows:

$$\delta(\Delta T_{sub}) = \left((\delta T_{in})^2 + \left(\left(\frac{dT}{dP} \right)_{sat} \delta P_{in} \right)^2 \right)^{\frac{1}{2}} \qquad \text{(C.17)}$$

where

$$\delta P_{in} = \frac{dP}{dV} \delta V_{xdcr} = (45.311 \text{ kPa / V}) \cdot (\pm\ 0.003 \text{ V}) = \pm\ 0.14 \text{ kPa} \qquad \text{(C.18)}$$

Assuming an uncertainty in the measured inlet temperature of ± 0.12 °C, the estimated uncertainty in the bulk liquid subcooling is approximately ± 0.22 °C.

APPENDIX D

ELECTRICAL CIRCUIT SCHEMATIC DIAGRAMS

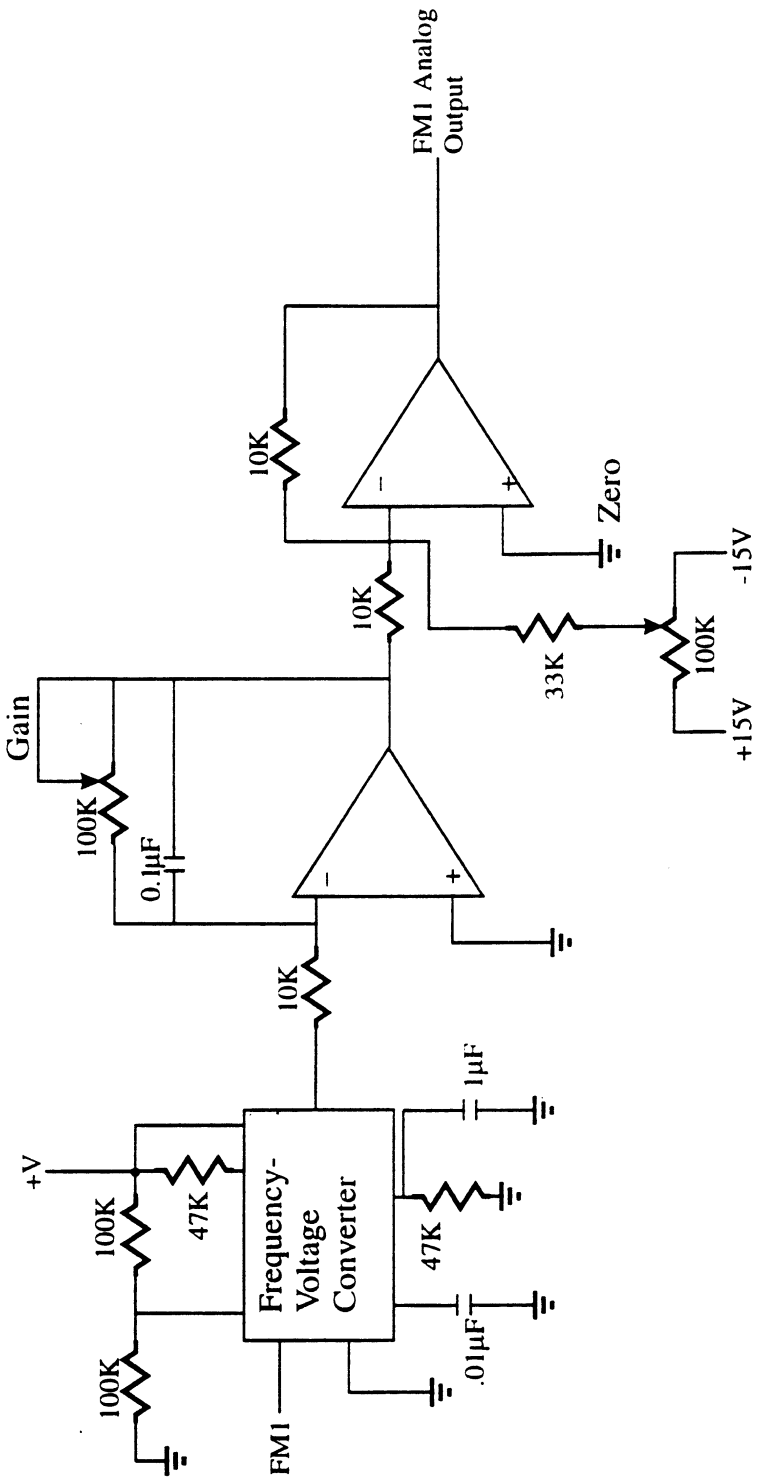

Figure D.1. Schematic of the signal conditioner circuit for the Turbine Flowmeter. Page 1 of 4.

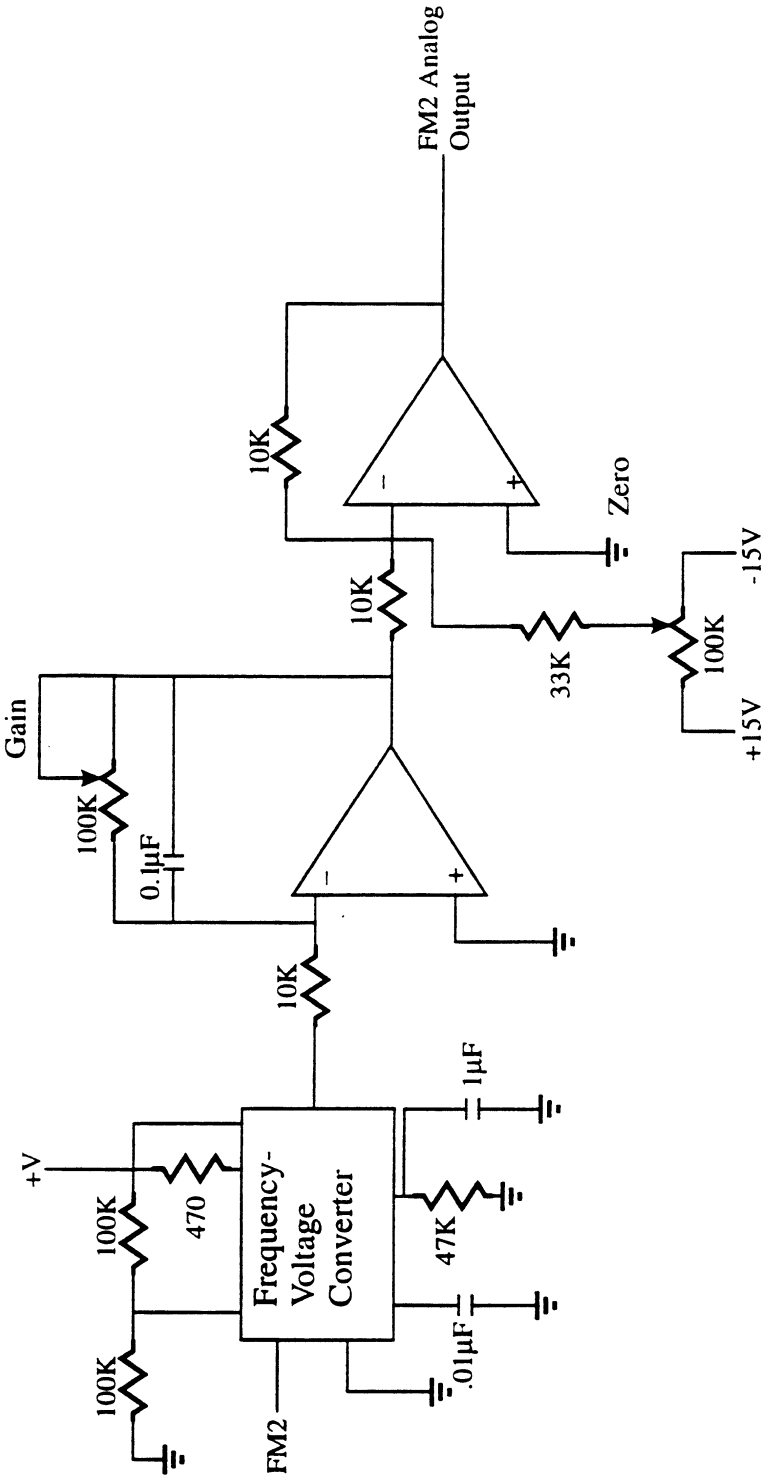

Figure D.1. Schematic of the signal conditioner circuit for the Turbine Flowmeter. Page 2 of 4.

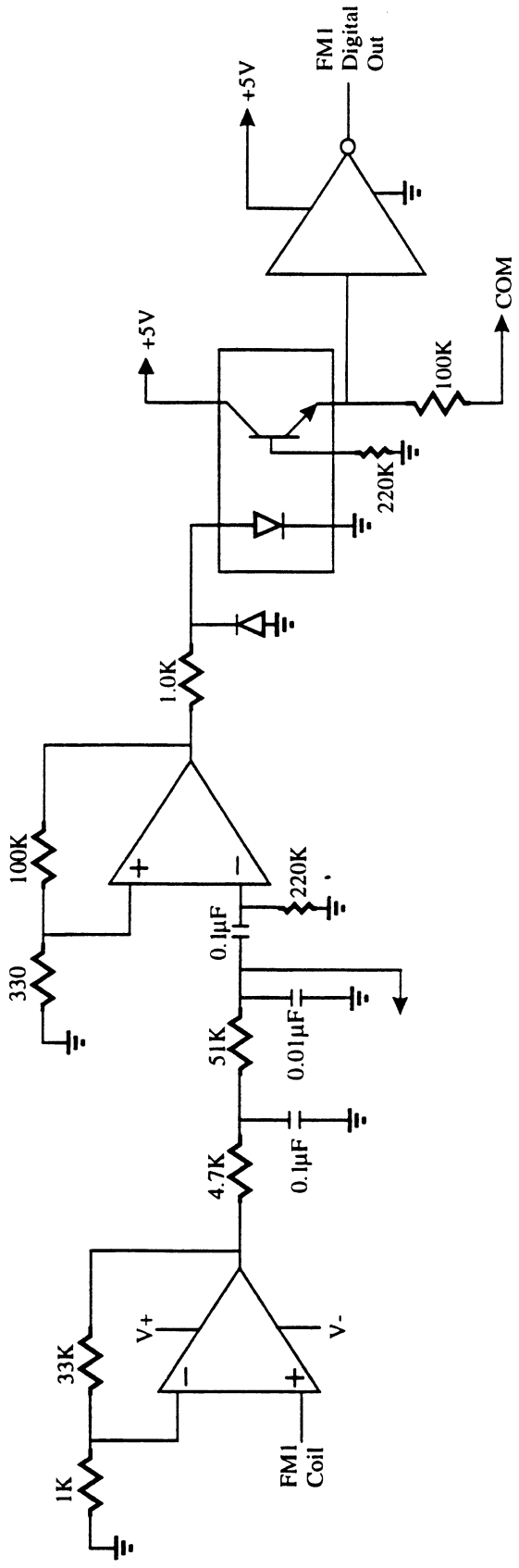

Figure D.1. Schematic of the signal conditioner circuit for the Turbine Flowmeter. Page 3 of 4.

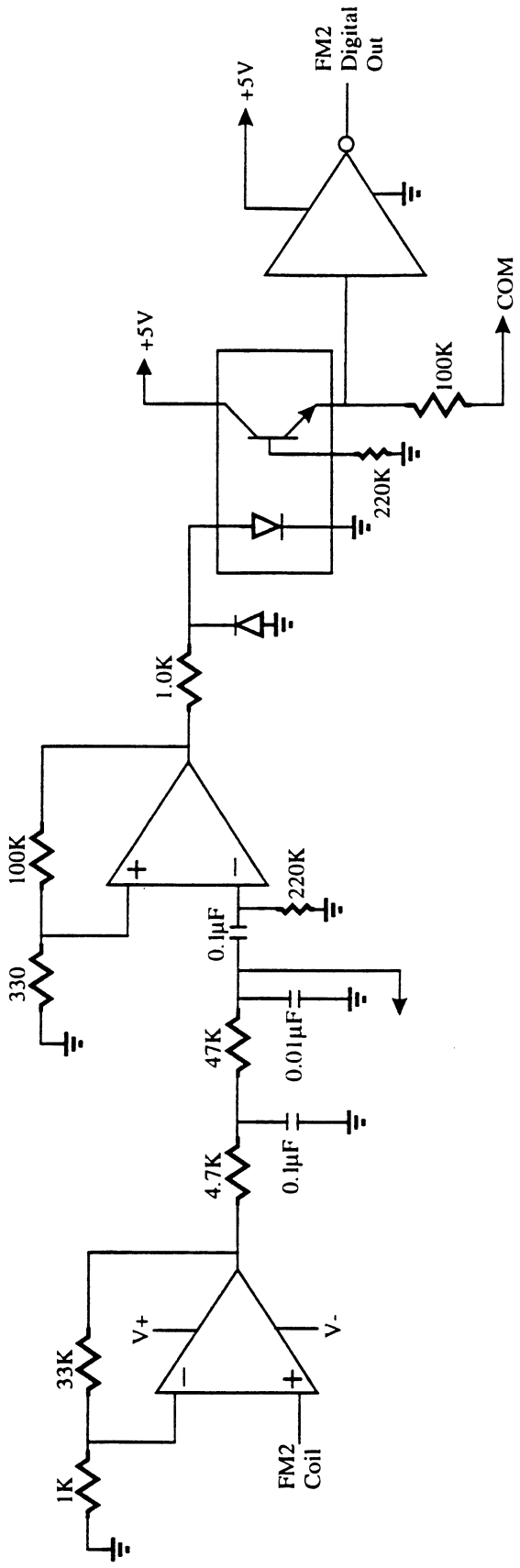

Figure D.1. Schematic of the signal conditioner circuit for the Turbine Flowmeter. Page 4 of 4.

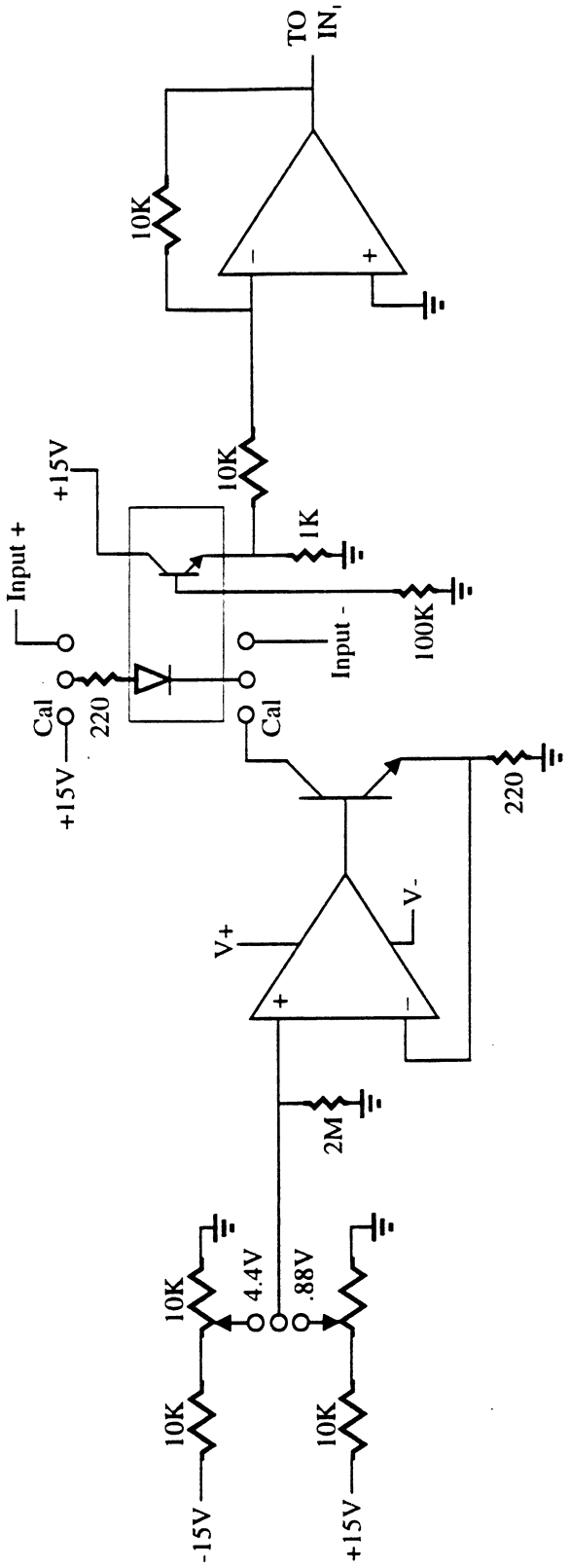

Figure D.2. Schematic of the driver circuit for the pressure controller. Page 1of 6.

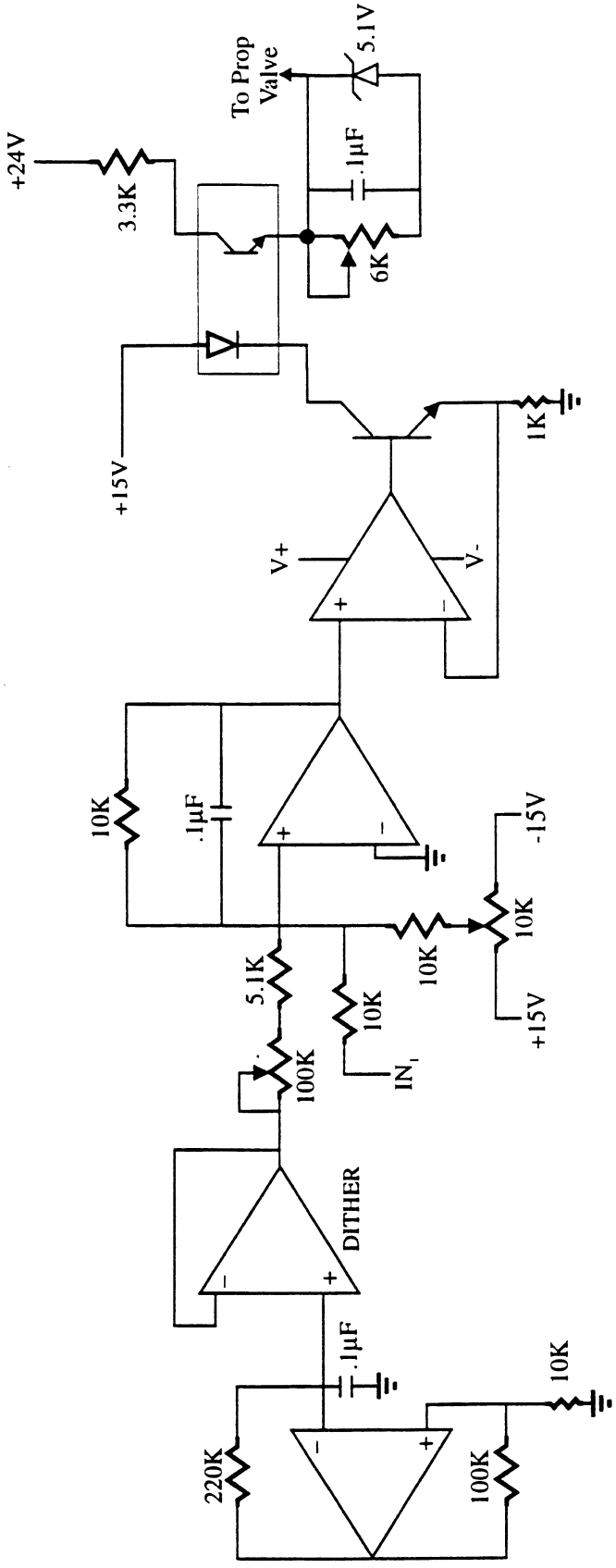

Figure D.2. Schematic of the driver circuit for the pressure controller. Page 2 of 6.

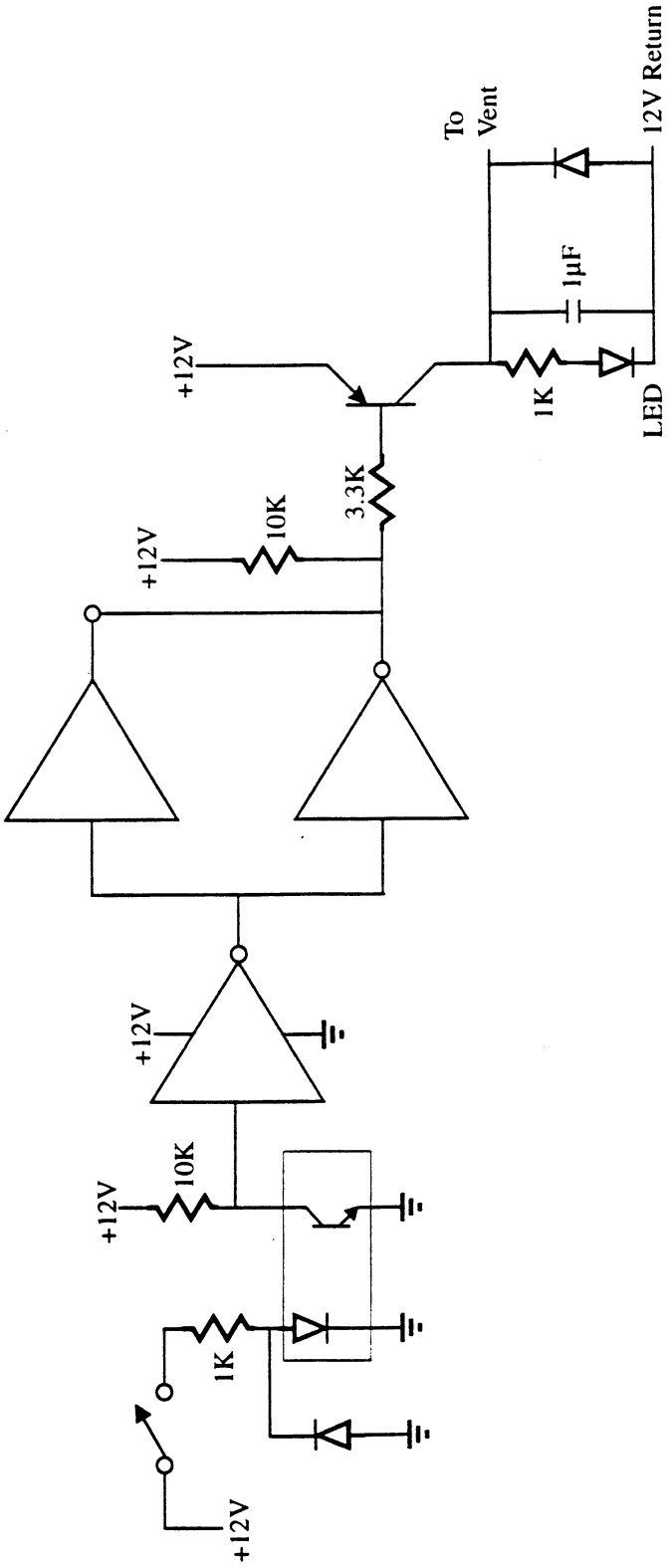

Figure D.2. Schematic of the driver circuit for the pressure controller. Page 3 of 6.

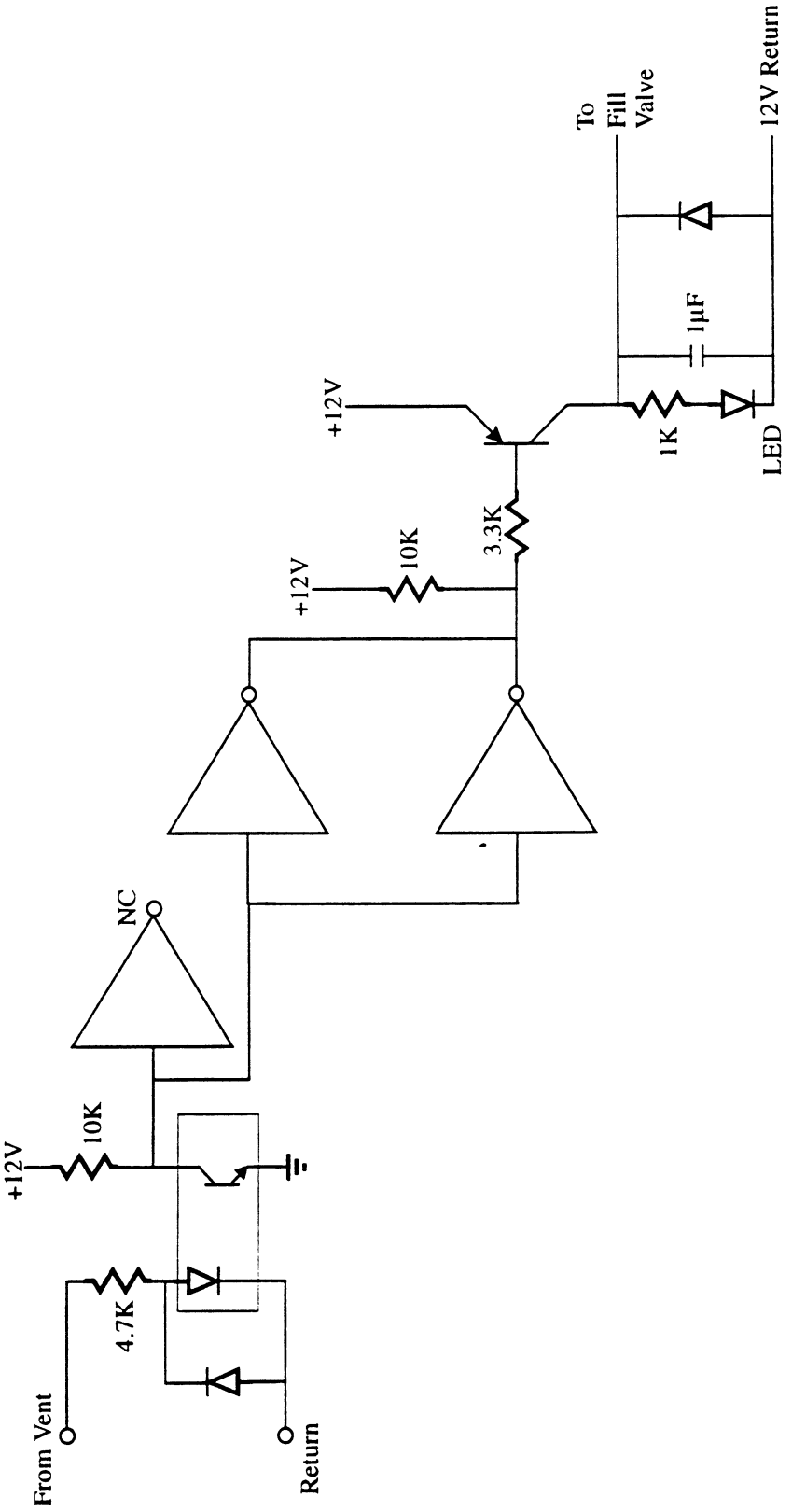

Figure D.2. Schematic of the driver circuit for the pressure controller. Page 4 of 6.

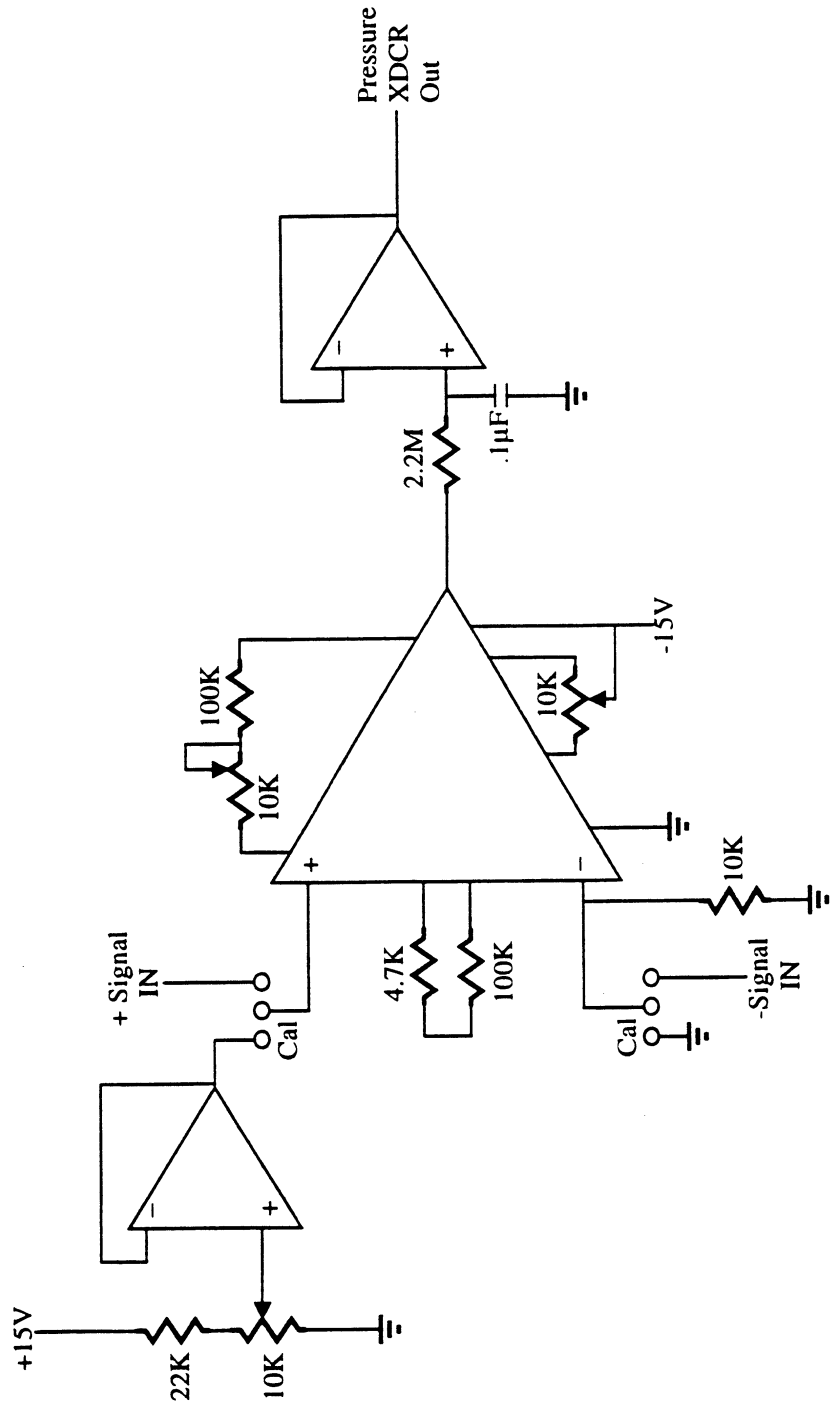

Figure D.2. Schematic of the driver circuit for the pressure controller. Page 5 of 6.

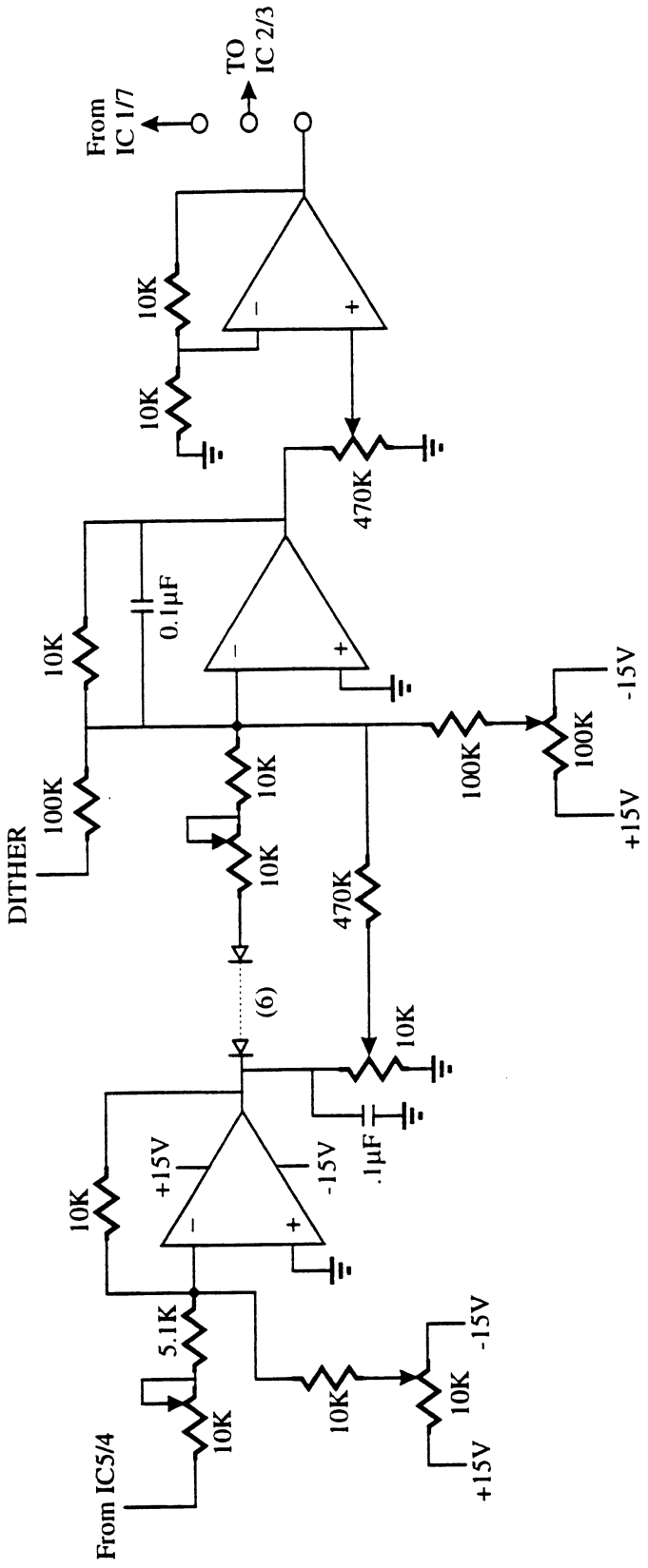

Figure D.2. Schematic of the driver circuit for the pressure controller. Page 6 of 6.

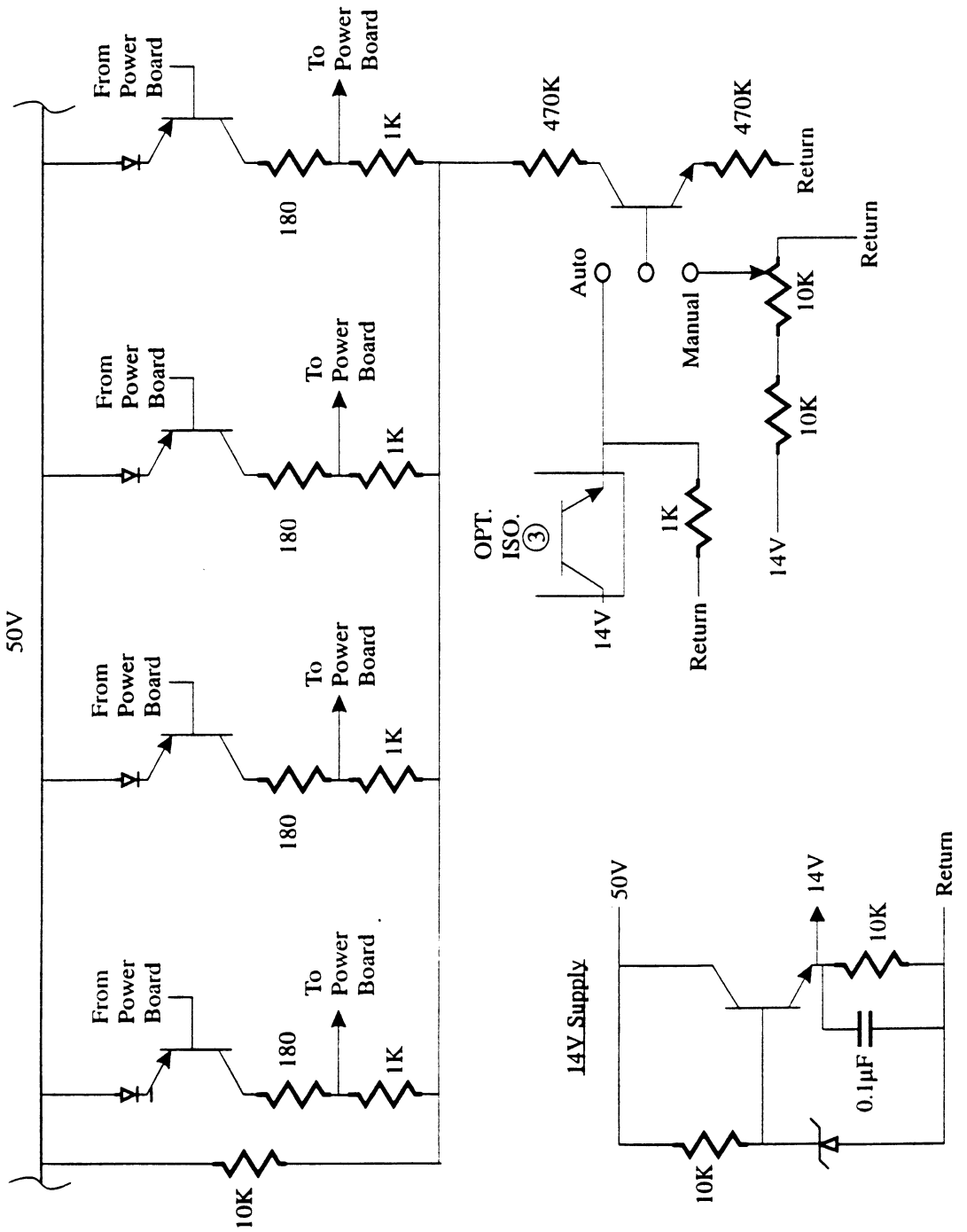

Figure D.3. Schematic of the controller and power supply for the gold film heaters. Page 1 of 2.

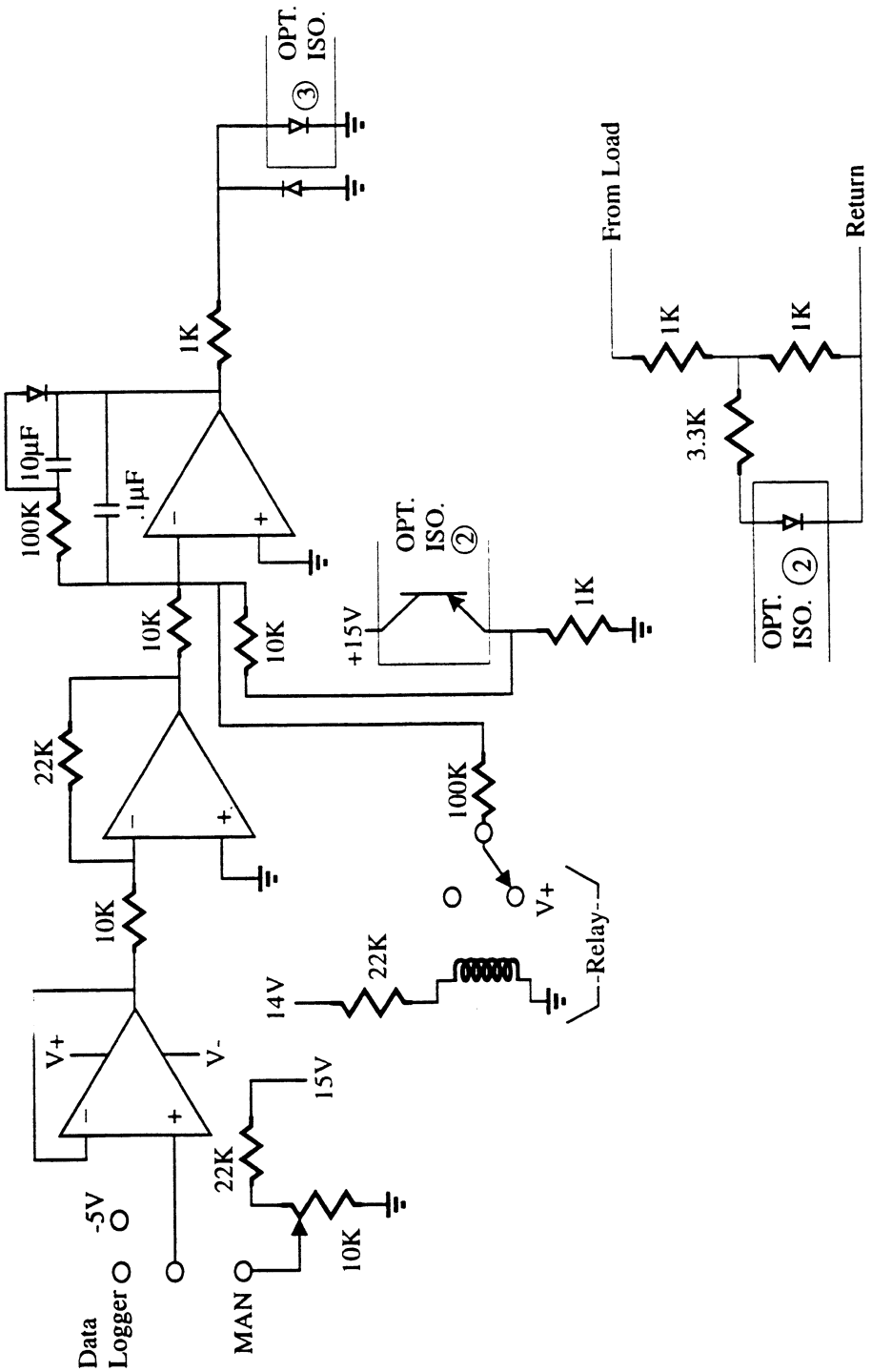

Figure D.3. Schematic of the controller and power supply for the gold film heaters. Page 2 of 2.

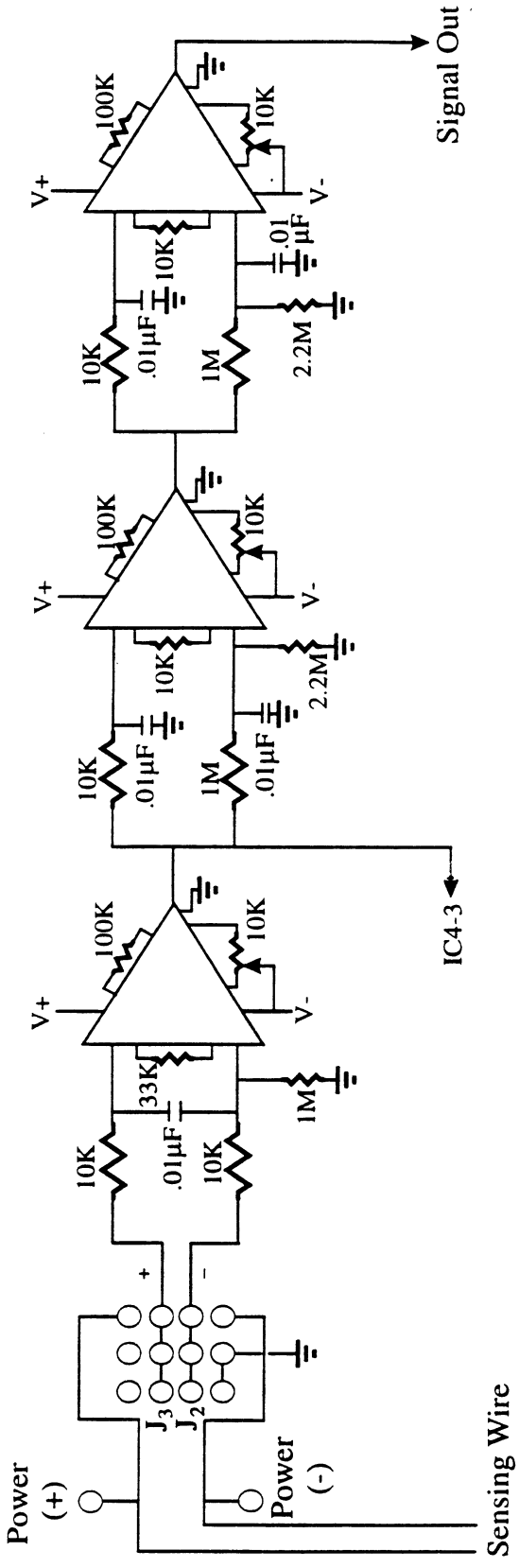

Figure D.4. Schematic of the driver and filter for the hot wire anemometer.

APPENDIX E

POOL BOILING CHF MODEL: EXTENSION TO CONVEX SURFACES

In a previous work (Brusstar and Merte, 1994), the effects of heater surface orientation on the CHF in pool boiling over an infinite flat plate were modeled by the following:

$$q_c = \begin{cases} q_{co} & 0^o \le \theta \le 90^o \\ q_{co}|\sin\theta|^{1/2} & 90^o \le \theta \le 270^o \\ q_{co} & 270^o \le \theta \le 360^o \end{cases} \qquad \text{(E.1)}$$

As was shown in Chapter 3, the forced convection model also reduces to a form nearly identical to this in the limit of no imposed flow.

If a convex shape is assumed to be composed of a series of several flat plates oriented at various angles with respect to gravity, with the CHF of each individual plate predicted according to Eqn. (E.1), then the equation may be integrated over the various orientations to predict the mean CHF over certain non-flat surfaces, as follows:

$$\bar{q}_c = \frac{1}{A_s}\int_{\theta} q_c(\theta)\, dA_s \qquad \text{(E.2)}$$

For this assumption to be true, however, the size of the body must be large in relation to the bubble size, otherwise the trajectory of the bubbles would not follow the curvature of the surface.

In the case of an infinite horizontal cylinder, the orientation of the surface varies from horizontal facing downward to horizontal facing upward about its circumference. Integration of Eqn. (E.1) over all orientation angles, according to Eqn. (E.2), yields a mean CHF equal to:

$$\left(\frac{\bar{q}_c}{q_{co}}\right)_{cylinder} = 0.881 \qquad \text{(E.3)}$$

This compares favorably with the result of 0.904 given by the model by Lienhard and Dhir (1973), based on the hydrodynamic instability of vapor jets leaving the surface of an infinite horizontal cylinder. This is also very close to the result of 0.894, obtained by Sun (1969).

For a large sphere, integration over the surface yields a mean CHF of:

$$\left(\frac{\bar{q}_c}{q_{co}}\right)_{sphere} = 0.937 \qquad \text{(E.4)}$$

This compares reasonably well with the value of 0.84 given by the hydrodynamic model of Ded and Lienhard (1972), although it generally overpredicts the experimental results.

The success of these predictions suggests that the CHF for more complex shapes can be predicted in pool boiling through integration of Eqn. (E.1).

APPENDIX F

CORRELATION OF THE LATENT HEAT FRACTION PARAMETER, χ, WITH SUBCOOLING

An expression for the net fraction of the surface heat flux that is absorbed as latent heat was given by Eqn. (3.31) as

$$\chi = \frac{\chi_0}{1 + 0.102\left(\frac{\rho_v}{\rho_l}\right)^{\frac{1}{4}} Ja} \tag{F.1}$$

This expression is derived from physical reasoning using continuity and the first law of thermodynamics, and is supported by experimental measurements. The development of this expression is given below.

From Eqn. (3.30), the net amount of energy per unit time leaving the heated surface as latent heat is given by the following:

$$\dot{Q}_{lh} = \chi q_s A_s = \dot{m}_v h_{fg} \tag{F.2}$$

In this case, the net mass flow of vapor away from the heater surface can also be expressed as

$$\dot{m}_v = \rho_v V_b \bar{f} N \tag{F.3}$$

where V_b is the volume of the bubble, f is the mean bubble frequency and N is the population of bubbles on the surface. If the sliding bubbles measured for the downward facing orientation are approximated as cylinders of height δ and diameter D_b, then the volume of the bubble is given by

$$V_b = \frac{\pi}{4} D_b^2 \delta \tag{F.4}$$

and the total number of bubbles on the heater surface by

$$N = \frac{A_s}{A_c} = \frac{A_s}{\frac{\pi}{4} D_b^2 \frac{1}{\alpha}} \tag{F.5}$$

where A_c is the average area occupied by a single bubble, and α is the mean void fraction above the surface.

Substitution of Eqns. (F.4) and (F.5) into Eqn. (F.3), and cancelling like terms yields:

$$\dot{m} = \rho_v \delta \bar{f} \alpha A_s \tag{F.6}$$

Substituting this result into Eqn. (F.2) then gives:

$$\chi q_c = \rho_v \delta \bar{f} \alpha h_{fg} \tag{F.8}$$

The right hand side of Eqn. (F.8), with δ, $\bar{f}$ and α obtained experimentally, is shown plotted against the heater surface orientation in Figure F.1 for various levels of subcooling, and is virtually constant, within acceptable uncertainty limits. As discussed in Chapter 2, and later in Chapters 5 and 6, the variation in the CHF with subcooling can be described by the correlation of Ivey and Morris (1962) as:

$$q_c = q_{co}\left[1 + 0.102\left(\frac{\rho_v}{\rho_l}\right)^{\frac{1}{4}} Ja\right] \tag{F.9}$$

Substitution of Eqn. (F.9) into Eqn. (F.8) and rearranging slightly then yields the following:

$$\chi = \frac{\rho_v \delta \bar{f} \alpha h_{fg}}{q_c} = \frac{\rho_v \delta \bar{f} \alpha h_{fg}}{q_{co}\left(1 + 0.102\left(\frac{\rho_v}{\rho_l}\right)^{\frac{1}{4}} Ja\right)} \tag{F.10}$$

Therefore, if, as Figure F.1 shows, the right hand side of Eqn.(F.8) is a constant, then the expression used in Eqn. (F.1) is valid, and the constant χ_0 can be expressed in terms of known or measurable quantities as follows:

$$\chi_0 = \frac{\rho_v \delta \bar{f} \alpha h_{fg}}{q_{co}} \tag{F.11}$$

From Figure F.1, the value obtained for χ_0 was approximately 0.30.

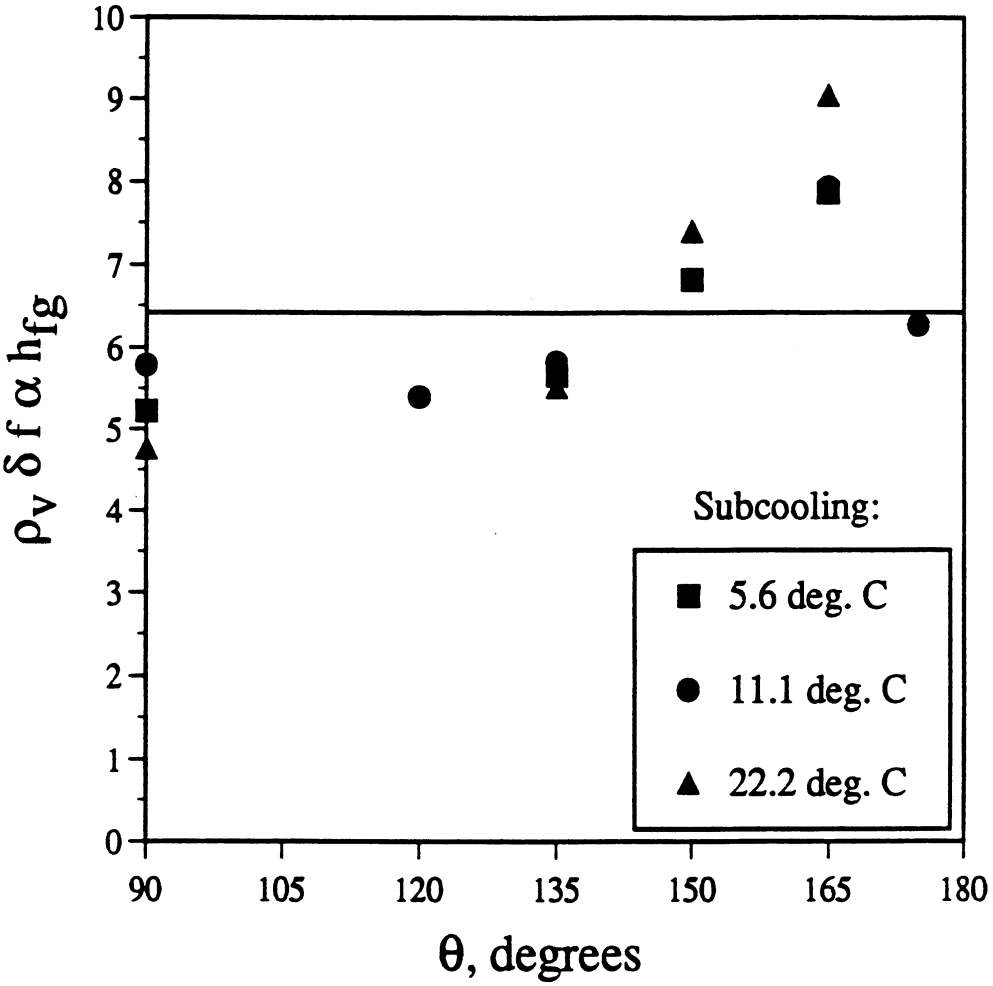

Figure F.1. Graph of the measured net portion of the heat flux going into latent heat versus heater surface orientation

APPENDIX G

FORTRAN-77 CODE "FCMODEL.FOR"

```
c       Program FCMODEL.FOR
c       Written by Matthew Brusstar
c    Latest Revision:  94 July 14
c    Program Objective: to predict the residence time
c       of bubbles growing at a high rate on a heated surface with
c       a prescribed heat flux.  When the product of the residence
c       time and the heat flux exceeds a fixed value, dryout is
c       said to occur.
c       ....VARIABLE DEFINITIONS.....
c
c    qsurf = surface heat flux (W/m^2)
c    rol = density of the liquid phase(kg/m^3)
c    rov =    "   "  " vapor   "
c    sigma = surface tension(N/m)
c    vnu = kinematic viscosity (Ns/m)
c    cp = specific heat (J/kgK)
c    hfg = latent heat (J/kg)
c    eps = convergence limit for qt to qtcrit
c    qeps =    "       "    " qsurf
c    dh = hydraulic diameter
c    pi = 3.14159
c    g = acceleration due to gravity
c    taylam = Taylor wavelength
c    chi = net fraction of the surface heat flux going to latent heat
c    chi0 = chi at Tsub = 0
c    redh = Reynolds # based on the hydraulic diameter
c    iquit = iteration upper bound safety
c    dxdt = bubble translational velocity tangent to the surface
c    dydt =   "       "          "    normal  "  "    "
c    x = bubble displacement tangent to the surface
c    y =  "       "      normal  "  "    "
c    tau = elapsed time
c    fdrag = drag force contribution
c    flift = lift   "       "
c    vgen = mean rate of vapor generation in the bubble
c    umean = mean flow velocity in the test section
c    ubar = mean flow velocity over the bubble
c    urel = velocity of the liquid relative to the bubble
c    cd = drag coeff.
c    cl = lift coeff.
c    qinc = increment for qsurf
c    sig = character string indicating the direction of bubble departure
c    yplus = dimensionless turbulent profile y variable
c    uplus =    "          "       "  velocity "
c    ustar = friction velocity
```

```
c     fbfl = ratio of the buoyancy to lift force
c     fbfd =  "   " "    "   " drag force
c     x1, x2, ubar1, ubar2 = intermediate variables
c     w = weighting factor for determining mean velocity
c
      implicit real*8 (a-h, o-z)
      dimension dxdt(10000), x(10000), dydt(10000), y(10000)
c
      open(5, file = 'c:\users\matthew\model\fcmodel.dat')
c
      open(6, file = 'c:\users\matthew\model\fcmodel.out')
      write(6,500)
c
      open(7, file = 'c:\users\matthew\model\fcexcel.out')
      write(7,600)
c
      open(8, file = 'c:\users\matthew\model\fratio.out')
      write(8,700)
c
c     ...fcmodel.dat contains input parameters...
c     orient = heater surface orientation in degrees
c     umean = mean flow velocity in m/s
c     h = test section height in m
c     tsub = subcooling in deg. F
c     qinc = surface heat flux increment in W/m^2
c     qtcrit = critical value of Q*tau
c     dt = time increment
5     read(5,*, end = 999)orient, umean, h, tsub, qinc, qtcrit, dt
c
          qsurf = 0.d0
c
          rol = 1500.
          rov = 8.
          sigma = 0.017
          vnu = 3.3e-07
          cp = 980.
          hfg = 144000.
c
          eps = 1.0e-4
          qeps = 5.
c
          dh = 4*(0.108*h)/(2*h + 2*0.108)
          pi = 3.14159
          g = 9.8
c
```

```
      taylam = dsqrt(3.d0)*2*pi*dsqrt(sigma/(g*(rol - rov)))
c
c      ....Subcooling correlation for chi from Ivey and Morris....
        chi0 = 0.3
        chi = chi0/(1 + 0.102*(rol/rov)**0.75*cp*(tsub/1.8)/hfg)
c
        redh = umean*dh/vnu
c
        iquit = 1
c
10        qsurf = qsurf + qinc
c
        iquit = iquit + 1
      if(iquit .gt. 2000)goto 40
      if(qinc .lt. qeps)goto 40
c
        dxdt(1)=0.d0
        x(1) = 0.d0
        tau= 0.d0
        fdrag = 0.d0
c
        flift = 0.d0
        dydt(1) = 0.d0
        y(1) = 0.d0
c
        i = 1
c
        vgen = qsurf*taylam**2*chi/(rov*hfg)
c
20        tau = tau + dt
        i = i + 1
c
    r = (3.d0/(4.d0*pi)*vgen*tau)**(1.d0/3)
c
c   ...Determine the average velocity over the bubble (evaluated at y = R)...
     if(r .le. h/4)then
        call uturb(r, vnu, redh, umean, ubar)
     elseif( r .gt. h/4 .and. r .le. h/2)then
        x1 = h/4
        x2 = 0.75*h - r
        w = (2*r - h/2)/(2*r)
        call uturb(x1, vnu, redh, umean, ubar1)
        call uturb(x2, vnu, redh, umean, ubar2)
c
        ubar = (1-w)*ubar1 + w*ubar2
```

```
      else
          call uturb(h/4, vnu, redh, umean, ubar)
      endif
c
          urel = (dxdt(i-1) - ubar)
c     ....Determine the corresponding drag coefficient....
          call cdrag(r, urel, vnu, cd)
c
c     ....fdrag is the integration of the drag force wrt time....
      fdrag = fdrag +
     #    plusmin(urel)*pi/2*rol*(9.d0/(16*pi**2*vgen))**(1.d0/3)
     #    *cd*urel**2*tau**(2.d0/3)*dt
c
c     ....Calculate the velocity of the bubble PARALLEL to the surface...
c
      dxdt(i) = 1.d0/((19.d0/32*rol + rov)*tau)*(g*dsin(orient*pi/180)
     #    *(rol-rov)*tau**2/2 + fdrag)
c
c     ....Find the displacement of the bubble PARALLEL to the surface...
c
      x(i) = x(i-1) + (dxdt(i) + dxdt(i-1))/2*dt
c
c     ...Do a force balance normal to the surface to determine
c        if liftoff occurs before the bubble slides away...
      call clift(r, h, vnu, redh, umean, urel, cl)
c
      flift = flift +
     #    pi/2*rol*(9.d0/(16*pi**2*vgen))**(1.d0/3)
     #    *cl*urel**2*tau**(2.d0/3)*dt
c
c     ....Calculate the velocity of the bubble NORMAL to the surface...
c
      dydt(i) = 1.d0/((11.d0/16*rol + rov)*tau)*(g*dcos(orient*pi/180)
     #    *(rol-rov)*tau**2/2 + flift)
c
c     ....Find the displacement of the bubble NORMAL to the surface...
        if(dydt(i) .lt. 0.d0)dydt(i) = 0.d0
c
        y(i) = y(i-1) + (dydt(i) + dydt(i-1))/2*dt
c
c     ...Determine the ratio of the buoyancy force to drag and lift forces...
      call fratio(fdrag, flift, rol, rov, orient, tau, fbfd, fbfl)
c
        disp = dsqrt(y(i)**2 + x(i)**2)
          if(disp .ge. r)goto 30
```

```
c
          goto 20
c
c     ....Manipulate the parameter units, etc. for the output...
c
30        qs = qsurf/10000
        qt = qs*tau
c
      if (dabs(qt - qtcrit) .le. eps)then
         goto 40
      elseif (qt .lt. qtcrit)then
          goto 10
      else
         qsurf = qsurf - qinc
          qinc = qinc/2
          goto 10
      endif
c
40        falpha = 1./tau
        ddep = 2*r*1000
c
      write(*,*)cd, urel, cl
      write(6,200)qs, qt, falpha, ddep, redh
      write(7,300)orient, qs
      write(8,400)orient, fbfd, fbfl
c
      goto 5
c
200   format(f8.2, f8.5, 2f10.3, 3x, f8.1)
300   format(f8.1, f8.2)
400   format(f8.1, 2e10.3)
500   format(3x,'Qs',5x,'Q*Tau',5x,'1/Tau',6x,'Ddep'/
     #    2x,'W/cm^2',2x,'J/cm^2',4x, '1/sec', 7x,'mm')
600   format(2x,'Orient',4x,'Qsurf')
700   format(2x, 'Orient', 4x, 'Fb/Fd', 4x, 'Fb/Fl')
999   write(*,*)"Program is finished"
c
      end
c
c     ....SUBROUTINES AND FUNCTIONS.....
c
c     ...Subroutine UTURB contains the turbulent velocity profile....
c     ...It returns UBAR, the mean velocity over the bubble (at y = R)
      subroutine uturb(r, vnu, redh, umean, ubar)
c
```

```
      implicit real*8 (a-h, o-z)
c
      ustar = 0.1988/redh**0.125*umean
c
c     ...Determine the average velocity over the bubble (evaluated at y = R)...
        yplus = ustar*r/vnu
      if(yplus .le. 5.d0)then
        uplus = yplus
      elseif(yplus .gt. 5.d0 .and. yplus .le. 70.d0)then
        uplus = 2.5*dlog(yplus) + 5.5
      else
        uplus = 8.74*yplus**(1.d0/7.d0)
      endif
      ubar = uplus*ustar
c
      return
      end
c
c     ...Subroutine cdrag calculates the mean drag coefficient....
c     ...It returns CD, the mean Cd over the bubble...
c        ....Ref. Ishii and Zuber....
      subroutine cdrag(r, urel, vnu, cd)
c
      implicit real*8 (a-h, o-z)
c
        reb = dabs(urel*2*r/vnu)
      if(reb .le. 150.)then
        cd = 24.d0/reb*(1 + 0.1*reb**0.75)
      else
c       ....lower limit to drag coefficient...
       cd = 0.54
      endif
c
      return
      end
c
c     ...Subroutine CLIFT returns the value for the shear lift coefficient...
c     ...Ref. Klausner, et al., 1993....
c     ...Ref. Auton, 1987 also, establishing the high Re limit...
      subroutine clift(r, h, vnu, redh, umean, urel, cl)
c
      implicit real*8 (a-h, o-z)
c
        reb = dabs(urel*2*r/vnu)
c
```

```
      if(redh .gt. 2300.)then
        ustar = 0.1988/redh**0.125*umean
c
c     ...Determine the average velocity over the bubble (evaluated at y = R)...
        yplus = ustar*r/vnu
        if(yplus .le. 5.d0)then
          dudy = ustar**2/vnu
        elseif(yplus .gt. 5.d0 .and. yplus .le. 30.d0)then
          dudy = 2.4*ustar/r
        else
          dudy = 1.25*ustar**2/vnu*yplus**(-6.d0/7.d0)
      endif
c
      else
        dudy = 6.d0*umean/h*(1.d0 - 2*r/h)
      endif
c
      gs = dabs(dudy*r/urel)
c
      cl = 3.877*gs**(0.5)*(1/reb**2 + 0.344**4*gs**2)**(0.25)
c
c     ....High Re limit, from Auton....
        if (cl .lt. 0.5)cl = 0.5
c
      return
      end
c
c             ...Subroutine FRATIO...
c     ...Calculates the ratio of the buoyancy force components to the
c        drag and lift forces acting on the bubble....
c     ...Returns (1) fbfd = Fbuoy/Fdrag
c             (2) fbfl = Fbuoy/Flift
c
      subroutine fratio(fdrag, flift, rol, rov, orient, tau, fbfd, fbfl)
c
      implicit real*8 (a-h, o-z)
c
          pi = 3.14159
          g = 9.8
c
      fbfl = (g*dcos(orient*pi/180)*(rol-rov)*tau**2/2)/flift
c
      fbfd = (g*dsin(orient*pi/180)*(rol-rov)*tau**2/2)/fdrag
c
      return
```

```
      end
c
c     .....Function PLUSMIN determines the sign on the drag force....
c     ....This is used in place of the SIGN intrinsic function....
      function plusmin(x)
      implicit real*8 (a-h, o-z)
c
      if(x .le. 0.d0)then
        plusmin = 1.d0
      else
        plusmin = -1.d0
      endif
c
      return

      end
```

REFERENCES

REFERENCES

Ahmad, S. Y., 1973, "Fluid to Fluid Modeling of Critical Heat Flux: A Compensated Distortion Model", *Int. J. Heat Mass Transfer*, 16 (2), 641-662.

Al-Hayes, R. A. M., Winterton, R. H. S., 1981, "Bubble Diameter on Detachment in Flowing Liquids", *Int. J. Heat Mass Transfer*, 24(1), 223-230.

Auton, T. R., 1987, "The Lift Force on a Spherical Body in a Rotational Flow", *J. Fluid Mech.*, 183, 199-218.

Balasubramaniam, R., 1987, "Thermocapillary Bubble Migration for Large Marangoni Numbers", NASA Contractor Report 179628, May 1987.

Bankoff, S. G., 1990, "Dynamics and Stability of Thin Heated Liquid Films", *Trans. ASME, J. Heat Transfer*, 112 (3), 538-546.

Bar-Cohen, A., McNeil, A., 1992, "Parametric Effects on Pool Boiling Critical Heat Flux in Highly Wetting Liquids", *Proc. of the Eng. Foundation Conf. on Pool and External Flow Boiling, Santa Barbara, CA, March 22-27*, pp. 171-176.

Berenson, P. J., 1961, "Film-Boiling Heat Transfer from a Horizontal Surface", *Trans. ASME, J. Heat Transfer*, 83 (3), 351-358.

Bergles, A., 1988, "High Flux Boiling Applied to Microelectronics Thermal Control", *Int. Comm. Heat Mass Transfer*, 15, 509-531.

Bhat, A. M., Prakash, R., Saini, J. S., 1983a, "On the Mechanism of Macrolayer Formation in Nucleate Pool Boiling at High Heat Flux", *Int. J. Heat Mass Transfer*, 26 (5), 735-740.

Bhat, A. M., Prakash, R., Saini, J. S., 1983b, "Heat Transfer in Nucleate Pool Boiling at High Heat Flux", *Int. J. Heat Mass Transfer*, 26 (6), 833-840.

Borishanskii, V. M., 1956, "An Equation Generalizing Experimental Data on the Cessation of Bubble Boiling in a Large Volume of Liquid", *Sov. Phys.-Tech. Phys.*, 1, p. 438.

Brusstar, M. J., Merte, H., Jr., 1994, "Effects of Buoyancy on the Critical Heat Flux in Forced Convection", *J. Thermophys. Heat Transfer*, 8 (2), 322-328.

Carvalho, R. D. M., Bergles, A. E., 1992, "The Effects of the Heater Thermal Conductance/Capacitance on the Pool Boiling Critical Heat Flux", *Proc. of the*

Eng. Foundation Conf. on Pool and External Flow Boiling, Santa Barbara, CA, March 22-27, pp. 2-17.

Carvalho, R. D. M., Bergles, A. E., 1994, "The Pool Nucleate Boiling Flow Patterns of Vertically Oriented, Small Heaters Boiling on One Side", *Proc. 10th Int. Heat Transfer Conf., Brighton, UK, August 14-18*; Vol. 5, Paper 10-PB-5, pp. 25-30.

Celata, G. P., Cumo, M., Mariani, A., 1994, "Assessment of Correlations and Models for the Prediction of CHF in Water Subcooled Flow Boiling", *Int. J. Heat Mass Transfer*, 37 (2), 237-255.

Chandrasekhar, S., 1961, *Hydrodynamic and Hydromagnetic Stability*, Oxford University Press, pp. 428-514.

Costello, C. P., Frea, W. J., 1965, "A Salient Nonhydrodynamic Effect on Pool Boiling Burnout of Small Semicylindrical Heaters", *Chem. Eng. Prog. Symp. Series, Heat Transfer*, 61 (57), 258-268.

Davidson, J. F., Schueler, B. O. G., 1960a, "Bubble Formation at an Orifice in an Inviscid Liquid", *Trans. Instn. Chem. Engrs.*, 38, 335-342.

Davidson, J. F., Schueler, B. O. G., 1960b, "Bubble Formation at an Orifice in a Viscous Liquid", *Trans. Instn. Chem. Engrs.*, 38, 144-154.

Ded, J. S., Lienhard, J. H., 1972, "The Peak Pool Boiling Heat Flux from a Sphere", *AIChE Journal*, 18 (2), 337-342.

Dhir, V. K., Lienhard, J. H., 1974, "Peak Pool Boiling Heat Flux in Viscous Liquids", *Trans. ASME, J. Heat Transfer*, 96 (1), 71-78.

Dhir, V. K., Tung, V. X., 1988, "A Thermal Model For Fully Developed Nucleate Boiling of Saturated Liquids", *Collected Papers in Heat Transfer*, ASME HTD-Vol. 104, 153-164.

Dhuga, D. S., Winterton, R. H. S., 1985, "Measurement of Surface Contact in Transition Boiling", *Int. J. Heat Mass Transfer*, 28 (3), 1869-1880.

Elkassabgi, Y., Lienhard, J. H., 1988, "Influences of Subcooling on Burnout of Horizontal Cylindrical Heaters", *Trans. ASME, J. Heat Transfer*, 110 (2), 479-486.

Engelberg-Forster, K., Greif, R., 1959, "Heat Transfer to a Boiling Liquid-Mechanisms and Correlations", *Trans. ASME, J. Heat Transfer*, 81 (2), 43-53.

Ervin, J. S., 1991, "Incipient Boiling in Microgravity", Ph. D. Thesis, University of Michigan, Ann Arbor.

Gaertner, R. F., 1965, "Photographic Study of Nucleate Pool Boiling on a Horizontal Surface", *Trans. ASME, Ser. C, Journ. Heat Transfer*, 88 (1), 17-29.

Galloway, J. E., Mudawar, I., 1993a, "CHF Mechanism in Flow Boiling from a Short Heated Wall-I. Examination of Near-Wall Conditions with the Aid of Photomicrography and High-Speed Video Imaging", *Int. J. Heat Mass Transfer*, 36 (10), 2511-2526.

Galloway, J. E., Mudawar, I., 1993b, "CHF Mechanism in Flow Boiling from a Short Heated Wall-II. Theoretical CHF Model", *Int. J. Heat Mass Transfer*, 36 (10), 2527-2540.

Gambill, W. R., Lienhard, J. H., 1989, "Upper Bound for the Critical Boiling Heat Flux" *Trans. ASME, J. Heat Transfer*, 111 (3), 815-818.

Gersey, C. O., Mudawar, I., 1992, "Effects of Orientation on Critical Heat Flux from Chip Arrays during Flow Boiling", *ASME J. Electronic Packaging*, Vol. 114, 290-299.

Gersey, C. O., Mudawar, I., 1993, "Orientation Effects on Critical Heat Flux from Discrete, In-Line Heat Sources in a Flow Channel", *Trans. ASME, J. Heat Transfer*, 115 (4), 973-985.

Gersey, C. O., Mudawar, I., 1995, "Effects of Heater Length and Orientation on the Trigger Mechanism for Near-Saturated Flow Boiling Critical Heat Flux-II. Critical Heat Flux Model", *Int. J. Heat Mass Transfer*, 38 (4), 643-654.

Goldstein, R. J., Sparrow, E. M., Jones, D. C., 1973, "Natural Convection Mass Transfer Adjacent to Horizontal Plates", *Int. J. Heat Mass Transfer*, 16 (5), 1025-1035.

Guo, Z., El-Genk, M. S., 1992, "An Experimental Study of Saturated Pool Boiling from Downward Facing and Inclined Surfaces", *Int. J. Heat Mass Transfer*, 35 (9), 2109-2117.

Haramura, Y., 1990, "Characteristics of Pool Boiling Heat Transfer in the Vicinity of the Critical Heat Flux (Relations between Bubble Motion and Heat Flux Fluctuations)", *Heat Transfer-Japanese Research*, 18 (3), 18-31.

Haramura, Y., Katto, Y., 1983, "A New Hydrodynamic Model of Critical Heat Flux, Applicable to Both Pool and Forced Convection on Submerged Bodies in Saturated Liquids", *Int. J. Heat Mass Transfer*, 26 (3), 389-399.

Harmathy, T. Z., 1960, "Velocity of Large Drops and Bubbles in Media of Infinite or Restricted Extent", *AIChE Journal*, 6 (2), 281-288.

Henry, R. E., 1974, "A Correlation for the Minimum Film Boiling Temperature", *AIChE Symp. Ser., Heat Transfer-Research and Design*, No. 138, Vol. 70, 81-90.

Ishigai, S., Inoue, K., Kiwaki, Z., Inai, T., 1961, "Boiling Heat Transfer from a Flat Surface Facing Downward", *Int. Dev. Heat Transfer: Proc. of the 1961 Heat Transfer Conf.*, Paper 26, 224-229.

Ishigai, S., Kuno, T., 1966, "Experimental Study of Transition Boiling on a Vertical Wall in Open Vessel", *Bull. JSME*, 9 (34), 361-368.

Ishii, M., Zuber, N., 1979, "Drag Coefficient and Relative Velocity in Bubbly, Droplet or Particulate Flows", *AIChE Journal*, 25 (5), 843-855.

Ivey, H. J., Morris, D. J., 1962, "On the Relevance of the Vapour-Liquid Exchange Mechanism for Subcooled Boiling Heat Transfer at High Pressure", UKAEA, AEEW-R 137.

Jakob, M., 1958, *Heat Transfer*, Vol. 1, John Wiley, New York.

Jawurek, H. H., 1969, "Simultaneous Determination of Microlayer Geometry and Bubble Growth in Nucleate Boiling", *Int. J. Heat Mass Transfer*, 12 (2), 843-848.

Katto, Y., 1978, "A Generalized Correlation of Critical Heat Flux for the Forced Convection Boiling in Vertical Uniformly Heated Round Tubes", *Int. J. Heat Mass Transfer*, 21 (10), 1527-1542.

Katto, Y., 1985, "Critical Heat Flux", *Adv. Heat Transfer*, 17, 1-64.

Katto, Y., Ishii, K., 1978, "Burnout in a High Heat Flux Boiling System with a Forced Supply of Liquid through a Plane Jet", *Proc. 6th Int. Heat Transfer Conf., Toronto, Canada, August 7-11*; Vol. 1, Paper FB-28, pp. 435-440.

Katto, Y., Otokuni, S., 1994, "Behavior of Vapor Masses on a Vertical Flat Surface of Comparatively Large Height Near Critical Heat Flux Conditions in Saturated Pool Boiling", *Int. J. Heat Mass Transfer*, 37 (1), 255-263.

Katto, Y., Yokoya, S., 1968, "Principal Mechanism of Boiling Crisis in Pool Boiling", *Int. J. Heat Mass Transfer*, 11, 993-1002.

Kirby, D. B., Westwater, J. W., 1965, "Bubble and Vapor Behavior on a Heated Horizontal Plate During Pool Boiling Near Burnout", *Chem. Eng. Prog. Symp. Series, Heat Transfer*, 238-248.

Kirk, K. M., 1992, "A Study of the Relative Effects of Buoyancy and Liquid Momentum in Forced Convection Nucleate Boiling", Ph. D. Thesis, University of Michigan, Ann Arbor.

Klausner, J. F., Mei, R., Bernhard, D. M., Zeng, L. Z., 1993, "Vapor Bubble Departure in Forced Convection Boiling", *Int. J. Heat Mass Transfer*, 36 (3), 651-662.

Kumada, T., Sakashita, H., 1992, "Proposed Model for Kutateladze Correlation and New Correlation of CHF", *Proc. of the Eng. Foundation Conf. on Pool and External Flow Boiling, Santa Barbara, CA, March 22-27*, pp. 177-183.

Kutateladze, S. S., 1948, "On the Transition to Film Boiling under Natural Convection", *Kotloturbostroenie*, 3, p. 10.

Kutateladze, S. S., 1963, *Fundamentals in Heat Transfer*, Arnold, London, p. 387.

Kutateladze, S. S., Leont'ev, A. I., 1966, "Some Applications of the Asymptotic Theory of the Turbulent Boundary Layer", *Proc. 3rd Int. Heat Transfer Conf., Chicago, Illinois, August 7-12*; Vol. 3, Paper 81, pp. 1-6.

Lahey, R. T., Jr., 1992, *Boiling Heat Transfer: Modern Developments and Advances*, Elsevier Science Publishers, pp. 85-120.

Li, L., Schultz, W. W., Merte, H., Jr., 1993, "The Velocity Potential and the Interacting Force for Two Spheres Moving Perpendicularly to the Line Joining their Centers", *J. Eng. Math.*, 27, 147-160.

Liaw, S. P., Dhir, V. K., 1989, "Void Fraction Measurements During Saturated Pool Boiling of Water on Partially Wetted Vertical Surfaces", *Trans. ASME, J. Heat Transfer*, 111 (3), 731-738.

Lienhard, J. H., Dhir, V. K., 1973, "Hydrodynamic Prediction of Peak Pool-Boiling Heat Fluxes from Finite Bodies", *Trans. ASME, J. Heat Transfer*, 95 (2), 152-158.

Lienhard, J. H., Eichhorn, R., 1976, "Peak Boiling Heat Flux on Cylinders in a Cross Flow", *Int. J. Heat Mass Transfer*, 19 (6), 1135-1142.

Lienhard, J. H., Hasan, M. M., 1979, "On Predicting Boiling Burnout with the Mechanical Energy Stability Criterion", *Trans. ASME, J. Heat Transfer*, 101 (2), 276-279.

Mastroianni, M. J., Stahl, R. F., Sheldon, P. N., 1978, "Physical and Thermodynamic Properties of 1, 1, 2-Trifluorotrichloroethane (R-113)", *J. Chemical and Engineering Data*, 23 (2), 113-118.

Mattson, R. J., Hammitt, F. G., Tong, L. S., 1973, "A Photographic Study of the Subcooled Flow Boiling Crisis in Freon-113", ASME paper 73-HT-39.

McFadden, P. W., Grassman, P., 1962, "The Relation Between Bubble Frequency and Diameter During Nucleate Pool Boiling", *Int. J. Heat Mass Transfer*, 5 (1), 169-173.

McGillis, W. R., Carey, V. P., Strom, B. D., 1991, "Geometry Effects on Critical Heat Flux for Subcooled Convective Boiling from an Array of Heated Elements", *Trans. ASME, J. Heat Transfer*, 113 (2), 463-471.

Mei, R., Klausner, J. F., 1992, "Unsteady Force on a Spherical Bubble at Finite Reynolds Number with Small Fluctuations in the Free-Stream Velocity", *Phys. Fluids*, 4, 63-70.

Merte, H., Jr., 1990, "Nucleate Pool Boiling in Variable Gravity", *Prog. Astronautics and Aeronautics*, AIAA, Wash. D. C., vol. 30, pp. 15-69.

Merte, H., Jr., Clark, J. A., 1964, "Boiling Heat Transfer with Cryogenic Fluids at Standard, Fractional, and Near-Zero Gravity", *Trans. ASME, Ser. C, J. Heat Transfer*, 86 (3), 315-319.

Merte, H., Jr., Lee, H. S., Ervin, J. S., 1994, "Transient Nucleate Pool Boiling in Microgravity", *Microgravity Sci. Technol.*, VII (2), 173-179.

Milne-Thomson, L. M., 1956, *Theoretical Hydrodynamics*, 3rd Ed., MacMillan & Co., 476-479.

Mishima, K., Nishihara, H., 1985, "The Effect of Flow Direction and Magnitude on CHF for Low Pressure Water in Thin Rectangular Channels", *Nuc. Eng. and Design*, 86, 165-181.

Moissis, R., Berenson, P. J., 1963, "On the Hydrodynamic Transitions in Nucleate Boiling", *Trans. ASME, J. Heat Transfer*, 85 (3), 351-358.

Mudawar, I., Maddox, D. E., 1989, "Critical Heat Flux in Subcooled Flow Boiling of Fluorocarbon Liquid on a Simulated Electronic Chip in a Vertical Rectangular Channel", *Int. J. Heat Mass Transfer*, 32 (1), 379-394.

Noyes, R. C., 1963, "An Experimental Study of Sodium Pool Boiling Heat Transfer", *Trans. ASME, J. Heat Transfer*, 85 (2), 125-131.

Nukiyama, S., 1934, "The Maximum and Minimum Values of the Heat Q Transferred from Metal to Boiling Water under Atmospheric Pressure", *J. Japan Soc. Engrs.*, 37, 367-374 (reprinted in *Int. J. Heat Mass Transfer*, 9 (9), 1419-1433, 1966).

Oker, E., Merte, H., Jr., 1981, "Semi-Transparent Gold Film as Simultaneous Surface Heater and Resistance Thermometer for Nucleate Boiling Studies", *Trans. ASME, J. Heat Transfer*, 103 (1), 65-68.

Okuyama, K., Iida, Y., 1991, "Premature Transition to Film Boiling with Stepwise Heat Generation", *Trans. JSME*, 57 (538), 2118-2123.

Papell, S. S., 1967, "Buoyancy Effects on Forced-Convective Boiling", ASME Report 67-HT-63.

Pasamehmetoglu, K. O., Nelson, R. A., Gunnerson, F. S., 1990, "Critical Heat Flux Modeling in Forced Convection Boiling During Power Transients", *Trans. ASME, J. Heat Transfer*, 112 (3), 1058-1062.

Peebles, F. N., Garber, H. J., 1953, "Studies on the Motion of Gas Bubbles in Liquid", *Chem. Eng. Prog.*, 49, 88.

Rajvanshi, A. K, Saini, J. S., Prakash, R., 1992, "Investigation of Macrolayer Thickness in Nucleate Pool Boiling at High Heat Flux", *Int. J. Heat Mass Transfer*, 35 (2), 343-350.

Ramilison, J. M., Sadasivan, P., Lienhard, J. H., 1992, "Surface Factors Influencing Burnout on Flat Heaters", *Trans. ASME, J. Heat Transfer*, 114 (1), 287-290.

Rohsenow, W., Griffith, P., 1956, "Correlation of Maximum-Heat-Flux Data for Boiling of Saturated Liquids", *Chem. Eng. Prog. Symp. Series, Heat Transfer*, 52 (18), 47-49.

Schlichting, H., 1979, *Boundary-Layer Theory*, 7th Ed., McGraw-Hill, Inc., pp. 602-609.

Siegel, R., 1967, "Effects of Reduced Gravity on Heat Transfer", *Adv. Heat Transfer*, 4, 143-228.

Simoneau, R. J., Simon, F. F., 1966, "A Visual Study of Velocity and Buoyancy Effects on Boiling Nitrogen", NASA TN D-3354.

Sun, K. H., 1969, "The Peak Pool Boiling Heat Flux on Horizontal Cylinders", College of Engineering Bulletin No. 88, University of Kentucky, Lexington.

Tong, L. S., 1968, "Boundary-Layer Analysis of the Flow Boiling Crisis", *Int. J. Heat Mass Transfer*, 11 (9), 1208-1211.

Tong, W., Simon, T. W., Bar-Cohen, A., 1988, "A Bubble Sweeping Heat Transfer Mechanism for Low Flux Boiling on Downward-Facing Inclined Surfaces", *Collected Papers in Heat Transfer*, ASME HTD-Vol. 104, 173-178.

Torikai, K., Suzuki, K., Yamaguchi, M., 1991, "Study on Contact Area of Pool Boiling Bubbles on a Heated Surface (Observation of Bubbles in Transition Boiling)", *JSME Int. Journal, Ser. II*, 34 (2), 195-201.

Tsung-Chang, G., Bankoff, S. G., 1990, "On the Mechanism of Forced-Convection Subcooled Nucleate Boiling", *Trans. ASME, J. Heat Transfer*, 112 (1), 213-218.

Vishnev, I. P., Filatov, I. A., Vinokur, Ya. G., Gorokhov, V. V., Svalov, G. G., 1976, "Study of Heat Transfer in Boiling of Helium on Surfaces with Various Orientations", *Heat Transfer-Sov. Res.*, 8 (4), 104-108.

Voutsinos, C. M., Judd, R. L., 1975, "Laser Interferometric Investigation of the Microlayer Evaporation Phenomenon", *Trans. ASME, J. Heat Transfer*, 97 (1), 88-92.

Weisman, J., Pei, B. S., 1983, "Prediction of Critical Heat Flux in Flow Boiling at Low Qualities", *Int. J. Heat Mass Transfer*, 26 (10), 1463-1477.

Yilmaz, S., Westwater, J. W., 1980, "Effect of Velocity on Heat Transfer to Boiling Freon-113", *Trans. ASME, J. Heat Transfer*, 102 (2), 26-31.

Yu, C.-L., Mesler, R. B., 1977, "A Study of Nucleate Boiling Near the Peak Heat Flux through Measurement of Transient Surface Temperature", *Int. J. Heat Mass Transfer*, 20 (2), 827-840.

Zell, M., Straub, J., Weinzierl, A., 1984, "Nucleate Pool Boiling in Subcooled Liquid Under Microgravity-Results of TEXUS Experimental Investigations", *Proc. of the 5th European Symp. on Matl. Sci. Under Microgravity, Schloss Elmau, Nov. 5-7*, pp. 327-333.

Zuber, N., 1958, "On the Stability of Boiling Heat Transfer", *Trans. ASME, Ser. C, J. Heat Transfer*, 80 (4), 711-720.

Zuber, N., Tribus, M., Westwater, J. W., 1961, "The Hydrodynamic Crisis in Pool Boiling of Saturated and Subcooled Liquids", *Int. Dev. Heat Transfer: Proc. of the 1961 Heat Transfer Conf.*, Paper 27, 230-236.